UCGE Reports

Number 20255

Department of Geomatics Engineering

Development of a Precise GPS/INS/On-Board Vehicle Sensors Integrated Vehicular Positioning System

(URL: http://www.geomatics.ucalgary.ca/research/publications/GradTheses.html)

By

Jianchen Gao

June 2007

THE UNIVERSITY OF CALGARY

Development of a Precise GPS/INS/On-Board Vehicle Sensors

Integrated Vehicular Positioning System

by

Jianchen Gao

A THESIS

SUBMITTED TO THE FACULTY OF GRADUATE STUDIES

IN PARTIAL FULFILLMENT OF THE REQUIREMENTS FOR THE

DEGREE OF Doctor of Philosophy

DEPARTMENT OF GEOMATICS ENGINEERING

CALGARY, ALBERTA

June, 2007

Abstract

As a commonly used system for a land vehicle positioning system, a GPS/INS integrated system harnesses either a tactical grade or low cost IMU. The high cost of a tactical grade IMU constitutes its main limitation to commercial deployment. The performance of a low cost IMU degrades quickly over a short time interval of GPS outages. A larger error drift of a low cost IMU is not well suited to a land vehicle positioning system that has a strict requirement on positioning accuracy such as an intelligent or autonomous vehicle control system.

With a consideration of low cost and high accuracy, several on-board vehicle sensors built-in an actual vehicle stability control system are integrated with GPS and low cost IMU. The on-board vehicle sensors are dedicated to bridging the gap and limit low cost IMU rapid drift errors during GPS outages.

The on-board vehicle sensors used and analyzed include four wheel speed sensors, G sensors (accelerometers), yaw rate sensor (angular rate gyro) and steering angle sensor. Three basic and two combined integration strategies and algorithms are developed. The integration of the steering angle sensor is particularly novel. A mechanism is developed to detect and alleviate the violation of the lateral non-holonomic constraint widely used in the wheel speed sensor. The integrated system is implemented in both post-mission and real-time.

The benefits gained from the on-board vehicle sensors are investigated in terms of the positioning accuracy and the time-to-fix GPS ambiguities. The integration strategy with all on-board vehicle sensors performs best among all the proposed integration strategies. With respect to the GPS and low cost IMU integrated system, its percentage improvements are 92.6% for a post-mission test in an open-sky area by simulating GPS outages, 65.1% for a suburban area real-time test and 79.2 % for a pseudo-urban area real-time test. For ambiguity resolution, the percentage improvement over GPS-only in terms of the average time-to-fix ambiguity by integrating all on-board vehicle sensors with a low cost IMU is about 15% for 40 s GPS outages.

Acknowledgements

I would like to express my sincere gratitude to those who helped me complete this dissertation:

To my supervisor, Dr. Elizabeth Cannon, for her continuous support, encouragement and guidance on my studies and research. She provided me with an opportunity to study in the Position, Location And Navigation (PLAN) group with a very good facility, a strong academic environment and a multidisciplinary research team. She also assigned me a challenging research topic, which was of great benefit to the improvement of my knowledge as well as to my future career.

To Dr. Gérard Lachapelle for his many constructive suggestions on my studies and research.

To Dr. Mark Petovello for his insightful advice and kind help in many ways. My research is primarily built on his previous work. I feel fortunate to have worked with him on a research project for more than two years. Without his help, my research could not have gone so smoothly.

To Jared Bancroft and Kirk Collins for their patience and hard work in carrying the very heavy batteries and the rack as well as conducting field tests on icy or muddy roads in very cold or hot weather. They provided me with not only valuable datasets, but also set

me an example of how to find pleasure from helping others.

To current and past PLAN group members, such as John Schleppe, Saurabh Godha, Wei Yu, Sanjeet Singh, Haitao Zhang, Haitao Qiu, Ping Lian, Changlin Ma, Bo Zheng, to name a few. Many thanks to my Chinese friends outside the PLAN group, YuFeng Zhang, Xaioji Niu and Guangcai Meng.

I greatly appreciate all the examining committee members for their time and advice on the revision of this dissertation.

Last but not least, the never-ending understanding and encouragement from my parents, my wife, my daughter, my brother and my sister are the main reasons for keeping me optimistic in the face of many hardships. I owe a lot to my family.

Table of Contents

List of Tables

List of Figures

xiv

Notation

List of Acronyms

ABS	Anti-Block System
ADOP	Ambiguity Dilution of Precision
b frame	Body frame
C/A	GPS Coarse/Acquisition code
DOP	Dilution of Precision
ECEF	Earth-Centreed-Earth-Fixed Frame
e frame	ECEF frame
GL	G Sensors
GX	X Accelerometer of G Sensors
GY	Y Accelerometer of G Sensors
HDOP	Horizontal Dilution of Precision
SAS	Steering Angle Sensor
STD	Standard Deviation
Sigma	1σ (Standard deviation)
TC	Traction Control
IMU	Inertial Measurement Unit
INS	Inertial Navigation System
LAMBDA	Least-Squares Decorrelation Adjust Method
GPS	Global Positioning System
v frame	Vehicle frame
VCV	Variance and Covariance Matrix
VDOP	Vertical Dilution of Precision
VSC	Vehicle Stability Control System

WL	Widelane
WSS	Wheel Speed Sensors
YRS	Yaw Rate Sensor
LQR	Linear Quadratic Regulation

List of Symbols

ϕ	Carrier phase measurement in cycles
ϕ_{L1}	L1 carrier phase measurements
ϕ_{L2}	L2 carrier phase measurements
ϕ_{WL}	Widelane measurement
P	Pseudorange measurement in metres
ρ	Geometric range between the satellite the receiver
BW_{GL}	Bandwidth of G sensors and yaw rate sensor
BW_{YRS}	Bandwidth of G sensors and yaw rate sensor
dp	Orbital error
dt	Satellite clock error
dT	Receiver clock error
d_{ion}	Ionospheric error
d_{trop}	Tropospheric error
ε_M	Multipath error
ε_N	Measurement noise
N	Ambiguity integer
$\nabla\Delta$	Double difference operator
δf^b	Accelerometer errors

b^b	Accelerometer biases
S_f	Scale factor error of the accelerometer
f^b	Accelerometer measurement
$c_T \cdot \delta T$	Error effect with respect to the temperature
$\delta\omega_{ib}^b$	Gyro errors
d^b	Gyro biases
S_ω	Gyro scale factor error
ω_{ib}^b	Gyro measurement
γ_f	Non-orthogonalities errors of accelerometers
γ_ω	Non-orthogonalities errors of gyros
r^e	Position vector
v^e	Velocity vector
R_b^e	Direction cosine matrix between b and e frame
g^e	Gravity vector in e frame
Ω_{ib}^b	Skew-symmetric matrix of the gyro measurement
Ω_{ie}^e	Skew-symmetric matrix of the Earth rotation rate
ω_{ie}^e	Earth rotation rate
ΔV^b	Incremental velocity
$\Delta\theta^b$	Incremental angle
Δt	IMU data sampling rate
δr^e	Position error vector

δv^e	Velocity error vector
ε^e	Misalignment angle error vector
δb^b	Vector of the accelerometer bias errors
δd^b	Vector of the gyro bias errors
$\Delta\nabla N$	Vector of double difference carrier phase ambiguities
w_f	Accelerometer noise
w_w	Gyro noise
$diag(\alpha_i)$	Diagonal matrix of the correlated time constant reciprocals for the accelerometer bias model
$diag(\beta_i)$	Diagonal matrix of the correlated time constant reciprocals for the gyro bias models
w_b	Driving noise for the accelerometer biases
w_d	Driving noise for the gyro biases
F^e	Skew-symmetric matrix of specific force in e frame
N^e	Tensor of the gravity gradients
x	True value of a state
$\hat{x}$	Estimated state
δx	Error state vector
F_{INS}	Dynamics matrix for stand-alone INS system
G_{INS}	Shaping matrix of the driving noise of the stand-alone INS system
w	Noise matrix
σ_{WSS}^2	Wheel speed sensor average measurement variance
$\sigma_{WSS\rightarrow GPS}^2$	Average variance of wheel speed sensor relative to OEM2 GPS receiver
σ_{GPS}^2	Average measurement variance of OEM2 GPS receiver

$\sigma^2_{GLNoise}$	Noise level of G sensors and yaw rate sensor
$\sigma^2_{YRSNoise}$	Noise level of G sensors and yaw rate sensor
$\sigma_{b_{GL}}$	Temporal standard deviation of G sensor biases
$\sigma_{b_{YRS}}$	Temporal standard deviation of yaw rate sensor bias
z	Measurement vector
H	Design matrix
w_m	Measurement noise
$\Phi_{k,k+1}$	Transition matrix in Kalman filter
P^-	A priori estimated covariance matrix
P	A posteriori estimated covariance matrix
Q_k	Process noise matrix
q_{GL}	Noise spectral density of G sensors and yaw rate sensor
q_{YRS}	Noise spectral density of G sensors and yaw rate sensor
$q_{b_{GL}}$	Spectral density of the biases of G sensors
$q_{b_{YRS}}$	Spectral density of the biases of yaw rate sensor
K	Kalman filter gain
I	Identity matrix
$P^e_{IMU \rightarrow GPS}$	Position in e frame transformed from IMU to GPS antenna phase centre
P^e_{IMU}	IMU position in e frame
$L^b_{IMU \rightarrow GPS}$	Lever arm vector between IMU and GPS antenna phase centre
$V^e_{IMU \rightarrow GPS}$	Velocity in e frame transformed from IMU to GPS antenna phase centre

V_{IMU}^{e}	IMU velocity in e frame
$V_{WSS \to GPS}^{e}$	Velocity in e frame transformed from the rear wheel axis to GPS antenna phase centre
V_{WSS}^{e}	Velocity at the centre point of the rear wheel axis in e frame
$L_{WSS \to GPS}^{b}$	Lever arm vector from the centre point of the rear wheel axis to GPS antenna phase centre,
$V_{SAS \to GPS}^{e}$	Velocity in e frame transformed from the centre point of the front wheel axis to GPS antenna phase centre
V_{SAS}^{e}	Velocity at the centre point of the front wheel axis in e frame
$L_{SAS \to GPS}^{b}$	Lever arm vector from SAS to the GPS antenna phase centre
$V_{GL/YRS \to GPS}^{e}$	Velocity in e frame transformed from GL/YRS unit to GPS antenna phase centre
$V_{GL/YRS}^{e}$	Velocity at the centre point of GL/YRS unit in e frame
$L_{GL/YRS \to GPS}^{b}$	Lever arm vector from GL/YRS unit to GPS antenna phase centre
V_{WSS}	Velocity for wheel speed sensor update in vehicle frame
S	Wheel speed sensor scale factor
$v_{GPS/INS/WSS}^{e}$	Velocity of the GPS/INS/WSS integrated system in e frame
O	Zero matrix with the subscripted dimensions
AR	Number of float ambiguities
$F_{GPS/INS}$	Dynamics matrix for GPS/INS integration strategy
$G_{GPS/INS}$	Shaping matrix of the driving noise in GPS/INS system
$F_{GPS/INS/WSS}$	Dynamics matrix for GPS/INS/WSS integration strategy
$G_{GPS/INS/WSS}$	Shaping matrix for GPS/INS/WSS integration strategy

δS	Wheel speed sensor scale factor error state
ε_{b-v}	Error vector of the tilt angles between body frame and vehicle frame
V_{RR}	Rear right wheel speed sensor measurement
V_{RL}	Rear left wheel speed sensor measurement
v_{WSS}	Average of the rear wheel speed sensor measurements
α, β, γ	Tilt angles between b and v frames with respect to the X, Y and Z axes, respectively
R_b^v	Direction cosine matrix between b and v frames
δb_{GL}	Error vector of G sensor biases
δd_{YRS}	Error vector of the yaw rate sensor bias
β_{GL}, β_{YRS}	Time constant reciprocals of the first-order Gauss-Markov process model for the GL and YRS biases respectively
$\beta_{b_{GL}}, \beta_{b_{YRS}}$	Time constant reciprocal of G sensors and yaw rate sensor biases
w_{GL}, w_{YRS}	Driving noises for the GL and YRS biases respectively
$F_{GPS/INS/GL/YRS}$	Dynamics matrix for the GPS/INS/GL/YRS integration strategy
$G_{GPS/INS/GL/YRS}$	Shaping matrix for GPS/INS/GL/YRS integration strategy
f_x, f_y	Specific force measurements from the G sensors
γ	Yaw rate sensor measurement
V_x^b, V_y^b, V_z^b	Velocities in b frame

g_x^b, g_y^b, g_z^b	Gravity elements in the b frame
$b_{GL}, \; d_{YRS}$	Biases of G sensors and yaw rate sensor respectively.
g^e	Gravity vector in e frame
V^b	Velocity vector in b frame
f	Specific force vector from G sensors
$H_{GL/YRS}$	Design matrix for GL/YRS update
δS_{SAS}	Error state of the steering angle sensor scale factor
δd_{SAS}	Error state of the steering angle sensor bias
$F_{GPS/INS/SAS}$	Dynamics matrix of GPS/INS/SAS integration strategy
$G_{GPS/INS/SAS}$	Shaping matrix of GPS/INS/SAS integration strategy
S_{SAS}	Scale factor of the steering angle sensor
d_{SAS}	Bias of the steering angle sensor
ψ	Steering angle sensor measurement
$F_{GPS/INS/WSS/SAS/GL/YRS}$	Dynamics matrix of GPS/INS/WSS/SAS/GL/YRS strategy
$G_{GPS/INS/WSS/SAS/GL/YRS}$	Shaping matrix of GPS/INS/WSS/SAS/GL/YRS strategy
β_r	Rear wheel side slip angle
L_r	Distance between the GL/YRS and WSS
$P_{\hat{N}}$	Covariance matrix of estimated ambiguities

$P_{\hat{X}}$	Initial covariance matrix for ambiguity resolution
$P_{\hat{r}}$	Covariance matrix of the estimated error states
R_{WSS}	Radius of the wheel
N_{Pulse}	Number of pulses per second for wheel speed sensors
N_{Teeth}	Number of teeth for wheel speed sensors

Chapter 1   Introduction

1.1   Background

Vehicular positioning and navigation is one of the most important application areas for the Global Positioning System (GPS).   In modern society, significant attention has been paid to intelligent vehicle systems with the increase in demand for safe and flexible manuvering of a vehicle. Typical advanced vehicle systems include anti-lock brake systems (ABS), traction control (TC), and vehicle stability control systems (VSC), which have already found their way into the production of passenger vehicles (Tseng et al. 1999). In these systems, positioning accuracy and system redundancy have a crucial impact on their performance (Bevly 1999). Positioning accuracy and system redundancy also impact the performance and reliability of autonomous vehicle control systems and vehicle safety and stability control systems. The more accurate the positioning system, the more reliable the vehicle autonomy or the safety control. The importance of sensor redundancy lies in the fact that any sensor failure due to mechanical, electrical or external disturbances could lead to a disastrous result if the failed sensor was the only sensor on-board (Redmill et al. 2001).

For autonomous vehicle control, Carlson (2003) focused on parameter estimation of vehicle models used for navigation and stability control, including the estimation of

longitudinal stiffness and wheel effective radius. Bevly (2001) investigated the automatic steering control of farm vehicles. By devising a new model for the farm vehicle's yaw dynamics, a Linear Quadratic Regulation (LQR) controller was developed to implement accurate lateral control of farm vehicles.

In autonomous vehicle control and vehicle stability control systems, GPS and other dead-reckoning sensors can provide navigation and positioning information (Bevly 1999). With respect to GPS, centimetre-level accuracies can be achieved by using carrier phase measurements in a double difference approach whereby the integer ambiguities are resolved correctly. However, difficulties arise during significant shading from obstacles such as buildings, overpasses and trees. This has led to the development of integrated systems in which the GPS is complemented by an inertial navigation system (INS). GPS provides long-term, accurate, and absolute positioning information. It is also immune to gravity. However, it is subject to blockage of line-of-sight signals as well as signal interference or jamming. In addition, its measurement update rate is relatively low (< 20 Hz). By contrast, an INS is autonomous and non-jammable. Because of its high bandwidth, an INS provides relative navigation information at a high data rate. Most IMU data rates exceed 50 Hz with some reaching into several hundreds of Hz (Petovello 2003). However, the weak points of an INS lie in the fact that its navigation quality degrades with time, and its accuracy depends on the quality of INS sensors.

GPS/INS integration has been recognized as an effective means for kinematic positioning (Cannon 1990). In a GPS-aided INS integrated system, the INS derives position, velocity and attitude that are used as the primary navigator outputs. The GPS provides update information for the INS, and a Kalman filter can serve as an adequate formulation for system integration (Farrell et al. 2000 and Omerbashich 2002). The INS and GPS are usually coupled in one of three different ways: loose coupling, tight coupling and deep coupling (El-Sheimy 2004, Farrell & Barth 1998 and Schwarz & Wei 1999) to provide continuous navigation solutions. The integrated system can maintain centimetre-level accuracies with fully available GPS or during short GPS outages provided the inertial sensors are sufficiently accurate (Scherzinger 2000).

Significant research has been undertaken on GPS and INS integration for precise kinematic positioning. Petovello (2003) integrated carrier phase DGPS and a tactical grade IMU to provide decimetre-level accuracies during GPS outages. Both post processing and real-time tests were conducted. A comparison between the tight and loose coupling strategies shows that a tight coupling strategy outperformed a loose coupling strategy due to the reduction of noise in the integrated system. To compensate for the GPS time latency, a real-time system was implemented by storing INS data in a buffer and restoring it when the GPS data was available. Scherzinger (2000) investigated a precise robust positioning system by integrating GPS and a tactical grade IMU. Inertial navigation errors, gyro and accelerometer biases, as well as float double difference

ambiguities, were estimated. The positioning accuracy during partial and complete GPS outages was described. By integrating GPS and low cost inertial sensors, Sukkarieh (2000) developed a low cost, high integrity, aided inertial navigation system for autonomous land vehicle applications.

The accuracy of an integrated system can be further improved by applying some effective measures (Masson et al. 1996). These measures include non-holonomic constraints, Zero Velocity Updates (ZUPTs) as well as limiting attitude error growth (Shin 2001). When the vehicle does not jump off or slide on the ground, non-holonomic constraints assume the velocities in lateral and longitudinal directions to be zero (Sukkarieh 2000).

Due to the importance of fast and reliable GPS ambiguity resolution on high positioning accuracy, the aforementioned research done by Petovello (2003) and Scherzinger (2000) also discussed the benefits of inertial aiding on ambiguity resolution. The time to fix ambiguities is measured by the volume of the search space that is closely related to the covariance matrix of the estimated ambiguities. Skaloud (1998) derived a closed form of ambiguity covariance with an external update from the GPS L1 carrier phase. It indicated that an enhanced precision of the float ambiguities and a reduction in the search volume depends on the a priori INS position error. A relatively smaller the a priori INS position error with respect to the C/A code measurement accuracy will introduce a reduction in the time-to-fix ambiguity resolution after GPS outages.

To improve accuracy and redundancy, numerous sensors are being employed in advanced and intelligent vehicle systems. Significant work has also been done to integrate GPS with other lower cost sensors to aid positioning and/or attitude determination. These sensors have ranged from the use of a compass, tilt meter and fiber-optic gyro for vehicle pitch and azimuth estimation (Harvey 1998), to the integration of GPS with an on-board odometer in ABS as well as gyro for positioning in urban areas (Stephen 2000). Wheel speed sensors are fundamental components of ABS which is standard equipment on most vehicles (Hay 2005). The integration of a wheel speed sensor with GPS/INS has been extensively studied. Kubo et al. (1999) implemented a GPS/INS/Wheel speed sensor integrated system in the wander angle frame for land-vehicle positioning, and proposed an algorithm to calibrate two tilt angles (azimuth and pitch) between the wheel speed sensor and the IMU body frame. Numajima et al. (2002) investigated the integration of INS/DGPS/Vehicle Motion Sensor (VMS) for land-vehicle in-motion alignment that could compensate the poor initialization or large cumulative errors by using a decentralized Kalman filter. Bonnifait (2003) developed a very inexpensive vehicle localization system by using GPS and ABS sensors (four wheel speed sensors) available on most modern cars. It showed that wheel speed sensors can also provide positioning information at several metres accuracy by integrating with GPS. Since the wheel speed sensor only measures velocity in a forward direction, most of the previous research

related to the integration of wheel speed sensor information with GPS/INS applied two non-holonomic constraints on the lateral and vertical directions (Shin 2005).

1.2 Limitations of Previous Research

As a commonly used system for a land vehicle positioning system, a GPS/INS integrated system harnesses either a tactical grade or low cost IMU as shown in previous research. The high cost of a tactical grade IMU constitutes its main limitation to commercial deployment. By contrast, the performance of a low cost IMU degrades quickly over a short time interval of GPS outages. A larger error drift is not well suited to such a land vehicle positioning system that has a strict requirement on positioning accuracy.

Augmenting other low cost sensors with a GPS/INS is an effective way to bridge GPS gaps (a time period of partial or complete GPS signal blockage) and reduce the stand-alone INS drift error. On-board vehicle sensors built-in a modern automotive vehicle provide the most direct and cost-efficient external aid sources for a GPS/INS system. To date, research on GPS/INS/On-board vehicle sensor integration mainly focuses on wheel speed sensors and low cost gyros (Yaw rate sensors). To make full use of on-board vehicle sensors, the previous research can be extended to investigate the possibilities and benefits of integrating various on-board vehicle sensors through various sensor combinations. By evaluating various sensors and their integration strategies, the positioning accuracy can be improved.

It was shown through previous research that an automatic vehicle steering system had been studied extensively in terms of dynamic modeling and parameter estimation (Carlson 2003 and Bevly 2001). However, how to make use of the steering angle sensor to enhance positioning accuracy during GPS outages has not been thoroughly investigated to date.

Previous research shows that a lateral constraint applied to wheel speed sensor integration is effective only when the vehicle operates on a flat road and no side slip occurs (Brandit & Gardner 1998 and Dissanayake et al. 2001). It is no longer valid when the vehicle jumps off the road or is driven on an icy or bumpy road where a larger side slip angle can occur. In a land vehicle positioning system, the violation of non-holonomic constraints is always accompanied by larger side slip angles (ibid). Side slip is a very complicated phenomenon. A larger side slip angle that exceeds a specific threshold (5 degrees used in this dissertation) is usually coupled with road and tire conditions, high vehicle dynamics including fast driving, sharp turns as well as high pitch and roll angular rates. Typical side slip angles range approximately from 0 to 30 degrees (Ray 1995). Anderson & Bevly (2004) investigated a model-based Kalman filter with GPS velocity measurements to estimate side slip.   However, its estimation accuracy relies heavily on the correctness of the model which is difficult to develop for various road conditions.

Both real-time and post-mission processing is necessary for the development of an integrated system. The purpose of post-mission processing is to fine tune the parameters

of the Kalman filter, to assess the modeling of the sensors, and to check the validity of the algorithm. It saves time and cost during system development and reduces the need for conducting field tests each time a scenario needs to be evaluated. As an ultimate goal in practical applications, a real-time system provides an instantaneous positioning solution. The validity of the Kalman filter design and the impact of various sensor combinations can be evaluated by real-time test scenarios. Petovello (2003) successfully implemented a GPS/INS real-time integrated system. This work can be further extended into a GPS/INS/On-board vehicle sensor real-time system with enhancements.

For a tactical grade IMU, the benefit of inertial aiding on ambiguity resolution has been investigated extensively. A comparison between different grades of IMUs (tactical grade and automotive grade low cost IMU) in terms of a time-to-fix integer ambiguities will enrich these research findings even though the benefits gained from a low cost IMU may be somewhat limited than expected. When on-board vehicle sensors are integrated, the improvements on ambiguity resolution gained from on-board vehicle sensors can be analyzed in addition to the positioning accuracy.

1.3   Objectives and Contributions of This Dissertation

Based on the above discussion, with particular emphasis on Petovello (2003), this dissertation aims to develop an enhanced land vehicle integrated system. The primary objective of this research is to develop a precise land vehicle positioning system with a

consideration of low cost, high accuracy and fast ambiguity resolution. Several on-board vehicle sensors built-in the vehicle stability control system of an actual vehicle are designed to integrate with GPS and low cost IMU. The on-board vehicle sensors, including wheel speed sensors, G sensors and yaw rate sensor, and steering angle sensor, are dedicated to bridging the gap during GPS outages and limit low cost IMU rapid drift errors to some degree depending on the characteristics of the vehicle sensors.

To achieve this objective, this dissertation focuses on the following methodologies or research topics:

- *Analysis of on-board vehicle sensors and development of integration strategies as well as algorithms.* The characteristics of on-board vehicle sensors are analyzed to obtain key statistical specifications and error models. The integration strategies are investigated by making full use of on-board vehicle sensors in either an individual or combined manner. The basic integration modules are developed by integrating individual on-board vehicle sensors. Among all the basic integration modules, the integration of a steering angle sensor with GPS and INS constitutes a novel integration strategy. Another valuable investigation proposal is to develop combined integration strategies either by a sequential combination of the basic integration modules or by creating a complementary relationship between different types of sensors. With an appropriate modelling of on-board vehicle sensors, integration algorithms will be developed by deriving dynamics and measurement models.

- *Detection and alleviation of the lateral constraint violation.* With regard to the wheel speed sensor integration strategy and algorithm, the widely used lateral constraint is close to the real situation without the side slip or the side slip angle is small. The system positioning accuracy will be definitely degraded if the lateral constraint is violated by a larger side slip angle. To compensate the violation of the lateral constraint and enhance the positioning accuracy, how to detect and alleviate the violation of the lateral constraint will be investigated in this thesis.

- *Implementation of the integration strategies and algorithms.* A hardware platform is set up by including GPS receivers, a low cost IMU and on-board vehicle sensors time-tagging system, a pair of radio link transceivers as well as computers. The integration strategies and algorithms are implemented in both post-mission and real-time.

- *Benefits gained from the integration of on-board vehicle sensors.* It is important to investigate what benefits can be gained from integrating on-board vehicle sensors in terms of positioning accuracy and ambiguity resolution. With the reference solution provided by an integrated system with the superior quality IMU, positioning accuracy with respect to the proposed integration strategies will be analyzed by various tests for both tactical grade and low cost IMUs. The time-to-fix GPS ambiguity resolution after GPS outages will be compared between GPS-only, GPS/INS as well as GPS/INS/On-board vehicle sensors integration strategies for both tactical grade and low cost IMU integrated systems, respectively.

The major contributions of this dissertation are summarized below.

1. By considering a variety of on-board vehicle sensors, three basic and two combined integration strategies and algorithms are developed. The errors of on-board vehicle sensors are modelled in an appropriate manner. The dynamics and measurement models of the Kalman filter are developed for each integration strategy. Among all the integration strategies, the integration of the steering angle sensor is particularly novel for its application in a positioning and navigation system.

2. In one of the combined integration strategies, an interactive relationship is created between the wheel speed sensors, G sensors and yaw rate sensor. Using the relationship between different sensors, a mechanism is developed to detect and alleviate violations of the lateral non-holonomic constraint used in most of the previous research.

3. The GPS/INS/On-board vehicle sensor integration strategies and algorithms are successfully implemented in both real-time and post-processing after Petovello (2003). For various integration strategies, the benefits gained from on-board vehicle sensors in terms of positioning accuracy and ambiguity resolution are investigated in detail.

1.4   Dissertation Outline

This dissertation consists of eight chapters describing how to achieve the objectives outlined above. The chapters are organized as follows.

Chapter 2 introduces background information that is relevant to this research. Three different frames, namely the IMU body frame (b frame), the vehicle frame (v frame) and ECEF (Earth-Centred Earth-Fixed) frame (e frame), are defined. The fundamentals of GPS and INS are discussed and include: GPS observables, GPS errors, GPS ambiguity resolution, INS error sources and equations of motion as well the INS error dynamics model.

In Chapter 3, the characteristics of the selected on-board vehicle sensors are analyzed. With a reference velocity provided by the NovAtel OEM2 precise velocity GPS receiver, the measurement accuracy of the wheel speed sensors is assessed. G sensors and yaw rate sensors are evaluated using mathematical variance and wavelet decomposition for a static data set over seven hours. The temporal variability characteristics are analyzed by deriving a first-order Gauss-Markov process. The steering angle sensor is also introduced.

To illustrate in detail the development of integration strategies of GPS, INS and on-board vehicle sensors, Chapter 4 first gives an overview of the Kalman filter algorithm. On the basis of a comparison between a linearized and extended Kalman filter as well as between a centralized (tight coupling strategy) and decentralized (loose coupling strategy) Kalman filter, various integration strategies are proposed.

In Chapter 5, the lever arm effect and the way of estimating the wheel speed sensor lever arm vector are discussed due to the importance of the lever arm effect on the integrated

system positioning accuracy. The integration algorithms are described by showing the dynamics and measurement models for each integration strategy.

Chapter 6 describes the equipment used as well as the configuration of the hardware platform. By dealing with GPS time latency in real-time, a way to implement a real-time GPS/INS/On-board vehicle sensor integrated system is analyzed.

Chapter 7 first describes the tests conducted in different areas. By showing the data analysis and processing methods, the data collected is analyzed with respect to various integration strategies. The benefits gained from integrating all on-board vehicle sensors in terms of positioning accuracy as well as ambiguity resolution are investigated.

Chapter 8 concludes the entire work of this dissertation. Recommendations for future work are also presented.

Chapter 2   Fundamentals of GPS and INS

This chapter reviews background information that is necessary for the development and analysis in later chapters. These include coordinate frame definitions, GPS and INS.

2.1   Coordinate Frame Definitions

Three coordinate frames are important to this research. These include the ECEF frame (e frame), the body frame (b frame) and the vehicle frame (v frame), as described below. The three frames are shown in Figure 2.1.
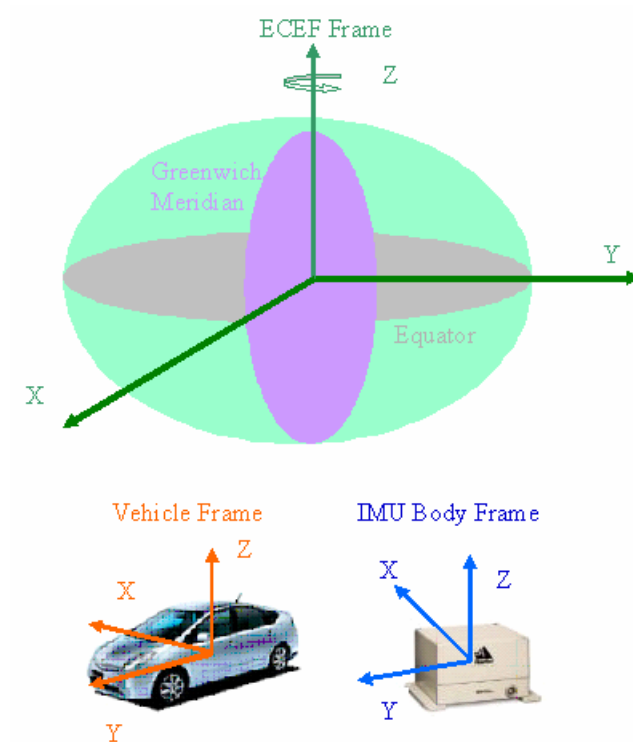
Figure 2.1 Coordinate frame definition

The origin of the ECEF frame is the centre of the Earth's mass. The X-axis is located in the equatorial plane and points towards the mean Greenwich Meridian. The Y–axis is also located in the equatorial plane and is 90 degrees east of the mean Greenwich Meridian. The Z-axis parallels the Earth's mean spin axis (Wang 2003).

The IMU body frame (b frame) represents the orientation of the IMU axes. The IMU sensitive axes are assumed to be approximately coincident with the moving platform upon which the IMU sensors are mounted. The origin of the body frame is at the centre of the IMU. The X-axis points towards the right of the moving platform upon which the IMU sensors are mounted, the Y-axis points toward the front of the moving platform, and the Z-axis is orthogonal to the X and Y axes to complete a right-handed frame.

The vehicle frame (v frame) refers to vehicle body frame, and represents the orientation of the vehicle. The origin is the vehicle centre of gravity. The X-axis points towards the right side of the vehicle and the Y-axis points towards the forward direction of the vehicle's motion. The Z-axis is orthogonal to the X and Y axes to complete a right-handed frame.

2.2   Global Positioning System

GPS is an all-weather satellite navigation system, and has been widely used in air, land and marine environments as the navigation and positioning tools. Depending on the measurements and data processing method, the accuracy of GPS positioning ranges from

several metres to the centimetre-level (Lachapelle 2003). To deal with GPS-related issues,

GPS observables, limitations, error sources and ambiguity resolution will be discussed

below.

2.2.1　GPS Observables and Limitations of GPS

GPS satellites broadcast a signal on a carrier wave with two frequencies (1575.42 MHz

for L1, 1227.60 MHz for L2) modulated by the C/A code and P code. By acquiring and

tracking satellite signals, most GPS receivers generate three GPS measurements:

pseudorange, carrier phase and Doppler. Pseudorange measurements are generated by

measuring the difference between the transmission time and reception time for tracking a

GPS signal code. GPS carrier phase measurements are generated by beating the

frequency between the received GPS carrier signal and the carrier signal generated within

the receiver. The carrier phase measurements are ambiguous by an unknown integer

number of cycles. The Doppler measures the instantaneous phase measurement rate,

which is the derivative of the carrier phase measurement (Kaplan & Hegarty 2006).

With dual frequencies, L1 and L2, carrier phase measurements, ϕ_{L1} and ϕ_{L2}, can be

linearly combined to generate a new measurement including widelane, narrowlane and

ionosphere-free. The widelane measurement, ϕ_{WL}, of interest to this study is given by

$$\phi_{WL} = \phi_{L1} - \phi_{L2} \tag{2.1}$$

The widelane combination exhibits a relatively longer wavelength at approximately 86 cm and reduces the ionospheric error (in cycles) four-fold with respect to L1 only observations. Thus, the widelane is more reliable and faster to resolve ambiguities under adverse conditions (Liu 2003). Despite the advantages of ambiguity resolution, the widelane combination amplifies noise compared to L1 and L2 raw observables in metres.

GPS is susceptible to line-of-sight blockage when operating in urban areas or under dense foliage. Signal blockage of several satellites may result in a sudden deterioration in positioning accuracy. Other causes of signal loss include intense ionospheric activity, satellite failure and inadvertent jamming. When using carrier phase measurements, cycle slips can occur due to loss of phase lock, which results in discontinuous measurements that limit positioning accuracy. To detect and correct cycle slips, the phase velocity trend method, the double frequency detection method or a Kalman filter innovation-based detection method can be used (Bisnath & Kim 2001). If cycle slips are detected, attempts can be made to correct the ambiguity by the number of slipped cycles. Additionally, when using Real-Time Kinematic (RTK) GPS, an outage can be caused by loss of radio communication between the base and the rover. An outage at the GPS base station can cause rapid deterioration of the GPS rover positioning accuracies (Woolven & Scherzinger 1997). All of these are limitations of GPS that need to be considered.

2.2.2 GPS Error Sources

GPS measurements are corrupted by errors. The main error sources include satellite and

receiver clock error, orbital error, ionospheric and tropospheric errors as well as multipath

and receiver noise. By taking into account these error sources, GPS measurement

equations are expressed by

$$P = \rho + d\rho + c(dt - dT) + d_{ion} + d_{trop} + \varepsilon_N + \varepsilon_M \tag{2.2}$$

$$\phi = \frac{1}{\lambda}\left[\rho + d\rho + c(dt - dT) - d_{ion} + d_{Trop} + \varepsilon_N + \varepsilon_M\right] + N \tag{2.3}$$

$$\dot{\phi} = \frac{1}{\lambda}\left[\dot{\rho} + d\dot{\rho} + c(d\dot{t} - d\dot{T}) - \dot{d}_{ion} + \dot{d}_{trop} + \dot{\varepsilon}_M + \dot{\varepsilon}_N\right] \tag{2.4}$$

where P is the pseudorange measurement in metres, ρ is the geometric range between

the satellite and receiver, dp is the orbital error, dt and dT are satellite and receiver

clock errors respectively, d_{ion} is the ionospheric error, d_{trop} is the tropospheric error,

ε_M is the multipath error, ε_N is the measurement noise, ϕ is the carrier phase

measurement in cycles, and N is the ambiguity integer.

To achieve centimetre-level accuracies, double differenced carrier phase measurements

must be used with ambiguities being resolved to their correct integers (Kaplan & Hegarty

2006 and Hofmann-Wellenhof et al. 1997). Double differenced GPS measurements are

computed between the reference and the rover as well as between two satellites to

eliminate the receiver and satellite clock errors. The orbital, ionospheric and tropospheric

errors are significantly reduced, and their reductions are correlated with spatial separation

between the base and rover stations. The noise level in the double differenced

measurements, however, is amplified due to the linear combinations in the double differenced operation.

On the basis of Equations (2.2) to (2.4), the double differenced measurements are expressed by

$$\nabla\Delta P = \nabla\Delta\rho + \nabla\Delta d\rho + \nabla\Delta d_{ion} + \nabla\Delta d_{trop} + \nabla\Delta\varepsilon_M + \nabla\Delta\varepsilon_N \qquad (2.5)$$

$$\nabla\Delta\phi = \frac{1}{\lambda}\left(\nabla\Delta\rho + \nabla\Delta d\rho - \nabla\Delta d_{ion} + \nabla\Delta d_{trop} + \nabla\Delta\varepsilon_M + \nabla\Delta\varepsilon_N\right) + \nabla\Delta N \qquad (2.6)$$

$$\nabla\Delta\dot\phi = \frac{1}{\lambda}\left(\nabla\Delta\dot\rho + \nabla\Delta d\dot\rho - \nabla\Delta\dot d_{ion} + \nabla\Delta\dot d_{trop} + \nabla\Delta\dot\varepsilon_M + \nabla\Delta\dot\varepsilon_N\right) \qquad (2.7)$$

where $\nabla\Delta$ is the double difference operator.

The satellite orbital error is characterized by a discrepancy between the computed satellite positions from the broadcast ephemeris in the navigation message and their actual values. The residual double differenced satellite orbit error is a function of the baseline length. It is around 0.1-0.3 ppm.

Ionospheric error is caused by electrons in the atmosphere layer from 50 to 1500 km above the Earth's surface that affect the propagation of radio waves. It is frequency dependent and spatially correlated, and varies with geographic position and solar activity (Hofmann-Wellenhof et al. 1997). The phase measurement is advanced and the code measurement is delayed by the ionospheric error with equal magnitude and opposite sign. The double differenced ionospheric error is approximately 1-3 ppm. It may reach 20 ppm or more under extreme ionospheric conditions (Lachapelle 2003 and Cannon 1991).

The troposphere delay is caused by the neutral troposphere atmosphere that slightly bends the traveling path of the GPS signal. The error consists of dry and wet parts with the dry delay being the larger of the two effects. It can be modeled as a function of atmospheric pressure, temperature, relative humidity and satellite elevation angle. Given explicit modeling or correction, the residual tropospheric error is generally less than 1 ppm (Misra & Enge 2001). Under the assumption of short to medium baselines, the tropospheric error is generally negligible after applying troposphere modeling.

Multipath is the error resulting from the reflection and diffraction of a direct GPS signal by such structures as buildings or the edges of sharp objects. Since it is highly dependent on the surroundings of the GPS receiver antenna, it is difficult to predict and to compensate for, and cannot be mitigated by double differencing. Typically, the undifferenced C/A-code multipath error tends to be at several metres under adverse conditions. With a benign environment, the C/A code multipath error is at the decimetre level (1σ level of 20 cm). By contrast, the L1 carrier phase multipath error is at the centimetre level (1σ level of 2 cm) (Kaplan & Hegarty 2006).

Measurement noise is generated by the effects of thermal noise and dynamic stress in a receiver tracking loop. Measurement noise is closely related to satellite elevation angle: the lower the elevation angle the higher the measurement noise. Measurement noise is actually amplified by double differencing. The standard deviation of C/A-code measurement noise can be around 5-10 cm by using narrow correlator GPS receivers. The

standard deviation of L1 carrier phase measurement noise is 1.2 mm (Kaplan & Hegarty 2006). The low multipath and noise error on carrier phase measurements illustrates the advantages of these measurements for high positioning accuracy. On the basis of the above analysis, Table 2.1 summarizes the characteristics and magnitudes of GPS errors.

Table 2.1 GPS Errors and Magnitudes (after Petovello 2003)

GPS Errors	Characteristics	Magnitude
Orbital	Spatially correlated	Typical: 0.1-0.3 ppm
Ionosphere	Spatially correlated Frequency dependent Varies with geographic location and solar activity	Typical: 1-3 ppm Extreme: > 10 ppm
Troposphere	Spatially correlated Frequency independent	Typical: < 1 ppm Extreme: 1-3 ppm
Multipath	Dependent on surroundings, antennas and elevation angle	Code: 20 cm Phase: 2 cm
Measurement Noise	Amplified by double differencing Elevation angle dependent	Code: 5-10 cm Phase: 1-2 mm

2.2.3   GPS Ambiguity Resolution

To achieve centimetre-level accuracies in a reasonable amount of time, double differenced carrier phase measurements must be used with ambiguities being resolved to their correct integers (Misra & Enge 2001 and Hofmann-Wellenhof et al. 1997).

Numerous methods are available for ambiguity resolution and validation such as the least-squares ambiguity search technique (Hatch 1994), the least-squares ambiguity decorrelation adjustment method (LAMBDA) (Teunissen & Kleusberg 1996 and Hein & Werner 1995), the fast ambiguity search filter (FASF) (Chen 1994), and sequential

integer rounding (Bootstrapping Method) (Han & Rizos 1997). Even though these methods are different in some aspects, most of them follow similar procedures that include estimation of real-valued ambiguity values and their corresponding covariance matrices by least squares or Kalman filtering, the definition of a search volume, the determination of correct integers and the validation of the selected set. The LAMBDA method is used in this research as it has been shown to be both computationally efficient and reliable (Teunissen & Kleusberg 1996).

Ambiguity resolution is significantly affected by many factors such as satellite availability, measurement reliability and GPS error sources. Deterioration in satellite availability increases the difficulty for ambiguity resolution by extending the time to search and fix the integers. Therefore, it is difficult to accomplish both fast and reliable ambiguity resolution in this case. The blunders caused by unreliable measurements can greatly affect parameter estimations including real-valued ambiguities. Consequently, measurement reliability has a crucial effect on the accuracy of ambiguity resolution. Furthermore, large error sources introduce uncertainty for ambiguity resolution and cause real-valued estimates to differ from an integer number of cycles. Thus, the larger the error, the more the ambiguity will vary from its correct integer value.

2.3   Inertial Navigation Systems

The IMU consists of a triad of accelerometers as well as a triad of gyros. It measures three dimensional specific force and angular rates with respect to the IMU axes. The IMU measurements are sensitive to temperature and are susceptible to errors and noise. By using a mechanization equation, the navigation solution including position, velocity and attitude can be derived from the IMU measurements. To improve accuracy, the external aid on an INS can update the mechanization output and compensate for IMU measurement errors (Rogers 2000 and Grewal et al. 2001).

2.3.1   IMU Error Sources and Classification of IMU

Typical IMU errors are classified into bias, scale factor, and non-orthogonality of sensor triads, temperature related error as well as noise (Shin 2005 and Petovello 2003). They are mathematically expressed by

$$\delta f^b = b^b + S_f \cdot f^b + \Gamma_f \cdot \gamma_f + c_T \cdot \delta T + w_f \tag{2.8}$$

$$\delta \omega_{ib}^b = d^b + S_f \cdot \omega_{ib}^b + \Gamma_\omega \cdot \gamma_\omega + c_T \cdot \delta T + w_w \tag{2.9}$$

where δf^b represents the accelerometer errors, b^b is the accelerometer biases, S_f is the accelerometer scale factor error, f^b is the accelerometer measurement, $c_T \cdot \delta T$ is the temperature error effect, $\delta \omega_{ib}^b$ is the gyro error , w_f is accelerometer noise, w_w is gyro noise, d^b is the gyro bias, S_ω is the gyro scale factor error, ω_{ib}^b is the gyro

measurement, γ_f and γ_ω are the non-orthogonalities errors of the accelerometers and gyros, and are defined by

$$\gamma_f = \begin{bmatrix} \gamma_{xy}^f & \gamma_{xz}^f & \gamma_{yx}^f & \gamma_{yz}^f & \gamma_{zx}^f & \gamma_{zy}^f \end{bmatrix}^T \tag{2.10}$$

$$\Gamma_f = \begin{bmatrix} f_y^b & f_z^b & 0 & 0 & 0 & 0 \\ 0 & 0 & f_x^b & f_z^b & 0 & 0 \\ 0 & 0 & 0 & 0 & f_x^b & f_y^b \end{bmatrix} \tag{2.11}$$

$$\gamma_\omega = \begin{bmatrix} \gamma_{xy}^\omega & \gamma_{xz}^\omega & \gamma_{yx}^\omega & \gamma_{yz}^\omega & \gamma_{zx}^\omega & \gamma_{zy}^\omega \end{bmatrix}^T \tag{2.12}$$

$$\Gamma_\omega = \begin{bmatrix} (\omega_{ib}^b)_y & (\omega_{ib}^b)_z & 0 & 0 & 0 & 0 \\ 0 & 0 & (\omega_{ib}^b)_x & (\omega_{ib}^b)_z & 0 & 0 \\ 0 & 0 & 0 & 0 & (\omega_{ib}^b)_x & (\omega_{ib}^b)_y \end{bmatrix} \tag{2.13}$$

The magnitude of the errors determines the accuracy of an IMU. The IMU is mainly classified in terms of accuracy into different grades, namely navigational, tactical as well as automotive grades. There is a trade-off between quality and cost. Table 2.2 gives a brief comparison of different grades of IMUs.

Table 2.2 Comparisons of different grades of IMUs (El-Sheimy 2004, Shin 2001 and Godha 2006)

IMU grades	Navigational	Tactical	Automotive
Gyro bias (deg/h)	0.005-0.01	1.0-10.0	>100
Accelerometer bias (mg)	0.05-0.1	0.1-1.0	>1.0
Cost	>$90000	>$20000	<$2000

It is desired to achieve a high positioning accuracy by making use of a low cost IMU.

Three grades of IMU are used in this dissertation. The navigational grade IMU integrated

with DD GPS provides the reference solution for the integrated system. Both the tactical

grade and the low cost IMUs are integrated with a GPS and on-board vehicle sensors by

comparing their positioning accuracy to the reference solution.

2.3.2 Equation of Motion and Mechanization Equation

With IMU measurements, the equation of vehicle motion in e frame is expressed by

(Schwarz & Wei 1999)

$$\begin{bmatrix} \dot{r}^e \\ \dot{v}^e \\ \dot{R}^e_b \end{bmatrix} = \begin{bmatrix} v^e \\ R^e_b f^b - 2\Omega^e_{ie}v^e + g^e \\ R^e_b(\Omega^b_{ib} + \Omega^b_{ei}) \end{bmatrix} \tag{2.14}$$

where r^e is the position vector, v^e is the velocity vector, R^e_b is the direction cosine

matrix between the b and e frames, g^e is the gravity vector in the e frame, f^b is the

accelerometer measurements, Ω^b_{ib} is the skew-symmetric matrix of the gyro

measurement ω^b_{ib}, Ω^e_{ie} is the skew-symmetric matrix of the Earth's rotation rate ω^e_{ie},

and Ω^b_{ei} is the skew-symmetric matrix of ω^b_{ei}.

The position, velocity and attitude information shown in the equation of motion are

solved by the mechanization equation. The mechanization equation algorithm

implemented in this dissertation is detailed in Savage (2000). Due to the dead reckoning

nature of an IMU, the initial values of position, velocity and attitude are required as a

start-up for the mechanization equation. Position and velocity are usually initialized by an external data source or an external aid. The alignment procedure, however, initializes the pitch and roll angles by levelling and the heading by gyro-compassing. When a low cost IMU runs in a static or constant velocity mode, the heading observability becomes poorer. Furthermore, larger gyro biases and a lower signal-to-noise ratio degrade its performance over time. In this scenario, the initial heading cannot be determined by gyro-compassing. Other sensors, such as a magnetic compass or a multi-antenna GPS attitude system, have to be considered as alternatives (Shin 2005).

The outputs of high grade IMUs are incremental angles and velocities due to precise digitization. Most low cost IMUs output specific forces and angular rates. The mechanization equation proposed by Savage (2000) is operated on incremental velocities and incremental angles. To be compatible with Savage's mechanization equations, low cost IMU outputs are transformed into incremental values by

$$\begin{cases} \Delta V^b = \int_t^{t+\Delta t} f^b dt \\ \Delta \theta^b = \int_t^{t+\Delta t} \omega_{ib}^b dt \end{cases} \tag{2.15}$$

where ΔV^b is the incremental velocity, $\Delta \theta^b$ is the incremental angle, and Δt is the IMU data sampling rate.

2.3.3   INS Error Dynamics Equation

When implementing the mechanization equation for a stand-alone INS system, the abovementioned typical IMU errors grow with time. The noise exhibits random walk

behaviour. To achieve high accuracy, it is necessary that the IMU errors are estimated and compensated. In the development of a real-time GPS, INS and on-board vehicle sensor integrated system, the augmentation and estimation of on-board vehicle sensor error states will increase the system complexity and the computational tasks. The trade-off between positioning accuracy and computational load as well as system observability is the main consideration in the system development.

As most low cost IMUs are equipped with an internal temperature compensator, the error effects with respect to temperature can thus be ignored. The impacts of accelerometer scale factor error and non-orthogonality of the sensor's installation are dependent on the vehicle's dynamics to a large extent. The high vehicle dynamics result in large inertial sensors errors (Salychev et al. 2000). A land vehicle usually operates at a much lower dynamic than marine and airborne systems. Consequently, scale factor and non-orthogonality errors can be neglected in a land vehicle positioning system without significant influence on positioning accuracy. On the basis of the above considerations, IMU biases and noise are taken into account in the system design. By modeling the biases as a first-order Gauss-Markov process to represent temporal characteristics, all IMU errors are simplified and lumped into biases and noises.

By applying perturbation analysis to the equation of motion and augmenting gyro and accelerometer biases into error states, the INS error dynamics model is given by (Schwarz & Wei 1999)

$$
\begin{bmatrix} \delta \dot{r}^e \\ \delta \dot{v}^e \\ \dot{\varepsilon}^e \\ \delta \dot{b}^b \\ \delta \dot{d}^b \end{bmatrix} = \begin{bmatrix} 0 & I & 0 & 0 & 0 \\ N^e & -2\Omega_{ie}^e & -F^e & R_b^e & 0 \\ 0 & 0 & -\Omega_{ie}^e & 0 & R_b^e \\ 0 & 0 & 0 & -diag(\alpha_i) & 0 \\ 0 & 0 & 0 & 0 & -diag(\beta_i) \end{bmatrix} \begin{bmatrix} \delta r^e \\ \delta v^e \\ \varepsilon^e \\ \delta b^b \\ \delta d^b \end{bmatrix}
$$

$$
+ \begin{bmatrix} 0 & 0 & 0 & 0 \\ R_b^e & 0 & 0 & 0 \\ 0 & R_b^e & 0 & 0 \\ 0 & 0 & I & 0 \\ 0 & 0 & 0 & I \end{bmatrix} \begin{bmatrix} w_f \\ w_w \\ w_b \\ w_d \end{bmatrix} = F_{INS} \delta x + G_{INS} w
$$

(2.16)

where δr^e is the position error vector, δv^e is the velocity error vector, ε^e is the misalignment angle error vector, δb^b is the vector of accelerometer bias errors, δd^b is the vector of gyro bias errors. All of aforementioned error states are 3x1 vectors. In addition, $diag(\alpha_i)$ is the diagonal matrix of the time constant reciprocals for the accelerometer bias model , $diag(\beta_i)$ is the diagonal matrix of time constant reciprocals for the gyro bias models, w_b is the driving noise for accelerometer biases, w_d is the driving noise for gyro biases, R_b^e is the direction cosine matrix between the b frame and the e frame, F^e is the skew-symmetric matrix of specific force in the e frame, N^e is the tensor of gravity gradients, Ω_{ie}^e is the skew-symmetric matrix of the Earth's rotation with respect to the e frame, δx is the error states vector, and F_{INS} is the dynamics matrix for the stand-alone INS system, G_{INS} is the shaping matrix of the driving noise of the stand-alone INS system, and w is the noise matrix.

With respect to the low cost IMU used in this research, Table 2.3 summarizes the mathematical variance (noise level) and the parameters of the first-order Gauss-Markov

model of low cost IMU biases. These parameters were obtained by using the sensor

analysis method described in Chapter 3.

Table 2.3 Low cost IMU mathematical variance and Gauss-Markov model parameters

IMU Sensors	Mathematical variance	Parameters of the first-order Gauss-Markov model for low cost IMU biases	
		Time Constant	Temporal standard deviation
X Accelerometer	0.0017 m^2/s^4	0.36 hr	0.006 m/s^2
Y Accelerometer	0.0039 m^2/s^4	1.07 hr	0.007 m/s^2
Z Accelerometer	0.0019 m^2/s^4	0.53 hr	0.004 m/s^2
X Gyro	2.5920e+4.0 deg^2/ h^2	0.89 hr	86.40 deg/h
Y Gyro	8.0352e+4.0 deg^2/h^2	0.73 hr	205.20 deg/h
Z Gyro	2.3328e+4.0 deg^2/h^2	0.70 hr	194.40 deg/h

2.3.4   External Aided INS

An INS is an autonomous system that can operate continuously in urban centres,

underpasses and underwater. It is immune to jamming and interference. The inherent

disadvantage of an INS is that its error sources grow with time. To limit its drift error or

improve its accuracy, an INS can be aided by complementary external sensors such as

GPS and on-board vehicle sensors as discussed in this research. With complementary

features to INS, GPS provides all-weather, accurate and absolute positioning information.

However, it is susceptible to blockage of line-of-sight signals as well as signal

interference or jamming. The augmentation of on-board vehicle sensors with GPS and

INS can bridge the gap during the masking of GPS signals and consequently improve the

accuracy of a stand-alone INS system.

The mechanism of the external aiding on an INS is described in Figure 2.2. In the external sensor aiding INS system, the position, velocity and attitude information are derived from the mechanization equation.
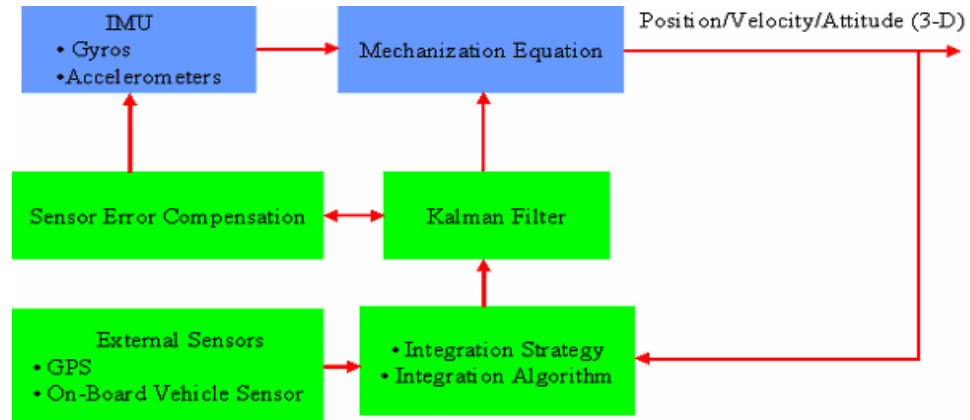
Figure 2.2 External aiding on INS

With an appropriate integration strategy and algorithm, the error states of the INS mechanization equation output (position, velocity and attitude) as well as the IMU measurement error can be estimated by Kalman filter through external aid. Consequently, the INS mechanization equation output can be updated, and the IMU sensor error can be compensated. The integration strategies and algorithms for GPS, INS and on-board vehicle sensors will be discussed in Chapters 4 and 5, respectively.

Chapter 3   Analysis of On-Board Vehicle Sensors

The on-board vehicle sensors used in this research come from the vehicle stability control system, including four wheel speed sensors, two horizontal G sensors (accelerometers) and a yaw rate sensor (i.e., a two dimensional automotive grade inertial unit), as well as the steering angle sensor. This chapter gives a description and analysis of these on-board vehicle sensors.

3.1   Description of On-Board Vehicle Sensors

Four wheel speed sensors are attached to the wheels of the vehicle. G sensors and yaw rate sensors are placed on the chassis of a vehicle to constitute a two dimensional automotive grade inertial unit. The location of the G sensor and yaw rate sensor (GL/YRS) unit is very close to the centre of gravity of the vehicle. The steering angle sensor is located in the centre of the front wheel axis to measure the front tire turning angle with respect to the neutral position.

Figure 3.1 illustrates the approximate location and geometric relationship of all the on-board vehicle sensors. In a general case, the vehicle is assumed to turn at an angular rate (yaw rate) γ with respect to an instantaneous rotation centre o, b is the track width between the two rear wheels, R is the length between the right rear wheel and the point o, v_{WSS} is the velocity at the centre point of the rear wheel axis, V_P is the velocity at the

gravity centre point, and θ is the angle between the velocity at the centre of gravity and the forward direction in the vehicle frame. The G sensors (GX and GY) and yaw rate sensor measure horizontal specific force and the yaw rate at a specific point near the centre of gravity, with a distance of L_r to the rear wheel axle as well as a distance of L_f to the front wheel axle. The front wheel speed v_f at the centre point of the front wheel axle is decomposed into the horizontal velocities, v_x and v_y. The steering angle ψ can be approximately derived from v_x and v_y. Given a rigid body of the vehicle, it is reasonable to assume that $v_y = v_{WSS}$.
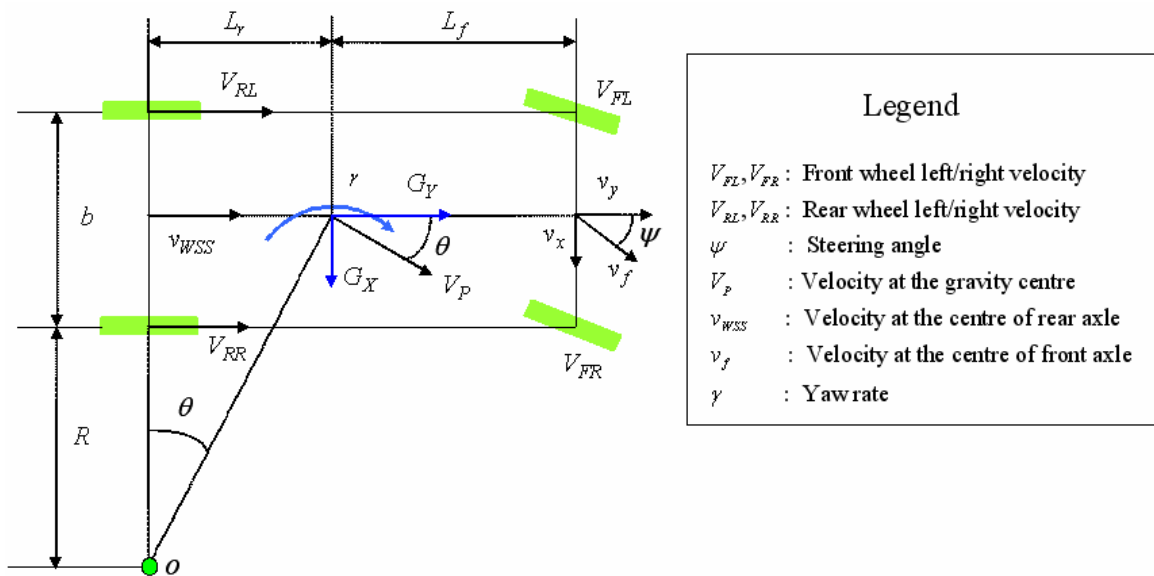
Figure 3.1 Relationship between the on-board vehicle sensors

3.2   Wheel Speed Sensors

Wheel speed sensors are fundamental components of an ABS which is standard equipment on most vehicles (Hay 2005). The wheel speed sensor measures the Y-direction velocity in the vehicle frame. The wheel speed sensors used in this research

are passive types which work on the principle of variable reluctance. The sensor teeth travel through a passive magnetic field at a sufficient speed to generate a low voltage analog waveform (ibid). The number of pulses per second is measured by the sensor teeth. The wheel speed is consequently correlated with the sensed pulses number per second, the teeth numbers per rotation as well as the radius of the wheel tire, which can be explicitly expressed by

$$v_{WSS} = 2\pi R_{WSS} \cdot (N_{Pulse}/N_{Teeth}) \qquad (3.1)$$

where R_{WSS} is the radius of the wheel, N_{Pulse} is the number of pulses per second sensed by the wheel speed sensor and N_{Teeth} is the number of teeth.

From Figure 3.1, the two rear wheel speeds can be computed from the yaw rate by (Carlson et al. 2002)

$$\begin{aligned} V_{RL} &= (R+b) \cdot \gamma \\ V_{RR} &= R \cdot \gamma \end{aligned} \qquad (3.2)$$

where V_{RR} and V_{RL} are the rear right and rear left wheel speed sensor measurements respectively

From the rear wheel speed sensor measurements, R and γ are derived by

$$\begin{aligned} \gamma &= \frac{V_{RL} - V_{RR}}{b} \\ R &= \frac{b \cdot V_{RR}}{V_{RL} - V_{RR}} \end{aligned} \qquad (3.3)$$

Equation (3.3) implies that the differential of two rear wheel speed sensors provides a way to estimate the yaw rate assuming no slip (ibid).

On the basis of Equation (3.3), the velocity v_{WSS} and V_P can be computed by

$$v_{WSS} = (R+b/2) \cdot \gamma = (V_{RR} + V_{RL})/2$$
$$V_P = \sqrt{(R+b/2)^2 + L_r^2} \cdot \gamma = \frac{1}{2b}\sqrt{b^2(V_{RL}+V_{RR})^2 + 4L_r^2(V_{RL}-V_{RR})^2} \qquad (3.4)$$

The angle θ is computed by

$$\theta = \tan^{-1}\left(\frac{L_r}{R+b/2}\right) = \tan^{-1}\left(\frac{2L_r(V_{RL}-V_{RR})}{b(V_{RL}+V_{RR})}\right) \qquad (3.5)$$

As a special case, when the vehicle operates without turning, the difference between the two rear wheel speed sensor measurements is very small. It makes sense that $\theta \approx 0$ and $V_P \approx v_{WSS}$.

The wheel speed sensor used in this research always outputs zero speed when the vehicle operates in static mode. Therefore, it is impossible to assess the characteristics of a wheel speed sensor using static data. Since the wheel speed sensor measurement noise is required in the Kalman filter when it is integrated with other sensors, another method was devised to assess measurement noise. The NovAtel OEM2 precise velocity GPS receiver can provide velocity accuracy at a millimetre per second level, and it can therefore be used as the reference speed to estimate wheel speed sensor measurement noise. By driving the vehicle at low (20 km/h), medium (50 km/h) and high (80 km/h) constant speeds on a flat road and in a straight direction, the speed error between the wheel speed

sensor and the OEM2 GPS velocity receiver can be computed to estimate wheel speed

sensor measurement accuracy. This basic idea is illustrated in Figure 3.2.
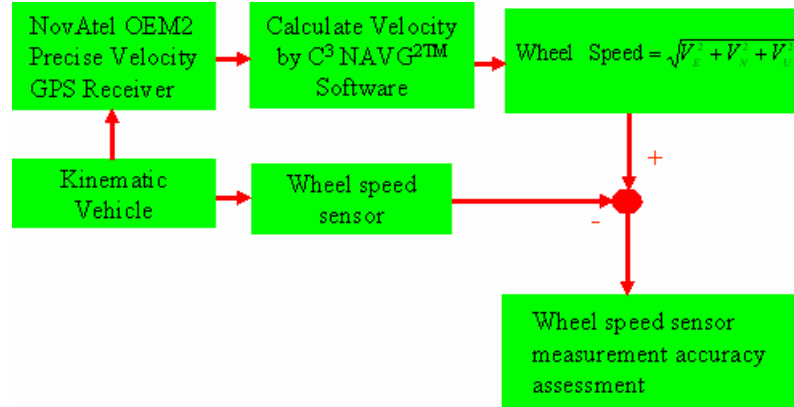
Figure 3.2 Estimation of wheel sensor measurement accuracy

To verify the measurement accuracy of NovAtel OEM2 GPS velocity receiver, one hour

static data was collected using NovAtel OEM2 GPS receiver. In static mode, the

reference velocity is at zero. Figure 3.3 shows the speed error and the average variance of

the NovAtel OEM2 precise velocity GPS receiver in static mode. By randomly taking 20

evenly spaced one-second intervals from the speed error, the average speed variance of

this velocity can be derived to be 1.0 mm^2/s^2. Consequently, its standard deviation is

1.0 mm/s, which verifies the fact that the accuracy of NovAtel OEM2 GPS receiver is at

millimetre per second level. The spikes appeared in Figure 3.3 is introduced by external

disturbance.

In dynamic mode, the speed of the wheel speed sensor and the OEM2 GPS receiver, as

well as the speed difference between the wheel speed sensor and the OEM2 GPS receiver,

are shown in Figure 3.4. This speed difference in dynamic mode mainly results from the

error sources of the wheel speed sensors such as the scale factor and side slip.
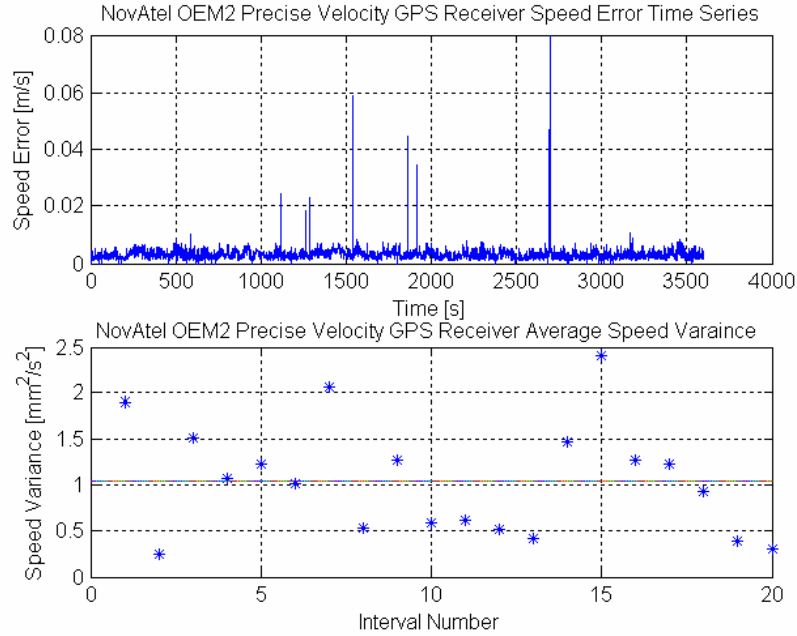
Figure 3.3 NovAtel OEM2 precise velocity GPS receiver speed error and speed average variance
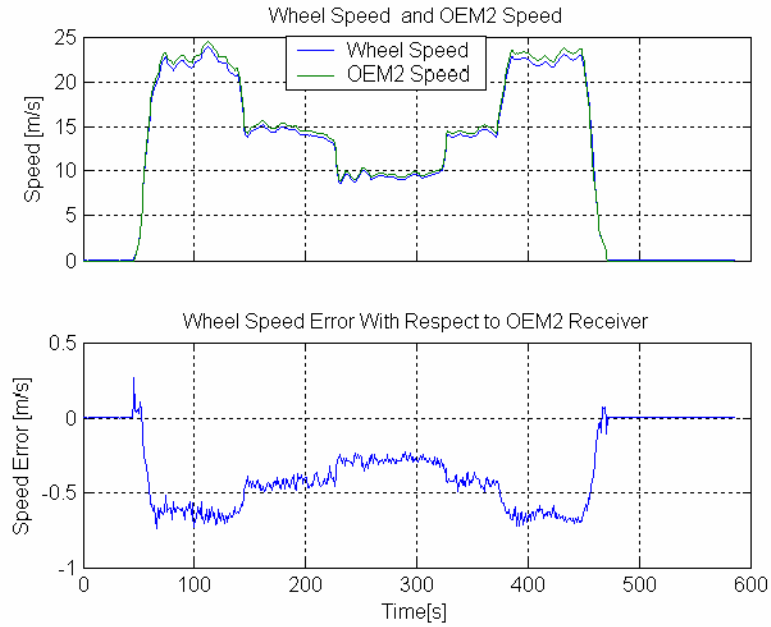
Figure 3.4 Speeds and the speed difference for the OEM2 GPS receiver and the wheel speed sensor

To avoid long term variation of the wheel speed difference, 20 evenly spaced one-second intervals were taken from Figure 3.4 for mathematical variance analysis. The average variance of the wheel speed sensor with respect to the OEM2 GPS receiver is computed and shown in Figure 3.5. In this test, the wheel speed sensor measurement is sampled at 20 Hz. Within a one-second time interval, 20 data samples are covered. Also, the 20 evenly spaced one-second time intervals are selected randomly. The average variance across all intervals is shown by the solid line. From this point of view, the mathematical variance computed in this way can statistically represent the measurement noise of the wheel speed sensors.
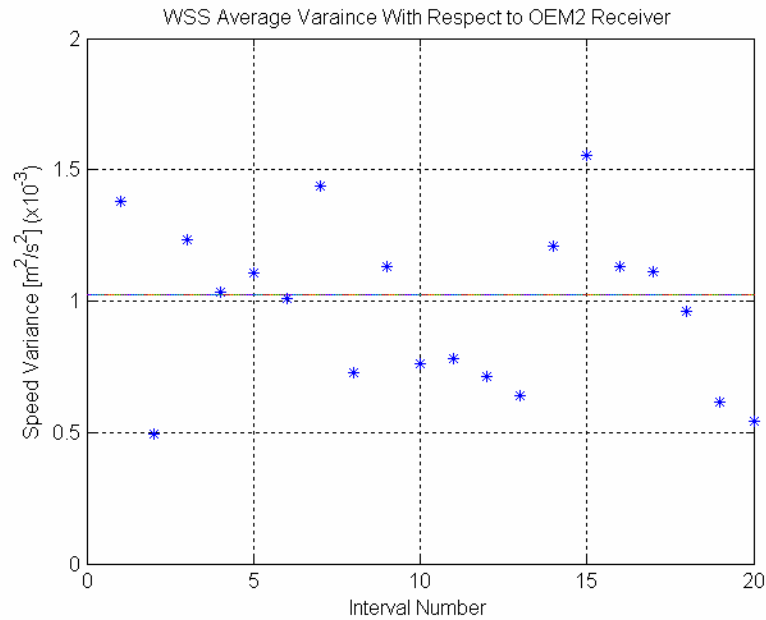
Figure 3.5 Average variance of the wheel speed sensor with respect to the OEM2 GPS receiver

Using covariance propagation theory, the wheel speed sensor variance can be computed by

$$\begin{cases} \sigma_{WSS}^2 = \sigma_{WSS \to GPS}^2 - \sigma_{GPS}^2 = 0.001 \ \text{m}^2/\text{s}^2 \\ \sigma_{WSS} = \sqrt{0.001} = 0.032 \ \text{m/s} = 3.2 \ \text{cm/s} \end{cases} \tag{3.6}$$

where σ_{WSS}^2 is the wheel speed sensor average variance, $\sigma_{WSS \to GPS}^2$ is the average variance of the wheel speed sensor variance relative to the GPS receiver, and σ_{GPS}^2 is the average variance of the OEM2 GPS receiver.

Therefore, the standard deviation or measurement noise of the wheel speed sensor is 3.2 cm/s. This value is used as the measurement noise in the Kalman filter when integrating WSS with GPS and INS later.

3.3   G Sensors and Yaw Rate Sensor

G sensors (accelerometers) measure the specific force in the lateral and longitudinal directions. The yaw rate sensor measures the angular rate with respect to vertical direction.

To assess the performance including noise and drift characteristics of the G sensors and the yaw rate sensor, a static test was conducted on March 10, 2006. Seven hours of static data was collected while the engine was idling. The idling engine speed was approximately 750 rpm. The data sampling rate was 100 Hz. The data logging system power was supplied by car batteries and an inverter. The outside temperature during the test was around -15 degree Celsius and thus the vehicle's heater was turned on.

In static mode, the yaw rate sensor measures the Earth's rotation. The outputs of the G sensors are theoretically zero if they are assumed to be highly aligned with the horizontal

plane. Practically, the static output of on-board vehicle sensors can be used to assess noise level or error variability.

The G sensor and yaw rate sensor raw data was processed to evaluate the noise level by a mathematical variance analysis, and a wavelet tool was used to decompose the raw data into high and low frequency data sets. The low-frequency data was utilized to approximate the error temporal variability as a first-order Gauss-Markov process (Lachapelle et al. 2003).

3.3.1 Mathematical Variance of G Sensors and Yaw Rate Sensor

To avoid long term variations in the data, 40 evenly spaced one-second intervals were chosen, and the corresponding variance of each interval was calculated for lateral and longitudinal G sensors, and yaw rate sensor, respectively. In Figure 3.6, the average variance across all intervals is shown by the solid line. The average mathematical standard deviation and variance of the G and yaw rate sensors are summarized in Table 3.1. These values provide the process noise level used in the Kalman filter. With the noise level and the double-sided bandwidth information, the noise spectral density of G sensors and yaw rate sensor can be computed by (Scherzinger 2004)

$$q_{GL} = \frac{\sigma^2_{GLNoise}}{2BW_{GL}}$$

$$q_{YRS} = \frac{\sigma_{YRS\,Noise}}{2BW_{YRS}}$$

(3.7)

where q_{GL}, q_{YRS} are the noise spectral density of G sensors and yaw rate sensor, respectively, $\sigma^2_{GLNoise}, \sigma^2_{YRSNoise}$ are noise level of G sensors and yaw rate sensor, respectively, and BW_{GL}, BW_{YRS} are the bandwidth of G sensors and yaw rate sensor, respectively.
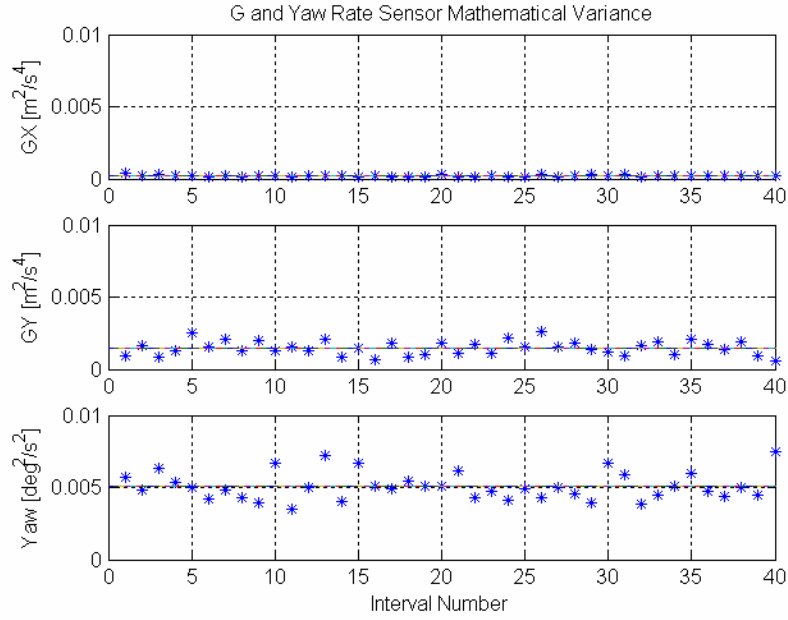
Figure 3.6 Mathematical variances of G and yaw rate sensors

Table 3.1 Average standard deviation and variance of raw data

Sensor	Average standard deviation	Average variance
GX	0.014 m/s^2	2.0620e-004 m^2/s^4
GY	0.039 m/s^2	1.4786e-003 m^2/s^4
Yaw Rate Sensor	256.32 deg/h	6.5699e+004 deg^2/h^2

3.3.2 Wavelet analysis of G and Yaw Rate Sensors

Similar to Fourier analysis, wavelet analysis can decompose a signal into low and high frequency components (Walker 1999). The main difference between Wavelet and Fourier analyses is that Wavelet analysis uses a wide variety of base functions whereas Fourier

analysis uses sine and cosine as its base functions. A Daubechies (db8) mother wavelet is used to decompose the raw data herein (Lachapelle et al. 2003). Since the noise has a zero mean, the wavelet decomposition level at which the mean of the high frequency components becomes non-zero is selected. After wavelet decomposition, the high frequency parts can be used to analyze noise, and the low frequency part can be used to analyze slowly varying errors.

Figure 3.7 shows the mean of the high frequency components across the levels of wavelet decomposition. It can be seen that the mean value of the high frequency noise starts to be non-zero when the decomposition level is greater than 10. Therefore a decomposition level of 10 is selected here. With respect to the decomposition level 10, the raw data, the decomposed high and low frequency data for G and yaw rate sensors are shown from Figure 3.8 to Figure 3.10, respectively. The raw data is a combination of high-frequency noise and slowly varying sensor errors. After wavelet decomposition, the high-frequency noise and slowly varying errors are separated effectively from the raw sensor data, and the slowly varying sensor noise becomes a relatively clean, low frequency signal.

The variance of the high-frequency components gives an estimate of the noise power. Table 3.2 summarizes the variance of the high frequency components for the G and yaw rate sensors, and gives a comparison with the mathematical variance computed in the last section. This comparison shows that the mathematical and decomposed high-frequency

variances are very close to each other, which indicates that no error was introduced by

the wavelet analysis.
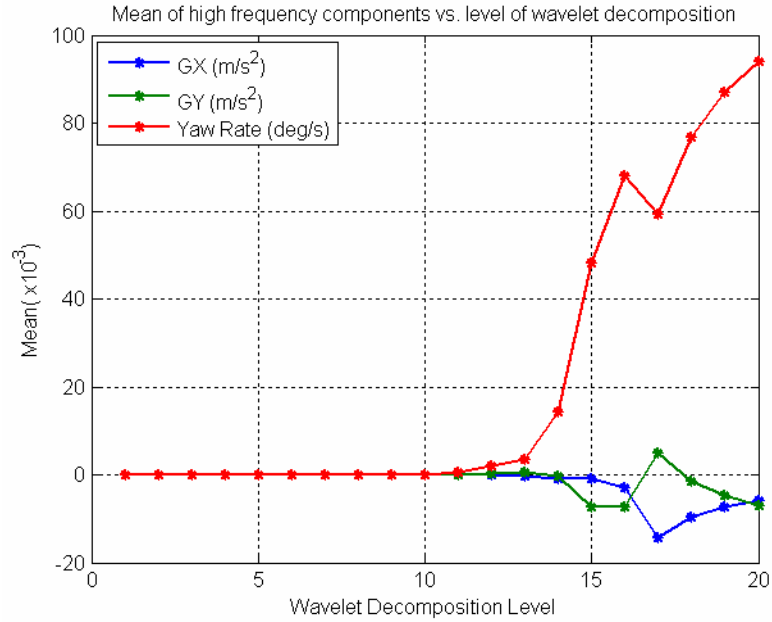
Figure 3.7 Means of high frequency components vs. the level of wavelet decomposition
of the G and yaw rate sensors
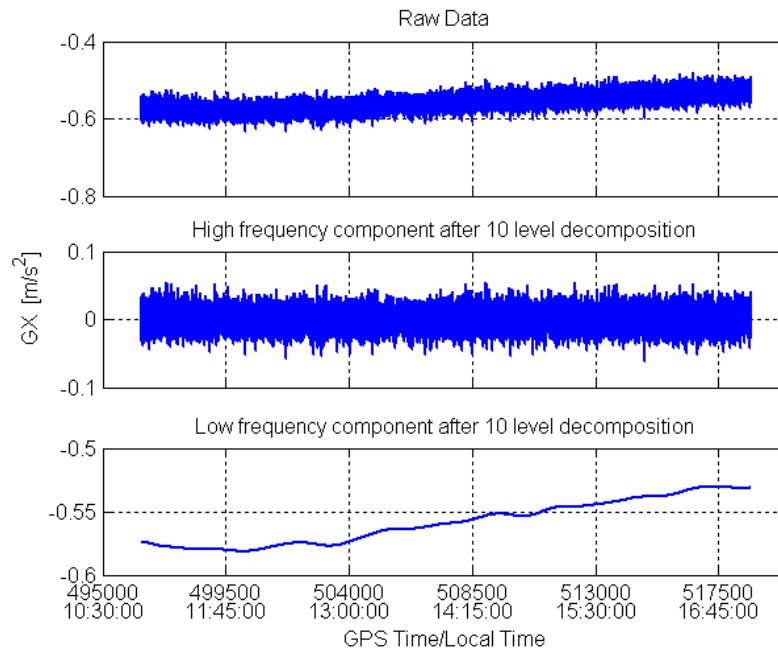
Figure 3.8 Raw and decomposed data from the GX sensor
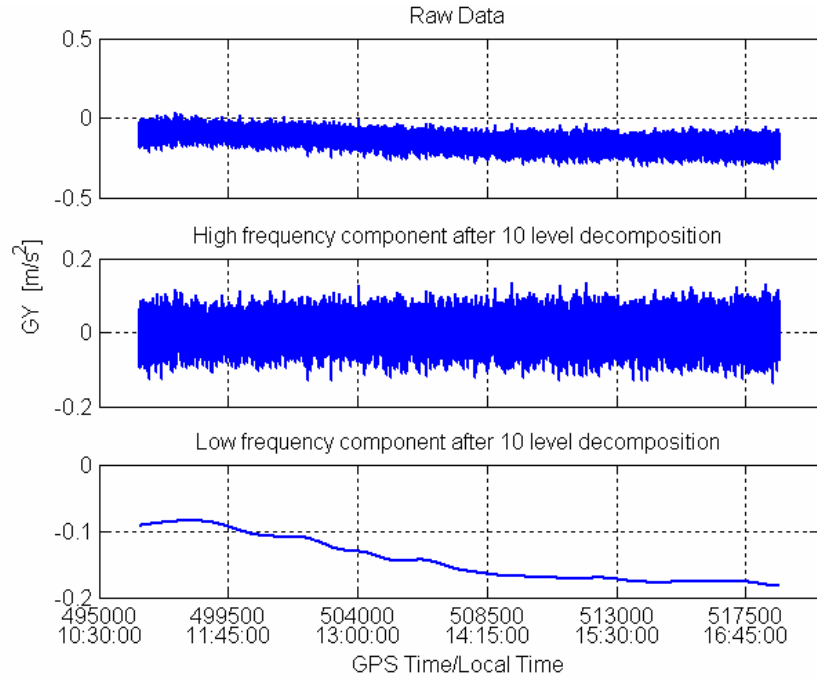
Figure 3.9 Raw and decomposed data from GY sensor
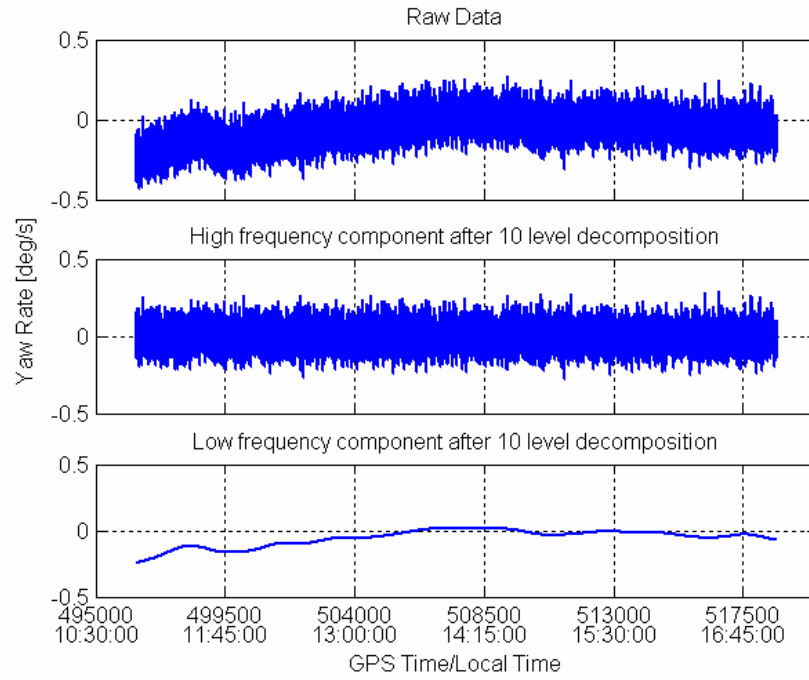
Figure 3.10 Raw and decomposed data from yaw rate sensor

Table 3.2 Comparison of the average standard deviation of the raw data and the average standard deviation of the high frequency noise after wavelet decomposition

Sensors	Standard deviation of the raw data	Standard deviation of Wavelet decomposition
GX	0.014 m/s^2	0.015 m/s^2
GY	0.039 m/s^2	0.038 m/s^2
YRS	256.32 deg/h	263.88 deg/h

3.3.3   First-Order Gauss-Markov Model of G Sensors and Yaw Rate Sensor

The low-frequency components after wavelet decomposition can be used to compute autocorrelation function. With the autocorrelation function, the slow varying error can be modeled as a first-order Gauss-Markov process. The first-order Gauss-Markov model is expressed by

$$\dot{x}(t) = -\beta x(t) + \sqrt{2\sigma^2 \beta} u(t) \qquad (3.8)$$

and its corresponding autocorrelation function is

$$R(\tau) = \sigma^2 e^{-\beta|\tau|} \qquad (3.9)$$

The parameters σ and β can be estimated from the autocorrelation series by using a least squares curve fitting technique. In an integrated system, the biases of the G and yaw rate sensors are modeled as first-order Gauss-Markov processes, and are estimated by Kalman filtering.

Figure 3.11 shows the raw and approximated autocorrelation functions from the least squares curve fitting technique for G and yaw rate sensors. In general, a first-order Gauss-Markov approximation is accurate for a time shift of up to a few hours. For longer

time shifts, the approximation no longer holds. The estimated parameters σ and β for the G and yaw rate sensors are summarized in Table 3.3.
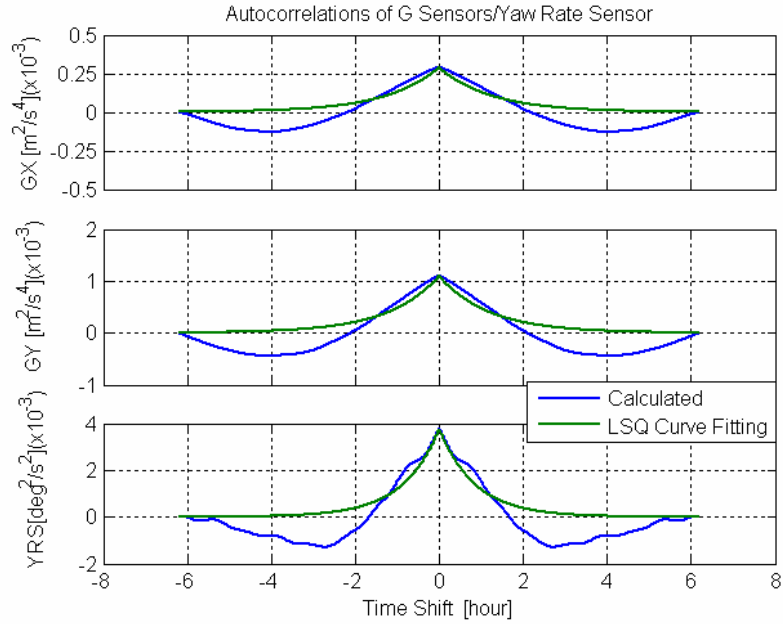
Figure 3.11 Raw and approximated autocorrelation functions for G and yaw rate sensors

Table 3.3 Parameters of the first-order Gauss-Markov process for the G and yaw rate sensors

Sensor	σ	$1/\beta$ [hour]
GX	0.017 m/s^2	1.25
GY	0.033 m/s^2	1.21
Yaw Rate Sensor	221.04 deg/h	0.87

These parameters provide the necessary information for modelling the biases of G sensors and yaw rate sensor as the first-order Gauss-Markov process. The noise spectral densities with respect to the biases of G sensors and yaw rate sensor can also be derived from σ and β as shown by (Gelb 1976)

$$q_{b_{GL}} = 2\sigma_{GL}^2\beta_{GL}$$
$$q_{b_{YRS}} = 2\sigma_{YRS}^2\beta_{YRS}$$

(3.10)

where $q_{b_{GL}}$, $q_{b_{YRS}}$ are the noise spectral density associated with G sensors and yaw rate sensor biases, respectively, $\sigma_{b_{GL}}$, $\sigma_{b_{YRS}}$ are the temporal standard deviation of G sensors and yaw rate sensor biases, respectively, and $\beta_{b_{GL}}$, $\beta_{b_{YRS}}$ are the time constant reciprocals of G sensors and yaw rate sensor biases, respectively.

3.4   Steering Angle Sensor

As illustrated by Figure 3.12, the steering angle sensor measures the front tire turning angle with respect to the neutral position. Through an electrical control unit, the operation of the steering wheel is transformed into steering angle information with respect to the neutral position by using a constant scale factor. Since the transformation implemented by the electrical control unit is nonlinear in nature, the constant scale factor is only an approximation of the real situation.
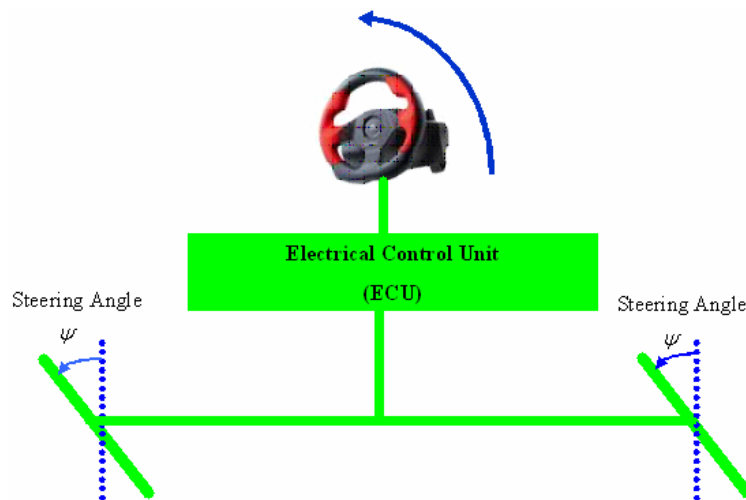
Figure 3.12 Steering angle sensor

Since it is difficult to find a reference for evaluating the measurement accuracy of the steering angle sensor, its measurement accuracy can be either determined empirically through testing various scenarios in the Kalman filter or indirectly estimated from the derived steering angle from other sensor measurements with the known measurement accuracy by using the variance propagation theory.

As shown in Figure 3.1, the steering angle can be derived from v_x and v_y. The relationship between v_x and v_y with the wheel speed sensor and the yaw rate is given by

$$
\begin{aligned}
v_x &= L_f \gamma \\
v_y &= v_{WSS}
\end{aligned}
$$

(3.11)

The steering angle is thus indirectly computed by (Carlson et al. 2002)

$$
\psi = -\tan^{-1}\left(\frac{L_f r}{v_{WSS}}\right)
$$

(3.12)

The opposite sign in Equation (3.12) is due to the definition of the vehicle frame as Right-Front-Up, while a positive steering angle is defined as being in the counter-clockwise direction.

With the known measurement accuracy of the wheel speed sensor and yaw rate sensor, the measurement accuracy of the steering angle sensor can be estimated in term of the variance propagation theory by

$$\sigma_{\psi}^2 = \left(\frac{\partial \psi}{\partial v_{WSS}}\right)^2 \sigma_{v_{WSS}}^2 + \left(\frac{\partial \psi}{\partial r}\right)^2 \sigma_r^2$$

$$= \left(\frac{L_f \cdot r}{v_{WSS}^2 + (L_f \cdot r)^2}\right)^2 \sigma_{v_{WSS}}^2 + \left(\frac{v_{WSS} \cdot L_f}{v_{WSS}^2 + (L_f \cdot r)^2}\right)^2 \sigma_r^2$$

(3.13)

where σ_{ψ}^2 is the variance of the steering angle sensor measurement, v_{WSS} is velocity at

the centre point of the rear wheel axle (the average value of two rear wheel speed sensor

measurement), $\sigma_{v_{WSS}}^2$ is the variance of v_{WSS}, γ is the yaw rate sensor measurement,

σ_r^2 is the variance of the yaw rate sensor measurement, and L_f is the distance between

the location of GL/YRS unit and the axle of the front wheel.

Chapter 4   GPS/INS/On-Board Vehicle Sensor Integration Strategies

Kalman filtering is well suited for information integration from different data sources. To develop integration strategies for the GPS, INS and on-board vehicle sensors analyzed in Chapter 3, this chapter first gives an overview of the Kalman filter algorithm. On the basis of a comparison between linearized and extended Kalman filters as well as centralized (tight coupling strategy) versus decentralized (loose coupling strategy) Kalman filters, various integration strategies are proposed.

4.1   Overview of Kalman Filter

Kalman filtering is an optimal recursive estimator that incorporates measurement information to estimate the current states of interest in a linear dynamic system (Maybeck 1979). Based on an assumption that the linear dynamics system and the measurement are perturbed by white noise, the Kalman filter utilizes the system dynamics model and measurement model, the statistics of the dynamics system noise and measurement noise as well as the required initial information to deduce the estimation (ibid).

4.1.1   The Algorithm of Kalman Filter

For practical use, the dynamics model is usually expressed in a continuous format by

$$\dot{x}(t) = F(t)x(t) + G(t)w(t) \tag{4.1}$$

where $x(t)$ is the continuous-time state vector, $F(t)$ is the continuous time dynamics matrix, $G(t)$ is the shaping matrix, $w(t)$ is a dynamic process noise vector with zero mean and uncorrelated Gaussian distribution. The covariance matrix of the noise vector is given by (Gelb 1974)

$$E[w(t)w(\tau)^T] = Q(t) \cdot \delta(t - \tau) \tag{4.2}$$

where t, τ denote different time epochs, $\delta(t)$ is called the Dirac delta function, and $Q(t)$ is the process noise matrix.

The continuous measurement model is given by

$$z = H \cdot x + w_m \tag{4.3}$$

where z is the measurement, H is the design matrix, and w_m is the measurement noise that has zero mean with uncorrelated Gaussian distribution. Similarly to the process noise in the dynamics model, the covariance matrix of the measurement noise is expressed by

$$E\left[w_m(t)w_m^T(\tau) \right] = R \cdot \delta(t - \tau) \tag{4.4}$$

where R is called the covariance matrix of the measurement noise.

In practical use, the continuous models are usually transformed into discrete form, and the discrete dynamics and measurement models are expressed as follows

$$\begin{aligned} x_k &= \Phi_{k-1,k}x_{k-1} + w_k \\ z_k &= H_k x_k + w_{m_k} \end{aligned} \tag{4.5}$$

where $\Phi_{k,k+1}$ is called the transition matrix, which can be approximately calculated through a Taylor series expansion (Brown & Hwang 1992)

$$\Phi_{k,k+1} = e^{F\Delta t} = I + F\Delta t + \frac{(F\Delta t)^2}{2!} + \frac{(F\Delta t)^3}{3!} + ... \tag{4.6}$$

where Δt is the sampling rate of the discrete system.

The discrete process noise w_k is computed by

$$w_k = \int_{t_k}^{t_{k+1}} \Phi\left(t_{k+1}, \tau\right) \cdot G(\tau) \cdot w(\tau) d(\tau) \tag{4.7}$$

The discrete process noise also has a zero mean with uncorrelated Gaussian distribution, namely

$$\begin{cases} E[w_k] = 0 \\ E[(w_k)_i (w_k)_j^T] = \begin{cases} Q_k, \; i = j \\ 0, \; i \neq j \end{cases} \end{cases} \tag{4.8}$$

where Q_k is the covariance matrix of the discrete process noise.

A numerical algorithm for the computation of the covariance matrix of w_k is expressed by the following formula (Grewal et al. 2001)

$$Q_k = E[w_k \cdot w_k^T] = (\Phi_{k,k+1} G_k Q G_k^T \Phi_{k,k+1}^T + G_k Q G_k^T) \frac{\Delta t}{2} \tag{4.9}$$

Similarly, the covariance matrix of the discrete measurement noise is characterized by

$$\begin{cases} E[w_{m_k}] = 0 \\ E[(w_{m_k})_i (w_{m_k})_j^T] = \begin{cases} R_k, \; i = j \\ 0, \; i \neq j \end{cases} \end{cases} \tag{4.10}$$

The state vector x_k and its covariance matrix P_k are computed by prediction and update steps. The prediction step propagates the current state to the next step, and the update step modifies the prediction results using currently available measurements. The optimal Kalman filter gain is calculated in the update step. These procedures are summarized here and are detailed in Gelb (1974).

The prediction step is

$$\begin{cases} x_{k+1}^- = \Phi \cdot \mathrm{x}_k \\ P_{k+1}^- = \Phi P_k \, \Phi^{\mathrm{T}} + Q_k \end{cases} \tag{4.11}$$

where x_k is a posteriori state vector at the current epoch, x_{k+1}^- is the a priori state vector at the next epoch, P^- is the a priori estimated covariance matrix, and P is the a posteriori estimated covariance matrix.

The update step is conducted by

$$\begin{cases} K_{k+1} = P_{k+1}^- H (H P_{k+1}^- H^T + R_k)^{-1} \\ X_{k+1} = X_{k+1}^- + K_{k+1}(z_{k+1} - H X_{k+1}^-) \\ P_{k+1} = (I - K_{k+1} H) P_{k+1}^- \end{cases} \tag{4.12}$$

where K is the Kalman filter gain, and I is the identity matrix.

The Kalman filter is an unbiased, recursive estimator on the condition of the minimum variance. Through the prediction step, followed by measurement update, the state vector and its covariance matrix are estimated on an epoch-by-epoch basis.

4.1.2 Linearized and Extended Kalman Filters

The Kalman filter is essentially linear in nature. In most practical applications, however, the measurement model and/or the system dynamics model are nonlinear. Kalman filter theory can be applied approximately to a nonlinear system when the nonlinear system is linearized with a trajectory. Depending on the trajectory used for linearization, a Kalman filter can be classified into a linearized or an extended approach (Brown & Hwang 1992).

With a nominal trajectory, relevant Kalman filter parameters, such as the Kalman filter gain and the design matrix, can be computed off-line. Thus, the linearized Kalman filter has an efficient real-time implementation. However, the deviation between actual and nominal trajectories drifts with time without bound, and the assumption of small error magnitudes tends to be violated in the process of linearization. With these features, the linearized Kalman filter is applicable for areas with an approximate trajectory and a short system running time.

On the contrary, the extended Kalman filter does not depend on any nominal trajectory. Its linearization trajectory is continuously updated with estimated results. In this way, the deviation between estimated trajectory and actual trajectory is bounded at a small level. However, a larger initial uncertainty and measurement noise may lead to a divergence of the extended Kalman filter. The pros and cons of the linearized and the extended Kalman filters are summarized in Table 4.1 and imply that the extended Kalman filter is appropriate for land vehicle positioning and navigation systems.

Table 4.1 Comparison of linearized and extended Kalman filters (Brown & Hwang 1992)

	Extended Kalman Filter	Linearized Kalman Filter
Advantages	The trajectory deviation is bounded	Efficient real-time computation
Disadvantages	Large initial uncertainty and measurement noise may lead to a divergence	Trajectory deviation drifts without bound
Application area	The approximate trajectory is not known in advance The running period is long	The approximate trajectory is known in advance The running period is short

To illustrate the linearization of the measurement model, assume the nonlinear measurement model is given by

$$z = h(x) + \omega_m \tag{4.13}$$

where $h(x)$ is the estimated measurement, and ω_m is the measurement noise, z is the raw measurement that is also a function of state x.

By defining the error state as

$$\delta x = x - \hat{x} \tag{4.14}$$

where δx is the error state, $\hat{x}$ is the estimated state, and x is the true value.

Using the Taylor series theory at the first-order, the linearization of the measurement model is expressed by

$$z + \frac{\partial z}{\partial x}\Big|_{x=\hat{x}} \delta x = h(\hat{x}) + \frac{\partial h}{\partial x}\Big|_{x=\hat{x}} \delta x + \omega_m \tag{4.15}$$

where $\delta z = \frac{\partial z}{\partial x}\big|_{x=\hat{x}} \delta x$ is the perturbation of the raw measurement, and $\delta h = \frac{\partial h}{\partial x}\big|_{x=\hat{x}} \delta x$

is the perturbation of the estimated measurement.

By defining the measurement misclosure (or innovation sequence) as

$$e_z = z - h(\hat{x}) \tag{4.16}$$

Equation (4.15) can be rearranged as

$$\begin{aligned}
e_z &= \delta h - \delta z + \omega_m = (\frac{\partial h}{\partial x}\big|_{x=\hat{x}} - \frac{\partial z}{\partial x}\big|_{x=\hat{x}})\delta x + \omega_m \\
&= H\delta x + \omega_m
\end{aligned} \tag{4.17}$$

where H is the design matrix.

4.1.3 Decentralized and Centralized Kalman Filters

Kalman filtering is well suited to information integration from different data sources (Maybeck 1979). Different sensor sources can be integrated with either a loose coupling or a tight coupling strategy. According to the coupling relationship between the local sensors and the filtering technique, Kalman filtering for integrated systems is usually implemented in decentralized and centralized ways (Schwarz et al. 1994).

Figure 4.1 illustrates the structure of loose coupling and decentralized Kalman filter (after Scherzinger 2004). Decentralized Kalman filtering processes the local Kalman filtering outputs within a master Kalman filter in a suboptimal and sequential way, and it corresponds to a loosely coupled integrated system. A decentralized Kalman filter has a

two-staged, distributed, architecture whereby the output of local sensor-related filters is subsequently processed and combined by a larger master filter (Gao et al. 1993).
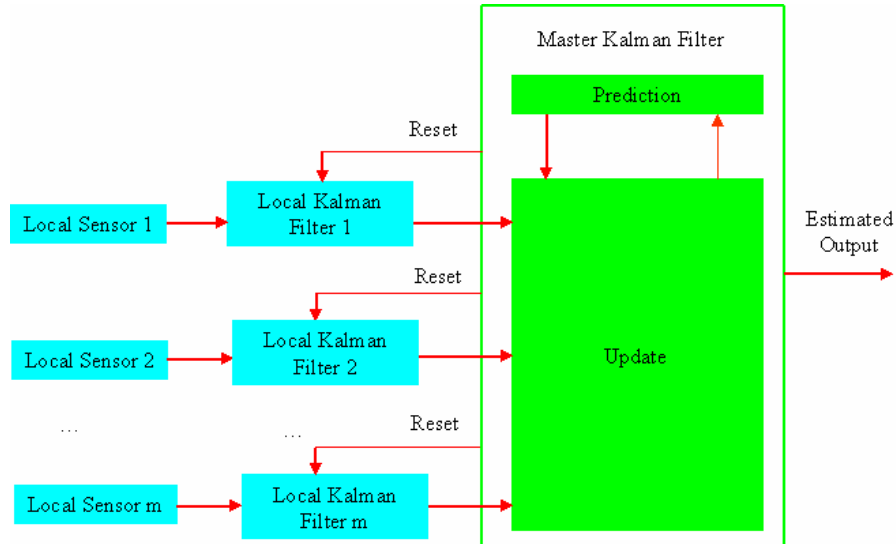
Figure 4.1 Loose coupling and decentralized Kalman filter

As shown in Figure 4.2 (after Scherzinger 2004), centralized Kalman filtering combines different sensor data optimally using one Kalman filter. It is associated with a tightly coupled integrated system. A centralized Kalman filter processes all available sensor measurements at each epoch to obtain a globally optimal solution.

Both centralized and decentralized Kalman filters have their advantages and disadvantages, and a tradeoff needs to be made for a specific application. Centralized Kalman filtering outperforms decentralized filtering in terms of overall system accuracy, which is attributed to reduced process noise in a centralized Kalman filter (Petovello 2003). Another noticeable advantage of centralized Kalman filtering is that ongoing aiding can be provided even when the number of GPS satellites is less than four

(Scherzinger 2001), and an optimal solution can be determined. However, data processing concentrated on one Kalman filter degrades system flexibility and tolerance to fault.
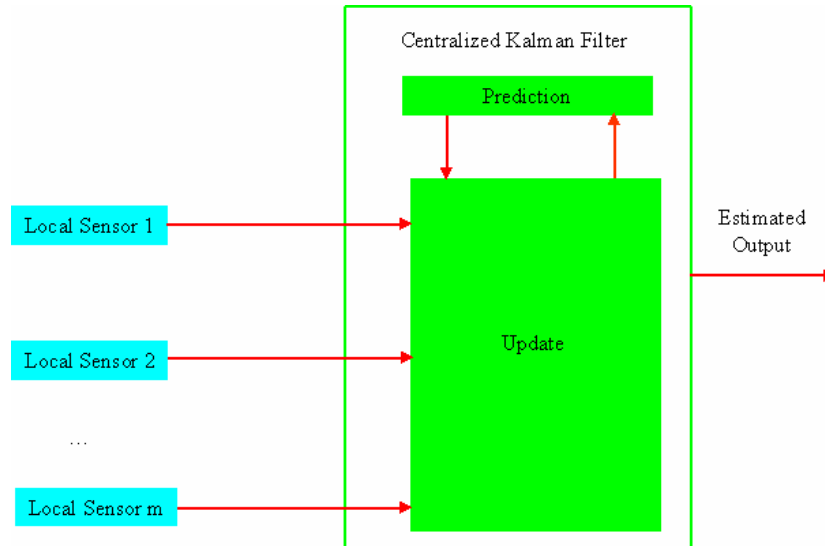
Figure 4.2 Tight coupling and centralized Kalman filter

The decentralized Kalman filter has a modular and flexible architecture that results in high computational efficiency and fault-tolerant characteristics. However, a decentralized Kalman filter only provides suboptimal solutions, and the GPS local Kalman filter inside a decentralized Kalman filter cannot work effectively when the number of GPS satellites is less than four. Table 4.2 makes a comparison between centralized and decentralized Kalman filters.

Based on the above analysis, a tight coupling strategy and extended Kalman filters are used in this research to tightly couple the GPS, INS and on-board vehicle sensors in an effective manner.

Table 4.2 Comparison of centralized and decentralized filters

	Centralized Filter (Tight coupling strategy)	Decentralized filter (Loose coupling strategy)
Advantages	Small noise level Global optimal solution GPS measurement can be less than 4 Fast ambiguity resolution	Flexible High computing efficiency Tolerance to fault
Disadvantages	Large size of error model Low calculation efficiency Low tolerance to fault	4 satellites are needed Suboptimal High noise

4.2 Integration Strategies

To make full use of the on-board vehicle sensors for the land vehicle positioning and navigation, Table 4.3 gives a description of the relationship of the on-board vehicle sensors and the navigation information.

Table 4.3 On-board vehicle sensors vs. navigation information

Sensor Name	Position	Velocity	Azimuth	Others
Wheel speed sensors (WSS)	Yes (Integrated from WSS and YRS)	Yes (Directly)	Yes (Derived from the differential of two wheel speed sensors)	Susceptible to the side slip
G Sensors (GL)	Yes (Integrated from GL and YRS)	Yes (Integrated from GL and YRS)	No	Can detect the side slip by cooperating with YRS
Yaw rate sensor (YRS)	No	No	Yes (Integrated from YRS)	Can detect the side slip by cooperating with GL
Steering angle sensor (SAS)	No	No	No	Constraint velocity error drift

Using a tight coupling strategy, five types of integration strategies are proposed by integrating GPS, an IMU (tactical grade or MEMS low cost IMUs) as well as several on-board vehicle sensors. The proposed integration strategies are summarized in Table 4.4.

Table 4.4 Descriptions of integration strategies

Integration strategies	Descriptions
GPS/INS/WSS	WSS provides the longitudinal velocity update Non-holonomic constraints are applied in lateral and vertical directions Constraints are violated by a larger side slip angle WSS performs ZUPT in static mode
GPS/INS/GL/YRS	Provides the lateral and longitudinal velocity update Lower quality of GL/YRS Computes the side slip angle
GPS/INS/SAS	Compute the steering angle from the horizontal velocity Velocity error drift is constrained by SAS
GPS/INS/WSS/SAS	WSS and SAS sequentially update the Kalman filter
GPS/INS/WSS/GL/YRS/SAS	SAS updates the Kalman filter in a sequential way WSS and GL/YRS are functioning in an interactive way WSS enhances the initial velocity accuracy for GL/YRS GL/YRS computes the side slip angle to detect and alleviate the violation of non-holonomic constraints

4.2.1 GPS/INS/Wheel Speed Sensor Integration Strategy

Figure 4.3 shows the integration strategy for GPS/INS/Wheel speed sensor combination. All available sensor measurements are integrated by a tight coupling strategy at each epoch to obtain a globally optimal solution using one centralized Kalman filter. For the equipment used, the IMU data rate is 100 Hz, and its mechanization equation output rate is set to 10 Hz. The position, velocity and attitude information of the integrated system

are given by implementing the mechanization equation of the IMU in ECEF frame. The

GPS measurements used herein are double differenced carrier phase, double differenced

Doppler and double differenced pseudorange at a 1 Hz rate. The on-board vehicle sensors

are sampled at 100 Hz. To make a tradeoff between system accuracy and computational

load in a real-time test, vehicle sensors data are thinned at 1 Hz for the update of the

centralized Kalman filter. The external update to the centralized Kalman filter, such as

GPS and on-board vehicle sensors, facilitates the estimation of error states including

position errors, velocity errors, misalignment angles, as well as accelerometer and gyro

biases.
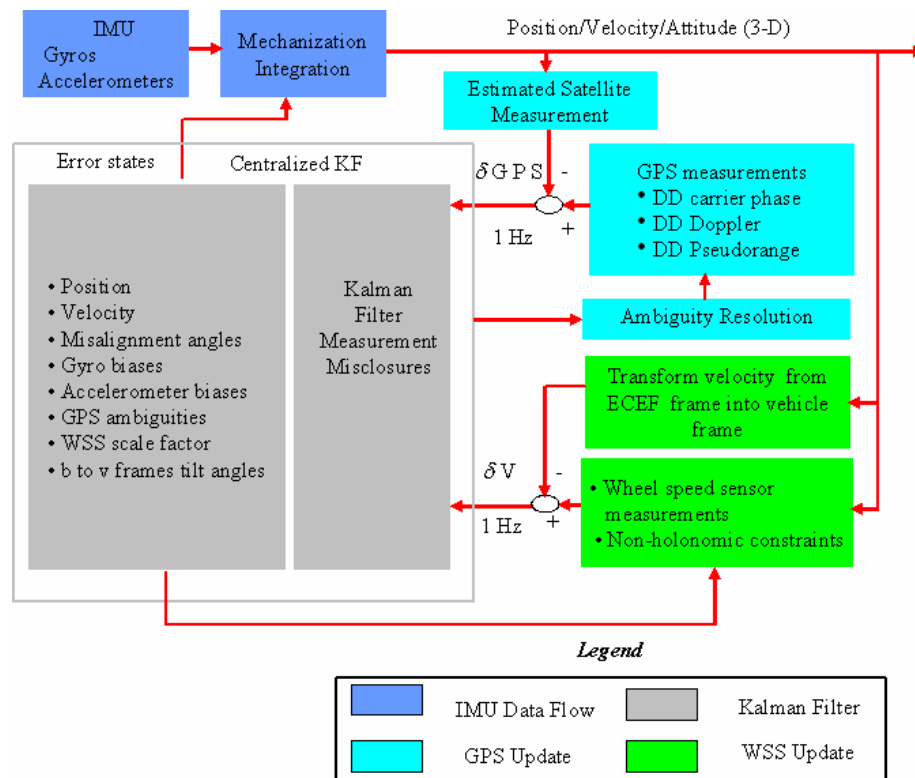
Figure 4.3 GPS/INS/ WSS integration strategy

Due to the centralized processing approach, the satellite measurements are estimated by

using the integrated position and velocity. The raw GPS measurements and the estimated

satellite measurements are compared to derive GPS measurement misclosures in the

centralized Kalman filter. When ambiguities need to be fixed, the float double differenced

ambiguities are augmented and estimated in the centralized Kalman filter. Integer

ambiguities are resolved by the LAMBDA method using real-valued ambiguities and

their relevant estimated standard deviations from the Kalman filter.

The centralized Kalman filter used for each integration strategy is a closed loop type. It

indicates that the relationship between the centralized Kalman filter and the external

update are bidirectional. In one manner, the GPS update provides an external aid to limit

the INS drift error when GPS is available. During GPS outages, on-board vehicle sensors

will continue to update the centralized Kalman filter and bridge the GPS data gap. In

another way, the estimated error states feedback to the integrated solutions as well as the

IMU and vehicle sensor measurements. With feedback information, the integrated

position, velocity and attitude angles can be corrected by the estimated error states of

position, velocity and misalignment angles. Also, the estimated accelerometer and gyro

biases, as well as augmented on-board vehicle sensor error states can rectify the IMU and

on-board vehicle sensor measurements.

In practical use, tire size is subject to many factors such as a payload, driving conditions,

temperature, tire-air pressure and tread wear. Additionally, the IMU body frame does not

always coincide with the vehicle frame. Thus, the scale factor of the wheel speed sensor

and the tilt angles between the vehicle and the body frames are augmented into error states of the centralized Kalman filter.

The wheel speed sensor estimates the forward-direction velocity in the vehicle frame, while two non-holonomic constraints are applied to vertical and lateral directions. The non-holonomic constraints imply that the vehicle does not move in vertical or the lateral directions assuming the land vehicle does not jump off or slide on the road. The lateral non-holonomic constraint is very close to a real condition when the vehicle runs on a flat road with a very small side slip, and it is violated when the vehicle runs on an icy or bumpy road with a larger side slip. This constitutes a weak point of the GPS/INS/WSS integration strategy.

The wheel speed sensor provides absolute velocity information to update the centralized Kalman filter. The measurement misclosure is computed in the vehicle frame by comparing the difference between integrated velocity and WSS measurements plus two non-holonomic constraints. With feedback from the centralized Kalman filter, the raw WSS measurement corrected by the estimated scale factor becomes closer to reality, and the estimated tilt angles between the body and vehicle frames make the WSS update more precise. During GPS outages, non-holonomic constraints as well as absolute velocity information can constrain the velocity and consequently the position drift of the stand-alone INS system. Furthermore, the zero velocity output of the WSS in static mode provides the possibility to perform a zero velocity update (ZUPT). Hence, it contributes

to limit the drift error in such a scenario that the vehicle runs in a static mode.

4.2.2 GPS/INS/G Sensors/Yaw Rate Sensor Integration Strategy

The GSP/INS/G sensors/Yaw rate sensor integration strategy is described in Figure 4.4.

Instead of providing absolute velocity as WSS, the GL/YRS unit constitutes a

dead-reckoning, horizontally two-dimensional IMU. Consequently, lateral and

longitudinal velocity can be derived from GL/YRS measurements with the initial velocity

being provided from the integrated system.
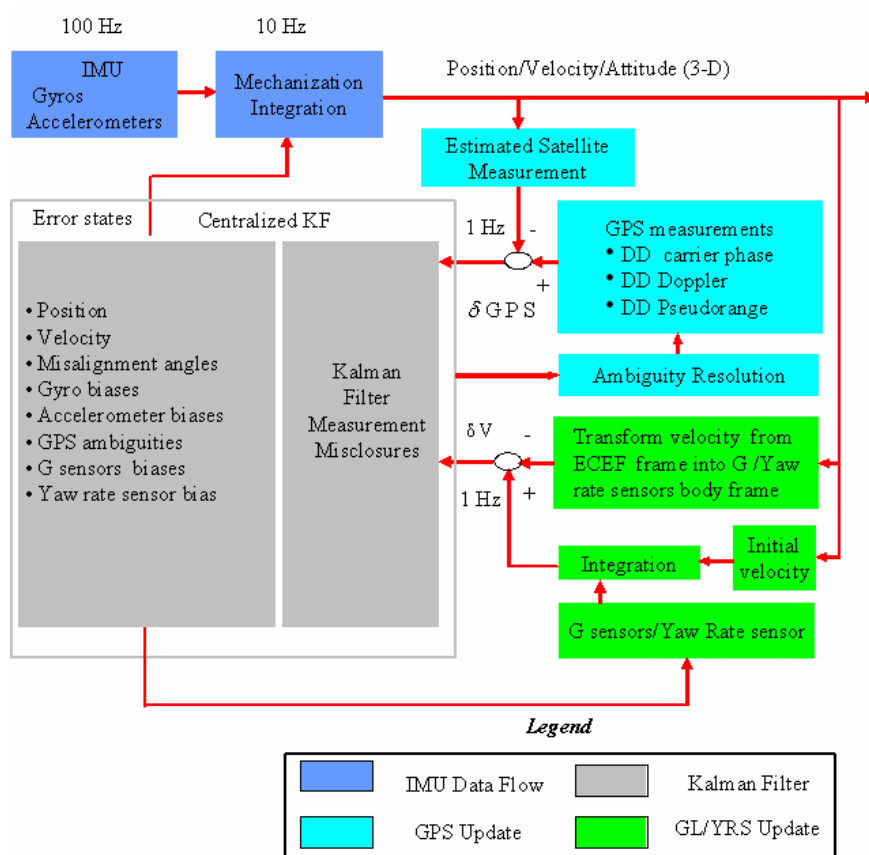
Figure 4.4 GPS/INS/GL/YRS integration strategy

The GL/YRS unit performs a velocity update in its body frame by computing

measurement misclosures between the integrated velocity (being transformed from the ECEF frame into the body frame) and the lateral/longitudinal velocity derived from the GL/YRS. Similarly to an IMU, the biases of the G sensor and yaw rate sensor are augmented into error states of the closed loop centralized Kalman filter. On the other hand, estimated GL/YRS biases are used to compensate raw GL/YRS measurements.

The quality of an automotive grade GL/YRS is of the same order as the low cost IMU, and is much lower than a tactical grade IMU. Thus, its error will drift at the same rate as a low cost IMU or at a much greater rate than a tactical grade IMU during GPS outages. Consequently, the improvement on positioning accuracy gained from the GL/YRS is expected to be somewhat limited and less significant than that from the WSS.

4.2.3   GPS/INS/Steering Angle Sensor Integration Strategy

Using a similar structure as that of the other two integration strategies discussed above, the basic idea of integrating the steering angle sensor is to compute the estimated steering angle from the integrated velocity output in the vehicle frame, and then to employ the steering angle measurement to update the centralized Kalman filter as shown in Figure 4.5.

As described in Chapter 3, the steering angle sensor measures the angle of the steering wheel. By passing through the Electrical Control Unit (ECU) and the actuator, the steering wheel angle is transformed into the vehicle tire angle relative to its neutral position. The steering angle is referred to as the vehicle tire angle relative to its neutral

position hereafter. The transformation between the steering wheel angle and the vehicle

tire angle is performed by a constant gain or scale factor.
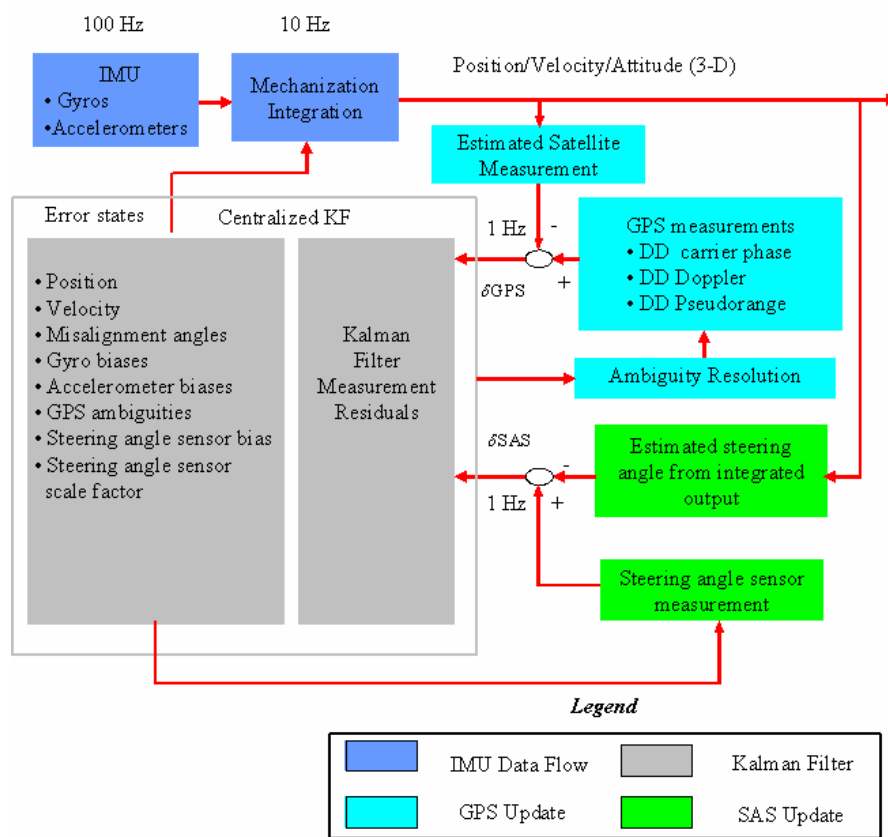
Figure 4.5 GPS/INS/SAS integration strategy

Due to some of the non-linear characteristics in the ECU and the actuator, however, this

transformation is far from linear in nature. To adapt to the variation of the transformation

gain, the scale factor and bias of the steering angle sensor are augmented into error states

of the Kalman filter. Similarly to the G sensors and the yaw rate sensor, a constant bias

exists in the steering angle sensor measurement. It will degrade the steering angle sensor

measurement accuracy, and needs to be estimated by the centralized Kalman filter.

The literature indicates that using the steering angle sensor to aid an INS to constrain the INS velocity error drift is novel. To date, the steering angle sensor is mainly used in the land vehicle steering system for the autonomous control of the vehicle. This research develops a new way to put the steering angle sensor into the land vehicle positioning and navigation by effectively integrating the steering angle sensor with GPS and INS.

4.2.4 Combined Integration Strategy for GPS/INS/On-Board Vehicle Sensors

Based on the aforementioned basic integration strategies, namely the GPS/INS/WSS (with two non-holonomic constraints), GPS/INS/GL/YRS as well as GPS/INS/SAS, two combined integration strategies can be derived from the basic modules or by creating a relationship between different vehicle sensors. These include:

- GPS/INS/WSS/SAS , and

- GPS/INS/WSS/SAS/GL/YRS

Either the basic or the combined integration strategies can be flexibly selected and implemented in software. Since the wheel speed sensor and the steering angle sensor produce independent measurements, sequential updating is used in the combined integration strategy GPS/INS/WSS/SAS. This integration strategy performs velocity and steering angle update in a sequential way.

The combined integration strategy GPS/INS/WSS/SAS/GL/YRS integrates all on-board vehicle sensors with the GPS/INS. With a sequential and independent update from the steering angle sensor, the WSS and GL/YRS work in a coordinated way to compensate

their weak points in one way or another. Figure 4.7 describes this interactive relationship

between the WSS and GL/YRS.
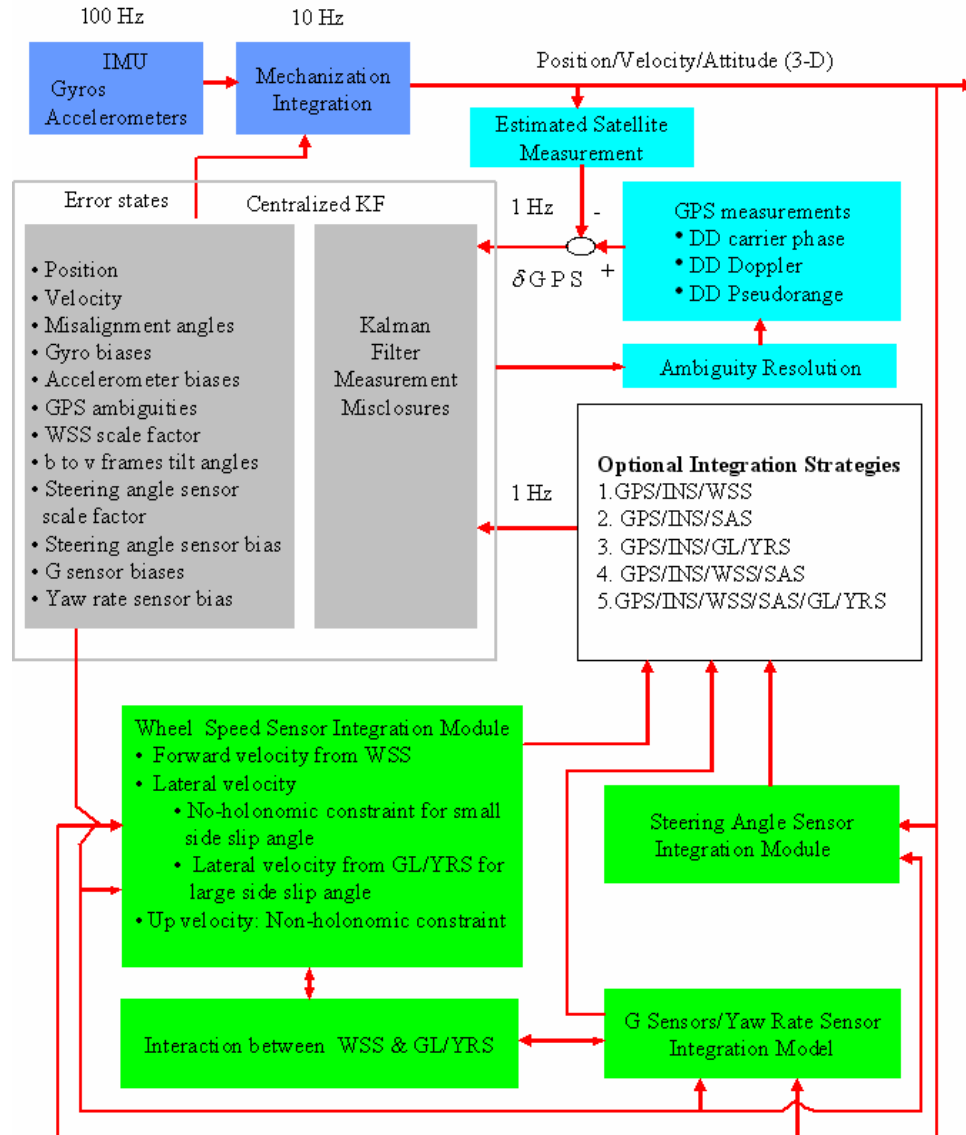
Figure 4.6 Combined integration strategies of GPS/INS/On-board vehicle sensors

The absolute velocity update from the WSS measurements limits the longitudinal

velocity drift error. Consequently, the accuracy of the initial longitudinal velocity for the

GL/YRS is increased. On the other hand, the side slip angle can be calculated from the

lateral and longitudinal velocities. The side slip angle information provides a way to detect and alleviate violation of the lateral non-holonomic constraint. When the side slip angle is smaller than a specific threshold, the lateral constraint is most likely valid. However, when the side slip angle goes beyond a specific threshold, the lateral non-holonomic constraint is violated.

One possible way to compensate for the violation of the lateral non-holonomic constraint is to make use of the lateral velocity calculated from the GL/YRS to replace the lateral non-holonomic constraint.
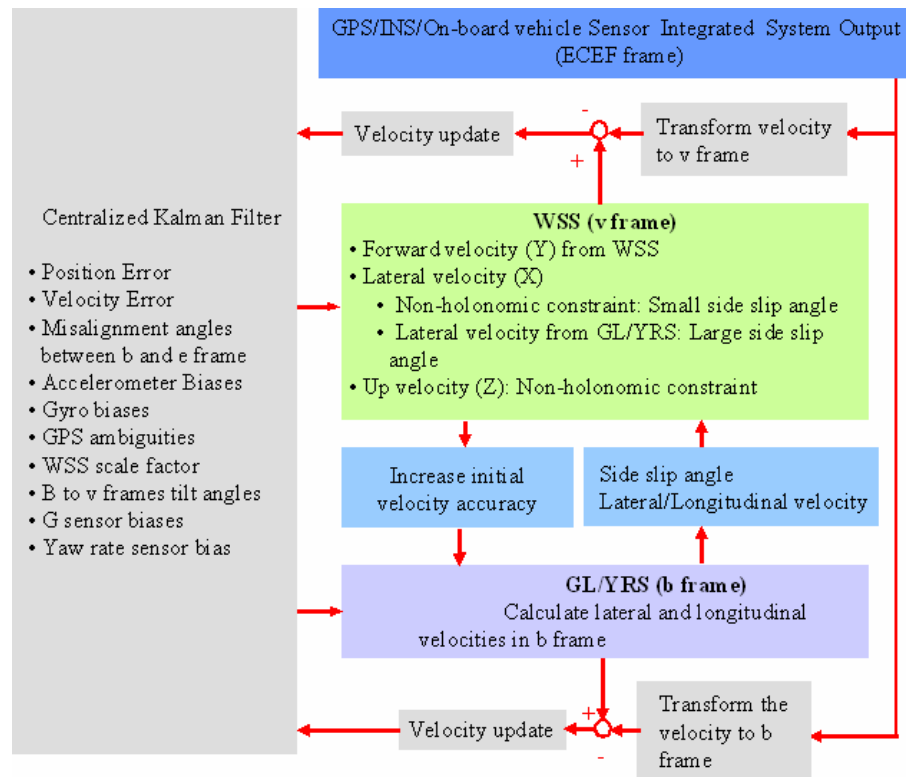
Figure 4.7 Interactive relationship between WSS and GL/YRS

Chapter 5   GPS/INS/On-Board Vehicle Sensor Integrated Algorithms

Integration algorithms are developed by deriving the dynamics and measurement models used in the Kalman filter for each basic integration module discussed in Chapter 4, namely, GPS/INS/WSS, GPS/INS/GL/YRS and GPS/INS/SAS, as well as a combined integration strategy GPS/INS/WSS/SAS/GL/YRS. Due to the importance of the lever arm effect on the integrated system positioning accuracy, the lever arm effect and the way of estimating the wheel speed sensor lever arm vector will be discussed first.

5.1   Lever Arm Effect

In the GPS/INS/On-board vehicle sensor integrated system, the GPS antenna is placed on the roof of the vehicle. The low cost IMU is fixed near the driver seat. The wheel speed sensors (WSS) are attached to the vehicle's wheels. The average value of the two rear wheel speed sensor measurements is used for system integration. Thus, the centre point of the rear wheel axle is the virtual location of the wheel speed sensor. The steering angle sensor is located on the centre point of the front wheel axle. The G sensors/Yaw rate sensor (GL/YRS) unit is installed on the chassis of the vehicle, and lies between the wheel speed sensor and the yaw rate sensor. The offsets of these locations introduce spatial vectors, which are called lever arms. When the GPS, IMU and on-board vehicle

sensors are integrated, lever arm effects must be taken into account since they are significant relative to the accuracy required.

Using the GPS antenna phase centre as a reference point, the lever arm vectors are computed from the IMU and on-board vehicle sensors to the GPS antenna phase centre. These lever arm vectors are represented by $L_{IMU \to GPS}^b$, $L_{WSS \to GPS}^b$, $L_{SAS \to GPS}^b$ and $L_{GL/YRS \to GPS}^b$ in Figure 5.1.
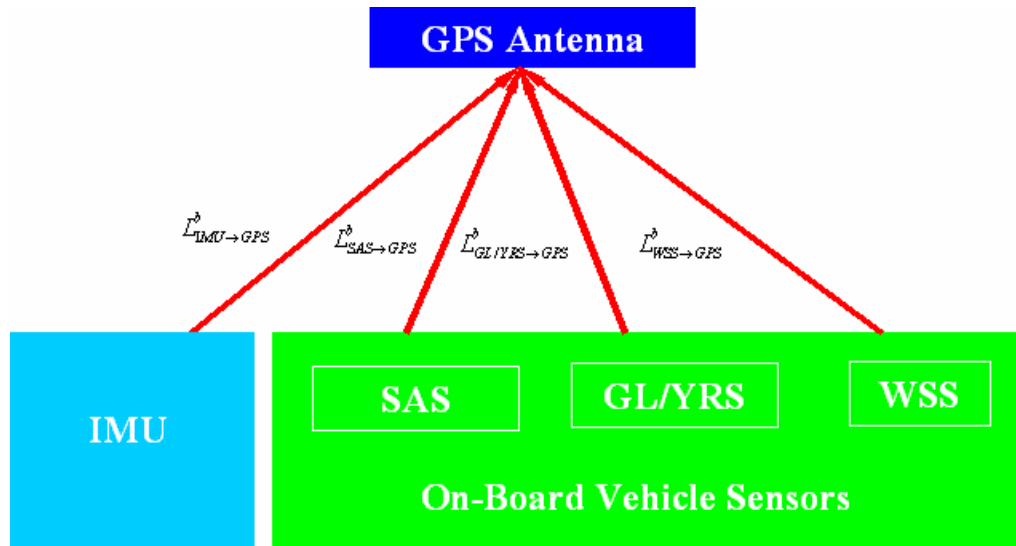
Figure 5.1 Lever arm vector for GPS, INS and on-board vehicle sensors

With the defined lever arm vectors, the position and velocity at the IMU and on-board vehicle sensors are mapped to the GPS antenna phase centre. In this way, the outputs of the integrated system are referenced to the GPS antenna phase centre. The position and velocity at the IMU are transformed into the GPS antenna phase centre by Equation (5.1) (Petovello et al. 2005).

$$\begin{cases} P^e_{IMU \to GPS} = P^e_{IMU} + R^e_b L^b_{IMU \to GPS} \\ V^e_{IMU \to GPS} = V^e_{IMU} + \dot{R}^e_b L^b_{IMU \to GPS} = V^e_{IMU} + (R^e_b \Omega^b_{ib} - \Omega^e_{ie} R^e_b) L^b_{IMU \to GPS} \end{cases} \qquad (5.1)$$

where $P^e_{IMU \to GPS}$ is the e frame position mapped from the IMU to the GPS antenna phase centre, P^e_{IMU} is the e frame position at the IMU, R^e_b is the direction matrix between the b and e frames, $L^b_{IMU \to GPS} = \begin{bmatrix} x^b_{IMU \to GPS} & y^b_{IMU \to GPS} & z^b_{IMU \to GPS} \end{bmatrix}^T$ is the lever arm vector between the IMU and the GPS antenna phase centre, $V^e_{IMU \to GPS}$ is the e frame velocity mapped from the IMU to the GPS antenna phase centre, V^e_{IMU} is e frame velocity at the IMU, Ω^b_{ib} is the skew-symmetric matrix of the gyro measurement, and Ω^e_{ie} is the skew-symmetric matrix of the Earth's rotation (which can be neglected for low cost IMUs).

For on-board vehicle sensors, the position information does not get involved in the system integration or in the update of the Kalman filter. Thus, only a velocity transformation from the on-board vehicle sensors into the GPS antenna phase centre is required, as shown in Equation (5.2).

$$\begin{cases} V^e_{WSS \to GPS} & = V^e_{WSS} + (R^e_b \Omega^b_{ib} - \Omega^e_{ie} R^e_b) L^b_{WSS \to GPS} \\ V^e_{SAS \to GPS} & = V^e_{SAS} + (R^e_b \Omega^b_{ib} - \Omega^e_{ie} R^e_b) L^b_{SAS \to GPS} \\ V^e_{GL/YRS \to GPS} = V^e_{GL/YRS} + (R^e_b \Omega^b_{ib} - \Omega^e_{ie} R^e_b) L^b_{GL/YRS \to GPS} \end{cases} \qquad (5.2)$$

where $V^e_{WSS \to GPS}$ is the e frame velocity mapped from the centre point of the rear wheel axle to the GPS antenna phase centre, V^e_{WSS} is e frame velocity at the centre point of the rear wheel axle, $L^b_{WSS \to GPS} = \begin{bmatrix} x^b_{WSS \to GPS} & y^b_{WSS \to GPS} & z^b_{WSS \to GPS} \end{bmatrix}^T$ is the lever arm vector from the centre point of the rear wheel axle to the GPS antenna phase centre, $V^e_{SAS \to GPS}$ is

the e frame velocity transformed from the centre point of the wheel axle to the GPS antenna phase centre, V^e_{SAS} is e frame velocity at the centre point of the front wheel axle, $L^b_{SAS \to GPS} = \begin{bmatrix} x^b_{SAS \to GPS} & y^b_{SAS \to GPS} & z^b_{SAS \to GPS} \end{bmatrix}^T$ is the lever arm vector from the SAS to the GPS antenna phase centre, $V^e_{GL/YRS \to GPS}$ is the e frame velocity from the GL/YRS unit to the GPS antenna phase centre, $V^e_{GL/YRS}$ is e frame velocity at the centre point of the GL/YRS unit, and $L^b_{GL/YRS \to GPS} = \begin{bmatrix} x^b_{GL/YRS \to GPS} & y^b_{GL/YRS \to GPS} & z^b_{GL/YRS \to GPS} \end{bmatrix}^T$ is the lever arm vector from the GL/YRS unit to the GPS antenna phase centre.

5.2 Wheel Speed Sensor Lever Arm Estimation

The lever arm vector between the centre point of the rear wheel axle and the GPS antenna phase centre can be estimated by the Kalman filter using a loose coupling strategy. The method discussed in this section also applies to the estimation of the IMU lever arm vector. A geometric layout of on-board vehicle sensors can be found from the vehicle manual. With the estimation of the lever arm vector of the wheel speed sensor, the lever arm vectors of other on-board vehicle sensors can be determined accordingly in terms of the geometric dimension of the sensors.

The loose coupling strategy used for the estimation of WSS lever arm, as shown in Figure 5.2, consists of a GPS-Only Kalman filter and an INS Kalman filter. The GPS-only Kalman filter estimates the position and velocity from GPS measurements. Instead of using the raw GPS measurement to update the centralized Kalman filter in the tight coupling strategy, the position and velocity estimated by the GPS-Only Kalman filter as

well as the WSS measurement are used to update the INS Kalman filter. Given the initial

values of the lever arm vector, the error state of the lever arm vector is estimated by the

INS Kalman filter.
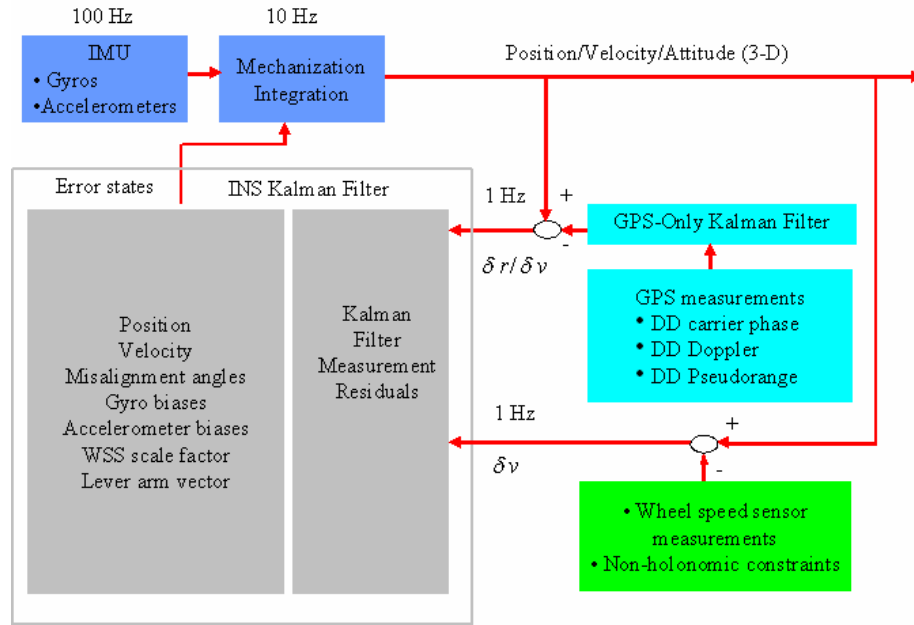
Figure 5.2 Loose coupling strategy for the estimation of the WSS lever arm effect

For simplification, misalignment angles between the IMU body frame and the vehicle

frame are not considered in the lever arm estimation. The error states of the lever arm

vector and the wheel speed sensor scale factor are modeled as random constants, and are

augmented to the state vector of the INS Kalman filter. The state vector of the Kalman

filter consequently becomes,

$$\delta x = \begin{bmatrix} \delta r^e & \delta v^e & \varepsilon^e & \delta b^b & \delta d^b & \delta L^b_{WSS \rightarrow GPS} & \Delta S \end{bmatrix} \tag{5.3}$$

where $\delta L^b_{WSS \rightarrow GPS}$ is the error state of the lever arm vector, and δS is the error state of

the wheel speed sensor scale factor.

For the low cost IMU, the Earth's rotation rate in Equation (5.2) can be neglected. The measurement equation is shown as follows

$$v^e_{GPS/INS/WSS} = R^e_b V_{WSS} + R^e_b \Omega^b_{ib} L^b_{WSS \to GPS} + w \qquad (5.4)$$

where $V_{WSS} = \begin{bmatrix} 0 & S \cdot v_{WSS} & 0 \end{bmatrix}^T$ contains two non-holonomic constraints and the wheel speed sensor measurement v_{WSS}, S is the wheel speed sensor scale factor, and $v^e_{GPS/INS/WSS}$ is the velocity of the integrated system in the e frame.

The perturbation of the right hand side of the measurement model in Equation (5.4) is shown in Equation (5.5)

$$\delta \left(R^e_b \cdot V_{WSS} + R^e_b \Omega^b_{ib} L^b_{WSS \to GPS} \right)$$
$$= (\delta R^e_b) \cdot V_{WSS} + R^e_b \cdot V_{WSS} \cdot \delta S + (\delta R^e_b) \Omega^b_{ib} L^b_{WSS \to GPS} + R^e_b (\delta \Omega^b_{ib}) L^b_{WSS \to GPS} + R^e_b \Omega^b_{ib} \delta L^b_{WSS \to GPS} \quad (5.5)$$
$$= -(V^E_{WSS} + L^{\Omega E}_{WSS \to GPS}) \cdot \varepsilon^e + R^e_b \cdot V_{WSS} \cdot \delta S - R^e_b L^{SB}_{WSS \to GPS} \cdot d^b + R^e_b \Omega^b_{ib} \delta L^b_{WSS \to GPS}$$

where V^E_{WSS} is the skew-symmetric matrix of $R^e_b \cdot V_{WSS}$, $L^{\Omega E}_{WSS \to GPS}$ is the skew-symmetric matrix of $R^e_b \Omega^b_{ib} L^b_{WSS \to GPS}$, and $L^{SB}_{WSS \to GPS}$ is the skew-symmetric matrix of $L^b_{WSS \to GPS}$.

On the basis of Equations (5.4) and (5.5), the measurement model for the WSS lever arm vector estimation is shown in Equation (5.6)

$$H = \begin{bmatrix} O_{3 \times 3} & I_{3 \times 3} & V^E_{WSS} + L^{\Omega E}_{WSS \to GPS} & O_{3 \times 3} & R^e_b L^{SB}_{WSS \to GPS} & -R^e_b \Omega^b_{ib} & -R^e_b V_{WSS} \end{bmatrix} \quad (5.6)$$

where O is the null matrix with the subscripted dimensions.

5.3 Modeling of the On-Board Vehicle Sensor Errors Using a Stochastic Process

Random constant, random walk and the first-order Gauss-Markov processes are commonly used stochastic processes to model random phenomena (Gelb 1974).

A random constant is a non-dynamic quantity with a fixed, albeit random amplitude. It is modelled as an integrator with no input but with an initial condition,

$$\dot{x} = 0 \tag{5.7}$$

The random constant is appropriate for modelling typical phenomena that do not change their values over time (Maybeck 1979). As steering and turning operations generally occur over short time spans, it makes sense to model the steering angle sensor scale factor and bias as random constants. Similarly, other on-board vehicle sensor error parameters that are long-term stable, such as the tilt angles between the IMU body and vehicle frames, the wheel speed sensor scale factor as well as the lever arm vectors are also modelled as random constants. When IMU and on-board vehicle sensors are mechanically installed on a certain point, the tilt angles between the IMU body and vehicle frames as well as the lever arm vector are almost constant. The scale factor of the wheel speed sensor is closely related to payload on the vehicle, and is susceptible to the side slip. The side slip is associated with road conditions and high vehicle dynamics. It is not easy to predict. Without losing generality, it is reasonable to model the scale factor of the wheel speed sensor as the random constant.

However, it is a more appropriate way to model error states that vary slowly over time as a random walk or a first-order Gauss-Markov process.

A random walk represents the output of an integrator driven by Gaussian white noise. It is an independent increment process, whose stochastic differential equation is expressed by

$$\dot{x} = w \qquad\qquad (5.8)$$

where w is the Gaussian white noise.

The first-order Gauss-Markov process is used to model an exponentially correlated process comprised of white noise. It is characterized by an exponential autocorrelation

$$\dot{x} = -\beta x + w \qquad\qquad (5.9)$$

where β is the reciprocal of the correlation time constant.

Between the first-order Gauss-Markov process and the random walk, the first-order Gauss-Markov process can approximate the random walk when the correlation time is extreme large or $\beta = 0$.

The typical usage of a first-order Gauss-Markov process is to model the slow varying errors in the IMU and on-board vehicle sensors, such as gyro and accelerometer biases as well as G sensors and yaw rate sensor biases.

In the random walk process, if the noise power in the random walk process is expressed by

$$E\left[w(t)w(\tau)^{T}\right]=q\delta(t-\tau) \tag{5.10}$$

The variance of the random walk process is consequently (Brown & Hwang 1992),

$$\sigma_{x}^{2}=q(t-t_{0}) \tag{5.11}$$

where t_{0} is the initial time, and t is the time at current epoch.

It explicitly indicates that the variance of the random walk grows with time. The noises in IMU and some on-board vehicle sensors behave as the random walk when integrating the noise corrupted measurements of accelerometers/G sensors or gyros/yaw rate sensor into velocity or attitude angles. In this way, the accuracy of mechanization outputs of IMU or G sensor/Yaw rate sensor degrade with time due to the integral of noise in the random walk process. It can be seen the noise is another factor that leads to the drift error in the stand-alone inertial system in addition to the error sources such as biases.

5.4   GPS/INS/Wheel Speed Sensor Integration Algorithm

When using a centralized Kalman filter, the GPS/INS integrated system augments double differenced ambiguities ($\Delta\nabla N$) when necessary into the INS dynamics error model in Equation (2.16). The dynamics model for the GPS/INS centralized Kalman filter is consequently given by Equation (5.12) (Petovello 2003).

Equation (5.12) implies that the bias states for the accelerometers and gyros are modeled as first-order Gauss-Markov processes, although any other suitable models could be used instead.

$$
\begin{bmatrix} \delta\dot{r}^e \\ \delta\dot{v}^e \\ \dot{\varepsilon}^e \\ \delta\dot{b}^b \\ \delta\dot{d}^b \\ \Delta\nabla\dot{N} \end{bmatrix} = \begin{bmatrix} 0 & I & 0 & 0 & 0 & 0 \\ N^e & -2\Omega_{ie}^e & -F^e & R_b^e & 0 & 0 \\ 0 & 0 & -\Omega_{ie}^e & 0 & R_b^e & 0 \\ 0 & 0 & 0 & -diag(\alpha_i) & 0 & 0 \\ 0 & 0 & 0 & 0 & -diag(\beta_i) & 0 \\ 0 & 0 & 0 & 0 & 0 & 0 \end{bmatrix} \begin{bmatrix} \delta r^e \\ \delta v^e \\ \varepsilon^e \\ \delta b^b \\ \delta d^b \\ \Delta\nabla N \end{bmatrix}
$$

$$
+ \begin{bmatrix} 0 & 0 & 0 & 0 \\ R_b^e & 0 & 0 & 0 \\ 0 & R_b^e & 0 & 0 \\ 0 & 0 & I & 0 \\ 0 & 0 & 0 & I \\ 0 & 0 & 0 & 0 \end{bmatrix} \begin{bmatrix} w_f \\ w_w \\ w_b \\ w_d \end{bmatrix} = F_{GPS/INS}\delta x + G_{GPS/INS} w
$$

$$(5.12)$$

where $\Delta\nabla N$ is the vector of double difference carrier phase ambiguities, and $F_{GPS/INS}$ is the dynamics matrix for the GPS/INS integration strategy, $G_{GPS/INS}$ is the shaping matrix of the driving noise, and w is the noise matrix.

In terms of the GPS/INS/WSS integration strategy shown in Figure 4.3, the scale factor of the wheel speed sensor and the tilt angles between the vehicle and body frames are augmented to the error states of the GPS/INS centralized Kalman filter. Thus, the dynamics model in Equation (5.12) is augmented into Equation (5.13). The wheel speed sensor scale factor and the tilt angles between the b and v frames are modeled as random constants.

$$
\begin{bmatrix} \delta\dot{r} \\ \delta\dot{v} \\ \dot{\varepsilon}^e \\ \delta\dot{b}^b \\ \delta\dot{d}^b \\ \Delta\nabla\dot{N} \\ \delta\dot{S} \\ \dot{\varepsilon}_{b-v} \end{bmatrix} =
\left[\begin{array}{ccccccc|cc}
 & & & F_{GPS/INS} & & & & O & \\
\hline
0 & 0 & 0 & 0 & 0 & 0 & & 0 & 0 \\
0 & 0 & 0 & 0 & 0 & 0 & & 0 & 0
\end{array} \right]
\begin{bmatrix} \delta r \\ \delta v \\ \varepsilon^e \\ \delta b^b \\ \delta d^b \\ \Delta\nabla N \\ \delta S \\ \varepsilon_{b-v} \end{bmatrix}
$$

$$
+ \begin{bmatrix} 0 & 0 & 0 & 0 \\ R_b^e & 0 & 0 & 0 \\ 0 & R_b^e & 0 & 0 \\ 0 & 0 & I & 0 \\ 0 & 0 & 0 & I \\ 0 & 0 & 0 & 0 \\ 0 & 0 & 0 & 0 \\ 0 & 0 & 0 & 0 \end{bmatrix}
\begin{bmatrix} w_f \\ w_w \\ w_b \\ w_d \end{bmatrix} = F_{GPS/INS/WSS}\,\delta x + G_{GPS/INS/WSS}\,w
$$

$$
\tag{5.13}
$$

where $F_{GPS/INS/WSS}$ is the dynamics matrix for the GPS/INS/WSS integration strategy, $G_{GPS/INS/WSS}$ is the shaping matrix, δS is the wheel speed sensor scale factor error state, and $\varepsilon_{b-v} = \begin{bmatrix} \delta\alpha & \delta\beta & \delta\gamma \end{bmatrix}^T$ is the error vector of the tilt angles between the body frame and the vehicle frame corresponding to the X, Y and Z axes, respectively.

Since wheel speed is measured in the vehicle frame, whereas velocities in the integrated system are parameterized in the ECEF frame, the WSS update can be carried out either in the e frame by transforming the WSS measurement into the e frame, or alternatively it can be carried out in the v frame by transforming the integrated velocities into the v frame. In this research, the WSS update is carried out in the v frame.

The velocity at the centre point of the rear wheel axle represents the average of the two rear wheel speed sensor measurements. It is used as the external velocity update to aid the INS. The wheel speed sensor provides the velocity information in the longitudinal direction (along-track) of the vehicle. The non-holonomic constraints are applied in vertical and lateral (cross-track) directions of the vehicle frame. As shown in Figure 5.3, the non-holonomic constraints mean that the velocities in vertical and lateral (cross-track) directions are zero if the vehicle does not jump off and slide on the ground.
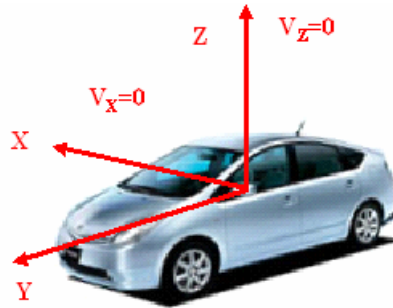
Figure 5.3 Non-holonomic constraints

The measurement equation in the Kalman filter is expressed by Equation (5.14) with two non-holonomic constraints being applied to the X and Z axes of the vehicle frame.

$$\begin{bmatrix} 0 \\ S \cdot v_{wss} \\ 0 \end{bmatrix} = R_b^v (R_b^e)^T v^e + w_m \qquad (5.14)$$

where S is the wheel speed sensor scale factor, and R_b^v is the direction cosine matrix between the b and v frames as calculated by Equation (5.15)

$$R_b^v = R_3(\gamma) R_1(\alpha) R_2(\beta) \qquad (5.15)$$

where α, β, γ are the tilt angles between the b and v frames with respect to the X, Y and Z axes, respectively.

The perturbation of the left hand side of Equation (5.16) is expressed by the following equation

$$\delta\left(\begin{bmatrix} 0 \\ S\ v_{WSS} \\ 0 \end{bmatrix}\right) = \begin{bmatrix} 0 \\ v_{WSS} \\ 0 \end{bmatrix} \delta S = V_{WSS} \delta S \qquad (5.16)$$

where $V_{WSS} = \begin{bmatrix} 0 & v_{WSS} & 0 \end{bmatrix}^T$ is the measurement used for the WSS update. It is a 3x1 vector.

The perturbation of the right hand side of Equation (5.14) is shown in Equation (5.17)

$$\delta(R_b^v (R_b^e)^T v^e) = R_b^v (R_b^e)^T \delta v^e + R_b^v (R_b^e)^T V^E \varepsilon^e - V^V \varepsilon_{b-v} \qquad (5.17)$$

where v^e is the velocity in the integrated system in the e frame, and $v^v = R_b^v (R_b^e)^T v^e$ is the integrated velocity in the v frame. V^E is the skew-symmetric matrix of the integrated velocity in the e frame v^e, and V^V is the skew-symmetric matrix of the integrated velocity expressed in the vehicle frame v^v.

From Equations (4.16) and (5.14), the measurement misclosure is shown in Equation (5.18).

$$e_z = \begin{bmatrix} 0 \\ S \cdot v_{wss} \\ 0 \end{bmatrix} - R_b^v (R_b^e)^T v^e \qquad (5.18)$$

From Equations (4.17) and (5.14), the design matrix is derived from Equation (5.19)

$$e_z = R_b^v (R_b^e)^T \delta v^e + R_b^v (R_b^e)^T V^E \varepsilon^e - V^V \varepsilon_{b-v} - V_{WSS} \delta S + \omega_m$$
$$= H_{WSS} \delta x + \omega_m \tag{5.19}$$

Thus, the design matrix H_{WSS} is summarized below

$$H_{WSS} = \begin{bmatrix} O_{3\times3} & R_b^v (R_b^e)^T & R_b^v (R_b^e)^T V^E & O_{3\times3} & O_{3\times3} & O_{3\times AR} & -V_{WSS} & -V^V \end{bmatrix} \tag{5.20}$$

Equation (5.20) is a hyper-matrix in which each sub-matrix corresponds to the error states defined in (5.13). O is a null matrix with subscripted dimensions.

5.5   GPS/INS/G Sensors/Yaw Rate Sensor Integration Algorithm

As shown in Figure 4.4, the biases of the G sensors and yaw rate sensor are augmented into the GPS/INS centralized Kalman filter as a first-order Gauss-Markov process. Consequently, the dynamics model for the GPS/INS/GL/YRS integration strategy is shown in Equation (5.21)

$$
\begin{bmatrix} \delta\dot{r} \\ \delta\dot{v} \\ \dot{\varepsilon} \\ \delta\dot{b}^b \\ \delta\dot{d}^b \\ \Delta\nabla\dot{N} \\ \delta\dot{b}_{GL} \\ \delta\dot{d}_{YRS} \end{bmatrix} =
\left[\begin{array}{cccccc|cc}
& & & & & & & \\
& & F_{GPS/INS} & & & & O & \\
& & & & & & & \\
& & & & & & & \\
& & & & & & & \\
\hline
0 & 0 & 0 & 0 & 0 & 0 & -\beta_{GL} & 0 \\
0 & 0 & 0 & 0 & 0 & 0 & 0 & -\beta_{YRS}
\end{array}\right]
\begin{bmatrix} \delta r \\ \delta v \\ \varepsilon \\ \delta b^b \\ \delta d^b \\ \Delta\nabla N \\ \delta b_{GL} \\ \delta d_{YRS} \end{bmatrix}
$$

$$
+ \begin{bmatrix}
0 & 0 & 0 & 0 & 0 & 0 \\
R_b^e & 0 & 0 & 0 & 0 & 0 \\
0 & R_b^e & 0 & 0 & 0 & 0 \\
0 & 0 & I & 0 & 0 & 0 \\
0 & 0 & 0 & I & 0 & 0 \\
0 & 0 & 0 & 0 & 0 & 0 \\
0 & 0 & 0 & 0 & 1 & 0 \\
0 & 0 & 0 & 0 & 0 & 1
\end{bmatrix}
\begin{bmatrix} w_f \\ w_w \\ w_b \\ w_d \\ w_{GL} \\ w_{YRS} \end{bmatrix} \tag{5.21}
$$

$$
= F_{GPS/INS/GL/YRS}\,\delta x + G_{GPS/INS/GL/YRS}\,w
$$

where δb_{GL} is the (2x1) error vector of the G sensor biases, δd_{YRS} is the (1x1) error vector of the yaw rate sensor bias, β_{GL} and β_{YRS} are the time constant reciprocals of the first-order Gauss-Markov process model for the GL and YRS biases respectively, w_{GL} and w_{YRS} are the driving noises for the GL and YRS biases respectively, $F_{GPS/INS/GL/YRS}$ is the dynamics matrix for the GPS/INS/GL/YRS integration strategy and $G_{GPS/INS/GL/YRS}$ is the shaping matrix.

When using the G sensors and yaw rate sensor, the equations of motion in the body frame are shown in Equation (5.22) (Dissanayake et al. 2001). Since the non-holonomic

constraint is applied in the vertical direction, the vertical velocity is only coupled with

gravity.

$$\begin{cases} \dot{V}_x^b = \left(f_x - b_{GL1} \right) - V_y (r - d_{YRS}) + g_x^b \\ \dot{V}_y^b = \left(f_y - b_{GL2} \right) + V_x (r - d_{YRS}) + g_y^b \\ \dot{V}_z^b = g_z^b \end{cases} \tag{5.22}$$

where f_x and f_y are the specific force measurements from the G sensors, γ is the yaw

rate measurement , V_x^b, V_y^b, V_z^b are the velocities in the b frame, and g_x^b, g_y^b, g_z^b are the

gravity elements in the b frame, $b_{GL} = \begin{bmatrix} b_{GL1} & b_{GL2} & 0 \end{bmatrix}$ and d_{YRS} are the biases of the G

sensors and the yaw rate sensor respectively.

The gravity vector in Equation (5.22) is derived from the gravity vector in the e frame by

Equation (5.23).

$$g^b = (R_b^e)^T g^e \tag{5.23}$$

where g^e is the gravity vector in the e frame, and R_b^e is the direction cosine matrix

between the b and e frames.

By defining

$$M = \begin{bmatrix} 1 & 0 & 0 \\ 0 & 1 & 0 \\ 0 & 0 & 0 \end{bmatrix}, \ f = \begin{bmatrix} f_x \\ f_y \\ 0 \end{bmatrix}, \ J = \begin{bmatrix} 0 & -1 & 0 \\ 1 & 0 & 0 \\ 0 & 0 & 0 \end{bmatrix} \tag{5.24}$$

Equation (5.22) can be replaced by the state space vector in Equation (5.25), which

simplifies the mathematical analysis.

$$\dot{V}^b = M\left(f - b_{GL}\right) + JV^b\left(\gamma - d_{YRS}\right) + g^b \tag{5.25}$$

where V^b is the velocity vector in the b frame, f is the specific force vector from the

G sensors, g^b is the gravity vector in the b frame, and M, J are the coefficients defined

in Equation (5.24).

Using the trapezoid method of integration (Jekeli 2000), the velocity in the body frame

can be integrated from Equation (5.25) as

$$\begin{cases} V^b = V_0^b + \dfrac{1}{2}(k_1 + k_2) \cdot \Delta t \\ k_1 = M(f_{(0)} - b_{GL(0)}) + JV_0^b(\gamma_{(0)} - d_{YRS(0)}) + g_0^b \\ k_2 = M(f - b_{GL}) + J(V_0^b + k_1 \cdot \Delta t)(\gamma - d_{YRS}) + g^b \end{cases} \tag{5.26}$$

where V_0^b is the initial velocity that comes from the integrated system, $f_{(0)}$ and $\gamma_{(0)}$

are the G sensors and yaw rate sensor measurements at the last epoch, $b_{GL(0)}$ and $d_{YRS(0)}$

are the G sensors and yaw rate sensor biases at the last epoch, g_0^b is the last epoch's

gravity vector in the b frame, k_1 and k_2 are parameters for the trapezoid integration,

and Δt is the integration time interval (defined to be 1 s in this research). As

aforementioned, the update rate on the centralized Kalman filter from the external aid

(GPS, WSS, GL/YRS and SAS) is selected at 1 Hz by making a tradeoff between the

computational load and the system performance. Additionally, the integration of GL/YRS

unit is bounded by retrieving the initial velocity from the integrated system output within

each integration time interval. Hence the integration time interval for GL/YRS

mechanization equation is selected at 1 Hz.

To conduct the GL/YRS update in the b frame, the velocity in the integrated system is transformed from the e frame into the b frame, and the measurement equation is expressed by Equation (5.27).

$$V^b = (R_b^e)^T v^e \tag{5.27}$$

where V^b is the velocity computed from Equation (5.26), and v^e is the velocity of the integrated system in the e frame.

The perturbation of the gravity vector in Equation (5.23) can be derived as shown in Equation (5.28).

$$\delta g^b = (R_b^e)^T N^e \delta r^e + (R_b^e)^T G^e \varepsilon^e \tag{5.28}$$

where N^e is the tensor of gravity gradients, G^e is the skew-symmetric matrix of the gravity vector in the e frame.

Using Equations (5.26) and (5.28), the perturbation of the velocity vector V^b is expressed by Equation (5.29)

$$
\begin{aligned}
\delta V^b &= \frac{1}{2}(\delta k_1 + \delta k_2)\Delta t \\
&= \frac{\Delta t}{2}(R_b^e)^T N^e \delta r^e + \frac{\Delta t}{2}(R_b^e)^T G^e \varepsilon^e \\
&\quad + \frac{\Delta t}{2} M \delta b_{GL} + \frac{\Delta t}{2} J (V_0^b + k_1 \cdot \Delta t)\delta d_{YRS}
\end{aligned}
\tag{5.29}
$$

The perturbation of the right hand side of Equation (5.27) is shown in Equation (5.30)

$$\delta\left((R_b^e)^T v^e\right) = (R_b^e)^T \delta v^e + (R_b^e)^T V^E \varepsilon^e \tag{5.30}$$

where V^E is the skew-symmetric matrix of the integrated velocity in the e frame.

Similarly to the WSS update, the measurement misclosure can be derived from Equations (4.16) and (5.27), as shown below

$$e_z = V^b - (R_b^e)^T v^e \tag{5.31}$$

Based on Equations (5.29) and (5.30), the design matrix related to the GL/YRS velocity update is consequently derived in Equation (5.32) in terms of Equations (4.17)

$$
\begin{aligned}
e_z &= \delta\left((R_b^e)^T v^e\right) - \delta V^b + w_m \\
&= -\frac{\Delta t}{2}(R_b^e)^T N^e \delta r^e + (R_b^e)^T \delta v^e + \left[(R_b^e)^T V^E - \frac{\Delta t}{2}(R_b^e)^T G^e \Delta t\right]\varepsilon^e \\
&\quad -\frac{\Delta t}{2} M \delta b_{GL} - \frac{\Delta t}{2} J(V_0^b + k_1 \Delta t)\delta d_{Yaw} + w_m \\
&= H_{GL/YRS}\delta x + w
\end{aligned}
\tag{5.32}
$$

where $H_{GL/YRS}$ is the design matrix for the GL/YRS update, which is coupled with the error states of position, velocity, b to e frame misalignment angles and GL/YRS biases. More specifically, the design matrix is:

$$
\begin{aligned}
&H_{GL/YRS} = \\
&\left[\frac{\Delta t}{2}(R_b^e)^T N^e \quad (R_b^e)^T \quad (R_b^e)^T V^E - \frac{\Delta t}{2}(R_b^e)^T G^e \Delta t \quad O_{3\times3} \quad O_{3\times3} \quad O_{3\times AR} \quad -\frac{\Delta t}{2}M \quad -\frac{\Delta t}{2}J(V_0^b + k_1 \Delta t)\right]
\end{aligned}
\tag{5.33}
$$

In this research, the noise power of the GL/YRS was determined using data from a static test by calculating the average standard deviation across 40 evenly spaced one-second intervals of static data. When performing integration with the GL/YRS measurements to derive velocity, the noise in the GL/YRS generates a random walk error because of the integration. In terms of Equation (5.11), the integral of G sensor noise into the velocity

behaves as a random walk process. The variance resulting from the propagation of noise

is

$$\sigma_{V^b_{Noise}}^2 = \sigma_{GL}^2 \Delta t \tag{5.34}$$

where $\sigma_{v^b_{Noise}}^2$ is the noise power of the G sensors, Δt is the time interval for integration,

and $\sigma_{V^b_{Noise}}^2$ is the variance propagated by measurement noise.

Considering that integration is performed every 1 s, and the initial value comes from the

integrated system every 1 s, $\sigma_{V^b_{Noise}}^2 = \sigma_{GL}^2$ herein. Therefore, the velocity variance for the

GL/YRS velocity update can be tuned adaptively in terms of variance propagation theory

from Equation (5.26), which is shown in Equation (5.35)

$$\begin{cases} \sigma_{V^b}^2 = \sigma_{V_0^b}^2 + \dfrac{1}{4}(\sigma_{k1}^2 + \sigma_{k2}^2)\Delta t^2 \\[2mm] \sigma_{g^b}^2 = (R_b^e)^T N^e \sigma_{r^e}^2 (N^e)^T R_b^e \\[2mm] \sigma_{k1}^2 = M(\sigma_f^2 + \sigma_{b_{GL(0)}}^2)M^T + J\sigma_{V_0^b}^2 (\gamma_{(0)} - d_{YRS(0)})^2 J^T + JV_0^b(\sigma_\gamma^2 + \sigma_{d_{YRS(0)}}^2)(JV_0^b)^T + \sigma_{g_0^b}^2 \\[2mm] \sigma_{k2}^2 = M(\sigma_f^2 + \sigma_{b_{GL}}^2)M^T + J(\sigma_{V_0^b}^2 + \sigma_{k1}^2 \Delta t^2)(\gamma - d_{YRS})^2 \cdot J^T \\[2mm] \qquad + J(V_0^b + k_1\Delta t)(\sigma_\gamma^2 + \sigma_{d_{YRS}}^2)(V_0^b + k_1\Delta t)^T J^T \\[2mm] \qquad + \sigma_{g^b}^2 \end{cases} \tag{5.35}$$

where $\sigma_{V^b}^2$ is the velocity variance of the GL/YRS, $\sigma_{b_{GL}}^2$ and $\sigma_{d_{YRS}}^2$ are the estimated

variances of GL/YRS biases provided by the Kalman filter, $\sigma_{b_{GL(0)}}^2$ and $\sigma_{d_{YRS(0)}}^2$ are the

variances of GL/YRS biases at the previous step, $\sigma_{V_0^b}^2$ is the initial velocity variance

from the integrated system, $\sigma_{g^b}^2$ is the variance of the gravity vector in the b frame, and

$\sigma_{r^e}^2$ is the position variance in the e frame.

5.6   GPS/INS/Steering Angle Sensor Integration Algorithm

In the dynamics model for the GPS/INS/Steering angle sensor integrated system, the scale factor and the bias of the steering angle sensor are augmented into the error state vector of the GPS/INS centralized Kalman filter. The scale factor and steering angle sensor bias are all modeled as random constants. The dynamics model is therefore expressed by

$$
\begin{bmatrix} \delta \dot{r} \\ \delta \dot{v} \\ \dot{\varepsilon}^e \\ \delta \dot{b}^b \\ \delta \dot{d}^b \\ \Delta \nabla \dot{N} \\ \delta \dot{S}_{SAS} \\ \delta \dot{d}_{SAS} \end{bmatrix} =
\left[\begin{array}{ccccccc|cc}
& & & F_{GPS/INS} & & & & O & \\
\hline
0 & 0 & 0 & 0 & 0 & 0 & | & 0 & 0 \\
0 & 0 & 0 & 0 & 0 & 0 & | & 0 & 0
\end{array} \right]
\begin{bmatrix} \delta r \\ \delta v \\ \varepsilon^e \\ \delta b^b \\ \delta d^b \\ \Delta \nabla N \\ \delta S_{SAS} \\ \delta d_{SAS} \end{bmatrix}
$$

$$
+ \begin{bmatrix} 0 & 0 & 0 & 0 \\ R_b^e & 0 & 0 & 0 \\ 0 & R_b^e & 0 & 0 \\ 0 & 0 & I & 0 \\ 0 & 0 & 0 & I \\ 0 & 0 & 0 & 0 \\ 0 & 0 & 0 & 0 \\ 0 & 0 & 0 & 0 \end{bmatrix}
\begin{bmatrix} w_f \\ w_w \\ w_b \\ w_d \end{bmatrix}
= F_{GPS/INS/SAS} \delta x + G_{GPS/INS/SAS} w \tag{5.36}
$$

where δS_{SAS} is the error state of the steering angle sensor, δd_{SAS} is the error state of the steering angle sensor bias, $F_{GPS/INS/SAS}$ is the dynamics matrix of the GPS/INS/SAS integration strategy, and $G_{GPS/INS/SAS}$ is the shaping matrix of the GPS/INS/SAS integration strategy.

Assuming the sideslip of the front tire is zero, the steering angle can be estimated from the velocity in the vehicle frame. The measurement model for the GPS/INS/Steering angle sensor is shown in Equation (5.37)

$$S_{SAS}\psi - d_{SAS} = -\tan^{-1}\left(\frac{v_x^v}{v_y^v}\right) + w_m \tag{5.37}$$

where S_{SAS} is the scale factor of the steering angle sensor, d_{SAS} is the bias of the steering angle sensor, ψ is the steering angle sensor measurement, and w_m is measurement noise.

The opposite sign on the right hand side of Equation (5.37), which represents the estimated steering angle from the velocity in the vehicle frame, is due to the definition of the vehicle frame as Right-Front-Up, while a positive steering angle corresponds to a left turn which is contrary in sign to the value calculated from the estimated velocity.

The velocity in Equation (5.37) is defined in the vehicle frame, which is obtained by transforming the velocity from the ECEF frame, as shown in Equation (5.38)

$$v^v = R_b^v (R_b^e)^T v^e \tag{5.38}$$

The measurement misclosure is computed below

$$e_z = S_{SAS}\psi - d_{SAS} + \tan^{-1}\left(\frac{v_x^v}{v_y^v}\right) \tag{5.39}$$

The perturbation of the measurement on the left hand side of Equation (5.37) is shown in Equation (5.40)

$$\delta z = \delta(S_{SAS}\psi - d_{SAS}) = \psi \delta S_{SAS} - \delta d_{SAS} \qquad (5.40)$$

The perturbation of the velocity in the vehicle frame shown in Equation (5.38) is derived by

$$\delta v^v = R_b^v(R_b^e)^T \delta v^e + R_b^v(R_b^e)^T V^E \varepsilon^e$$
$$= C_{v^e}\delta v^e + C_{\varepsilon^e}\varepsilon^e \qquad (5.41)$$

where $C_{v^e} = R_b^v(R_b^e)^T$ is the coefficient of the perturbation of velocity (in the v frame) with respect to the velocity error state, V^E is the skew-symmetric matrix of the integrated velocity in the ECEF frame, and $C_{\varepsilon^e} = R_b^v(R_b^e)^T V^E$ is the coefficient of perturbation of the velocity (in the v frame) with respect to misalignment angles

The perturbation of the estimated steering angle is:

$$\delta h = \delta\left[-\tan^{-1}(\frac{v_x^v}{v_x^v})\right] = \frac{\partial h}{\partial v_x^v}\delta v_x^v + \frac{\partial h}{\partial v_y^v}\delta v_y^v$$
$$= -\frac{v_y^v}{\left(v_x^v\right)^2 + \left(v_y^v\right)^2}\delta v_x^v + \frac{v_x^v}{\left(v_x^v\right)^2 + \left(v_y^v\right)^2}\delta v_y^v \qquad (5.42)$$

Substituting Equation (5.41) for Equation (5.42) gives,

$$\delta h = \frac{C_{v^e}(2,1)v_x^v - C_{v^e}(1,1)v_y^v}{\left(v_x^v\right)^2 + \left(v_y^v\right)^2}\delta v_x^e + \frac{C_{v^e}(2,2)v_x^v - C_{v^e}(1,2)v_y^v}{\left(v_x^v\right)^2 + \left(v_y^v\right)^2}\delta v_y^e$$
$$+ \frac{C_{v^e}(2,3)v_x^v - C_{v^e}(1,3)v_y^v}{\left(v_x^v\right)^2 + \left(v_y^v\right)^2}\delta v_z^e + \frac{C_{\varepsilon^e}(2,1)v_x^v - C_{\varepsilon^e}(1,1)v_y^v}{\left(v_x^v\right)^2 + \left(v_y^v\right)^2}\cdot\varepsilon_x^e$$
$$+ \frac{C_{\varepsilon^e}(2,2)v_x^v - C_{\varepsilon^e}(1,2)v_y^v}{\left(v_x^v\right)^2 + \left(v_y^v\right)^2}\varepsilon_y^e + \frac{C_{\varepsilon^e}(2,3)v_x^v - C_{\varepsilon^e}(1,3)v_y^v}{\left(v_x^v\right)^2 + \left(v_y^v\right)^2}\varepsilon_z^e$$
$$= C_{Hv^e}\delta v^e + C_{H\varepsilon^e}\delta\varepsilon^e \qquad (5.43)$$

where $C_{v^e}(i,j)$ represents the element of C_{v^e} matrix at the *i-th* row and *j-th* column.

$C_{\varepsilon^e}(i,j)$ represents the element of C_{ε^e} matrix at the *i-th* row and *j-th* column.

$\delta v^e = \begin{bmatrix} \delta v_x^e & \delta v_y^e & \delta v_z^e \end{bmatrix}$ is the velocity error state vector, and $\varepsilon^e = \begin{bmatrix} \varepsilon_x^e & \varepsilon_y^e & \varepsilon_z^e \end{bmatrix}$ is the misalignment angle vector.

$$C_{H\delta v^e} = \begin{bmatrix} \dfrac{C_{v^e}(2,1)v_x^v - C_{v^e}(1,1)v_y^v}{\left(v_x^v\right)^2 + \left(v_y^v\right)^2} & \dfrac{C_{v^e}(2,2)v_x^v - C_{v^e}(1,2)v_y^v}{\left(v_x^v\right)^2 + \left(v_y^v\right)^2} & \dfrac{C_{v^e}(2,3)v_x^v - C_{v^e}(1,3)v_y^v}{\left(v_x^v\right)^2 + \left(v_y^v\right)^2} \end{bmatrix} \text{ and}$$

$$C_{H\varepsilon^e} = \begin{bmatrix} \dfrac{C_{\varepsilon^e}(2,1)v_x^v - C_{\varepsilon^e}(1,1)v_y^v}{\left(v_x^v\right)^2 + \left(v_y^v\right)^2} & \dfrac{C_{\varepsilon^e}(2,2)v_x^v - C_{\varepsilon^e}(1,2)v_y^v}{\left(v_x^v\right)^2 + \left(v_y^v\right)^2} & \dfrac{C_{\varepsilon^e}(2,3)v_x^v - C_{\varepsilon^e}(1,3)v_y^v}{\left(v_x^v\right)^2 + \left(v_y^v\right)^2} \end{bmatrix}$$

$$\delta h = C_{H\delta v^e}\delta v^e + C_{H\varepsilon^e}\varepsilon^e \tag{5.44}$$

On the basis of Equations (5.40) and (5.44), the design matrix for the steering angle sensor update can be derived from Equation (5.45)

$$\begin{aligned} e_z &= \delta h - \delta z + \omega_m = C_{Hv^e}\delta v^e + C_{H\varepsilon^e}\varepsilon^e - \psi\delta S_{SAS} + \delta d_{SAS} \\ &= H_{GPS/INS/SAS}\delta x + \omega_m \end{aligned} \tag{5.45}$$

Therefore, the design matrix is summarized below:

$$H_{SAS} = \begin{bmatrix} O_{1\times3} & C_{H\delta v^e} & C_{H\varepsilon^e} & O_{1\times3} & O_{1\times3} & O_{1\times AR} & -\psi & 1.0 \end{bmatrix} \tag{5.46}$$

5.7   GPS/INS/WSS/SAS/GL/YRS Integrated Algorithms

As described in Section 4.2.4, the integration strategy GPS/INS/WSS/SAS/GL/YRS integrates all on-board vehicle sensors with the GPS/INS. The WSS and GL/YRS are incorporated as a mechanism for the detection/alleviation of lateral non-holonomic constraint violation applied in the WSS update. Following the GPS/INS/WSS/GL/YRS

update, the steering angle sensor updates the centralized Kalman filter sequentially. By

augmenting all error states associated with on-board vehicle sensors into the error state

vector of the GPS/INS centralized Kalman filter, the dynamics model for this integration

strategy is evolved into Equation (5.47).

$$
\begin{bmatrix}
\delta \dot{r} \\
\delta \dot{v}^e \\
\dot{\varepsilon}^e \\
\delta \dot{b}^b \\
\delta \dot{d}^b \\
\Delta \nabla \dot{N} \\
\delta \dot{S} \\
\dot{\varepsilon}_{b-v} \\
\delta \dot{b}_{GL} \\
\delta \dot{d}_{YRS} \\
\delta \dot{S}_{SAS} \\
\delta \dot{d}_{SAS}
\end{bmatrix}
=
\left[
\begin{array}{ccccccc|cccccc}
\multicolumn{7}{c|}{GPS/INS} & \multicolumn{6}{c}{O} \\
\hline
0 & 0 & 0 & 0 & 0 & 0 & 0 & 0 & 0 & 0 & 0 & 0 \\
0 & 0 & 0 & 0 & 0 & 0 & 0 & 0 & 0 & 0 & 0 & 0 \\
0 & 0 & 0 & 0 & 0 & 0 & 0 & 0 & -\beta_{GL} & 0 & 0 & 0 \\
0 & 0 & 0 & 0 & 0 & 0 & 0 & 0 & 0 & -\beta_{YRS} & 0 & 0 \\
0 & 0 & 0 & 0 & 0 & 0 & 0 & 0 & 0 & 0 & 0 & 0 \\
0 & 0 & 0 & 0 & 0 & 0 & 0 & 0 & 0 & 0 & 0 & 0
\end{array}
\right]
\begin{bmatrix}
\delta r^e \\
\delta v^e \\
\varepsilon^e \\
\delta b^b \\
\delta d^b \\
\Delta \nabla N \\
\delta S \\
\varepsilon_{b-v} \\
\delta b_{GL} \\
\delta d_{YRS} \\
\delta S_{SAS} \\
\delta d_{SAS}
\end{bmatrix}
$$

$$
+
\begin{bmatrix}
0 & 0 & 0 & 0 & 0 & 0 \\
R_b^e & 0 & 0 & 0 & 0 & 0 \\
0 & R_b^e & 0 & 0 & 0 & 0 \\
0 & 0 & I & 0 & 0 & 0 \\
0 & 0 & 0 & I & 0 & 0 \\
0 & 0 & 0 & 0 & 0 & 0 \\
0 & 0 & 0 & 0 & 0 & 0 \\
0 & 0 & 0 & 0 & 0 & 0 \\
0 & 0 & 0 & 0 & 1 & 0 \\
0 & 0 & 0 & 0 & 0 & 1 \\
0 & 0 & 0 & 0 & 0 & 0 \\
0 & 0 & 0 & 0 & 0 & 0
\end{bmatrix}
\begin{bmatrix}
w_f \\
w_w \\
w_b \\
w_d \\
w_{GL} \\
w_{YRS}
\end{bmatrix}
\tag{5.47}
$$

$$
= F_{GPS/INS/WSS/SAS/GL/YRS} \, \delta x + G_{GPS/INS/WSS/SAS/GL/YRS} \, w
$$

where $F_{GPS/INS/WSS/SAS/GL/YRS}$ is the dynamics matrix for this integration strategy, and

$G_{GPS/INS/WSS/SAS/GL/YRS}$ is the shaping matrix.

With respect to the mechanism for detecting and alleviating the violation of the lateral non-holonomic constraint, Figure 5.4 describes the geometric relationship between the WSS and GL/YRS, as well as a simplified vehicle's bicycle model containing the rear wheel side slip angle. Vehicle's bicycle model actually simplifies the four-wheel vehicle model into a two-wheel vehicle model along the vehicle gravity center.
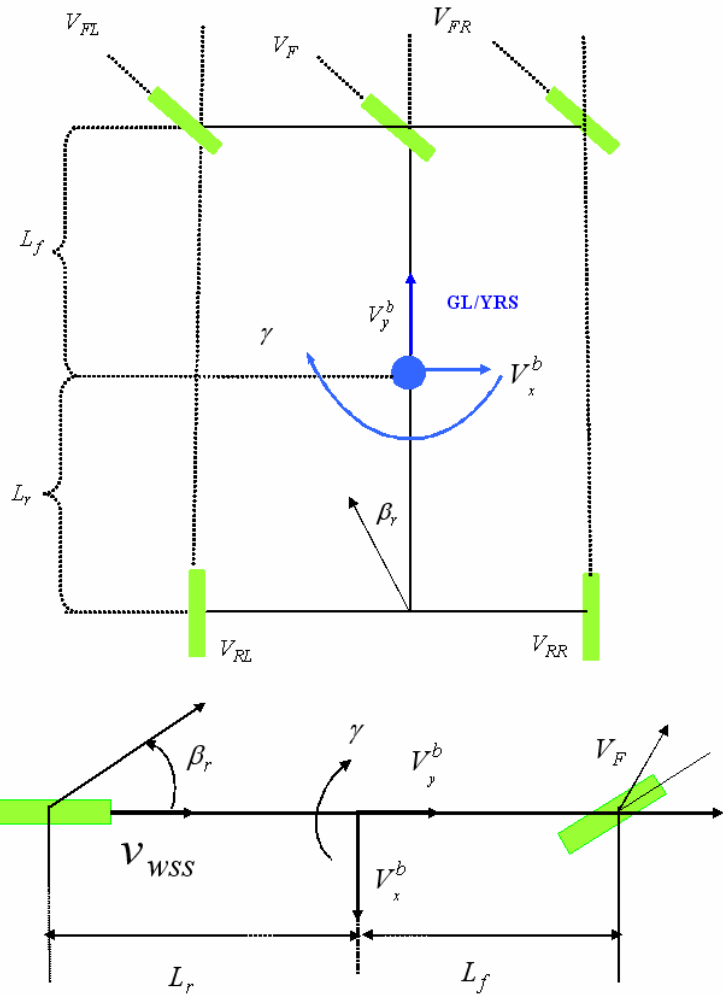
Figure 5.4 Geometric relationship between WSS and GL/YRS

The rear wheel side slip angle can be calculated in Equation (5.48) from the transformed

velocity in the lateral and longitudinal directions using Ray (1995).

$$\beta_r = \tan^{-1}\left[\frac{V_x^b - L_r\gamma}{V_y^b}\right] \tag{5.48}$$

where β_r is the rear wheel side slip angle, L_r is the distance between the GL/YRS and

WSS, and V_x^b and V_y^b are the lateral and longitudinal velocity derived from the

GL/YRS.

The lateral non-holonomic constraint is most frequently violated when the side slip angle

is large. Therefore, the side slip angle provides a way to detect and alleviate a violation of

this constraint. The design of this mechanism is described below.

With a statistical analysis on the side slip angle, the positioning accuracy starts to degrade

when the side slip angle is greater than 5 degrees whereas the lateral constraint is still

applied in WSS update. Thus, a threshold of 5 degrees is selected in this research for

detecting the violation of the lateral constraint. When the side slip angle is smaller than a

threshold, the non-holonomic constraint is valid, and the non-holonomic constraints are

applied in both the lateral and vertical directions. In this case, Equation (5.49) is used as

the measurement for the WSS update

$$V_{WSS} = \begin{bmatrix} 0 \\ v_{WSS} \\ 0 \end{bmatrix} \tag{5.49}$$

By contrast, if the side slip angle exceeds a threshold, the violation of the lateral non-holonomic constraint can be replaced by the GL/YRS derived lateral velocity, *i.e.*

$$V_{WSS} = \begin{bmatrix} V_x^b \\ v_{WSS} \\ 0 \end{bmatrix} \qquad (5.50)$$

The cooperation between the WSS and GL/YRS leads to a mechanism for the detection and alleviation of lateral non-holonomic constraint violation. As a result, the GPS/INS/ on-board vehicle sensor integrated positioning system can adapt to a variety of driving cases with high positioning accuracy.

The velocity in vehicle frame used for WSS update, V_{WSS}, is a vector that contains three elements. The longitudinal element is a real value that comes from WSS measurement. The lateral and vertical elements are virtual values that can be either non-holonomic constraints or other values from external measurements. Despite the fact that a lateral velocity can also be given from the INS mechanization output, it cannot be employed as an external or independent measurement to remove the lateral constraint if violated. Otherwise, a linear correlation or dependence will be introduced when performing external update to the centralized Kalman filter. GL/YRS unit, however, provides redundant and independent measurement for detecting and compensating the violation of the lateral constraint.

To achieve a high positioning accuracy, it is necessary to switch Equation (5.49) and Equation (5.50) in terms of a side slip angle threshold. With a small side slip angle, the

lateral constraint is more close to the real situation where the lateral velocity is very small. If Equation (5.50) is still being used when the lateral constraint is not violated, the error and noise from GL/YRS unit will degrade the positioning accuracy.

To match the dynamics model defined in Equation (5.47), the design matrices for WSS, SAS as well as GL/YRS measurements update are accordingly resized as follows:

$$H_{WSS} = \begin{bmatrix} O_{3\times3} & R_b^y(R_b^e)^T & R_b^y(R_b^e)^T V^E & O_{3\times3} & O_{3\times3} & O_{3\times AR} & -V_{WSS} & -V^N & O_{3\times2} & O_{3\times1} & O_{3\times1} & O_{3\times1} \end{bmatrix} \quad (5.51)$$

$$H_{GL/YRS} = \begin{bmatrix} \dfrac{\Delta t}{2}(R_b^e)^T N^e & (R_b^e)^T & (R_b^e)^T V^E - \dfrac{(R_b^e)^T G^e \Delta t^2}{2} & O_{3\times3} & O_{3\times3} & O_{3\times AR} & \cdots \\[4mm] O_{3\times1} & O_{3\times3} & -\dfrac{\Delta t}{2}M & -\dfrac{J(V_0^b + k_1 \cdot \Delta t)\Delta t}{2} & O_{3\times1} & O_{3\times1} \end{bmatrix} \quad (5.52)$$

$$H_{SAS} = \begin{bmatrix} O_{1\times3} & C_{H\delta v^e} & C_{H\varepsilon^e} & O_{1\times3} & O_{1\times3} & O_{1\times AR} & O_{1\times1} & O_{1\times3} & O_{1\times2} & O_{1\times1} & -\psi & 1.0 \end{bmatrix} \quad (5.53)$$

5.8   Error Compensations in a Closed Loop Integrated System

As discussed in Chapter 4, GPS, INS and on-board vehicle sensors are integrated in a closed loop. When on-board vehicle sensors and GPS perform external update, the error states of navigation information (position, velocity and attitude) as well as IMU and on-board vehicle sensor errors are estimated from the centralized Kalman filter. The estimated error states are fed back to the integrated system to update the integrated solution and compensate the errors in the raw measurements of the IMU and on-board vehicle sensors. In this way, the external measurements used in the Kalman filter as well as the integrated system solution become close to the true value, and a high positioning accuracy can be achieved.

The estimated error states of position, velocity and attitude are used to update the

navigation information computed from the INS by

$$r = \hat{r} + \delta r$$
$$v = \hat{v} + \delta v \qquad (5.54)$$
$$R_b^l = (I - E^\varepsilon)\hat{R}_b^l$$

where I is the identity matrix, E^ε is the skew-symmetric matrix of ε, $\hat{r}$ and $\hat{v}$ are the position and velocity from INS integrated solution, r and v are the position and velocity after updating from the error states in the Kalman filter, R_b^l is the updated direction cosine matrix, and $\hat{R}_b^l$ is the direction cosine matrix computed from the INS integrated system.

Using the estimated error states of accelerometer and gyro biases, the previous estimated IMU biases are updated by

$$b = \hat{b} + \delta b$$
$$d = \hat{d} + \delta d \qquad (5.55)$$

where $\hat{b}$ and $\hat{d}$ are the previous accelerometer gyro and accelerometer biases, and b and d are the updated value by the estimated error states of δb and δd in the Kalman filter.

The IMU raw measurements are compensated for the estimated biases by

$$f^b = \hat{f}^b - b$$
$$\omega_{ib}^b = \hat{\omega}_{ib}^b - d \qquad (5.56)$$

where f^b and ω_{ib}^b are the compensated IMU measurements on the basis of the raw IMU measurements $\hat{f}^b$ and $\hat{\omega}_{ib}^b$.

Similar to the IMU, the error states of the on-board vehicle sensors are updated by

$$
\begin{aligned}
S &= \hat{S} + \delta S \\
S_{SAS} &= \hat{S}_{SAS} + \delta S_{SAS} \\
d_{SAS} &= \hat{d}_{SAS} + \delta d_{SAS} \\
b_{GL} &= \hat{b}_{GL} + \delta b_{GL} \\
d_{Yaw} &= \hat{d}_{Yaw} + \delta d_{Yaw}
\end{aligned}
\tag{5.57}
$$

where the existing wheel speed sensor scale factor $\hat{S}$, the steering angle sensor scale factor $\hat{S}_{SAS}$, the steering angle sensor bias $\hat{d}_{SAS}$, the G sensor bias $\hat{b}_{GL}$ and the yaw rate sensor bias $\hat{d}_{Yaw}$ are updated by the error states δS, δS_{SAS}, δd_{SAS}, δb_{GL} and δd_{Yaw} respectively to introduce more accurate values of S, S_{SAS}, d_{SAS}, b_{GL} and d_{Yaw}.

Consequently, the on-board vehicle sensor raw measurements are compensated by the updated scale factors or the biases to give more accurate values used as the measurements in the centralized Kalman filter,

$$
\begin{aligned}
v_{WSS} &= \hat{v}_{WSS} / S \\
\psi &= \hat{\psi} / S_{SAS} - d_{SAS} \\
f_{GL} &= \hat{f}_{GL} - b_{GL} \\
\gamma &= \hat{\gamma} - d_{Yaw}
\end{aligned}
\tag{5.58}
$$

where $\hat{v}_{WSS}$, $\hat{\psi}$, $\hat{f}_{GL}$ and $\hat{\gamma}$ are the raw measurements of wheel speed sensor, steering angle sensor, G sensors and yaw rate sensor, respectively.

5.9   External Aiding on GPS Ambiguity Resolution

Reliable and fast ambiguity resolution has crucial effects on high-accuracy GPS applications. The search volume of ambiguity resolution is closely related to ambiguity

resolution speed, and is often measured by the Ambiguity Dilution of Precision (ADOP) given by Teunissen and Odijk (1997),

$$ADOP = \sqrt{\left| P_{\hat{N}} \right|^{\frac{1}{m}}}$$

(5.59)

where $P_{\hat{N}}$ is the covariance matrix of the estimated ambiguities, and m is the number of double difference ambiguities being estimated.

It can be seen from Equation (5.59) that the search volume for ambiguity resolution is closely related to the covariance of the float ambiguities. Scherzinger (2002) and Petovello (2003) as well as Zhang et al. (2005) analyzed the impact of inertial aiding on ambiguity resolution over GPS-only by investigating the covariance matrix. Based on this work, three strategies, including GPS-only, GPS/INS and GPS/INS/on-board vehicle sensors, are compared for the time to fix ambiguities after GPS outages.

Assuming that the covariance matrix after resetting the ambiguity resolution is $P_{\hat{x}}$, and no correlation exists between the error states of the Kalman filter and the ambiguity states, that is

$$P_{\hat{X}} = \begin{bmatrix} P_{\hat{r}} & 0 \\ 0 & P_{\hat{N}} \end{bmatrix}$$

(5.60)

where $P_{\hat{x}}$ is the initial covariance matrix after resetting the ambiguity resolution, $P_{\hat{N}}$ is the covariance matrix of estimated float ambiguities, and $P_{\hat{r}}$ is the covariance matrix of the estimated error states.

Scherzinger (2002) investigated the relationship between a posteriori covariance matrix

of floated ambiguity and estimated error states, as illustrated by

$$
\begin{cases}
P_{\hat{N}1} - P_{\hat{N}2} = \lambda^2 \sigma_N^4 D^T D R_{\hat{N}2}^{-1} D^T A (P_{\hat{r}1}^- - P_{\hat{r}2}^-) A^T D R_{N1}^{-1} D^T D \\
R_{\hat{N}1} \quad\quad = D^T A P_{\hat{r}1}^- A^T D + H_N P_{N1}^- H_N^T + R_\phi \\
R_{\hat{N}2} \quad\quad = D^T A P_{\hat{r}2}^- A^T D + H_N P_{N2}^- H_N^T + R_\phi
\end{cases}
\tag{5.61}
$$

where $P_{\hat{N}1}$ and $P_{\hat{N}2}$ are the a posteriori VCV matrix of the float ambiguities for

strategies 1 and 2, $P_{\hat{r}1}^-$ and $P_{\hat{r}2}^-$ are the initial the a priori VCV matrix of the error states

after the reset of ambiguity for Strategies 1 and 2, λ is the wavelength, σ_N is the

initial accuracy of the float ambiguities, D is the double difference operator, A is the

single-difference measurement model design matrix, $H_N = \lambda I$ is the design matrix

correlated with ambiguity, and R_ϕ is the carrier phase measurement accuracy.

Equation (5.61) implies qualitatively that a smaller the a priori covariance matrix of the

error states is associated with a smaller covariance matrix of the float ambiguities. For

example, if the a priori covariance matrix of the error states for Strategy 1 is smaller than

that for Strategy 2,

$$
P_{\hat{r}1}^- < P_{\hat{r}2}^-
\tag{5.62}
$$

then, the a priori VCV matrix of the float ambiguity for Strategy 1 is accordingly smaller

than for Strategy 2, namely

$$
P_{\hat{N}1} < P_{\hat{N}2}
\tag{5.63}
$$

Thus, a smaller the a priori covariance matrix of error states (such as the position error states) can introduce a smaller covariance matrix of the float ambiguities, which leads to a smaller ambiguity search volume and, consequently, to a reduction in the time-to-fix ambiguities.

With respect to resetting the ambiguity resolution process after GPS outages, the a priori covariance matrix of the error states can be initialized in three ways in terms of different integration strategies implemented for the integrated system. The effects of different strategies on the time-to-fix ambiguities are analyzed as follows.

Case I: GPS-Only. In this strategy, the position, velocity as well as the position and covariance matrix are initialized using DD C/A code solution when resetting ambiguities after GPS outages. The initial positioning accuracy derived from the DD pseudorange measurements is at the level of several metres.

Case II: INS aiding during ambiguity resolution. During GPS outages, the position and velocity are derived from the INS mechanization equation. The covariance matrix is propagated by a prediction without external updating, as illustrated by Equation (5.64).

$$\begin{cases} P^-_{\hat{r}_{k+1}} = \Phi P^+_{\hat{r}_k} \Phi^{\mathrm{T}} + Q_k \\ P^+_{\hat{r}_{k+1}} = P^-_{\hat{r}_{k+1}} \end{cases} \tag{5.64}$$

where Φ is the transition matrix, Q_k is the process noise matrix in the current epoch, $P^-_{\hat{r}_k}$ is the a priori covariance matrix at the current epoch, and $P^+_{\hat{r}_k}$ is the a posteriori covariance at the current epoch.

The posteriori covariance, $P_{\hat{r}_k}^+$, in Equation (5.64) measures the accuracy of the error states. Without external update, the INS error drifts with time. As noise is accumulated epoch by epoch, the propagated covariance matrix also increases with time. After GPS outages, $P_{\hat{r}_k}^+$ is used as the initial covariance matrix for ambiguity resolution.

Case III: INS/On-board vehicle sensor aiding ambiguity resolution. In this strategy, the on-board vehicle sensors perform the external update on the INS system. The measurement model for the on-board vehicle sensor update is expressed by Equation (5.65),

$$z_v = H_v \delta x + w_v \tag{5.65}$$

where z_v is the measurement misclosure of the on-board vehicle sensors, H_v is the design matrix of the on-board vehicle sensors, and w_v is the measurement noise of the on-board vehicle sensors.

The INS-only propagated covariance matrix is updated by on-board vehicle sensors, as shown below

$$\begin{cases} P_{\hat{r}_{k+1}}^- = \Phi P_{\hat{r}_k}^+ \Phi^T + Q_k \\ P_{\hat{r}_{k+1}}^+ = P_{\hat{r}_{k+1}}^- - P_{\hat{r}_{k+1}}^- H_v^T (H_v P_{\hat{r}_{k+1}}^- H_v^T + R_v)^{-1} H_v P_{\hat{r}_{k+1}}^- \end{cases} \tag{5.66}$$

where R_v is the measurement accuracy of the on-board vehicle sensors.

Since the term $P_{\hat{r}_{k+1}}^- H_v^T (H_v P_{\hat{r}_{k+1}}^- H_v^T + R_v)^{-1} H_v P_{\hat{r}_{k+1}}^-$ in Equation (5.66) is quadratic in nature, the external update from the on-board vehicle sensors can limit the INS drift error and

reduce the INS propagated covariance to some degree depending on the measurement accuracy of the on-board vehicle sensors.

In summary, the covariance matrix of the float ambiguities determines the ambiguity search space. A smaller initial covariance matrix of the error states in the Kalman filter (more specifically the position error states) is associated with a smaller covariance matrix of the float ambiguities. Thus, faster ambiguity resolution can be achieved by a smaller initial covariance of the error states. A comparison of the aforementioned three strategies on the performance of ambiguity resolution after GPS outages is therefore investigated by their initial covariance matrix of error states. Compared to INS-only aiding on ambiguity resolution, INS/on-board vehicle sensor aiding can reduce the covariance by an on-board vehicle sensor update. As a result, faster ambiguity resolution can be expected from INS/on-board vehicle sensor aiding than from INS-only aiding. The degree of improvement depends on the measurement accuracy of the on-board vehicle sensors. The initial position accuracy for ambiguity resolution with the GPS-only strategy can be about several metres. In contrast, the covariance of either the INS-only or INS/on-board vehicle sensor system increases with time and is correlated with the quality of the IMU. The benefits gained from stand-alone INS or INS/on-board vehicle sensor aiding over a GPS-only system is related to the duration of GPS outages and the quality of the IMU. With shorter duration GPS outages and higher quality of IMUs, aiding from a stand-alone INS or from INS/on-board vehicle sensors on ambiguity resolution performs better than

the GPS-only strategy assuming the estimated standard deviation of the position drift error is smaller than the standard deviation of DD C/A code solution. On the contrary, when positioning drift error of the stand-alone INS or INS/on-board vehicle sensor system goes beyond the positioning accuracy derived from pseudorange measurements due to longer duration GPS outages or a lower quality IMU, the benefits of the time-to-fix ambiguity resolution gained from the stand-alone INS or INS/On-board vehicle sensor are expected to be somewhat limited.

Chapter 6   Real-Time GPS/INS/On-Board Vehicle Sensor Integrated System

A hardware platform was set up to test the integration strategies and algorithms. The equipment used as well as the system configuration will be described in this chapter. By dealing with the GPS time latency in real-time, a method to implement the real-time GPS/INS/On-board vehicle sensor integrated system will also be discussed.

6.1   Hardware Platform Setup

Figure 6.1 gives an overview of the system used for the tests and data collection. It includes all the equipment used in the open-sky test that was processed in post-mission as well as all the real-time tests in open-sky, suburban and pseudo-urban areas, although only a subset of the IMUs (HG1700 IMU or CIMU) were used in each case for the generation of the reference trajectory. Through a connection to the interface unit, the on-board vehicle sensors and the low cost IMU data were time tagged and logged onto the PC1 via a serial port. This part was common to both the post-mission and real-time tests. All the GPS, low cost IMU and the on-board vehicle sensor data were collected or processed in real-time on PC2. Three NovAtel 600 antennas atop the van were connected to four NovAtel OEM4 GPS receivers for different purposes. To save antenna numbers and reduce the complexity of the lever arm effect, one splitter is used for two GPS

receivers. The FreeWave radio link antennas and transceivers were used to broadcast the

GPS base station data for the real-time test. The CIMU data were collected by an

Applanix POS LS system to generate the reference trajectory for all the real-time tests.

The HG1700 IMU data were time-tagged and logged by a NovAtel SPAN system to

provide the reference solution for the post-mission test in an open-sky area.
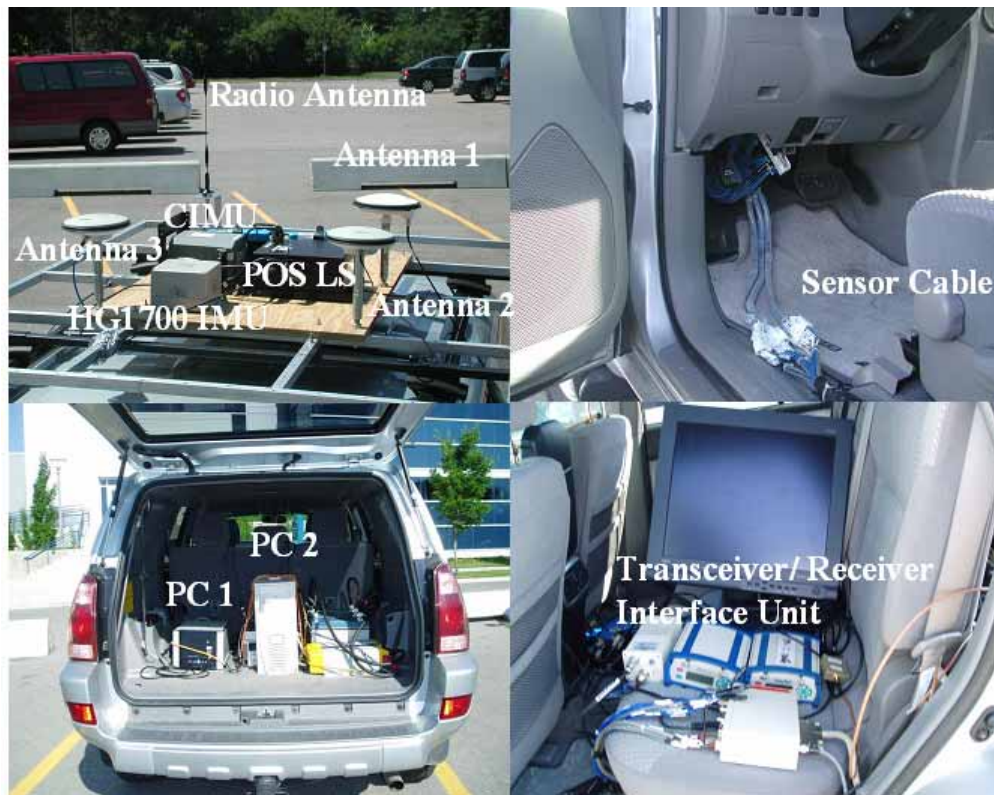
Figure 6.1 System setup

Figure 6.2 is a block diagram that illustrates the system setup. The GPS base station was

setup on a pillar with a surveyed coordinate. For the post-mission test in the open-sky

area, the GPS base station data was saved onto a flash card. For all the real-time tests,

however, the reference GPS data was broadcast from the base station to the rover station

via a pair of FreeWave radio link antennas and transceivers. The data stream from the

serial port of the base GPS receiver is packaged in a binary format defined by GPS

receiver manufacturer. This binary data stream is picked up and broadcast by a radio

transceiver at base station. With a radio link connection created between a pair of radio

link transceivers at base and rover ends, the binary data stream from the serial port of

base GPS receiver is consequently received at the rover station for real-time use.

Antenna 1 was connected to a GPS receiver (20 Hz data rate) that was built into the PC1

for time-tagging of the low cost IMU and the on-board vehicle sensor data. The low cost

IMU and the on-board vehicle sensor data were interfaced with the PC1 via an interface

unit and a serial port. The low cost IMU and the vehicle sensor data collected at 100 Hz

by the PC1 were packaged in a binary format and logged onto PC2 via a RS232 serial

port. The binary data stream with a combination of both low cost IMU and all on-board

vehicle sensors constitutes a large data volume for serial port communication. To fulfil a

real-time integrated system, a higher baud rate at 230400 bps is selected, which goes

beyond the limit of current PC system nominated at 115200 bps. To overcome this

limitation, a special PCI card (NI PCI-84304) for the enhancement of RS232 serial port

communication speed is embedded into the PC.
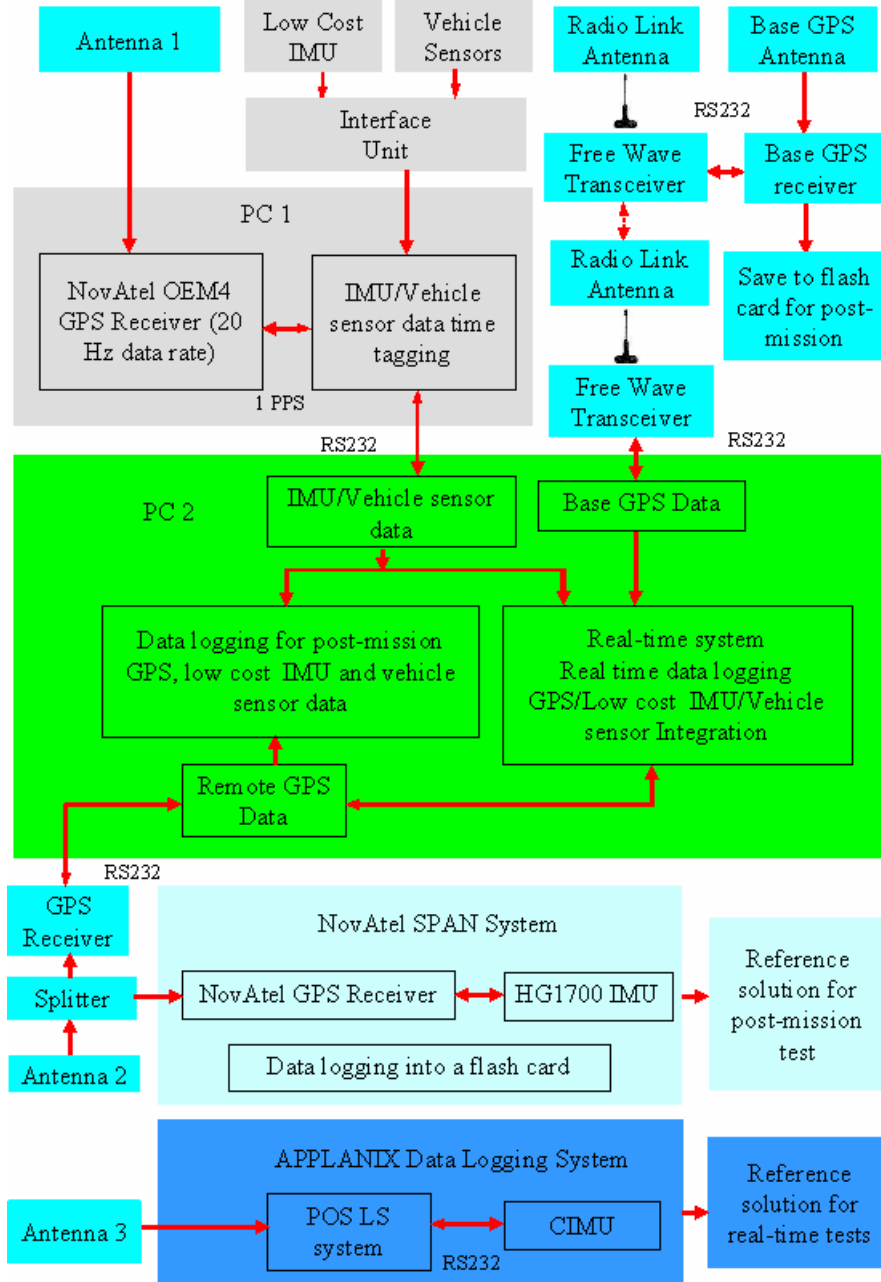
Figure 6.2 System set-up block diagram

As shown in Figure 6.2, the post-mission and real-time tests each collected and processed the data in different ways. In post-mission processing, the low cost IMU, the on-board vehicle sensors as well as the rover GPS data were collected and saved onto the hard drive of the PC2 by a specially designed data logging software. The GPS base station

data was saved onto a flash card. The GPS base and rover data as well as the low cost IMU and on-board vehicle sensor data was processed off-line to generate a post-mission solution.

Unlike the post-mission test, the real-time tests collected and processed the data in real-time using the SAINT^{TM} (Satellite And Inertial Navigation Technology) software. The real-time raw data was also logged onto the hard drive of PC2 for comparing the compatibility between the real-time and post-mission solutions. The GPS base station data (1 Hz data rate) was broadcast by a pair of radio transceivers. The SAINT^{TM} software on the PC2 collected the real-time raw data via three RS232 serial ports. The data included the low cost IMU and the on-board vehicle sensor data, the GPS base station data broadcast by the radio link antenna and the transceiver as well as the GPS rover data. The GPS, low cost IMU and on-board vehicle sensor data was processed in real-time on the PC2 to generate a real-time solution.

Using a splitter, Antenna 2 was connected to both a rover GPS receiver and the SPAN system GPS receiver. The GPS receiver in the SPAN system provided time-tagging to the HG1700 IMU data, which was saved on a flash card at 100 Hz data rate. The GPS/HG1700 IMU integrated solution provided a reference solution for the analysis of the post-mission test.

An embedded NovAtel OEM4 GPS receiver in the POS LS system was connected to antenna 3. The CIMU data was collected at 200 Hz by the Applanix POS LS data logging

system. For all the real-time tests, the reference trajectory was generated by GPS/CIMU integrated solution using the Applanix Pos Pac software.

6.2   GPS Latency

In the real-time integrated positioning system, the GPS base station data is broadcast to the land vehicle by a radio link. A time delay will be introduced due to a certain amount of time taken for the transmission of base GPS data to the land vehicle. The time delay depends on the amount of data to be broadcast, the Baud rate of the radio link, the power of the radio link transceiver as well as the length of the separation between the GPS receiver and the vehicle. When the integrated system computes the time-matched double differenced GPS data, the GPS time is "behind" the most recent IMU or vehicle sensor time by the amount of the time delay called GPS latency. In the GPS/INS/On-board vehicle sensor real-time integrated system, the low cost IMU and the on-board vehicle sensor data was received synchronously on a same data flow encoded in a binary data format. Hence, no time latency exists between the IMU and on-board vehicle sensors.

The GPS data is sampled at 1 Hz, and IMU data is sampled at 100 Hz. IMU data is processed at a higher rate than GPS. When the time matched double difference GPS data is received at the rover station, the GPS time latency is computed as the difference between the IMU time and the GPS time, i.e.

$$\text{GPS Time Latency=IMU time–GPS time}$$

As IMU and on-board vehicle sensor data are considered to be synchronous, the GPS time latency with respect to IMU coexist to the on-board vehicle sensors. To achieve a high positioning accuracy, the GPS latency needs to be taken into account when a real-time integrated system is implemented by integrating GPS with INS and on-board vehicle sensors.

6.3   Implementation of Real-Time Integrated System

The most effective way to handle the GPS time latency in real-time is to buffer the relevant data, including the IMU data, the on-board vehicle sensor raw measurements, the INS mechanization states as well as the Kalman filter covariance matrix, when GPS data is not available, and to restore and reprocess the buffered data when the GPS data is available.

In the software, the buffer was set up to tolerate a maximum GPS latency at 3 seconds. This selection represents a good compromise between the worst case of GPS latency and the data buffering/reprocessing capability in the real-time system. The GPS latency at 3 seconds can cover the most of the worst cases of GPS latency and make the real-time system work in a proper way. A much larger maximum GPS latency will increase the time for data buffering, data restoration and data reprocessing, and lead to a malfunction of the real-time system. With the data buffering/restoring technique, the real-time solution can be expected to be compatible with the post-mission solution when the GPS time latency is less than 3 s. The GPS time latency varies from test to test. By investigating the

GPS time latency in each real-time test, the compatibility between the real-time and the post-mission solution can also be verified if the GPS time latency is less than 3 s.

Figure 6.3 is a flowchart to show the procedure of the real-time data processing. The flowchart consists of three branches: IMU data processing, On-board vehicle sensor update and GPS data update. To keep the system accuracy and maintain computational efficiency of the real-time system, both the vehicle sensor and GPS update rates are selected to be 1 Hz.
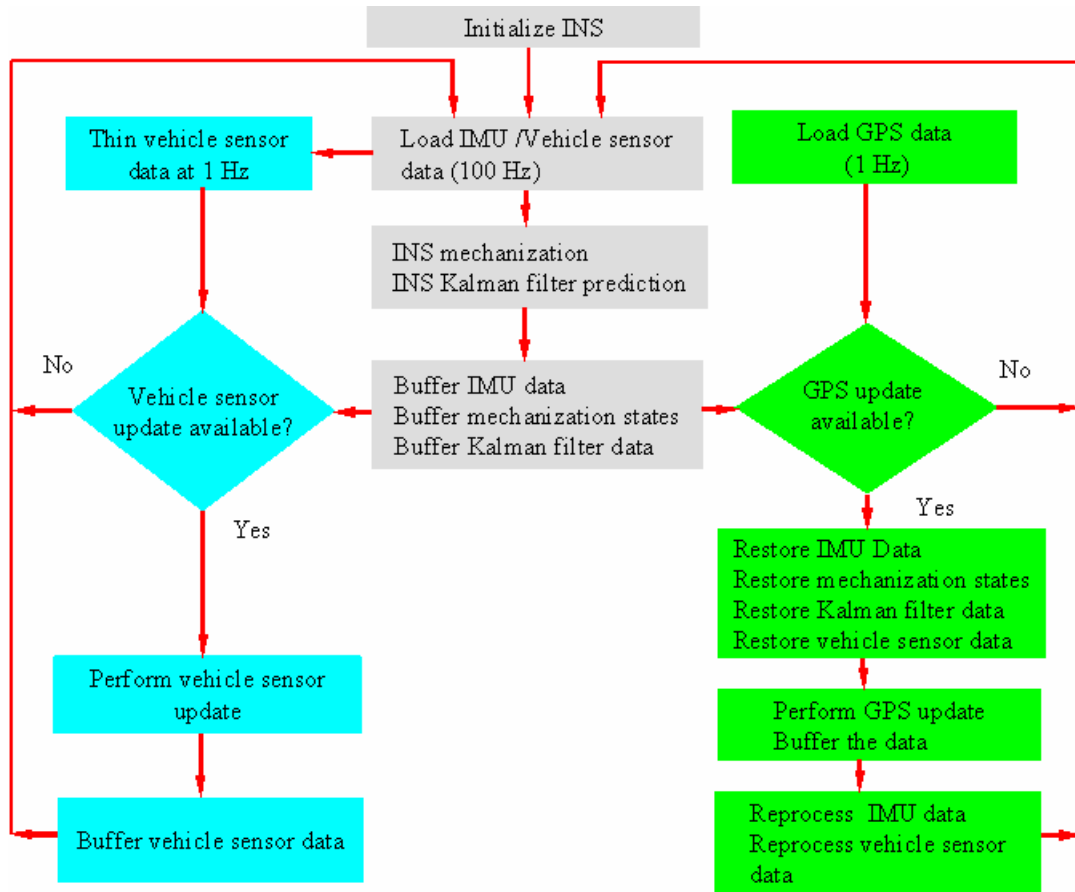
Figure 6.3 Real-time data processing flowchart

The INS is initialized by the GPS solution. The vehicle sensor and GPS data update the Kalman filter independently. During periods when no GPS and/or the vehicle sensor are available, the Kalman filter predicts ahead and the IMU mechanization equation is implemented at 10 Hz. The relevant IMU/INS parameters (including IMU raw data, the INS mechanization states as well as the centralized Kalman filter covariance matrix) are buffered. When the on-board vehicle sensor measurements are available, the on-board vehicle sensor raw measurements and other relevant parameters are buffered after the on-board vehicle sensor update on the Kalman filter is performed. Similarly, when GPS data is available, the following steps are performed:

1. The relevant IMU/INS parameters and the on-board vehicle sensor data if any are restored from the data buffers at the GPS measurement time;

2. The GPS update is performed, and;

3. All of the buffered IMU and vehicle sensor data is reprocessed to the latest IMU and vehicle sensor time.

To implement a real-time integrated system, Figure 6.4 illustrates the time sequence for real-time data processing (after Petovello 2003). Nine steps are classified and described below for the real-time data processing including INS mechanization, vehicle sensor update, GPS update, the buffering of the IMU/INS data and the vehicle sensor data, as well as the restoring/reprocessing the IMU and the on-board vehicle sensor data.

Step 1. Initialize the INS at time t1.

Step 2. Process the IMU data as it is received. This includes executing the INS mechanizations, predicting the INS Kalman filter error states and covariance matrix and buffering the relevant IMU data and INS mechanization states.

Step 3. When vehicle sensor data is available at time t2, it is used to update the INS Kalman filter. The data are then stored in a data buffer.

Step 4. Continue to process the IMU data until the next measurement update is received (assumed here to be a GPS update). As in Step 1, this involves executing the INS mechanizations, predicting the INS Kalman filter and buffering the relevant data.

Step 5. When GPS data, time-tagged for time t1, is received at time t3, the relevant parameters in the buffer at time t1 are restored and the GPS update is performed.

Step 6. Reprocess all of the buffered IMU/INS data from time t1 to t2. Note that the IMU/INS data is still buffered during this processing.

Step 7. At time t2, reprocess the buffered vehicle sensor data.

Step 8. Reprocess all of the buffered IMU/INS data from time t2 to t3. Note that the IMU/INS data is still buffered during this processing. After this step, the system has "caught up" to the current data being received. This is equivalent to Step 1, but the system is now "initialized" at time t3, instead of t1, and,

Step 9. Continue processing and buffering IMU/INS data as it is received. Continue performing on-board vehicle sensor update and buffering the on-board vehicle sensor data if available.
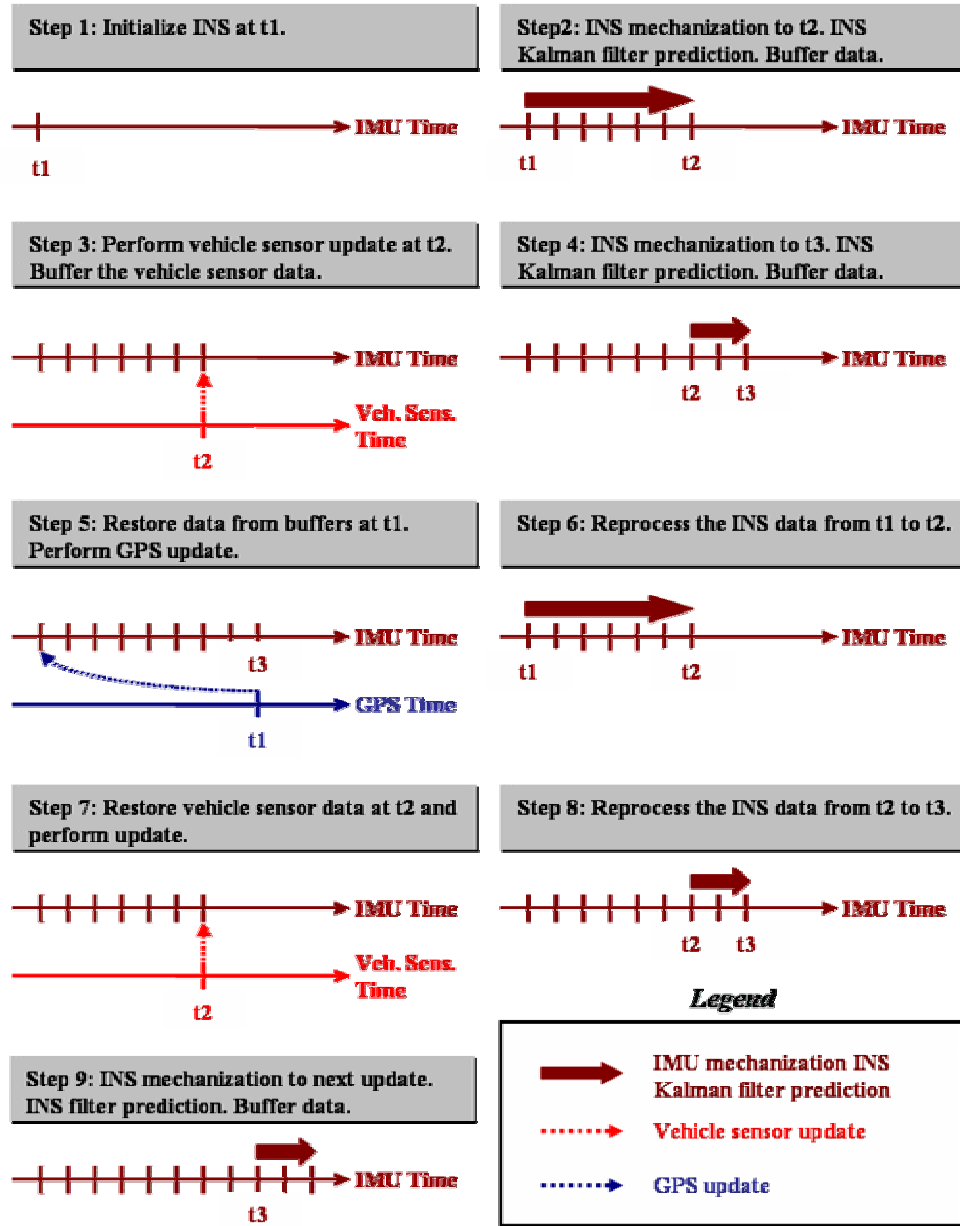
Figure 6.4 Data buffering, restoring and reprocessing sequence (after Petovello 2003)

Chapter 7   Tests, Results and Analysis

This chapter describes the tests conducted in different areas for either real-time or post-mission processing. The data processing and analysis method is presented. Data collected from all tests is analyzed with respect to all the integration strategies discussed in Chapter 4. The tuning of the Kalman filter is verified and the benefits gained from the integration of on-board vehicle sensors in terms of the position and velocity accuracy as well as the ambiguity resolution are investigated.

7.1   Test Descriptions

The tests included an open-sky kinematic test processed in post-mission and real-time tests in various areas (open-sky, suburban and pseudo-urban areas). Each test ran for several minutes in static mode for initialization and 20-30 minutes in kinematic mode. The reference solution for the open-sky kinematic test processed in post-mission was generated by GPS/HG1700 IMU.

For all real-time tests in open-sky, suburban and pseudo-urban areas, the integrated GPS/CIMU provided the reference information. During real-time tests, raw data was recorded along with the real-time solutions, which was used to assess the compatibility between the real-time and post-processed solutions. Due to an ideal GPS environment in the open-sky tests (post-mission and real-time), only L1 carrier phase measurement is

used. To maintain a reliable and fast ambiguity resolution under severe multipath effects in suburban and pseudo-urban areas, the widelane carrier phase measurements were employed in suburban and pseudo-urban area real-time tests.

7.1.1   Post-Mission Kinematic Test in Open-Sky Area

The purpose of the open-sky kinematic test processed in post-mission was to test the software for tuning of the Kalman filter, the modeling of sensors as well as the validity of the integration algorithm. The system performance and positioning accuracy for various integration strategies were assessed by simulating GPS outages over various times.

Figure 7.1 gives an overview of this test. It was conducted on March 21, 2006 in Springbank near Calgary, which is an open-sky area with good GPS satellite visibility.

Figure 7.1 Open-sky kinematic test processed in post-mission

The system ran several minutes in static mode for initialization, and approximately 30 minutes in kinematic mode for positioning and navigation testing with a maximum GPS baseline length of 4 km. With an ideal environment for GPS ambiguity resolution, the GPS measurements used in this test included L1 carrier phase, Doppler and the C/A code.

7.1.2　Real-Time Test Descriptions

The real-time tests are described in terms of the test areas, namely, the open-sky, suburban and pseudo-urban areas, respectively. The real-time tests gave an evaluation of the validity of the design of the Kalman filter as well as the impact of various sensor combinations when the satellite signals were masked in suburban and pseudo-urban areas.

The real-time open-sky test was conducted on June 28, 2006 in Springbank near Calgary. Figure 7.2 shows the GPS base station and the test surroundings. The GPS base station antenna was set up on a pillar with a surveyed coordinate.　Beside the pillar, a radio link antenna was erected on a tripod to broadcast the GPS base station measurement signals with a radio transceiver. The radio link transceiver broadcast the raw GPS measurements in a binary format from base station to the rover on the vehicle.

Figure 7.2 Description of real-time test in open-sky area

The real-time test in a suburban area started and ended in front of the Calgary Centre for Innovative Technology (CCIT) building at the University of Calgary on June 28, 2006. The test was conducted around the campus with a maximum baseline of 2.5 km, and several minutes of static mode for initialization, as well as approximately 20 minutes for the real-time kinematic test. As shown in Figure 7.3, the GPS base station and radio link antennas were set up on the roof of the CCIT building. Also, partial and complete GPS outages were mainly introduced by the dense foliage, small buildings near the street as well as bridges. Unlike the open-sky area, the multipath error significantly increases in suburban or urban areas. To guarantee reliable ambiguity resolution, the widelane (L1-L2) carrier phase (rather than L1 in the open-sky test), Doppler and the C/A code measurements were used.

Figure 7.3 Real-time test in suburban area

The pseudo-urban area approximates urban canyon environment but with overall lower masking angles and with severe masking conditions occurring for significantly shorter durations than in a real urban canyon (Petovello 2003). Using the same GPS base station and integration strategy as in the suburban area test, the pseudo-urban area test was conducted on the campus of the University of Calgary on June 28, 2006. The maximum baseline was around 1 km. The test ran several minutes in static mode for initialization as well as approximately 20 minutes in kinematic mode. The multipath error and GPS signal masking were more severe than that in the suburban area. Therefore, the widelane carrier phase, Doppler and C/A code measurements were also used.

Figure 7.4 gives a brief description of the environment in the pseudo-urban area test. The tall buildings, tunnels and trees frequently masked the GPS satellite signals to introduce a position and velocity drift when the low cost IMU lost external aiding. The position and

velocity drift errors were measured by comparing the integration strategy of GPS/Low

cost IMU/WSS/SAS/GL/YRS output with the GPS/CIMU integrated solution. Even

though the navigational grade CIMU also drifts with time without GPS aiding, it drifts to

a much smaller degree than the low cost IMU due to its high accuracy and quality.

Therefore, even with relatively longer GPS masking duration in the pseudo-urban area,

the accuracy of the reference solution generated by CIMU is still acceptable. The

accuracy of the reference solution will be detailed in the following sections.

Figure 7.4 Real-time test in pseudo-urban area

7.2   Data Processing and Analysis Methods

For each test, the data were processed and the results were analyzed among the six

integration strategies, which include:

1. GPS/INS,

   2.   GPS/INS/WSS,

   3.   GPS/INS/SAS,

   4.   GPS/INS/GL/YRS,

   5   GPS/INS/WSS/SAS, and

   6   GPS/INS/WSS/SAS/GL/YRS

The data processing and analysis methods are described as follows.

7.2.1   Analysis of GPS Information

In the GPS/Low cost IMU/On-board vehicle sensor integrated system, GPS is the driving factor in terms of system accuracy. When GPS is fully available, it plays a dominant role in the integrated system and determines the absolute accuracy of the integrated system. To this end, the GPS availability, namely, the satellite availability in both the base and rover stations, was analyzed in all tests. Also, the satellite DOPs (horizontal and vertical dilutions of precision) which are measures of the satellite geometry are also shown in each test. Lower DOP values give better position accuracies.

Correct and fast ambiguity resolution has crucial effects on the positioning accuracy when the carrier phase measurement is used.   In general, correct ambiguity resolution can result in a centimetre-level positioning accuracy. Associated with the number of satellites tracked, the number of double difference ambiguities that have been fixed is also shown.

In double differenced GPS, multipath, noise and the ionosphere are the main error sources. As discussed in Chapter 2, the ionospheric error is spatially correlated and its residual error level is about 2-3 ppm with respect to the baseline separation under normal conditions. The ionospheric error is generally negligible for short baselines. Multipath in the suburban and urban areas is much more severe than in open-sky conditions. In this research, the C/A code measurement is used for system integration in all tests. The C/A code is more susceptible to multipath error than the carrier phase. Even though C/A code can benefit ambiguity resolution by providing the unambiguous position information after GPS outages, the increased code error due to severe and highly variable multipath effects in the suburban and urban areas sometimes may lead to wrong and slowly converging ambiguity resolution. To improve the robustness of the ambiguity resolution, the widelane carrier phase measurement was used in the real-time suburban and pseudo-urban area tests. By contrast, the L1 carrier phase was used in the open-sky test due to a relatively benign multipath environment. The use of widelane measurements is at the cost of amplifying the noise by the linear combination of the L1 and L2 carrier phase. However, it is a tradeoff between fast and reliable ambiguity resolution and an increase in the noise.

The carrier phase results (L1 and widelane) with fixed ambiguities and the C/A code residuals are investigated to give some relevant information on the accuracy of GPS solution as well as the correctness of the ambiguity resolution. With a good estimated

position, the overall L1 carrier phase residuals with fixed ambiguities are around 1-2 cm.

The magnitudes of the WL carrier phase residuals are below 5 cm for the most part. If the

truth solution is accurate to the centimetre-level, the C/A code residuals are essentially

equivalent to the code errors (Petovello 2003). Unexpectedly large carrier phase residuals

and/or biased pseudorange residuals suggest a wrong ambiguity fix or large multipath

error may have occurred.

7.2.2   GPS Time Latency

For all real-time tests, the GPS latencies with respect to the IMU time are investigated.

They were typically on the order of 0.1-0.2 s (Petovello, 2003). With the data

buffering/restoring technique, the real-time solution can be compatible with the

post-mission solution when the GPS time latency is less than 3 s. The GPS time latency

varies from test to test. By investigating the GPS time latency in each real-time test, the

compatibility between the real-time and the post-mission solution can also be verified if

the GPS time latency is less than 3 s.

7.2.3   Reference Solution and Its Accuracy

To assess the performance of the GPS/Low cost IMU/On-board vehicle sensor integrated

system, a reference solution is generated from another independent system such as the

GPS/HG1700 IMU (tactical grade IMU) integrated system or GPS/CIMU (navigational

grade IMU). As shown in the hardware platform description, three different GPS units are

employed to integrate with navigational grade, tactical grade and low cost IMUs for generating independent solutions. Furthermore, the reference solution can be generated by either the optimal backward smoothing technique or by a forward Kalman filtering technique. In the open-sky test with good GPS availability, the GPS determines the absolute accuracy. Both the GPS/HG1700 IMU and GPS/CIMU integrated solutions are accurate to the centimetre-level, and there is no significant difference in the optimal smoothing and forward Kalman filtering solutions. However, in the suburban and urban areas, both tactical and navigation grade IMUs are susceptible to position and velocity drift due to the frequent masking of satellite signals by trees, buildings and underpasses. As the CIMU is about 100 times more accurate than the HG1700 IMU, the reference trajectory generated by the GPS/CIMU with an optimal backward smoothing technique would be more reliable than that generated by the GPS/HG1700 IMU in suburban and urban areas. With this in mind, the reference trajectory in the open-sky kinematic test with post-mission was generated by the GPS/HG1700 IMU integrated solution without optimal smoothing. For the real-time tests in the open-sky, suburban and the pseudo-urban areas, however, the GPS/CIMU integrated solution with backward optimal smoothing was used to generate the reference.

It is important to know the accuracy of the reference trajectory. For the reference generated by GPS/HG1700 solution, its accuracy was shown by the estimated standard deviations of position and velocity. Furthermore, some extra information can also be

given by investigating the carrier phase residuals with fixed ambiguity processing. The

GPS/CIMU solution processed by the Applanix POS Pac software gives the estimated

RMS error of the estimated position and velocity. The estimated RMS errors are

equivalent to the estimated standard deviation assuming the estimated error has zero

mean.

7.2.4   Performance Analysis of Various Integration Strategies

The performances of the six integration strategies were assessed with respect to the

reference by looking into their position and velocity difference and the estimated standard

deviations of the position and velocity difference. The estimated position and velocity

standard deviations are an estimate of the error by the Kalman filter, which should have

good agreement with the actual error in an ideal case. In practice, however, it indicates

that the model and parameters in the Kalman filter are well tuned if the estimated

standard deviation does not deviate too much from the variation of the actual error, or

more specifically the position and velocity differences in this case. The estimated

standard deviations of the position and velocity differences are computed by variance

propagation theory. Assuming the position (velocity) solution from the GPS/Low cost

IMU/On-board vehicle sensor integrated system is X_1 with an estimated standard

deviation σ_{X_1}, and the corresponding solution from the reference is X_2 with an

estimated standard deviation σ_{X_2}, the position (velocity) difference and the estimated

standard deviation were computed by Equation (7.1)

$$\begin{cases} \text{Difference} = X_1 - X_2 \\ \sigma_{\text{Difference}} = \sqrt{\sigma_{X_1}^2 + \sigma_{X_2}^2} \end{cases}$$

(7.1)

To confirm the consistency of the position (velocity) difference and the estimated standard deviation of the difference, the position (velocity) difference and the $\pm 3\sigma_{\text{Difference}}$ ("3-sigma") were plotted on the same plot. Statistically, the probability of the difference being $\pm 3\sigma_{\text{Difference}}$ is 99.74%. It implies that most of the difference should be within the scope of $\pm 3\sigma_{\text{Difference}}$ if the Kalman filter was well tuned.

To check the validity of the Kalman filter by comparing the actual difference and the estimated standard deviation of the difference, only the results for the GPS/INS and the GPS/INS/WSS/SAS/GL/YRS strategies are investigated and illustrated by figures. This is feasible since these two integration strategies are two extreme cases. Among all the GPS/INS/On-board vehicle sensors integrated strategies, GPS/INS/WSS/SAS/GL/YRS integration strategy is the most typical one which covers all the information of the low cost IMU and all the on-board vehicle sensors. If its Kalman filter is verified to be well tuned, it suggests that any other integration strategy should also work well.

7.3 Results and Analysis

By comparing the six integration strategies for all tests, the test results are analyzed in the following order:

1. Open-sky kinematic test - post-mission,

2. Open-sky area - real-time,

3. Suburban area - real-time, and

4. Pseudo-urban area – real-time.

7.3.1   Open-Sky Kinematic Test - Post-Mission

The post-mission results for the open-sky kinematic test were analyzed by using the GPS/HG1700 IMU tightly coupled solution as the reference. It is necessary to first analyze the performance and accuracy of the reference solution. Figure 7.5 shows the L1 carrier phase residuals when the ambiguities are fixed, the baseline length and the pseudorange code residuals (colour-coded by PRN) for the reference solution. With a maximum separation between the GPS reference station and the vehicle being approximately 4 km, most of the L1 carrier phase residuals were within 1-2 cm. The code residuals were also within a reasonable level. It implies that ambiguities are resolved correctly.

To be more specific, Figure 7.6 and Figure 7.7 show the estimated standard deviations of the position and velocity for the GPS/HG1700 integrated reference solution. The estimated standard deviation is a measure of the accuracy for the estimated solution. It can be seen that the reference is estimated to be accurate to the centimetre and cm/s level, which indicates that the GPS/HG1700 IMU integrated solution is sufficiently accurate to be used as the reference solution.
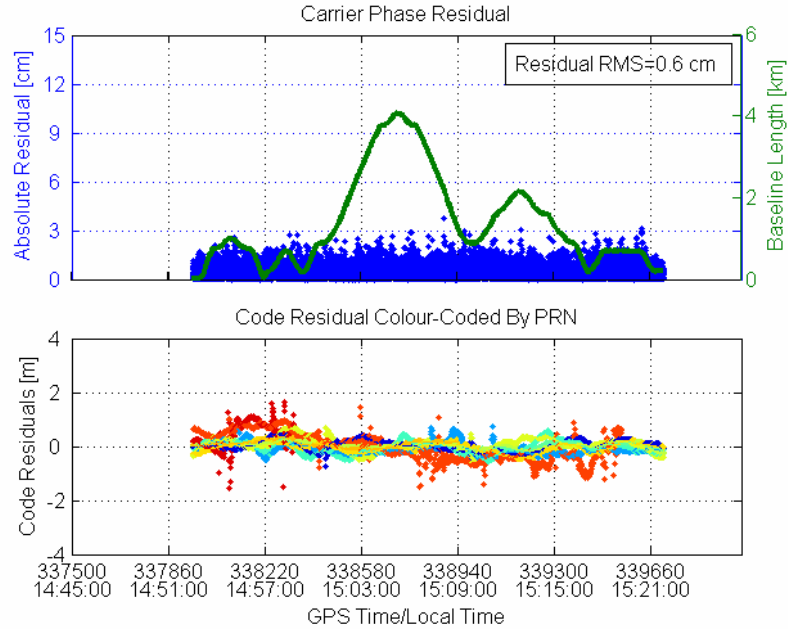
Figure 7.5 L1 Carrier phase and PRN code residuals for the reference solution (Open-sky test in post-mission)
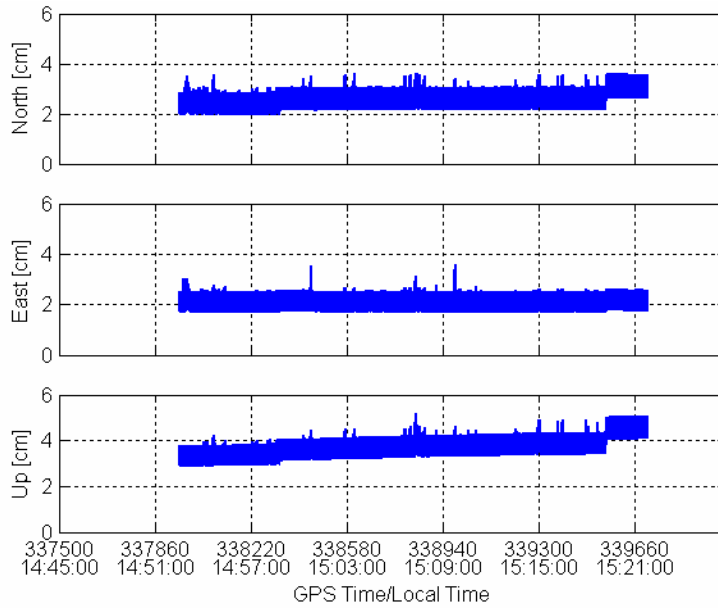
Figure 7.6 Estimated position standard deviation of the reference solution (Open-sky test in post-mission)
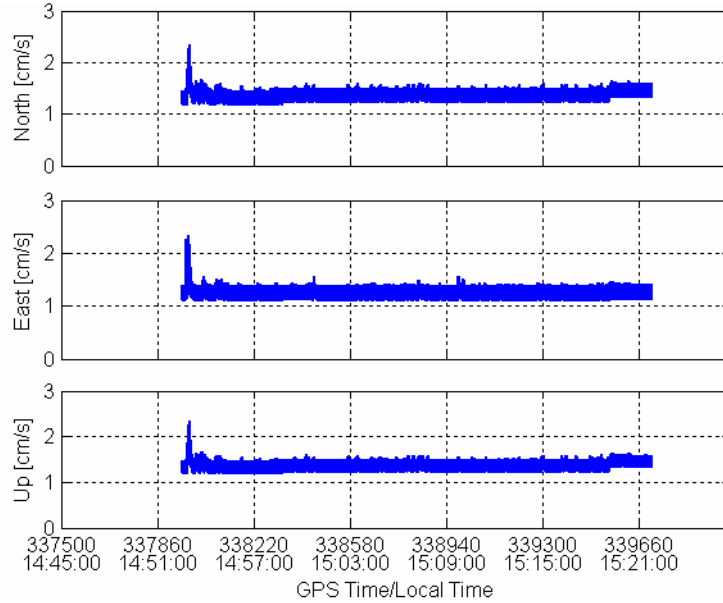
Figure 7.7 Estimated velocity standard deviation of the reference solution (Open-sky test in post-mission)

With respect to GPS/Low cost IMU integrated system, Figure 7.8 and Figure 7.9 show the L1 carrier phase residuals with fixed ambiguities, C/A code residuals colour-coded by PRN, the satellite horizontal and vertical DOPs, the number of satellites tracked as well as the number of resolved ambiguities. With good GPS availability and satellite geometry, the DD ambiguities were fixed correctly, which is also implied by the reasonable L1 carrier phase and the pseudorange code residuals.
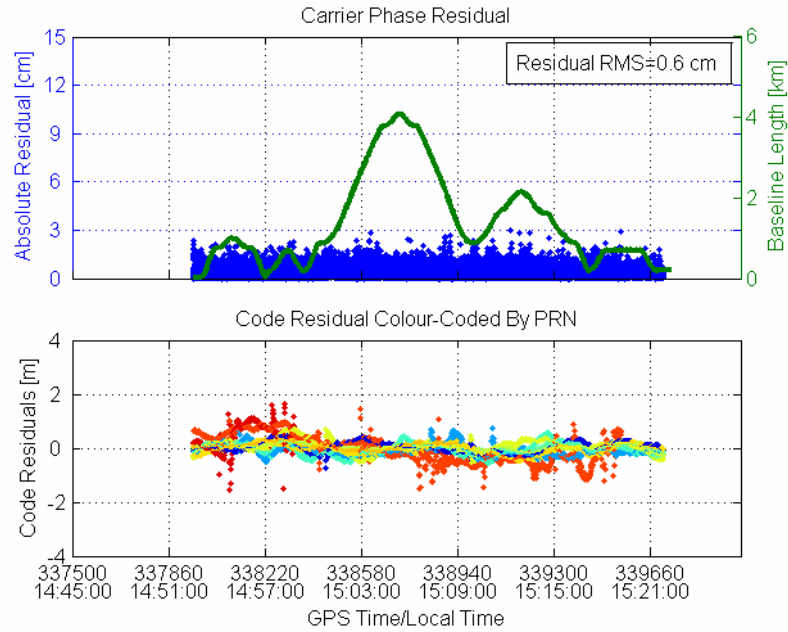
Figure 7.8 L1 carrier phase and code residuals for GPS/Low cost IMU integrated solution (Open-sky test in post-mission)
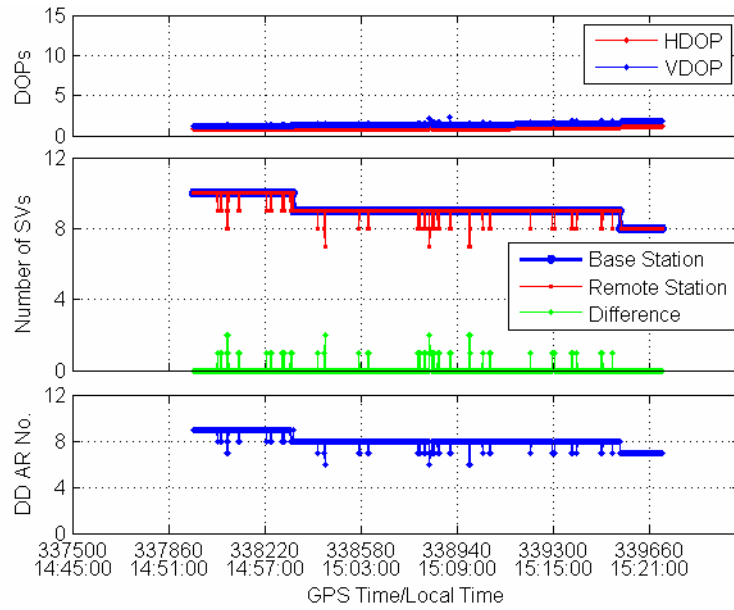
Figure 7.9 Satellite DOPs, SV numbers and fixed ambiguity numbers for GPS/Low cost IMU integrated solution (Open-sky test in post-mission)

To verify that GPS determines the absolute accuracy in open-sky conditions, the GPS/Low-cost IMU integrated position was compared with the GPS-only solution as

shown in Figure 7.10. Table 7.1 gives the statistics of the position differences. It shows that the position difference between the GPS/Low-cost IMU and GPS-only has a zero mean, and the standard deviation of the position difference is at the millimetre level. The small difference between the GPS/Low-cost IMU and the GPS-only solution indicates that the integration of the low cost IMU and GPS did not introduce a deviation of the integrated solution with respect to the GPS-only solution, and consequently it can be assumed that the Kalman filter was designed properly.
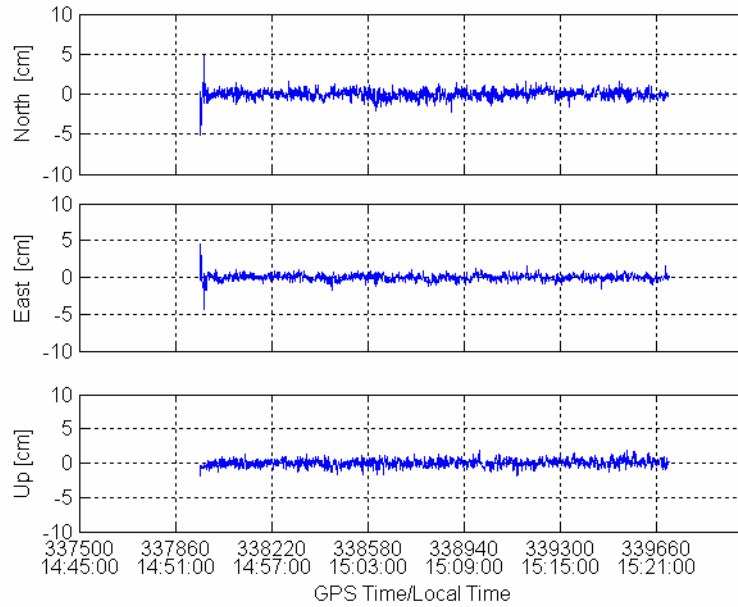
Figure 7.10 Position differences between GPS/Low cost IMU and the GPS-Only
(Open-sky test in post-mission)

Table 7.1 Statistics of the position differences between the GPS/Low cost IMU and the
GPS-only solutions (Open-sky test in post-mission)

Mean of position difference [cm]			Standard deviation of position difference [cm]		
North	East	Up	North	East	Up
0.0	0.0	0.0	0.5	0.4	0.5

To go one step further, the consistency of the actual position and velocity differences and the estimated standard deviation of the position and velocity differences are investigated for the GPS/Low-cost IMU and the GPS/Low-cost IMU/WSS/SAS/GL/YRS integrated solutions with respect to the reference solutions. Figure 7.11 to Figure 7.14 show the position and the velocity differences (with the corresponding 3-sigma envelope) of the GPS/Low cost IMU and GPS/Low cost IMU/WSS/SAS/GL/YRS solutions. It can be seen that the difference is at the centimetre level with more noise in the GPS/Low cost IMU/WSS/SAS/GL/YRS integration strategy. As expected, most of the differences were within the 3-sigma boundary. The consistency of the actual differences and the estimated standard deviations of the differences indicate that the Kalman filters for these two integration strategies were well tuned from this scenario.

Table 7.2 and Table 7.3 summarize the statistics of the position and velocity differences of all integration strategies with respect to the reference. The position and velocity differences of all integration strategies with respect to the reference are within the centimetre level when GPS is fully available.
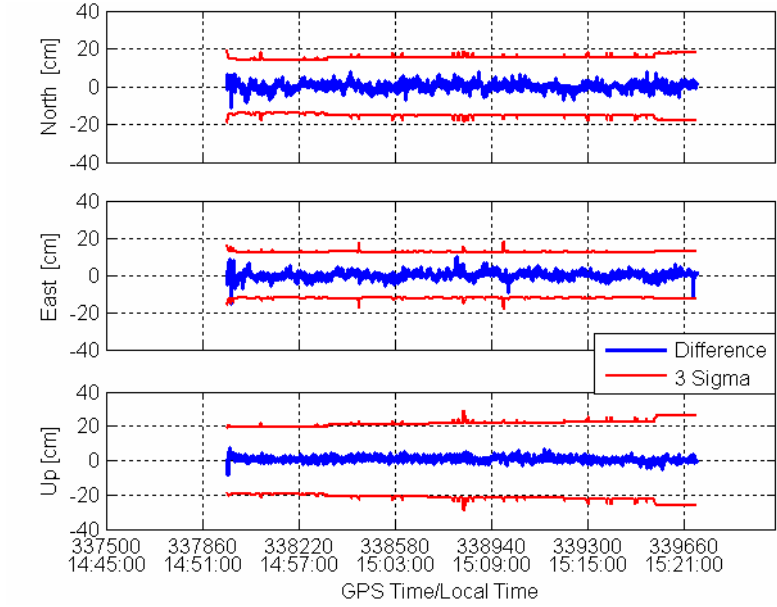
Figure 7.11 Position differences between GPS/Low cost IMU and the reference solution
(Open-sky test in post-mission)
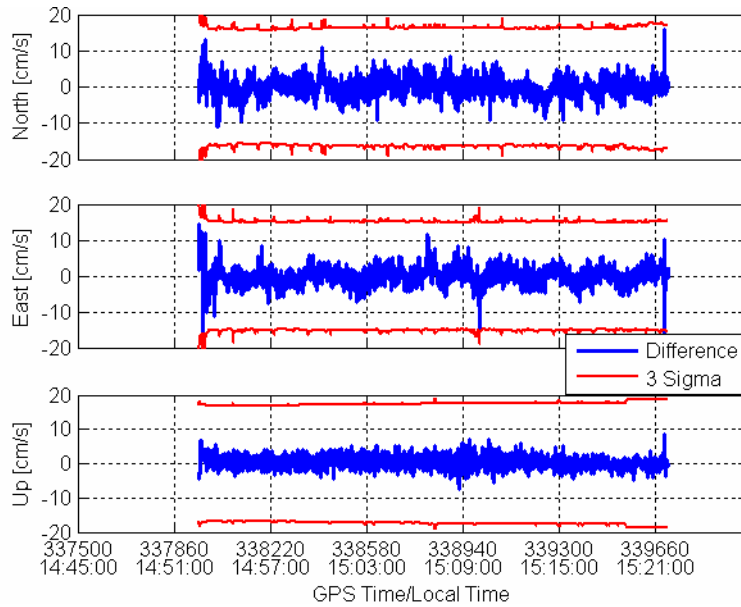
Figure 7.12 Velocity differences between GPS/Low cost IMU and the reference solution
(Open-sky test for post-mission)
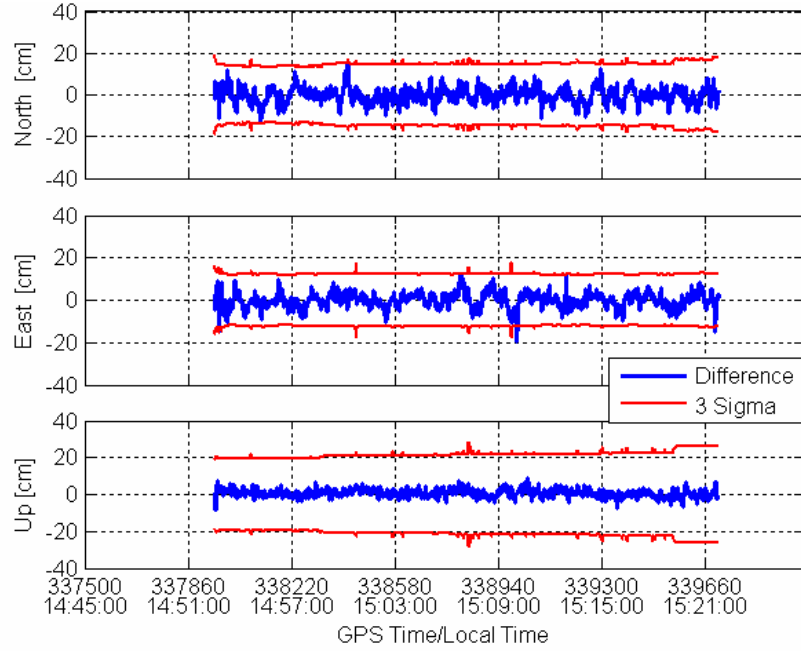
Figure 7.13 Position differences between GPS/Low cost IMU/WSS/SAS/GL/YRS and the reference solution (Open-sky test in post-mission)
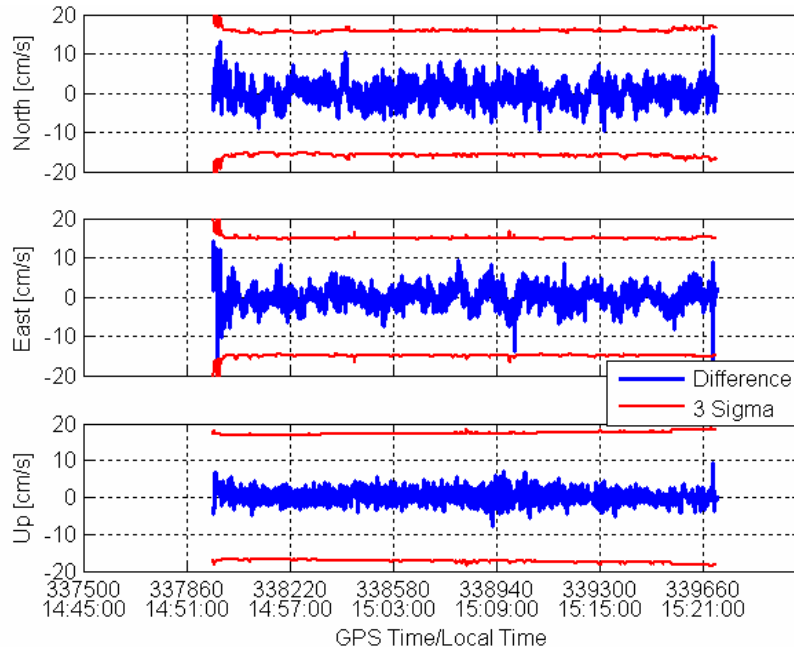
Figure 7.14 Velocity differences between GPS/Low cost IMU/WSS/SAS/GL/YRS and the reference solution (Open-sky test in post-mission)

Table 7.2 Statistics of the position differences between GPS/Low cost IMU/On-board
vehicle sensor and the reference solution (Open-sky test in post-mission)

Strategies	Mean position difference [cm]			standard deviation of position difference [cm]		
	North	East	Up	North	East	Up
GPS/INS	0.0	0.0	0.7	1.5	1.3	1.1
GPS/INS/WSS	0.0	0.0	0.0	3.3	3.1	1.9
GPS/INS/SAS	0.0	0.1	0.6	3.4	3.0	1.8
GPS/INS/GL/YRS	-0.2	0.0	0.6	3.9	3.7	2.0
GPS/INS/WSS/SAS	-0.2	-0.1	0.6	3.4	3.1	2.0
GPS/INS/WSS/SAS/GL/YRS	-0.2	-0.1	0.6	3.4	3.1	2.0

Table 7.3 Statistics of the velocity differences between GPS/Low cost IMU/On-board
vehicle sensor and the reference solution (Open-sky test in post-mission)

Strategies	Mean velocity difference [cm/s]			Standard deviation of velocity difference [cm/s]		
	North	East	Up	North	East	Up
GPS/INS	0.0	0.0	0.4	2.3	2.3	1.4
GPS/INS/WSS	0.0	0.0	0.4	2.3	2.4	1.4
GPS/INS/SAS	0.0	0.0	0.4	2.4	2.4	1.4
GPS/INS/GL/YRS	0.0	0.0	0.4	2.6	2.7	1.7
GPS/INS/WSS/SAS	0.0	0.0	0.4	2.3	2.4	1.4
GPS/INS/WSS/SAS/GL/YRS	0.0	0.0	0.4	2.3	2.4	1.4

To investigate the benefits gained from the integration of the on-board vehicle sensors, 12 GPS outages were simulated with a duration of 40 s. The simulated GPS outages are labelled by the red lines on the reference trajectory in Figure 7.15. The vehicle velocity and attitude associated with the 12 simulated GPS outages are shown in Figure 7.16 and Figure 7.17, respectively.

Table 7.4 outlines the maximum vehicle dynamics during GPS outages. From the range for speed and the attitude angles and the maximum attitude angular rate summarized in

Table 7.4, it can be concluded that the simulated GPS outages cover a wide range of

vehicle dynamics. Therefore, the simulated GPS outages are typical and useful for the

evaluation of the position and velocity drift error of various integration strategies.
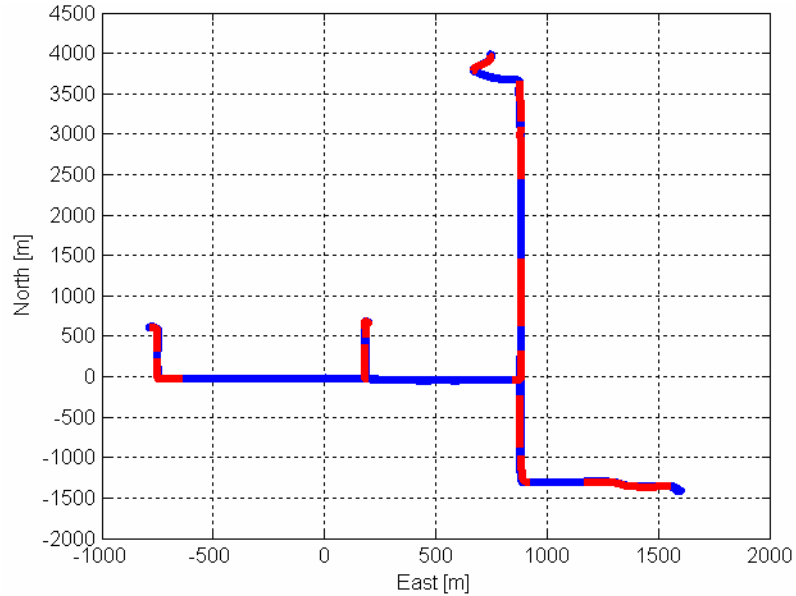
Figure 7.15 Reference trajectory with the 12 simulated GPS outages (Open-sky test in post-mission)
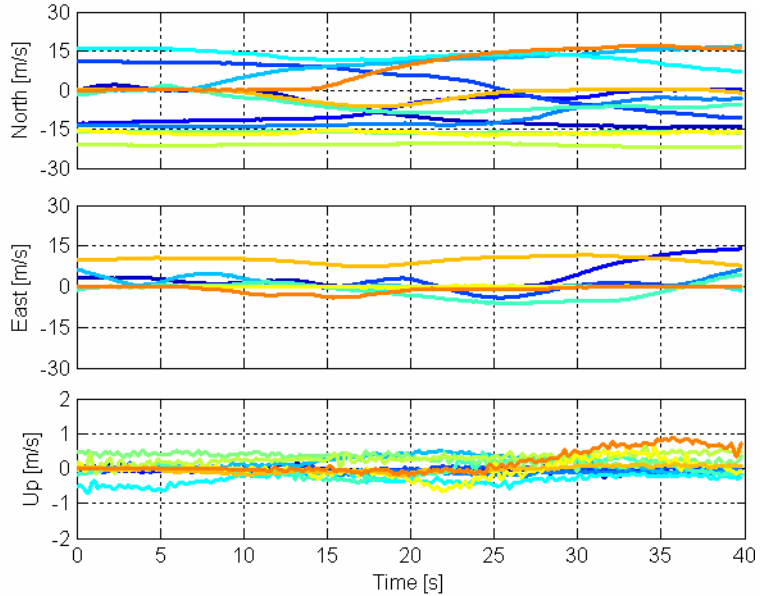
Figure 7.16 Velocity during 12 simulated outages (Open-sky test in post-mission)
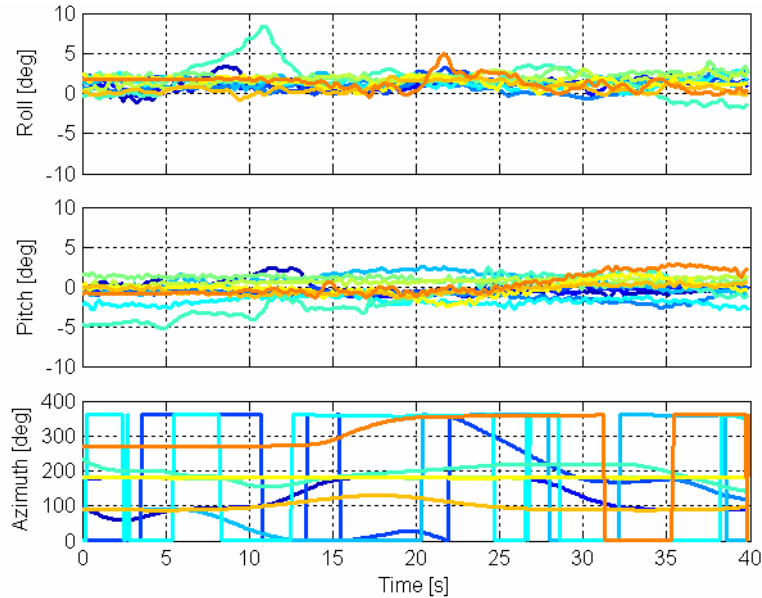
Figure 7.17 Attitude during 12 simulated GPS outages (Open-sky test in post-mission)

Table 7.4 Summary of the vehicle dynamics for 12 simulated GPS outages (Open-sky test in post-mission)

	Speed	Roll	Pitch	Azimuth
Minimum	0.0 km/h	-1.78 deg	-5.25 deg	0.0 deg
Maximum	78.8 km/h	8.34 deg	2.88 deg	359.0 deg
Maximum rate	-	8.58 deg/s	10.25 deg/s	27.13 deg/s

A side slip angle is closely related to a violation of the lateral non-holonomic constraint. When a larger side slip angle (exceeds the five-degree threshold) is detected, the removal of the lateral non-holonomic constraint will improve the positioning accuracy to some degree. As a complicated phenomenon, side slips are correlated with many factors, such as the vehicle dynamics and road conditions. Figure 7.18 shows the computed side slip angles during the 12 simulated GPS outages, with a maximum of side slip angle of about 20 degrees. By correlating the larger side slip angles with the vehicle dynamics (especially the vehicle attitude shown in Figure 7.17), the larger side slip angles that

appeared in the 12 simulated GPS outages mainly resulted from sharp turns, or larger

roll/pitch angular rates due to bumpy or icy roads in the winter. The side slip angles

appeared within the 12 simulated GPS outages are typical for the land vehicle positioning

and navigation system.
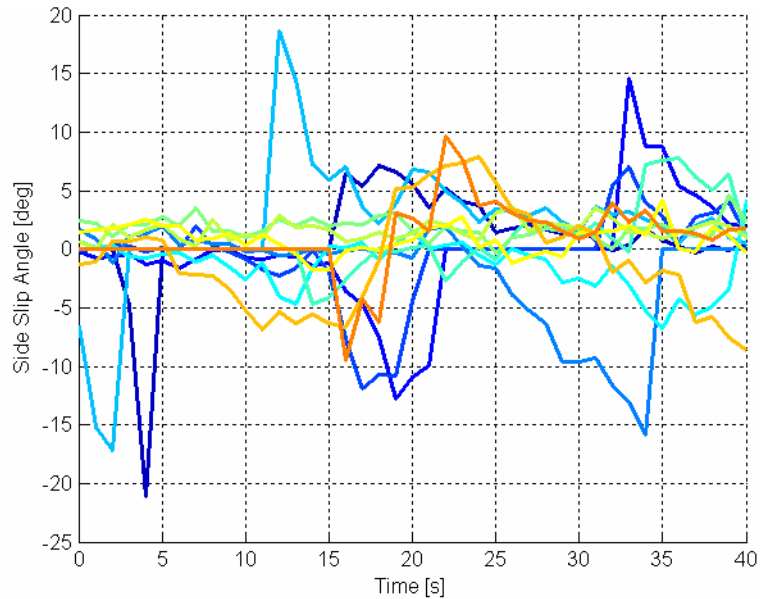
Figure 7.18 Side slip angles during 12 simulated GPS outages (Open-sky test in post-mission)

To illustrate the position and velocity drift error for the 12 simulated 40 s GPS outages

and to analyze the validity of the Kalman filter, Figure 7.19 to Figure 7.21 show the RMS

position error and the average estimated standard deviation in the horizontal, up and the

3D directions, respectively. Similarly, Figure 7.22 to Figure 7.24 show the RMS velocity

error and the average estimated standard deviation in the same directions. Also shown in

the figures (for comparison purposes) are the results of the associated GPS/HG1700

IMU/On-board vehicle sensor integration strategies. The solid lines represent the RMS error, and the dashed lines represent the average estimated deviation.

Table 7.5 and Table 7.6 compare the position RMS errors and the average estimated standard deviations using different integration strategies for both the low cost IMU and HG1700 IMU, respectively. The corresponding velocity results are summarized in Table 7.7 and Table 7.8.

Being consistent with the relevant results of the GPS/HG1700 IMU/On-board vehicle integration strategies, the stand-alone low cost IMU system drifts very rapidly. However, significant benefits can be gained from the integration of the wheel speed sensor by improving the horizontal positioning accuracy by 91%. The next best sensor is the steering angle sensor which can improve the horizontal positioning accuracy by 50%. The horizontal positioning accuracy can be further enhanced by sequentially integrating the wheel speed sensor and the steering angle sensor. The improvement gained from the integration of the G sensors and yaw rate sensor is less significant than the wheel speed sensor or the steering angle sensor as their accuracy is at the same grade with the low cost IMU. With several larger side slip angles during the simulated GPS outages, the lateral non-holonomic constraint will most likely be violated when the side slip angles are larger than the 5-degree threshold. In these cases, the G sensors and yaw rate sensor can be employed to detect and alleviate the violation of the lateral non-holonomic constraint, which can enhance the positioning accuracy when the side slip angles exceed the

pre-defined threshold. Overall, the integration strategy with GPS, INS and all the vehicle

sensors together (GPS/INS/WSS/SAS/GL/YRS) shows the best performance, as

expected.
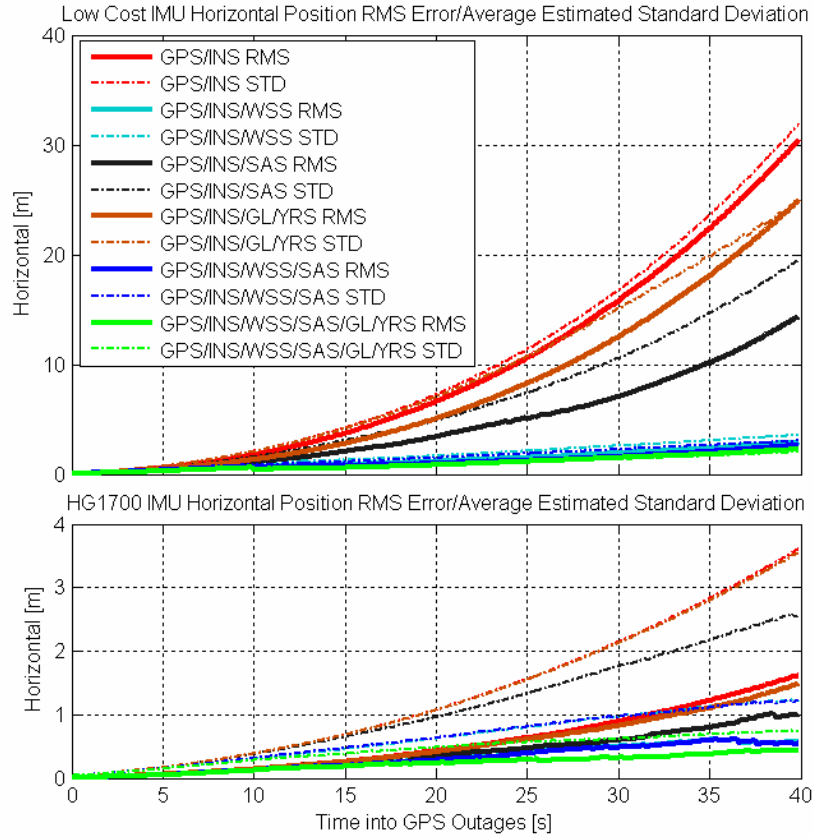
Figure 7.19 Horizontal position RMS error and average estimated standard deviation
(Open-sky test in post-mission)
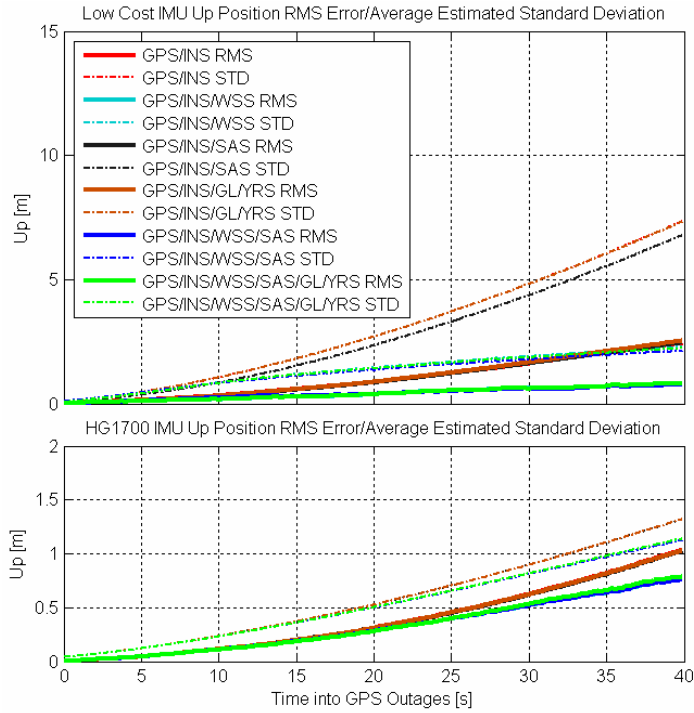
Figure 7.20 Up position RMS and average estimated standard deviation (Open-sky test in post-mission)
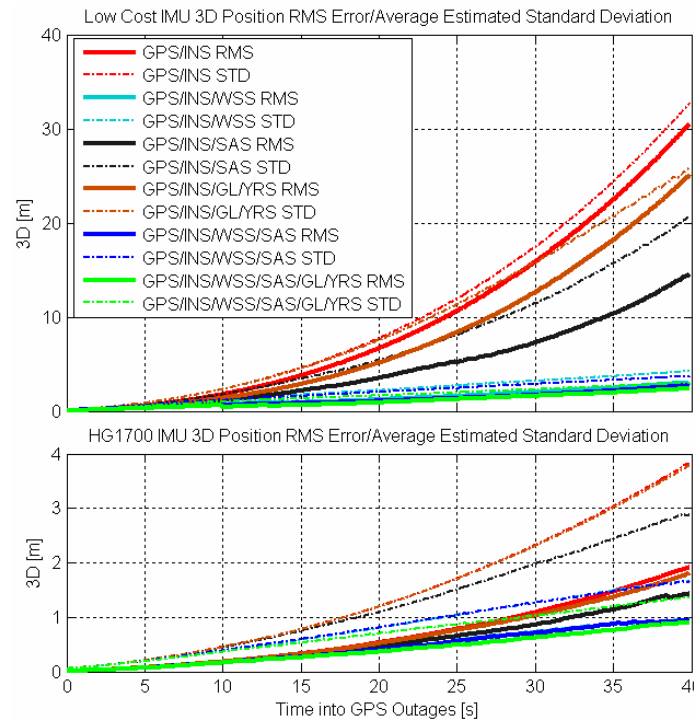
Figure 7.21 3D RMS position error and average estimated standard deviation (Open-sky test in post-mission)
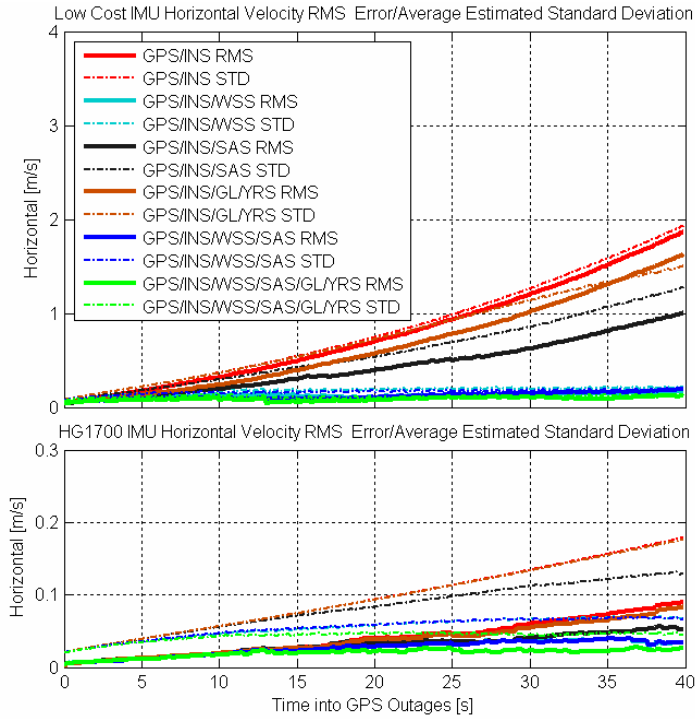
Figure 7.22 Horizontal RMS velocity error and average estimated standard deviation (Open-sky test in post-mission)
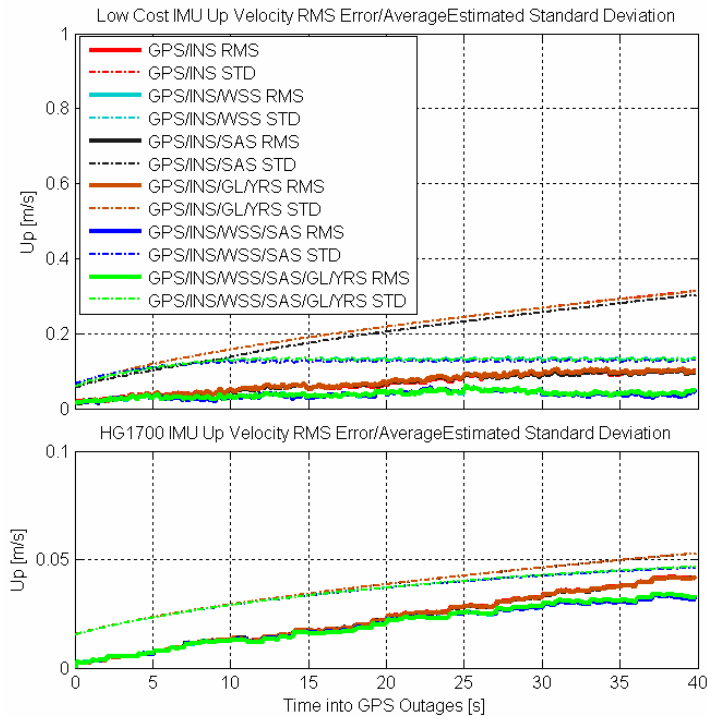
Figure 7.23 Up RMS velocity error and average estimated standard deviation (Open-sky test in post-mission)
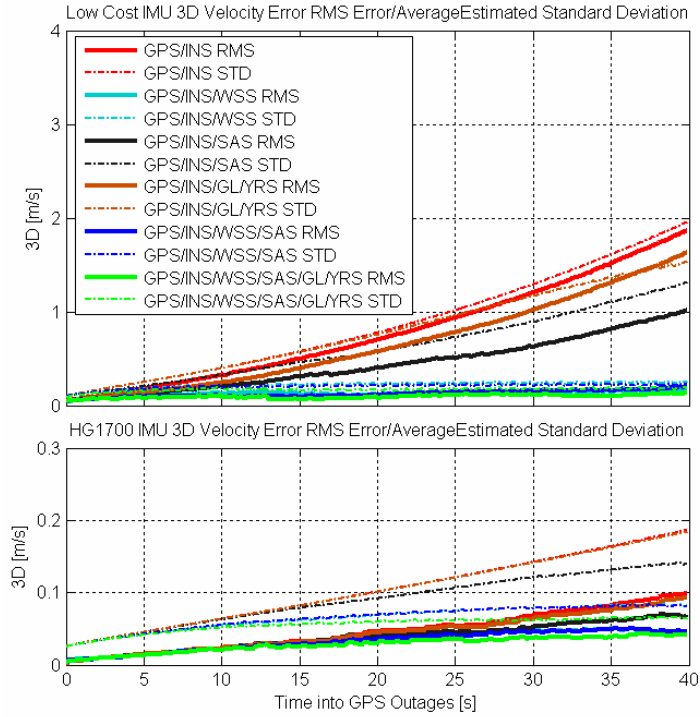
Figure 7.24 3D RMS velocity error and average standard deviation (Open-skytest in post-mission)

Table 7.5 RMS position error and average estimated standard deviation (Low cost IMU, Open-sky test in post-mission)

Strategies for Low Cost IMU	Horizontal RMS position error at the end of 40 s GPS outages [m]			Average estimated standard deviation at the end of 40 s GPS outages [m]		
	Horizontal	Up	3D	Horizontal	Up	3D
GPS/INS	30.48	2.45	30.58	31.98	7.36	32.82
GPS/INS/WSS	2.92	0.80	3.03	3.59	2.30	4.27
GPS/INS/SAS	14.38	2.47	14.59	19.59	6.80	20.74
GPS/INS/GL/YRS	25.00	2.54	25.13	24.91	7.35	25.97
GPS/INS/WSS/SAS	2.67	0.76	2.78	3.05	2.14	3.73
GPS/INS/WSS/SAS /GL/YRS	2.27	0.81	2.41	2.02	2.25	3.02

Table 7.6 RMS position error and average estimated standard deviation (HG1700 IMU, Open-sky test in post mission)

Strategies for HG1700 IMU	Horizontal RMS position error at the end of 40 s GPS outages [m]			Average position estimated standard deviation at the end of 40 s GPS outages [m]		
	Horizontal	Up	3D	Horizontal	Up	3D
GPS/INS	1.62	1.04	1.93	3.62	1.32	3.85
GPS/INS/WSS	0.57	0.76	0.95	1.23	1.13	1.67
GPS/INS/SAS	1.01	1.03	1.44	2.58	1.32	2.90
GPS/INS/GL/YRS	1.49	1.03	1.81	3.56	1.32	3.80
GPS/INS/WSS/SAS	0.55	0.76	0.94	1.22	1.13	1.66
GPS/INS/WSS/SAS /GL/YRS	0.43	0.79	0.90	0.74	1.14	1.36

Table 7.7 RMS velocity error and average velocity estimated standard deviation (Low cost IMU, open-sky test in post-mission)

Strategies for Low Cost IMU	Horizontal RMS position error at the end of 40 s GPS outages [m/s]			Average position estimated standard deviation at the end of 40 s GPS outages [m/s]		
	Horizontal	Up	3D	Horizontal	Up	3D
GPS/INS	1.87	0.10	1.87	1.94	0.31	1.96
GPS/INS/WSS	0.17	0.05	0.18	0.22	0.14	0.26
GPS/INS/SAS	1.01	0.10	1.02	1.28	0.30	1.32
GPS/INS/GL/YRS	1.63	0.10	1.63	1.51	0.31	1.54
GPS/INS/WSS/SAS	0.19	0.04	0.20	0.19	0.13	0.23
GPS/INS/WSS/SAS /GL/YRS	0.12	0.05	0.13	0.14	0.14	0.20

Table 7.8 RMS velocity error and average velocity estimated standard deviation
(HG1700 IMU, Open-sky test in post-mission)

Strategies for HG1700 IMU	Horizontal RMS velocity error at the end of 40 s GPS outages [m/s]			Average velocity estimated standard deviation at the end of 40 s GPS outages [m/s]		
	Horizontal	Up	3D	Horizontal	Up	3D
GPS/INS	0.09	0.04	0.10	0.18	0.05	0.19
GPS/INS/WSS	0.03	0.03	0.05	0.07	0.05	0.08
GPS/INS/SAS	0.05	0.04	0.07	0.13	0.05	0.14
GPS/INS/GL/YRS	0.08	0.04	0.10	0.18	0.05	0.18
GPS/INS/WSS/SAS	0.03	0.03	0.05	0.07	0.05	0.08
GPS/INS/WSS/SAS /GL/YRS	0.03	0.03	0.04	0.05	0.05	0.07

A full GPS outage is an extreme case in which the Kalman filter will only perform prediction or the on-board vehicle sensor update if selected. Using a tight coupling strategy implemented by a centralized Kalman filter, GPS can still update the Kalman filter and limit the INS position and velocity drift error with partial GPS outages (the double differenced observations are less than four). In land vehicle positioning applications, partial GPS outages can be introduced by dense foliage and tall buildings. To evaluate the effects of on-board vehicle sensors on positioning performance in the case of partial GPS availability, 12 partial GPS outages with 1, 2 and 3 double differenced satellites are simulated, respectively. As shown in Figure 7.25, the horizontal positioning accuracy is compared between various integration strategies for both the low cost and HG1700 tactical grade IMUs with partial and full GPS outages.

Table 7.9 gives the horizontal position RMS error at the end of the 40 second partial and full GPS outages with and without on-board vehicle sensor aiding on the GPS/Low cost IMU and GPS/HG1700 IMU integrated systems. With two or three double differenced satellites, the horizontal position error is relatively small. To be specific, the horizontal position RMS error is at the decimetre level for the low cost IMU integrated system, and is at the centimetre level for the HG1700 tactical grade IMU integrated system. GPS is a still a driving factor that determines the absolute system accuracy when two or more double differenced satellites are available. However, with only one double differenced satellite, the horizontal position error drifts with time rapidly without external aiding from the on-board vehicle sensors. However, its horizontal positioning error is still smaller than the case of a complete GPS outage. It implies that one double differenced satellite can still improve the horizontal positioning accuracy due to the structure of the centralized Kalman filter. Similar to the complete GPS outage, the integration of the on-board vehicle sensors can significantly reduce the horizontal positioning error when only one double differenced satellite is available.
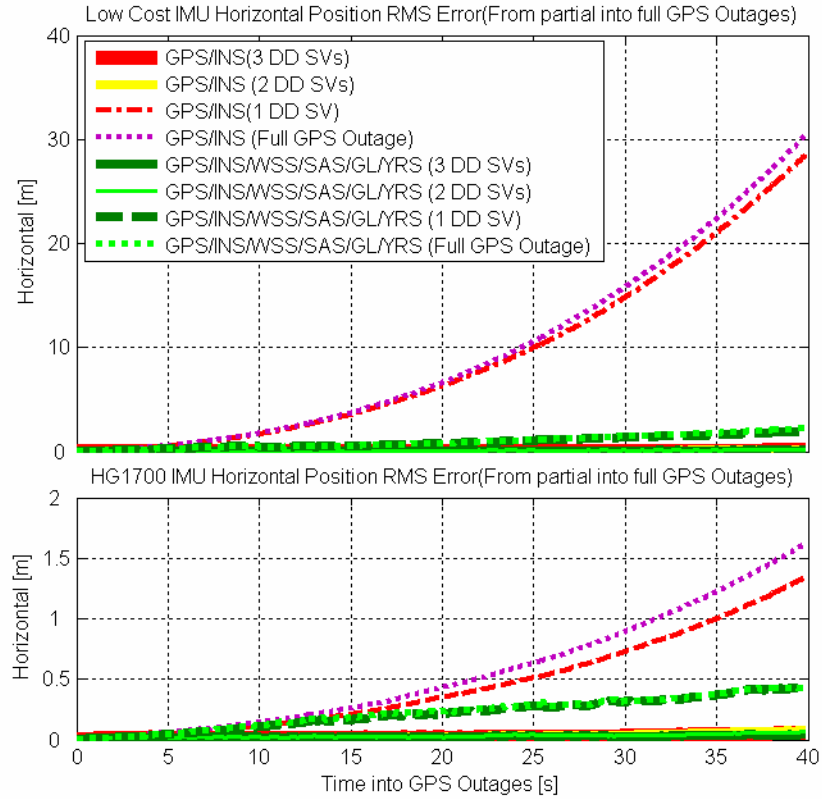
Figure 7.25 Horizontal RMS position drift error with 40 s partial and full GPS outages
(Open-sky test in post-mission)

Table 7.9 Horizontal RMS position error at the end of 40 s partial and full GPS outages
(Open-sky test in post-mission)

Number of DD satellites available	Horizontal RMS position drift error at the end of 40 s GPS outages for low cost IMU [m]		Horizontal RMS position drift error at the end of 40 s GPS outages for HG1700 IMU [m]	
	GPS/INS	GPS/INS/WSS /SAS/GL/YRS	GPS/INS	GPS/INS/WSS /SAS/GL/YRS
None	30.48	2.27	1.62	0.43
1	28.56	1.96	1.34	0.43
2	0.18	0.15	0.08	0.07
3	0.14	0.13	0.06	0.04

Since fast ambiguity resolution plays an important role in a precise positioning system,

the improvement from the IMU and on-board vehicle sensors on ambiguity resolution is

investigated. Twelve GPS outages are simulated with durations of 10 s, 20 s, 30 s and

40 s, respectively. For the data collected herein with the maximum baseline length at 4 km, the correct ambiguities were always selected and thus focus is only given to the time required to fix the ambiguities. Figure 7.26 compares the average time to fix GPS ambiguities after various GPS outage durations for the GPS-Only, GPS/INS (including low cost IMU and HG1700 IMU), as well as GPS/INS/WSS/SAS/GL/YRS integration strategies. Table 7.10 summarizes the average time to fix GPS integer ambiguities shown in Figure 7.26.

The time to fix integer ambiguities is determined by the search volume, which is closely related to the covariance of the estimated ambiguities reference. A GPS-only system is initialized by a differential pseudorange solution, which can be at the level of one to several metres. The initial positioning covariance matrix of either the stand-alone INS or INS/On-board vehicle sensor system grows with time and correlates with the quality of the IMU. With shorter GPS outage durations and a higher quality IMU, the stand-alone INS or INS/On-board vehicle sensor system outperforms the GPS-only strategy given that its estimated standard deviation of the position error state is smaller than the positioning standard deviation initialized by the DD pseudorange solution. Otherwise, the benefits gained from INS or INS/On-board vehicle sensor aiding is expected to be somewhat limited due to longer duration GPS outages or a lower quality of IMU. Compared to the stand-alone INS, the INS/On-board vehicle sensor system reduces the estimated covariance matrix by external aiding from the on-board vehicle sensors. Thus,

faster ambiguity resolution can be expected from the INS/On-board vehicle sensor system with respect to the stand-alone INS system.

It can be seen from Figure 7.26 and Table 7.10 that the IMU can reduce the time-to-fix ambiguities over GPS-only, especially when the duration of the GPS outage is less than 30 s. Due to a relatively lower quality, the low cost IMU has a larger estimated covariance than that for the tactical grade HG1700 IMU. Therefore, the benefits on the ambiguity resolution gained from the low cost IMU is less than that from the tactical grade HG1700 IMU. Furthermore, when all the on-board vehicle sensors are integrated with the IMU, the time to fix ambiguities can be further reduced on the basis of an IMU due to the fact that the on-board vehicle sensors increase the positioning accuracy and significantly reduce the estimated covariance of the ambiguities when integrated with an IMU.
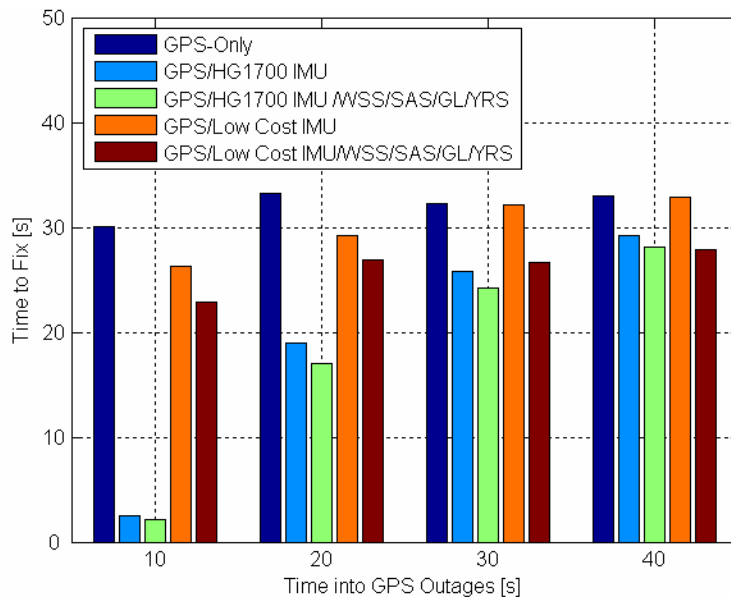
Figure 7.26 Average time to fix GPS ambiguities after GPS outages

Table 7.10 Average time to fix GPS ambiguities after GPS outages for different integration strategies (Open-sky test in post-mission)

Strategies	Average time to fix GPS ambiguities after GPS outages for different integration strategies [s]			
	10 s	20 s	30 s	40 s
GPS-Only	30.1	33.3	32.3	33.0
GPS/HG1700 IMU	2.5	19.0	25.8	29.2
GPS/HG1700 IMU/WSS/SAS/GL/YRS	2.1	17.0	24.3	27.9
GPS/Low cost IMU	26.3	29.3	32.1	32.9
GPS/Low cost IMU/WSS/SAS/GL/YRS	22.8	26.9	26.7	28.2

7.3.2 Open-sky Area – Real-time Test

With good GPS availability and satellite geometry in the open-sky real-time test, Figure 7.27 and Figure 7.28 show the L1 carrier phase and pseudorange code residuals, the satellite horizontal and vertical DOPs, the number of tracked satellites and the number of fixed ambiguities for the GPS/Low cost IMU/WSS/SAS/GL/YRS integration strategy, as obtained in real-time. Most of the L1 carrier phase and code residuals are at a similar level to the open-sky post-mission results analyzed in Section 7.3.1. However, the carrier phase residuals increased to be more than 5 cm with a biased pseudorange residual around GPS time 339720 s. At this time period, the separation between the reference station and the vehicle was about 3 km, and the vehicle was passing a construction site near the road. The increased multipath error resulted from the construction site could account for the increased carrier phase residuals and the biased code residual on one satellite. This conjecture is confirmed by the fact that the residuals return to smaller values later in the data set.
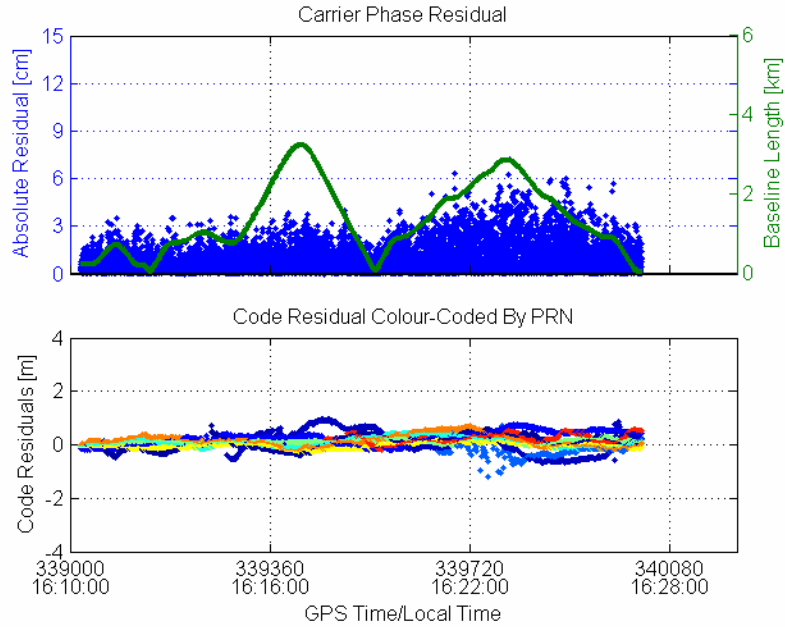
Figure 7.27 L1 carrier phase residuals with fixed ambiguities and the C/A code residuals
(Real-time open-sky test)
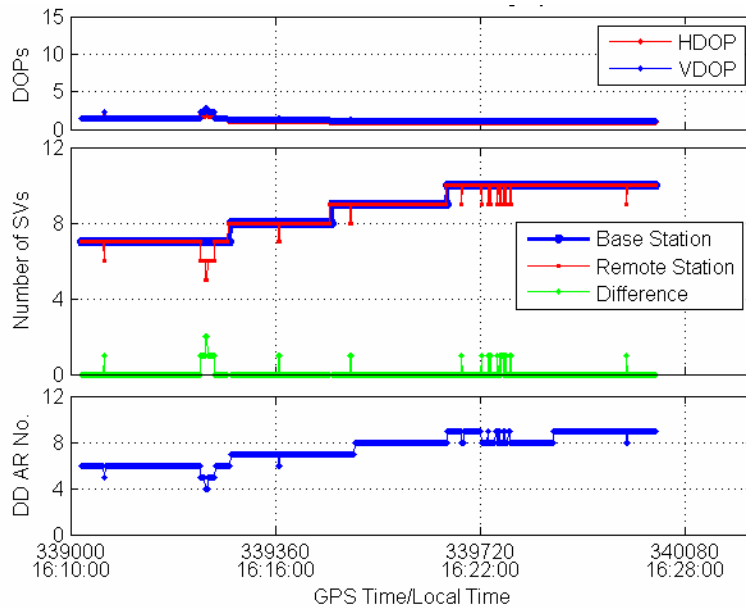
Figure 7.28 Satellite DOPs, satellite availability and number of fixed ambiguities
(Real-time open-sky test)

Figure 7.29 shows the estimated GPS time latency associated with the open-sky real-time

test. The GPS time latency was mostly on the order of 0.1 to 0.2 s with an exception of

the maximum 1.8 s GPS time latency during a short time period around 339810 s. During

this time period, the vehicle was running across a construction site with a 3 km separation between the GPS reference station and the vehicle. The radio link transceiver did not work in a normal way within this short time period. Nevertheless, the data buffer in the software can tolerate 3 s of GPS time latency. The abnormal GPS time latency within this short time period can be handled properly by using the data buffering/restoring technique discussed in Section 3 of Chapter 6. Thus, the compatibility between the real-time and post-mission solutions can be guaranteed.
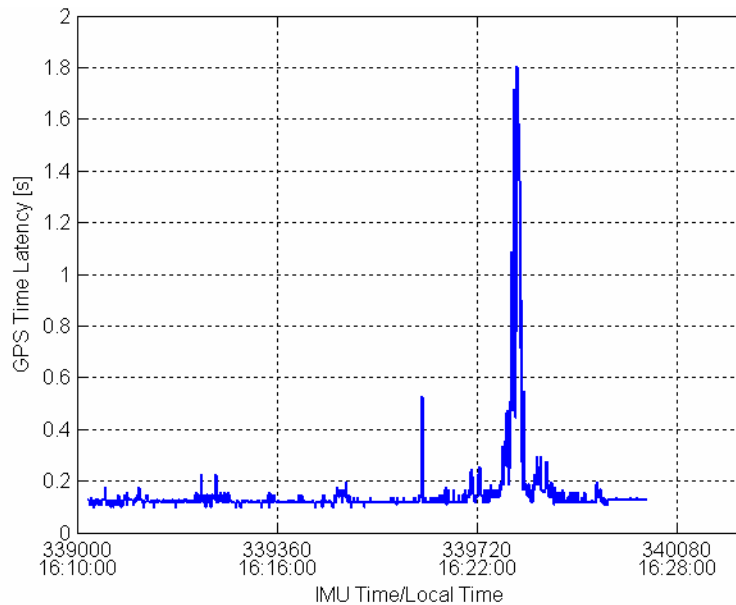
Figure 7.29 GPS time latency with respect to IMU time (Real-time open-sky test)

The vehicle dynamics (velocity and the attitude) and the side slip angles during the entire real-time test in the open-sky area are illustrated from Figure 7.30 to Figure 7.32, respectively. As the vehicle was operated on a flat road in the summer, the roll and pitch angles were less than 5 degrees. As a result, the side slip was less significant than the open-sky test conducted in the winter time for the post-mission analysis. Most of the side

slip angles are less than 5 degrees with the maximum values being about 8 degrees and

sparsely distributed around the specific epochs at 339180 s and 339600 s, respectively.

These two specific epochs are correlated with the vehicle's turning maneuver which can

be found from the azimuth and the side slip angle shown in Figure 7.31 and Figure 7.32.
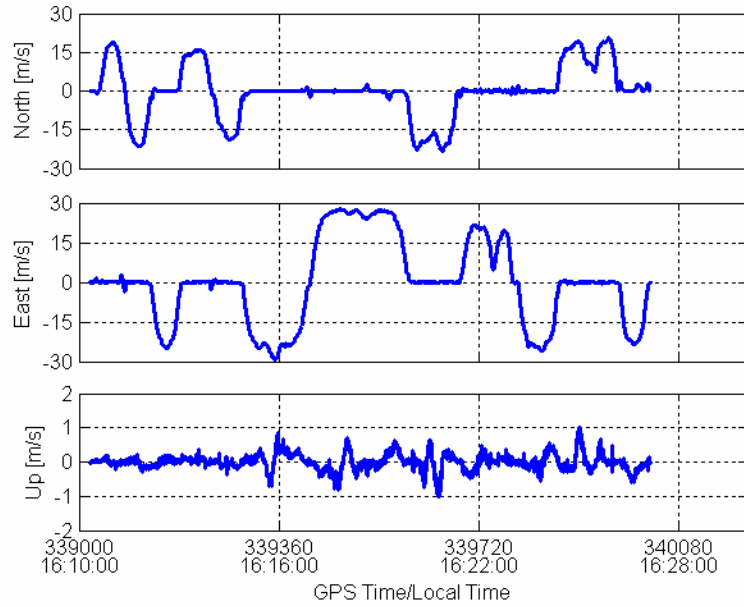
Figure 7.30 Vehicle velocity for real-time open-sky test
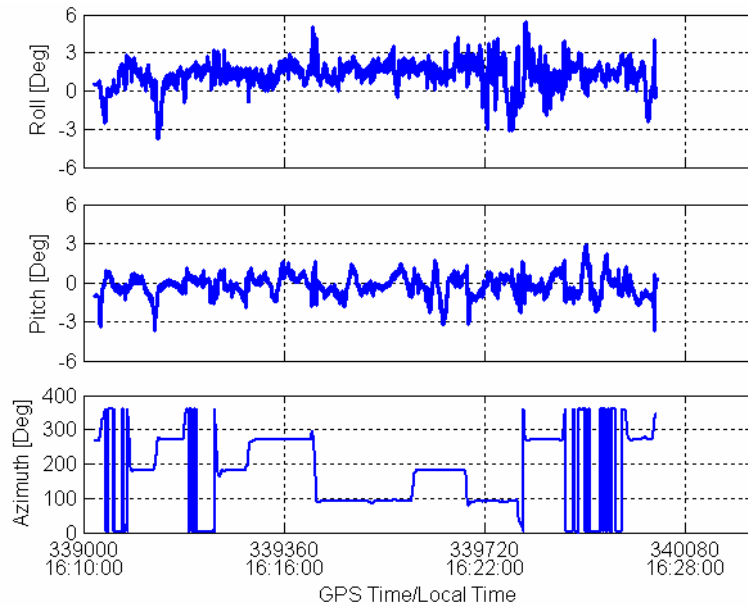
Figure 7.31 Vehicle attitude for real-time open-sky test
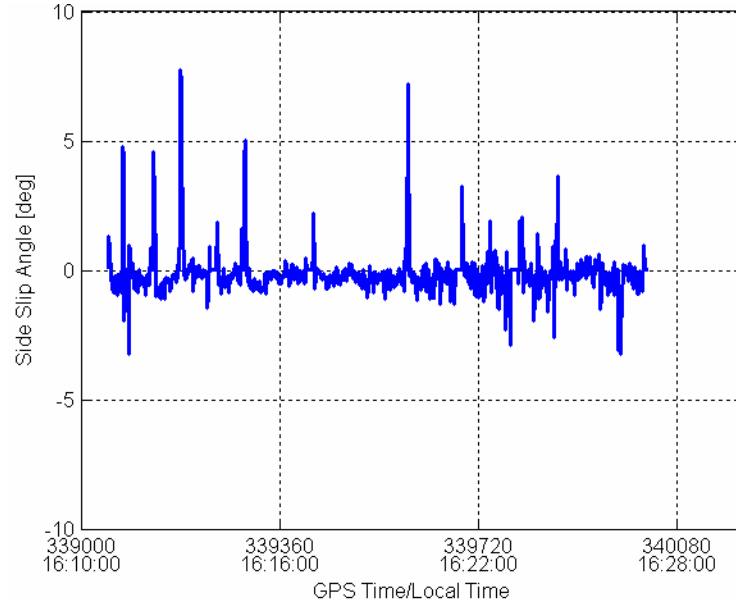
Figure 7.32 Side slip angle for open-sky real-time test

The reference trajectory generated by the GPS/CIMU is shown in Figure 7.33, and the estimated RMS for position and velocity are shown in Figure 7.34 and Figure 7.35, respectively. The estimated RMS of the position and velocity in GPS/CIMU integrated system is computed from Applanix POS PAC software. Some ripples in these figures are due to a higher CIMU mechanization output rate (20 Hz) and a lower GPS update rate (1 Hz). As an optimal backward smoothing was used, the estimated RMS is relatively large at the last epoch, because a backward Kalman filter is still not converged to a steady state. In general, the estimated horizontal position is accurate to be 1 cm, and the accuracy of the estimated position in the up direction is around 6 cm. The velocity accuracy is at the millimetre per second level.
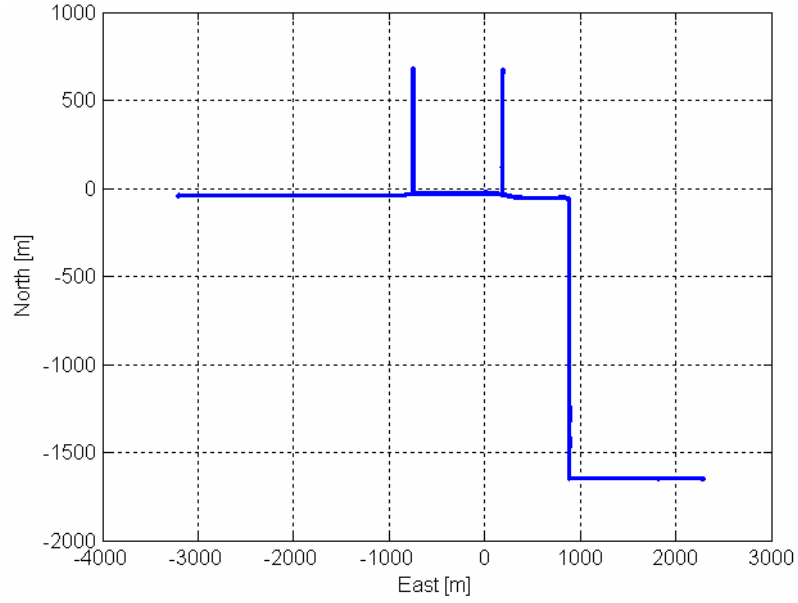
Figure 7.33 Reference trajectory generated by the GPS/CIMU integrated solution
(Open-sky real-time test)
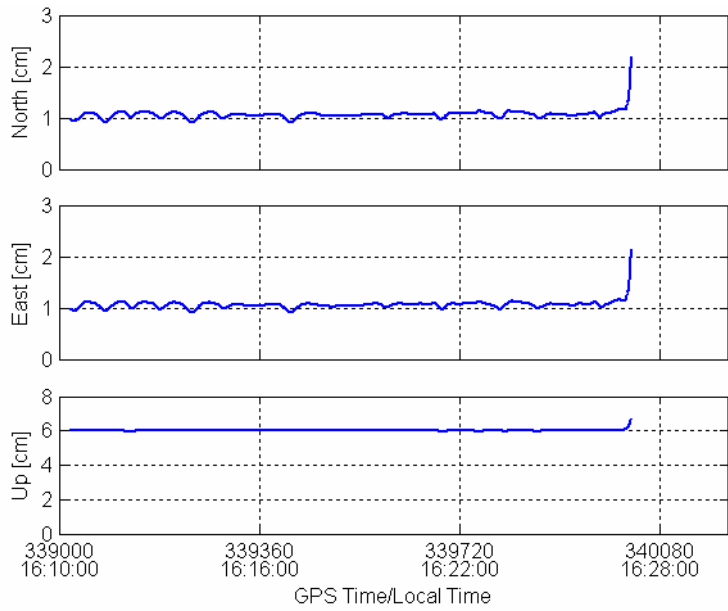
Figure 7.34 Estimated position RMS of reference solution (Open-sky real-time test)
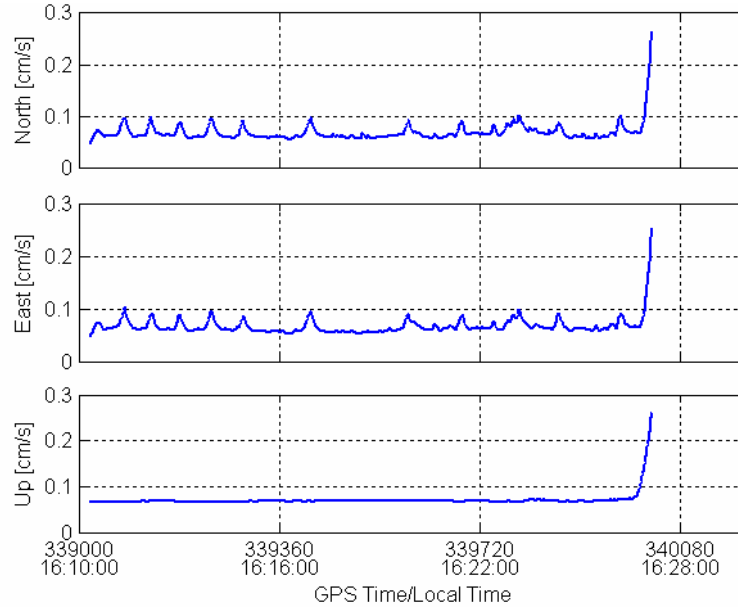
Figure 7.35 Estimated velocity RMS of the reference solution (Open-sky real-time test)

The position and the velocity differences between the real-time solution for the GPS/Low cost IMU/WSS/SASGL/YRS integration strategy and the reference solutions as well as the relevant 3–sigma envelopes are shown in Figure 7.36 and Figure 7.37, respectively. The statistics of the differences are given in Table 7.11. Similar to the open-sky post-mission results, the difference is also at the centimetre level. Most of the position and velocity differences are within the 3-sigma envelope. It indicates that the actual difference and the estimated standard deviation of the difference have a good agreement, and the Kalman filter is well tuned in the open sky area with good GPS availability.
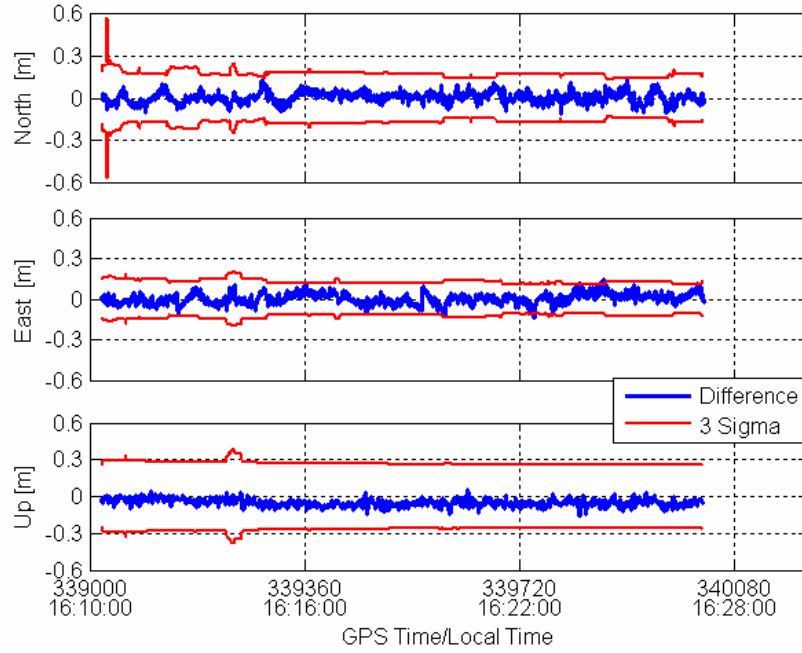
Figure 7.36 Position difference between GPS/Low cost IMU/WSS/SAS/GL/YRS and reference solution (open-sky real-time test)
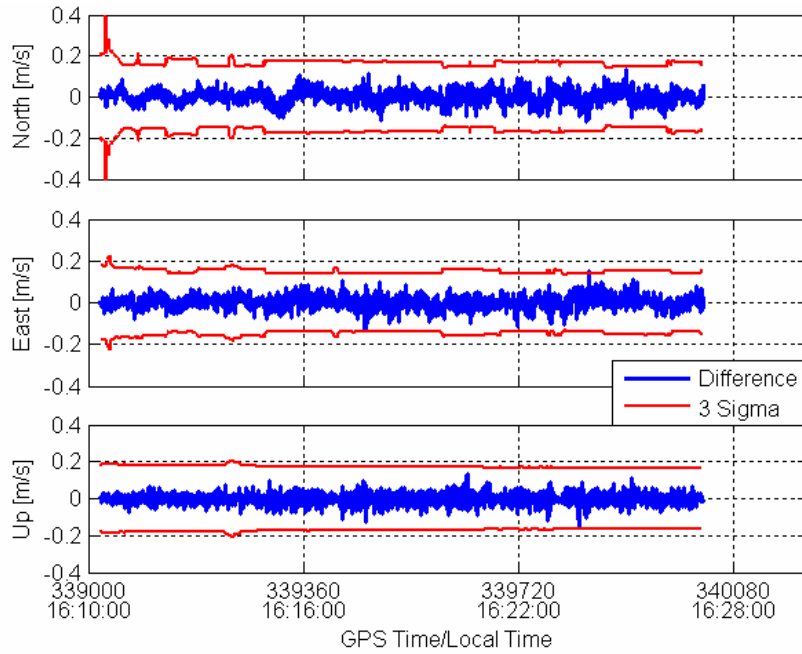
Figure 7.37 Velocity difference between GPS/Low cost IMU/WSS/SAS/GL/YRS and the reference solution for open-sky real-time test

Table 7.11 Statistics of the position and velocity differences between the GPS/Low cost IMU/WSS/SAS/GL/YRS and the reference solution (Open-sky real-time test)

Items	Mean			Standard deviation		
	North	East	Up	North	East	Up
Position difference [cm]	0.5	0.2	-0.5	3.4	3.5	2.5
Velocity difference [cm/s]	0.2	0.2	-0.2	2.9	2.8	2.4

7.3.3   Suburban Area – Real-time Test

For the real-time test in the suburban area, Figure 7.38 and Figure 7.39 show the detailed GPS information, which include the widelane carrier phase residuals with fixed ambiguities, baseline length, the pseudorange residuals, DOP values, the number of tracked satellites at the reference and rover stations (and their difference), as well as the number of fixed ambiguities. Since the widelane linear combination amplifies the noise, the widelane carrier phase residuals are larger (5 cm for the most part) than the L1 carrier phase residuals (1-2 cm for the most part) as shown in the open-sky test. The variable multipath in the suburban area adversely increases the pseudorange code residuals compared to that in the open-sky test. Some severe multipath scenarios lead to a maximum of 2 m pseudorange code residuals. Most of the horizontal DOPs are below two with several cases exceeding five. However, the GPS availability is far from ideal since dense foliage, underpasses and buildings near the road introduced partial and complete satellite masking. The satellite availability differences between the GPS reference and the rover stations indicate the level of GPS satellite masking. In Figure 7.39, for example, eight satellites are constantly tracked by the reference station Therefore, any

time when the difference of the satellite numbers overlaps with eight, it implies complete

satellite masking.
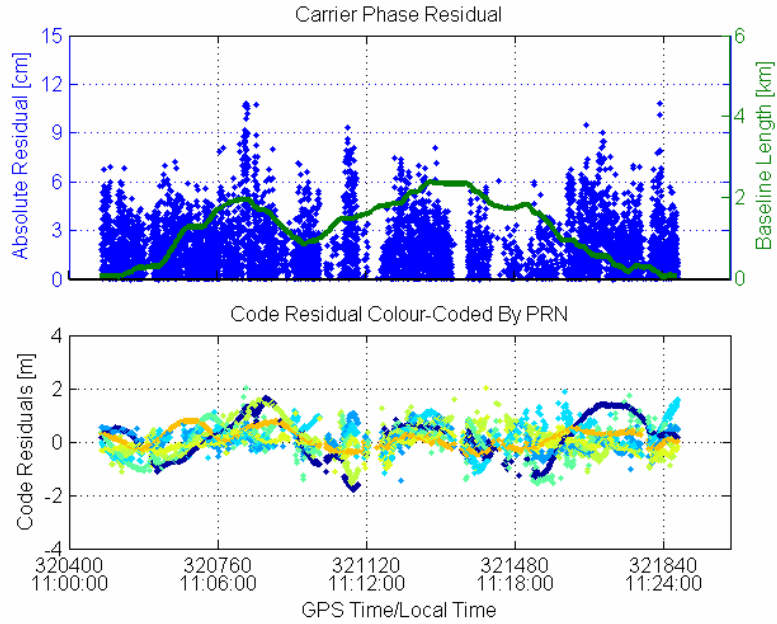
Figure 7.38 WL carrier phase and C/A code residuals (Suburban area real-time test)
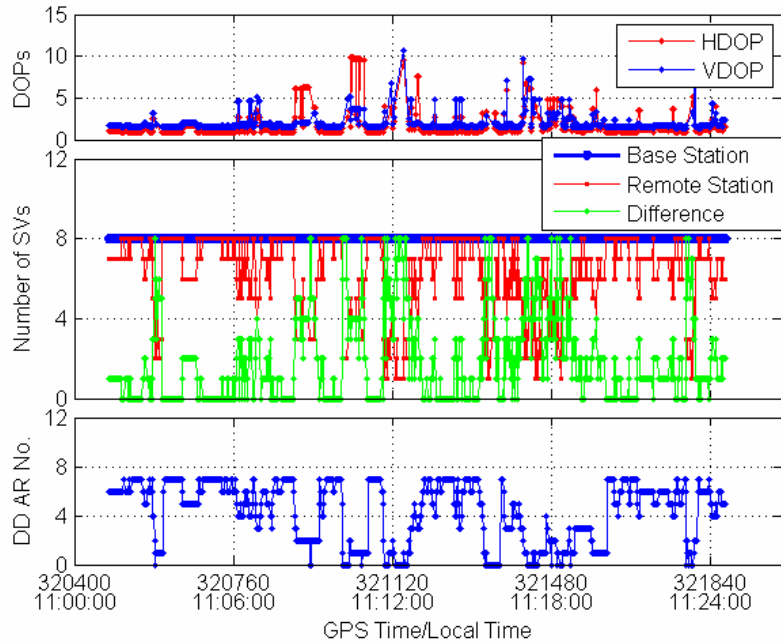
Figure 7.39 Satellite DOPs, satellite numbers and the fixed ambiguities numbers
(Suburban area real-time test)

Figure 7.40 shows the estimated GPS time latency during the test. Most of the latencies are on the order of 0.1-0.2 s with the maximum value being 0.4 s which indicates that the radio link was working well throughout the test. Since the time latency is far below the data buffer limit (3 s), the real-time and the post-mission solutions can be expected to be compatible.
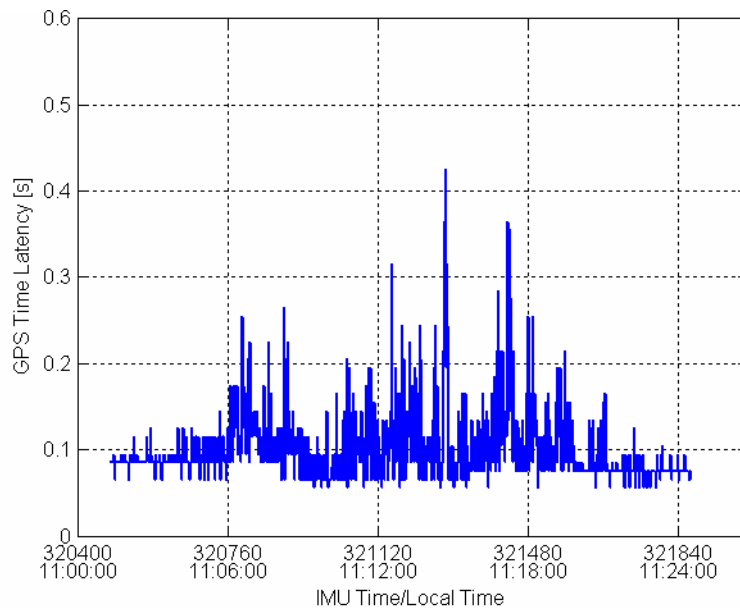
Figure 7.40 GPS time latency (Suburban area real-time test)

Figure 7.41 and Figure 7.42 indicate that the suburban area real-time test is associated with a relatively low vehicle dynamics including the vehicle velocity and attitude. Compared to the open-sky test conducted in the winter for post-mission processing, the side slip is less severe since the test was conducted in the summer time on a relatively flat road as shown in Figure 7.43. The side slip angles that are larger than 5 degrees are sparsely distributed around specific epochs at 321100 s, 321400 s and 321840 s, which are correlated with the vehicle turning operations.
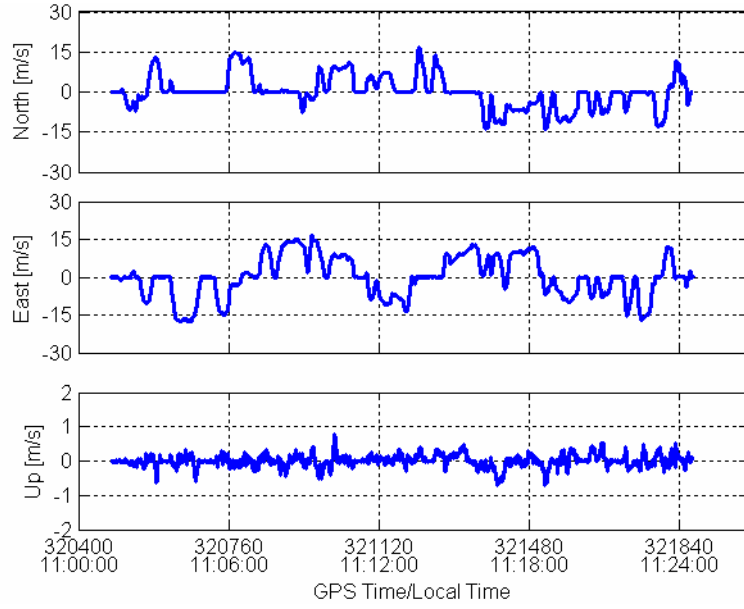
Figure 7.41 Vehicle velocity (Suburban area real-time test)
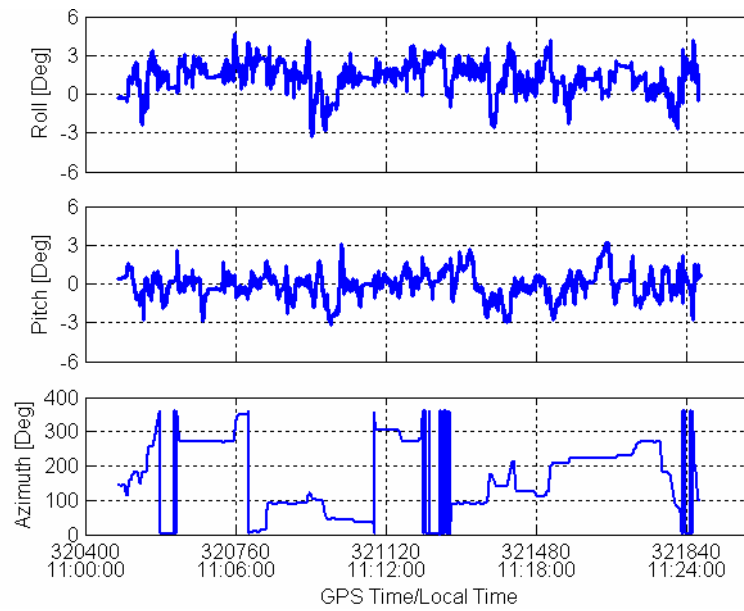
Figure 7.42 Vehicle attitude (Suburban area real-time test)
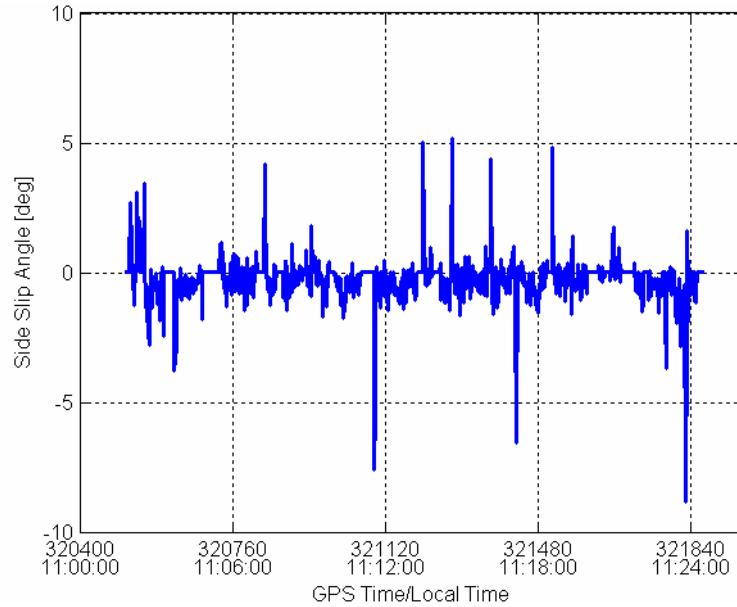
Figure 7.43 Vehicle side slip angle (Suburban area real-time test)

Figure 7.44 shows the reference trajectory generated by the GPS/CIMU integrated system with optimal backward smoothing. The map appeared on the plot comes from the database of Microsoft Map. Figure 7.45 and Figure 7.46 illustrate the estimated position and velocity accuracies for the reference solution. The estimated accuracy of the GPS/CIMU integrated solution with optimal smoothing is closely related to the GPS availability. When GPS is fully available, the estimated accuracy is comparable to that in open-sky conditions. However, the estimated accuracy is correlated to satellite masking, and relies heavily on the durations of the any outages. The longer the duration of the GPS blockage, the poorer the estimated accuracy it is. Nevertheless, due to the superior quality of the navigational grade CIMU, the worst case for the estimated accuracy is at the decimetre level (10-15 cm) for this test. Its accuracy is much higher than that in the low cost IMU integrated system.
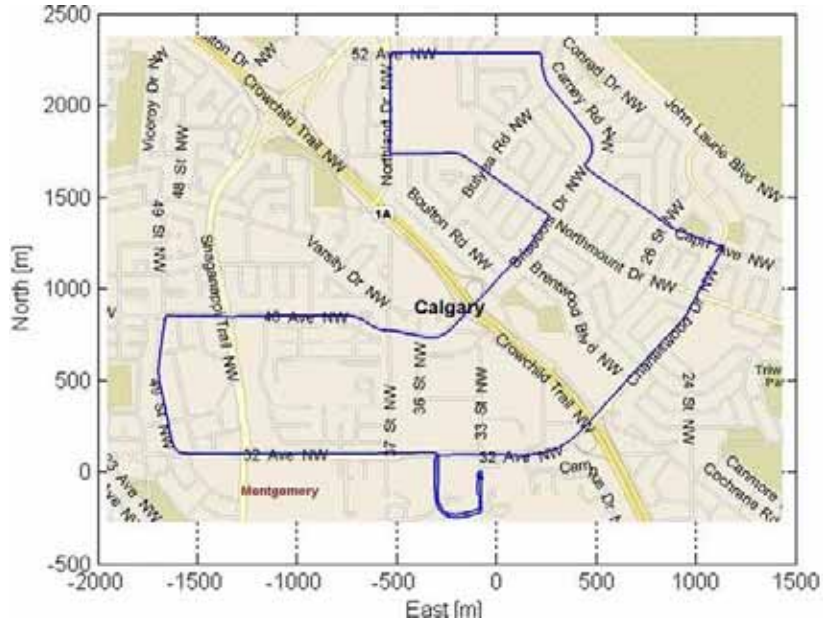
Figure 7.44 Reference trajectory generated by GPS/CIMU integrated solution (Suburban area real-time test)
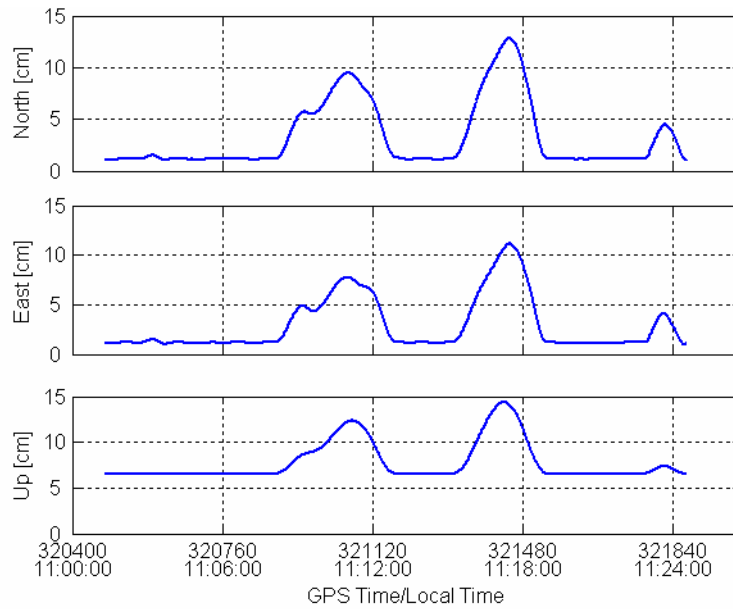
Figure 7.45 Estimated position RMS of the reference solution (Suburban area real-time test)
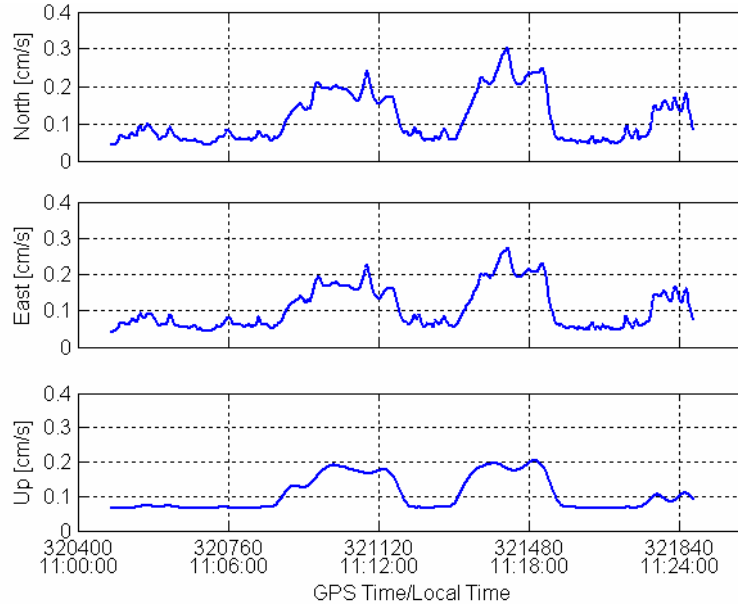
Figure 7.46 Estimated velocity RMS of the reference solution (Suburban area real-time test)

The position and velocity computed from both the GPS/Low cost IMU and GPS/Low cost IMU/WSS/SAS/GL/YRS integration strategies are compared with the reference solution. For the GPS/Low cost IMU integration strategy, Figure 7.47 and Figure 7.48 show the position and velocity differences respectively, along with the corresponding 3-sigma envelopes. Figure 7.49 and Figure 7.50 show the same plots for the GPS/Low cost IMU/WSS/SAS/GL/YRS integration strategy. Due to the well tuned Kalman filter, the actual differences and the estimated standard deviations are consistent at an acceptable level. When GPS is fully available, both the differences and the estimated standard deviations of the differences are very small. The actual differences and their estimated standard deviations increase significantly depending on the GPS outages and the duration of the outage, which can be seen from two specific epochs such as 321120 s and 321480 s. By comparing the two integration strategies, the aiding from all the

on-board vehicle sensors can significantly reduce the position and velocity drift of

stand-alone INS with the low cost IMU.
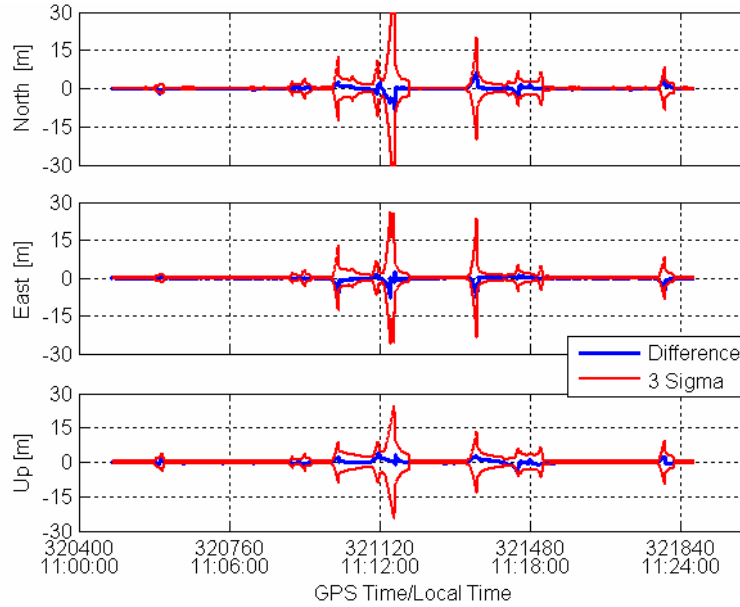
Figure 7.47 Position differences between GPS/Low cost IMU and the reference solution
(Suburban area real-time test)
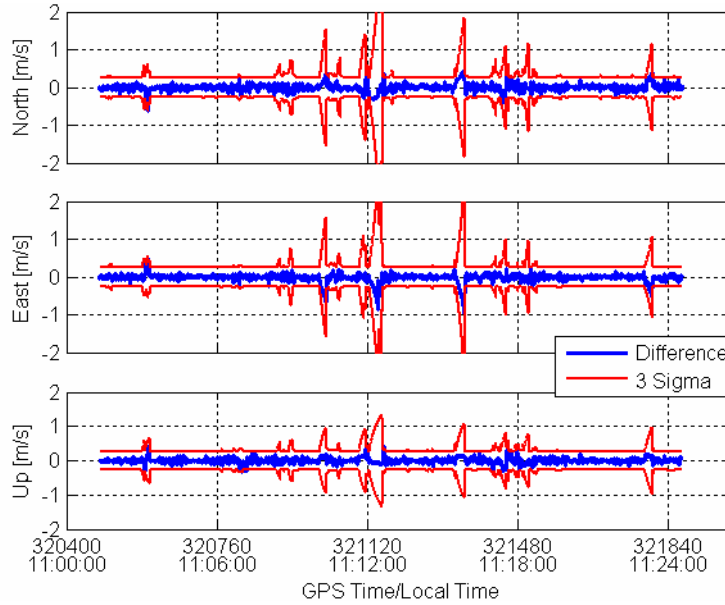
Figure 7.48 Velocity differences between GPS/Low cost IMU and the reference solution
(Suburban area real-time test)
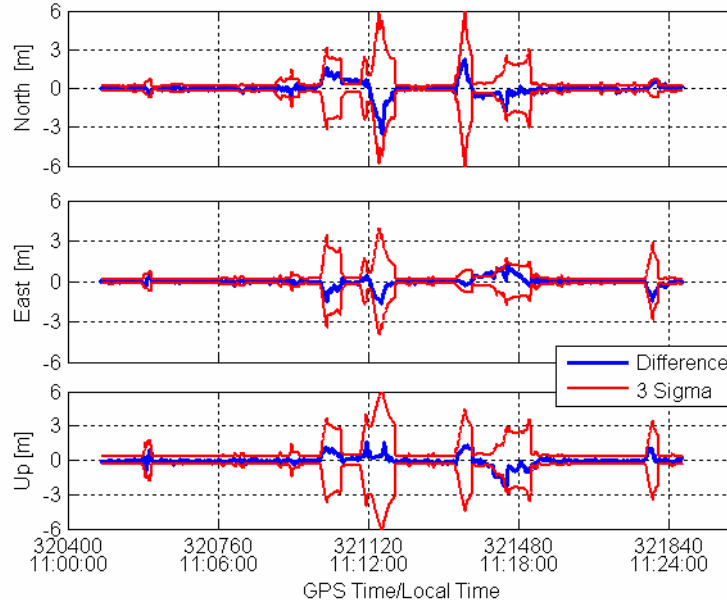
Figure 7.49 Position differences between GPS/Low cost IMU/WSS/SAS/GL/YRS and
the reference solution (Suburban area real-time test)
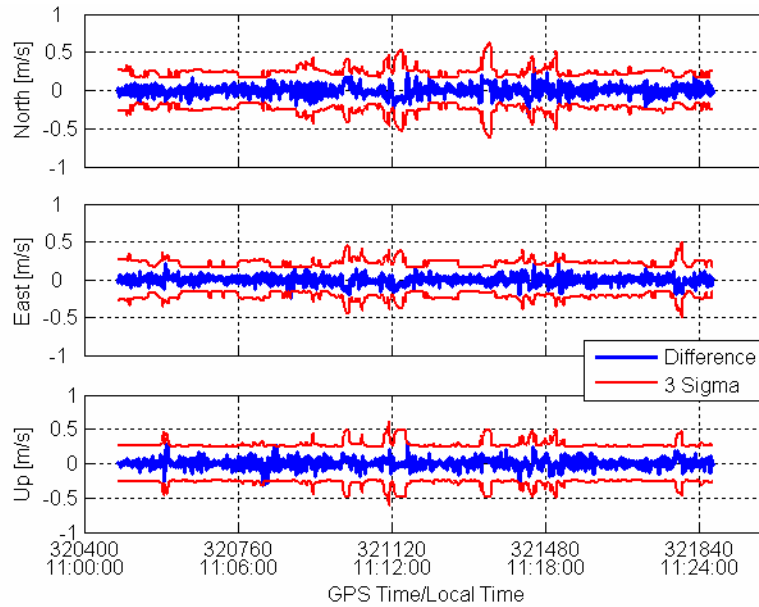
Figure 7.50 Velocity differences between GPS/Low cost IMU/WSS/SAS/GL/YRS and
the reference solution (Suburban area real-time test)

To detail the comparison of all the integration strategies, Figure 7.51 to Figure 7.53

compare the performance of all integration strategies on the same plot by investigating

the position differences in the horizontal, up and 3D directions. The velocity differences

for the different integration strategies and the associated estimated standard deviations of

the position and velocity differences are shown in Appendix C. For comparison purposes,

the results for both the tactical grade HG1700 IMU and the low cost IMU are analyzed.

The benefits gained from the on-board vehicle sensors on the stand-alone IMU (either the

low cost or tactical grade HG1700 IMU) is a significant reduction in the horizontal

position error. To be more specific, the horizontal position difference shown in Figure

7.51 at epochs 321120 s and 321320 s can be reduced from approximate 10 m with the

stand-alone low cost IMU to approximate 2-3 m by integrating all the sensors with the

low cost IMU. Due to a higher quality, the free-running HG1700 IMU drifts at a lower

rate than the low cost IMU. With external aiding on the HG1700 IMU from all the

on-board vehicle sensors, the horizontal position drift error can also be significantly

reduced from 5 m to less than 1 m at epoch 321120 s.

By zooming the horizontal positioning error between some epochs with a longer duration

of GPS outages, Figure 7.54 compares the horizontal positioning errors between different

integration strategies of the low cost IMU integrated system. On the same plot, the GPS

satellite HDOP is indicated by the black dots at a 1 Hz data rate. The discontinuity of the

HDOP output implies the satellite availability is less than four.
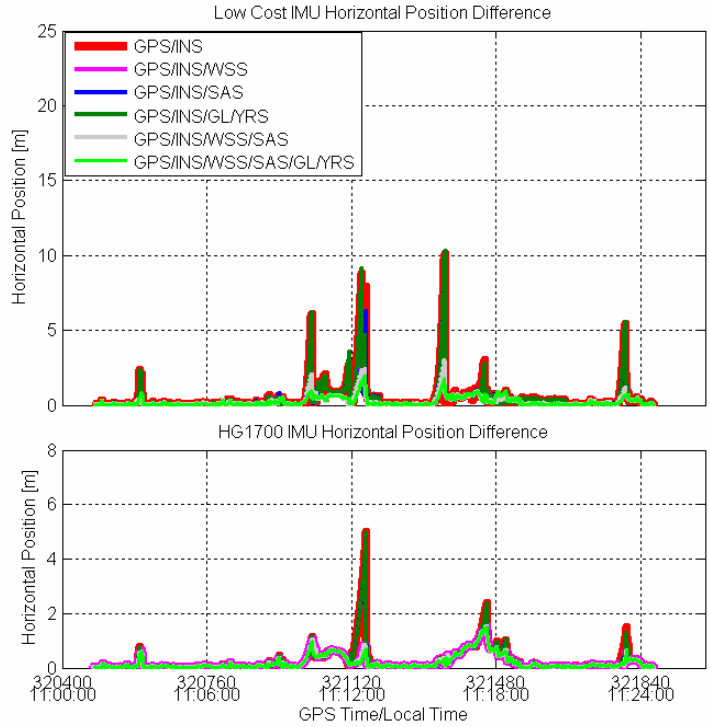
Figure 7.51 Horizontal differences of all integration strategies and the reference solution (Suburban area real-time test)
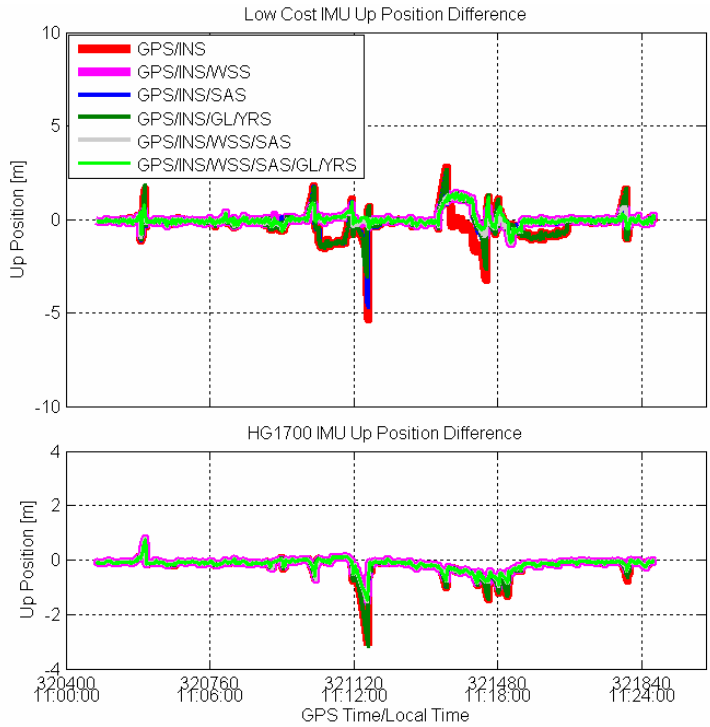
Figure 7.52 Up position differences of all integration strategies and the reference solution (Suburban area real-time test)
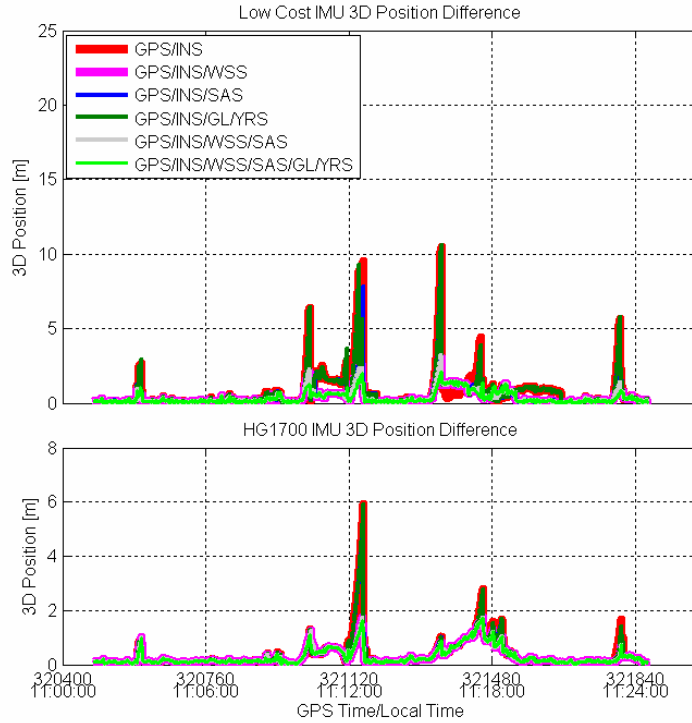
Figure 7.53 3D position differences of all integration strategies and the reference solution (Suburban area real-time test)
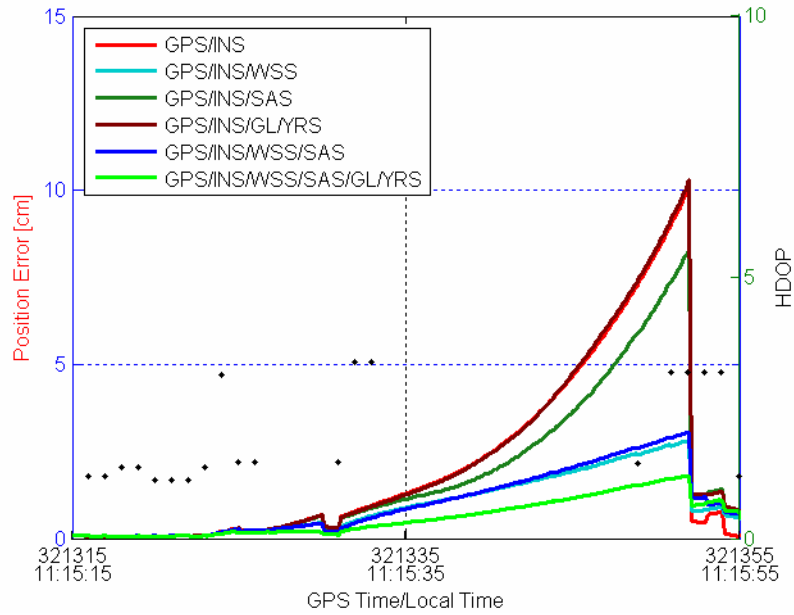

Figure 7.54 Zooming of horizontal position difference (Surban area real-time test)

Figure 7.55 compares the histograms of the positioning error for GPS/INS and GPS/INS/On-board vehicle sensors integration strategies with both the low cost IMU and the tactical grade IMU. Table 7.12 and Table 7.13 compare various integration strategies associated with two grades of IMUs statistically by computing their RMS position and velocity differences with respect to the reference solution. When GPS is fully available, GPS plays a dominant role that determines the absolute positioning accuracy of the system. During partial or complete satellite signal masking, any integration strategy that contains the wheel speed sensor has a relatively lower RMS difference. It implies that the wheel speed sensor is a key sensor to limit the position and velocity drift in the integrated system. This is mainly due to the fact that the wheel speed sensor provides an absolute velocity update at a high measurement accuracy. Furthermore, it performs a special function (ZUPT) to limit the drift error when the vehicle operates in static mode.
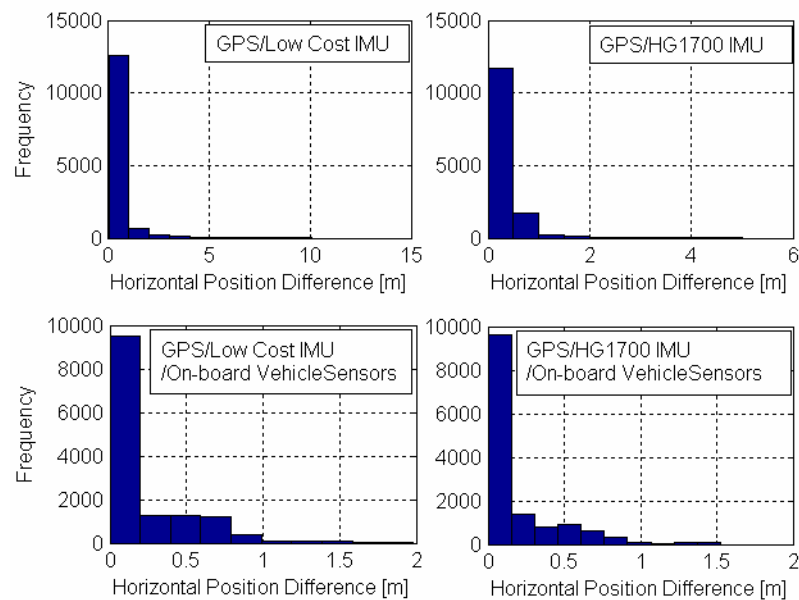
Figure 7.55 Histogram of horizontal position difference (Suburban area real-time test)

For the low cost IMU integrated system, the steering angle sensor can also benefit in the reduction of the position and velocity errors even though its improvement is less than the wheel speed sensor. In contrast to the wheel speed sensor that performs ZUPTs in static mode, the steering angle sensor does not work in static mode as the estimated steering angle derived from the velocity becomes undetermined at zero velocity. In kinematic mode, however, the steering angle sensor can constraint the velocity drift, and consequently limit the positioning error during partial and complete GPS outages.

With a relatively lower quality, the GL/YRS unit always provides a relative velocity update by retrieving its initial information from the integrated system every 1 second. Given the integrated system degrades at a rapid rate without external GPS aid, the benefit gained from GL/YRS is somewhat limited compared to WSS and SAS. However, if the side slip angle exceeds a specific threshold (5 degrees) to introduce a violation of the lateral constraint, the horizontal position accuracy can be further enhanced by using the G sensor and yaw rate sensor to remove the lateral constraint. Thus, the integration strategy that contains all the on-board vehicle sensors (GPS/INS/WSS/SAS/GL/YRS) performs best among all of the integration strategies. These results are consistent with the post-processed results for the open-sky kinematic test with simulated GPS outages.

Due to a relatively short duration of GPS masking in the suburban area as well as the relatively lower quality of the G sensors, yaw rate sensor and the steering angle sensor compared to the tactical grade HG1700 IMU, the benefits gained from the G sensors, yaw

rate sensor as well as the steering angle sensor on the HG1700 IMU integrated system

are somewhat limited compared to the low cost IMU integrated system.

Table 7.12 RMS position and velocity difference of all integration strategies and the
reference solution (Low cost IMU, Suburban area real-time test)

Strategy	RMS position difference [m]			RMS velocity difference [m/s]		
	Horizontal	UP	3D	Horizontal	UP	3D
GPS/INS	1.09	0.64	1.27	0.14	0.07	0.16
GPS/INS/WSS	0.48	0.36	0.60	0.08	0.06	0.09
GPS/INS/SAS	0.76	0.57	0.94	0.12	0.07	0.14
GPS/INS/GL/YRS	1.05	0.62	1.22	0.15	0.07	0.16
GPS/INS/WSS/SAS	0.47	0.36	0.59	0.07	0.06	0.09
GPS/INS/WSS/SAS /GL/YRS	0.38	0.35	0.51	0.06	0.05	0.08

Table 7.13 RMS position and velocity difference of all integration strategies and the
reference solution (HG1700 IMU, Suburban area real-time test)

Strategy	RMS position difference [m]			RMS velocity difference [m/s]		
	Horizontal	UP	3D	Horizontal	UP	3D
GPS/INS	0.53	0.40	0.67	0.03	0.02	0.04
GPS/INS/WSS	0.33	0.28	0.44	0.03	0.02	0.03
GPS/INS/SAS	0.51	0.39	0.65	0.03	0.02	0.04
GPS/INS/GL/YRS	0.53	0.40	0.66	0.03	0.02	0.04
GPS/INS/WSS/SAS	0.33	0.28	0.44	0.03	0.02	0.03
GPS/INS/WSS/SAS /GL/YRS	0.32	0.28	0.42	0.02	0.02	0.03

7.3.4 Pseudo-Urban Area – Real-time Test

For the real-time pseudo-urban area test, multipath is more severe than that in the open-sky and the suburban area. Consequently, some larger pseudorange residuals appear periodically. Figure 7.56 shows the carrier phase residuals, baseline length and pseudorange residuals. Most of the widelane carrier phase residuals were about 5 cm. Since the maximum baseline length was approximately 1 km, the main error sources in the carrier phase residuals are from multipath effects (Lachapelle 2003).

It is shown in Figure 7.57 that partial and complete GPS masking were more frequently encountered in the pseudo-urban area test because of the tall buildings, trees and underpasses. The masking duration was also longer than in the suburban area. The horizontal DOP was generally around two with some epochs exceeding five.
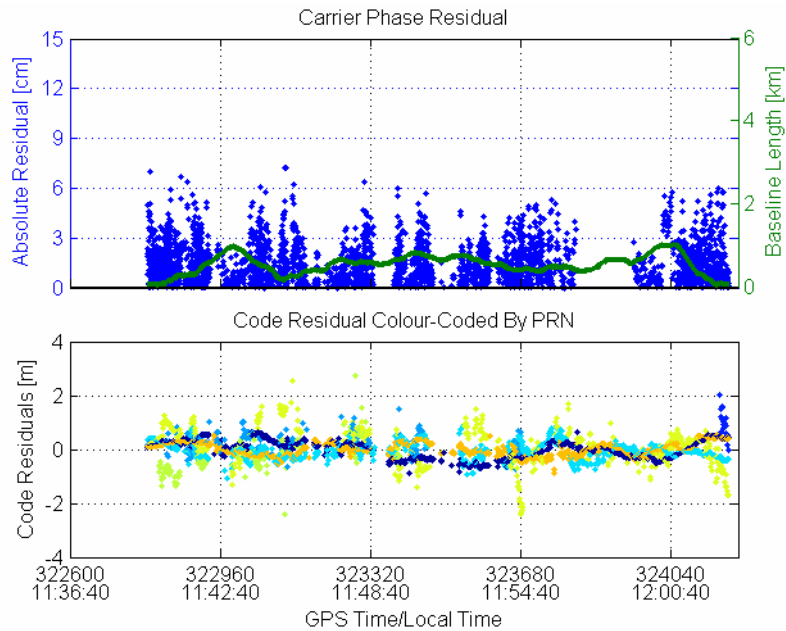
Figure 7.56 WL carrier phase residuals with fixed ambiguities and the code residuals
(Pseudo-urban area real-time test)
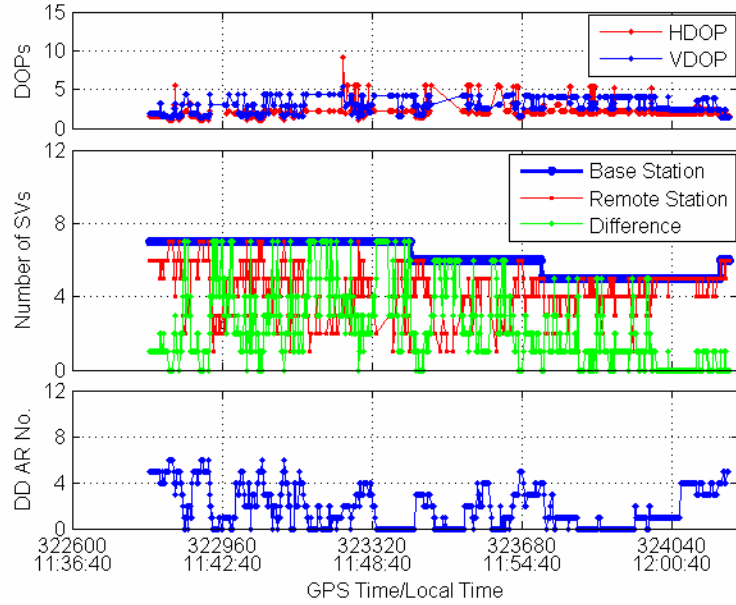
Figure 7.57 Satellite DOPS, satellite numbers and fixed ambiguity numbers
(Pseudo-urban area real-time test)

The GPS latencies with respect to the IMU time shown in Figure 7.58 are mostly on the

order of 0.1 s to 0.2 s with some on the order of 0.3 s to 0.5 s. It indicates that the radio

link transceiver and the real-time data collection system worked properly. Similar to the

open-sky and the suburban area tests, the real-time system generates the same solution as

that processed in post-mission since the GPS time latencies are far less than the time limit

(3 s) that the data buffer can accommodate.
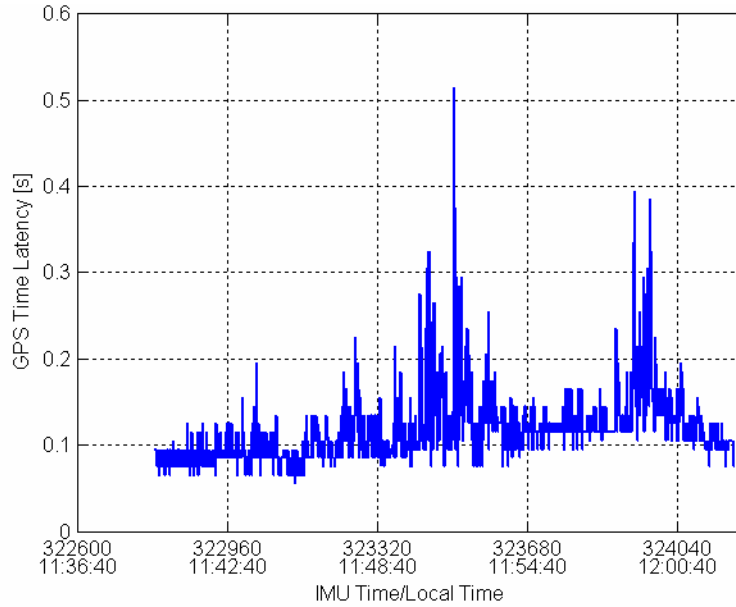
Figure 7.58 GPS latencies (Pseudo-urban area real-time test)

The vehicle velocity, attitude as well as the side slip angle during the entire pseudo-urban area real-time test are given in Figure 7.59 to Figure 7.61. The vehicle operated on a flat road in the summer time where the maximum pitch and roll angles were less than 5 degrees, and the maximum velocity was less than 15 m/s (54 km/h). It implies relatively low vehicle dynamics. More frequent vehicle turning in the pseudo-urban area leads to a maximum side slip angle of 8 degrees that are more densely distributed across the entire test than that in the suburban area test with more than 5 degree side slip angles distributed around three different epochs.
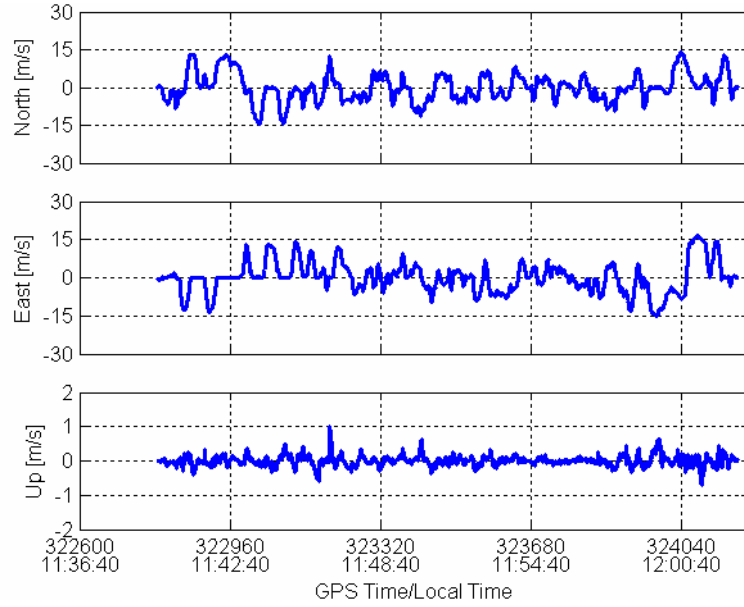
Figure 7.59 Vehicle velocity (Pseudo-urban area real-time test)
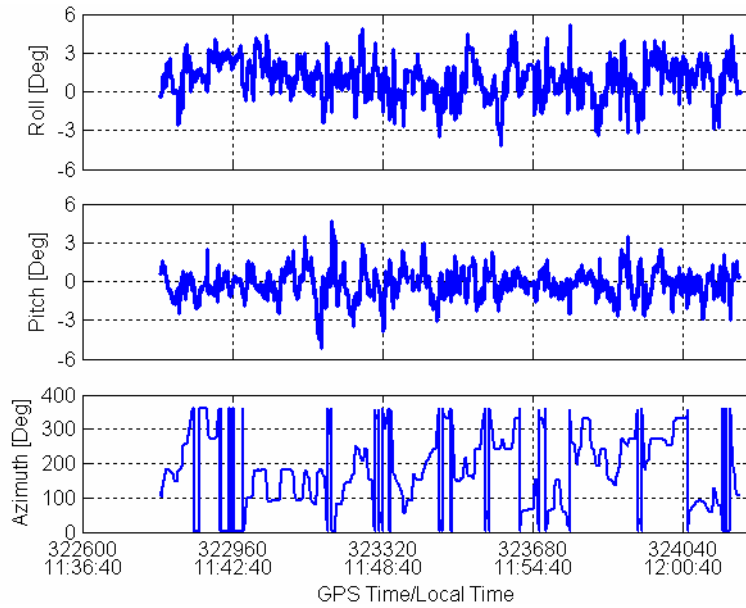
Figure 7.60 Vehicle attitude (Pseudo-urban area real-time test)
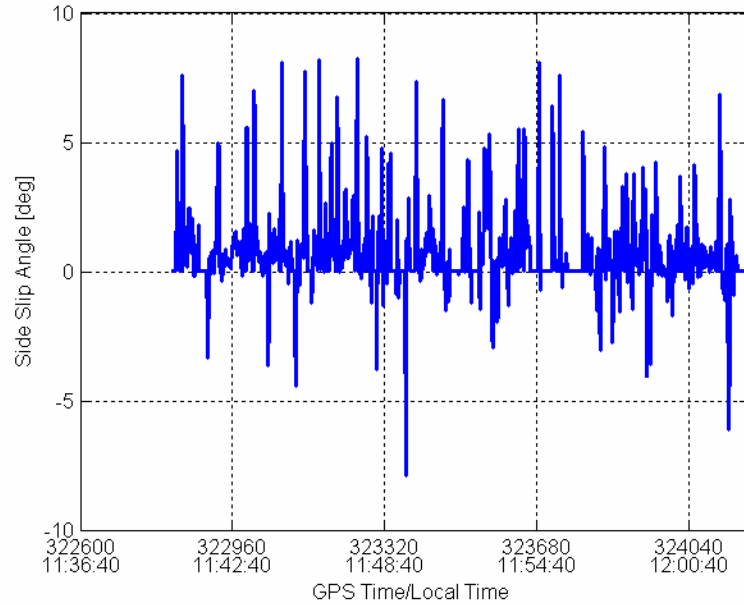
Figure 7.61 Vehicle side slip angle (Pseudo-urban area real-time test)

Figure 7.62 shows the reference trajectory generated by the GPS/CIMU integrated system. It can be seen from Figure 7.63 and Figure 7.64 that the position and velocity accuracies for the GPS/CIMU integrated solution was lower than that in the suburban area due to the more severe satellite masking and the longer duration of the masking. However, even in the worst cases, the position accuracy is still at the decimetre level, and the velocity is at the centimetre per second level.
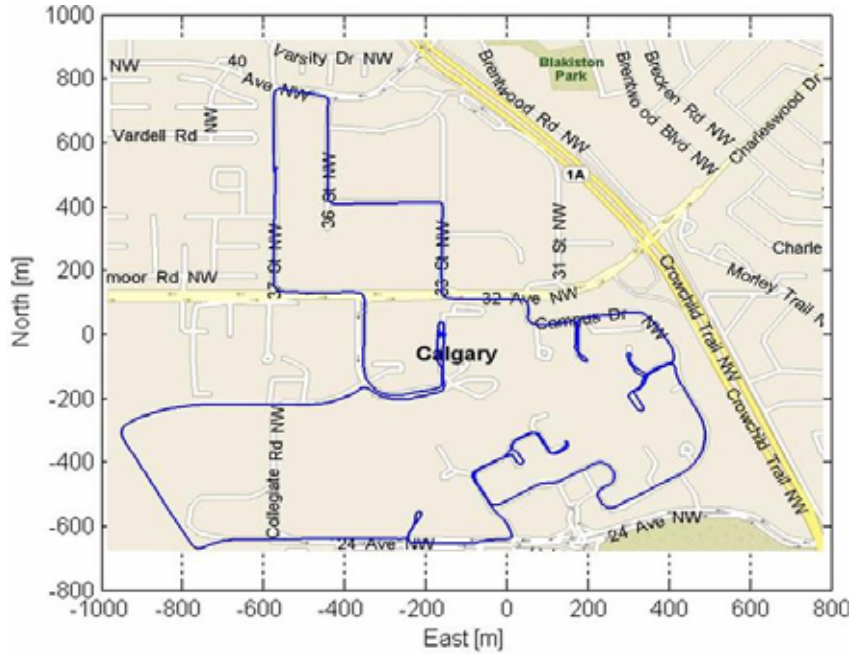
Figure 7.62   Reference trajectory generated by GPS/CIMU (Pseudo-urban area real-time test)
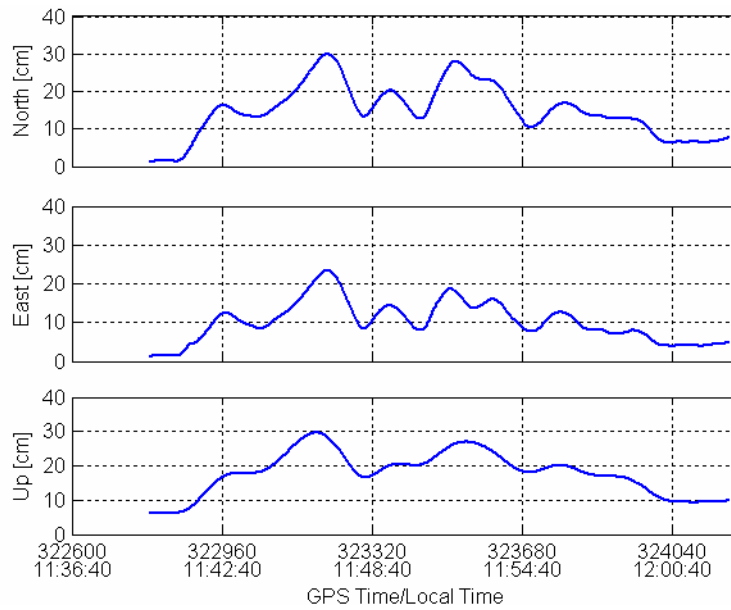
Figure 7.63 Estimated position RMS of the reference (Pseudo-urban area real-time test)
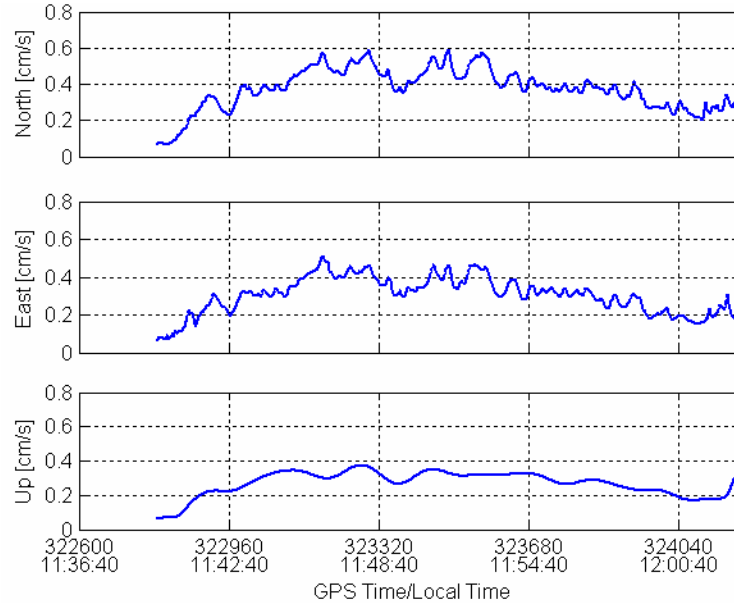
Figure 7.64 Estimated velocity RMS of the reference solution (Pseudo-urban area real-time test)

Similar to the analysis in the suburban area test, Figure 7.65 to Figure 7.68 are the position and the velocity differences of the GPS/Low cost IMU and GPS/Low cost IMU/WSS/SAS/GL/YRS systems with respect to the reference solution, along with the corresponding 3-sigma envelopes. Most of the position and the velocity differences of these two integration strategies fall within the 3-sigma range, as expected. Comparing to the suburban area test, the position and velocity drift errors are larger (maximum of approximately 15 m in the horizontal direction) for the low cost IMU system without any external aiding from GPS and the on-board vehicle sensors. On the other hand, the integration of the on-board vehicle sensors with the low cost IMU can also significantly reduce the position from 15 m to 1.5 m.
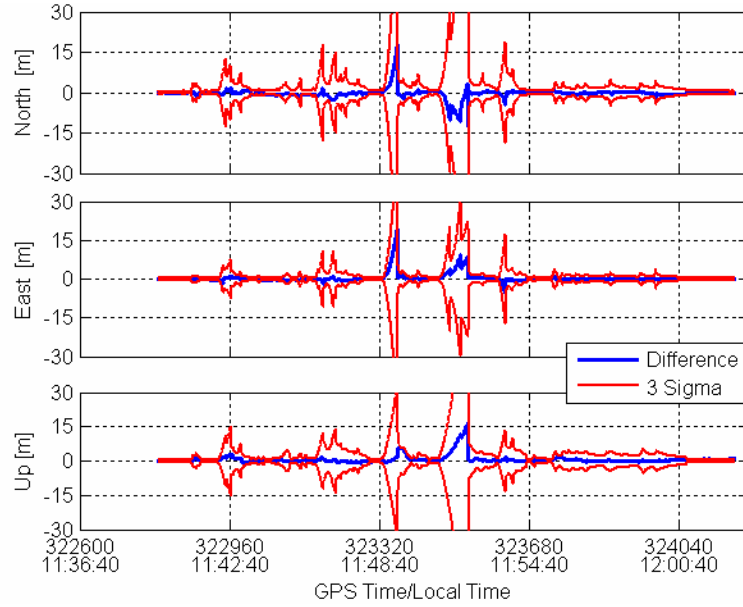
Figure 7.65 Position differences between GPS/Low cost IMU and the reference solution
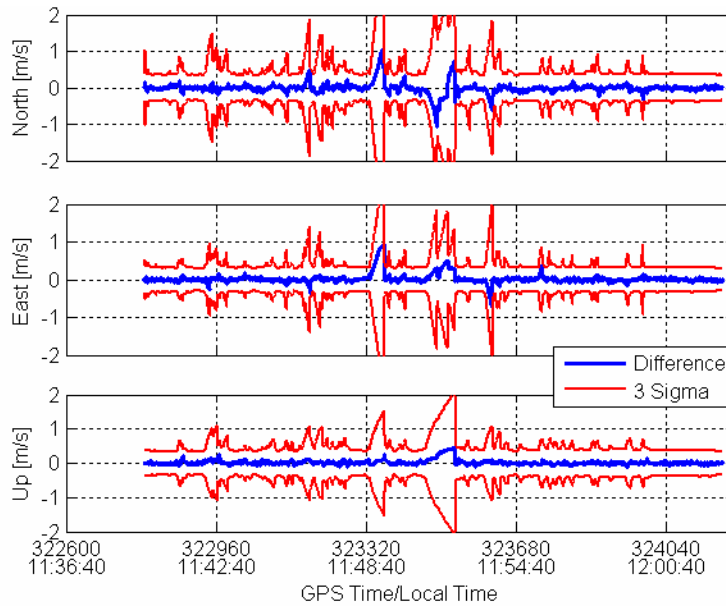(Pseudo-urban area real-time test)

Figure 7.66 Velocity differences of GPS/Low cost IMU and the reference solution
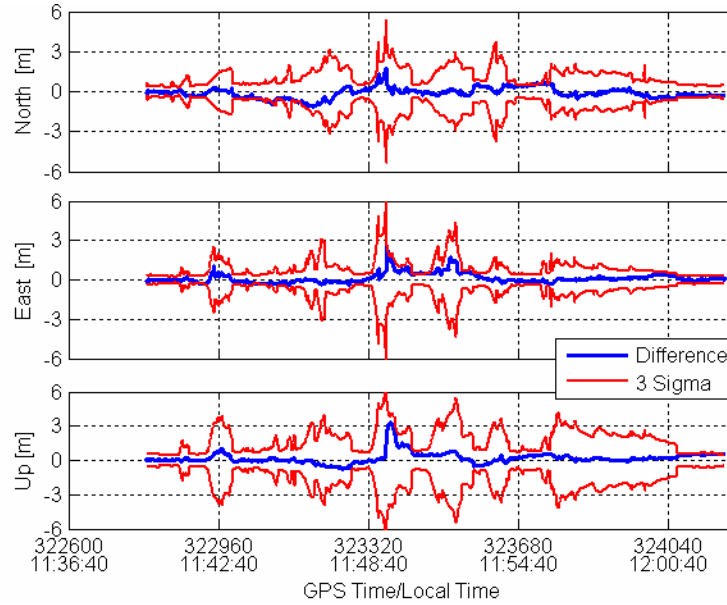(Pseudo-urban area real-time test)

Figure 7.67 Position differences of GPS/Low cost IMU/WSS/SAS/GL/YRS and the reference solution (Pseudo-urban area real-time test)
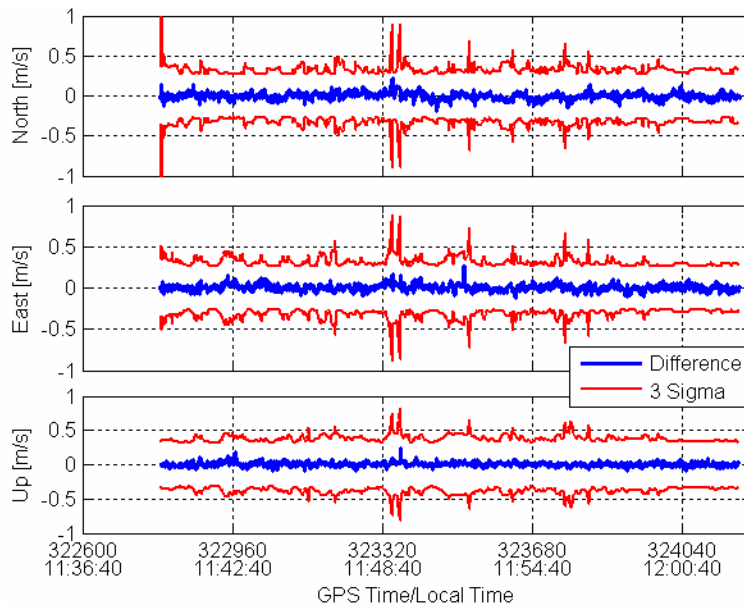

Figure 7.68 Velocity differences of GPS/Low cost IMU/WSS/SAS/GL/YRS and the reference solution (Pseudo-urban area real-time test)

Figure 7.69 to Figure 7.71 compare the position differences in the horizontal, up and 3D directions for all integration strategies. The velocity differences along with the estimated standard deviation of the position/velocity differences (1-sigma) in the horizontal, up and

3D directions for all integration strategies are shown in Appendix C. Figure 7.72

emphasizes the horizontal position error for the low cost IMU integrated system within a

longer duration of the GPS outage. Figure 7.73 shows the histograms of the horizontal

position error of the GPS/INS and GPS /INS/On-board vehicle sensor integration

strategies for both the low cost and tactical grade IMUs. Table 7.14 and Table 7.15

summarize the RMS of the position and velocity differences for all the integration

strategies in terms of the low cost IMU and the tactical grade HG1700 IMU, respectively.

During masking of the GPS satellite signals, the performance of either low cost IMU or

HG1700 IMU system without external aiding from the on-board vehicle sensors degrades

more severely than that in the suburban area. The improvement on the positioning

accuracy of the low cost IMU integrated system gained from the on-board vehicle sensor

is more significant and more evident than the tactical grade HG1700 IMU integrated

system. Among all the on-board vehicle sensors, the wheel speed sensor contributes the

most, with the steering angle sensor as the second, and the benefits from the G sensor and

yaw rate sensor being somewhat limited. However, using a mechanism for the detection

and alleviation of the lateral non-holonomic constraint violation, the

GPS/INS/WSS/SAS/GL/YRS integration strategy performs best among all the integration
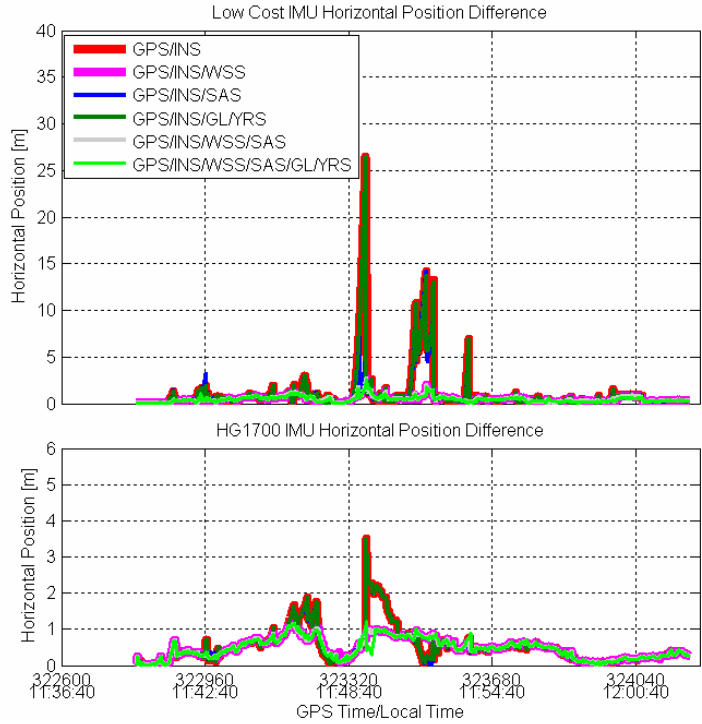
strategies.

Figure 7.69 Horizontal position differences of all integration strategies (Pseudo-urban area real-time test)
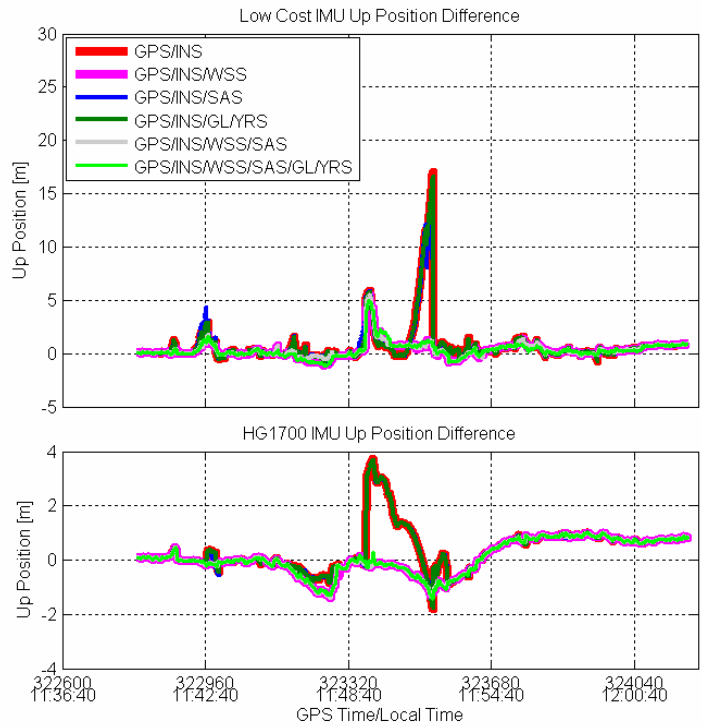

Figure 7.70 Up position differences for all integration strategies (Pseudo-urban area real-time test)
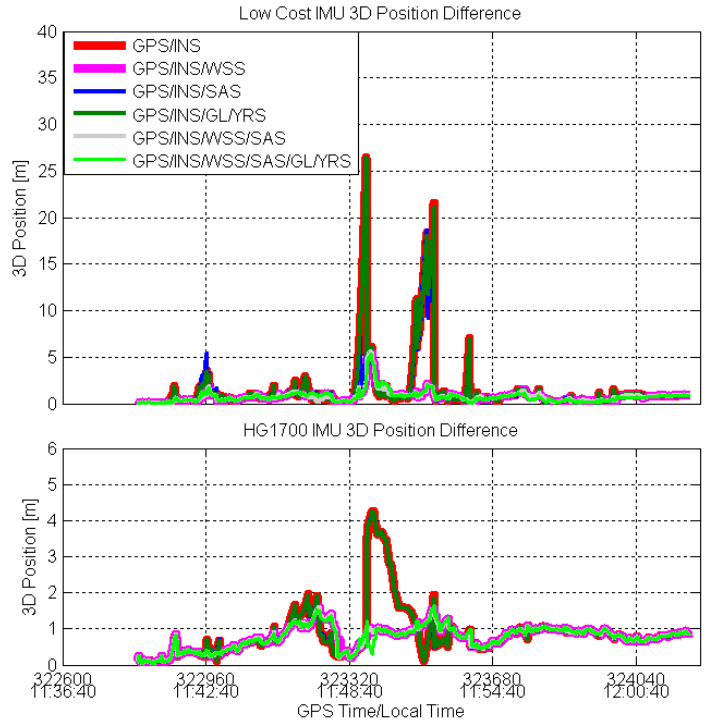
Figure 7.71 3D position differences of all integration strategies (Pseudo-urban area real-time test)
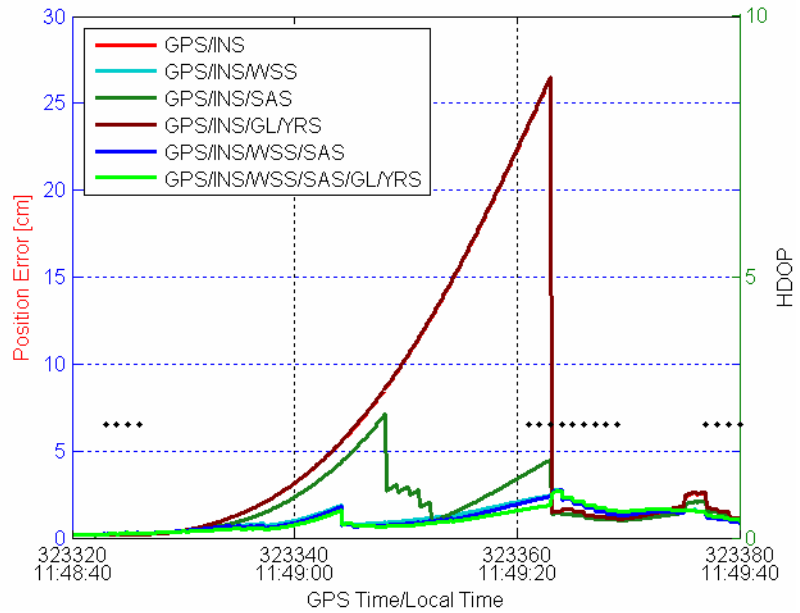

Figure 7.72 Zooming of horizontal position difference for low cost IMU integrated system (Pseudo-urban area real-time test)
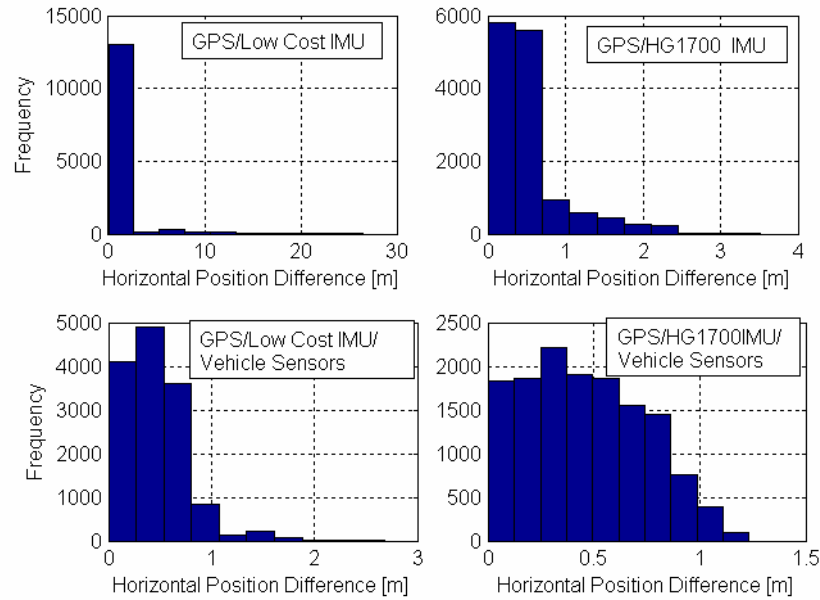
Figure 7.73 Histogram of horizontal position difference (Pseudo-urban area real-time test)

Table 7.14 RMS position and velocity differences of all integration strategies and the reference solution (Low Cost IMU, Pseudo-urban area real-time test)

Strategy	RMS position difference [m]			RMS velocity difference [m/s]		
	Horizontal	UP	3D	Horizontal	UP	3D
GPS/INS	2.60	2.03	3.30	0.21	0.08	0.22
GPS/INS/WSS	0.58	0.83	1.02	0.06	0.03	0.07
GPS/INS/SAS	1.76	1.88	2.58	0.16	0.08	0.18
GPS/INS/GL/YRS	2.58	2.03	3.29	0.21	0.08	0.22
GPS/INS/WSS/SAS	0.57	0.82	1.00	0.06	0.03	0.07
GPS/INS/WSS/SAS /GL/YRS	0.54	0.82	0.98	0.05	0.03	0.06

Table 7.15 RMS position and velocity differences of all integration strategies and the
reference solution (HG1700 IMU, Pseudo-urban area real-time test)

Strategy	RMS position difference [m]			RMS velocity difference [m/s]		
	Horizontal	UP	3D	Horizontal	UP	3D
GPS/INS	0.71	0.89	1.14	0.02	0.02	0.03
GPS/INS/WSS	0.55	0.62	0.83	0.02	0.01	0.03
GPS/INS/SAS	0.71	0.89	1.14	0.02	0.03	0.03
GPS/INS/GL/YRS	0.71	0.89	1.14	0.02	0.02	0.03
GPS/INS/WSS/SAS	0.54	0.62	0.83	0.02	0.01	0.03
GPS/INS/WSS/SAS /GL/YRS	0.53	0.62	0.82	0.02	0.01	0.03

7.3.5 Summary

It is consistently illustrated by all the tests that GPS plays a dominant role in determining

the absolute positioning accuracy of the system when double differenced GPS availability

is more than two. During GPS outages, the positioning accuracy can be enhanced by the

integration of on-board vehicle sensors. The wheel speed sensor is a key sensor to limit

the horizontal position drift error. The steering angle sensor is the second best sensor that

can moderately limit the positioning error drift. The improvement from G sensors and

yaw rate sensor is somewhat limited than the wheel speed sensor and the steering angle

sensor. However, when the lateral constraint is violated, the positioning accuracy can be

further enhanced by alleviating the violation of the lateral constraint with an interactive

relationship between WSS and GL/YRS. The integration strategy that contains all

on-board vehicle sensors performs best among all the proposed integration strategies. A

faster ambiguity resolution can be expected from INS/On-board vehicle sensor system

with respect to the stand-alone INS system.

Chapter 8   Conclusions and Recommendations

The goal of this research has been to develop a land vehicle positioning and navigation system at low cost and with high accuracy. To bridge GPS gaps and limit the drift error of a stand-alone INS, several on-board vehicle sensors are integrated with GPS and a low cost IMU. The on-board vehicle sensors are built-in the vehicle stability control system of an actual vehicle. To make full use of the built-in sensors and improve the positioning accuracy to a larger degree, the on-board vehicle sensors used in this research include wheel speed sensors, G sensors (accelerometers), a yaw rate sensor as well as a steering angle sensor.

Based on an analysis of the characteristics of the on-board vehicle sensors, three basic and two combined integration strategies and algorithms are developed. The basic integration module that integrates the steering angle sensor with GPS and INS is novel. The combined integration strategy that contains all on-board vehicle sensors creates an interactive relationship between the wheel speed sensors, G sensors and yaw rate sensor. A mechanism is developed to detect and alleviate the violation of a lateral non-holonomic constraint by using the interactive relationships between different sensors.

A hardware platform is set up by composing GPS receivers, a low cost IMU and on-board vehicle sensor time-tagging system, a pair of radio link transceivers and antennas and computers. The integration strategies and algorithms are implemented in post-mission

and real-time. Test results imply significant benefits in terms of positioning accuracy and ambiguity resolution can be gained through external aiding of the on-board vehicle sensors on INS.

The following summarizes the results of this dissertation and presents recommendations for future work.

8.1   Conclusions

The integration of on-board vehicle sensors can enhance the horizontal positioning accuracy during GPS outages, and reduce the time to fix GPS ambiguities after GPS outages. The benefits gained on the horizontal positioning accuracy and the ambiguity resolution is dependent on the performance or the measurement accuracy of the on-board vehicle sensors. The major conclusions are summarized below.

1. Performance of on-board vehicle sensors

The measurement accuracy of wheel-speed sensors is at 3-5 cm/s level. The wheel speed sensor has a capability of detecting zero velocity in static mode. As their limitations, the wheel speed sensors are susceptible to the change of the actual tire rolling radius as well as the side slips.

Similar to the grade and quality of the low cost IMU used in this research, the G sensors/Yaw rate sensor constitutes a two-dimensional automotive grade inertial unit.

GL/YRS unit provides a possible way to detect and alleviate negative impact of the side slip on the performance of the wheel speed sensor.

The scale factor and bias are main error sources of the steering angle sensor. The measurement accuracy of the steering angle sensor can be either empirically determined by tuning the Kalman filter or indirectly estimated from the measurement accuracy of wheel speed sensor and yaw rate sensor.

2. Positioning accuracy

It is consistently illustrated by all the tests that GPS plays the dominant role in determining the absolute positioning accuracy of the system, and the solution of the integrated system is accurate to be 2-3 centimetre level when GPS is fully available.

The wheel speed sensor provides absolute velocity update with relatively high measurement accuracy as well as ZUPT in static mode. Due to these characteristics, the wheel speed sensor can limit the velocity and consequently the position error drift of the free-running INS system during GPS outages. The wheel speed sensor is a key sensor to limit the horizontal position drift error. With respect to horizontal positioning accuracy, the percentage improvements from the wheel speed sensor over GPS and low cost IMU integrated system are 90.4% for the open-sky test (post-mission processing with 12 simulated GPS outages), 56.0% for suburban area real-time test and 77.7 % for pseudo-urban area real-time test, respectively.

The steering angle can be observed from the velocity in kinematic mode. Consequently, the steering angle sensor can create a constraint on velocity. The steering angle sensor is the second best sensor that can moderately limit the positioning error drift. Over GPS and low cost IMU integrated system, the percentage improvements on the horizontal positioning accuracy from the steering angle sensor are 52.8% for the open-sky test (post-mission processing with 12 simulated GPS outages), 30.3% for suburban area real-time test and 32.3 % for pseudo-urban area real-time test, respectively.

With a relatively lower quality, the automotive grade GL/YRS unit performs relative velocity update. Hence, the improvement from G sensors and yaw rate sensor is less significant than the wheel speed sensor and the steering angle sensor. The percentage improvements on the horizontal positioning accuracy from GL/YRS unit are only 18.0% for the open-sky test (post-mission processing with 12 simulated GPS outages), 3.7% for suburban area real-time test and 0.8% for pseudo-urban area real-time test, respectively.

The combined integration strategy with all on-board vehicle sensors performs best among all the proposed integration strategies. This strategy performs WSS and SAS update in a sequential way given the steering angle sensor and wheel speed sensor provide fundamentally independent measurements. More external updates on Kalman filter yield a better estimation of the navigation information. The positioning accuracy can be further enhanced by detecting and alleviating the violation of the lateral constraint with an interactive relationship between WSS and GL/YRS. Over GPS and low cost IMU

integrated system, its percentage improvements on the horizontal positioning accuracy are 92.6% for the open-sky test (post-mission processing with 12 simulated GPS outages), 65.1% for suburban area real-time test and 79.2% for pseudo-urban area real-time test, respectively.

GPS is a still a driving factor that determines the absolute system accuracy when two or three double differenced satellites are available. The horizontal position RMS error is at the decimetre level for the low cost IMU integrated system, and is at the centimetre level for the HG1700 tactical grade IMU integrated system. One double differenced satellite can still improve the horizontal positioning accuracy over full GPS outage by 6.3% for low cost IMU and by 17.3% for the tactical grade IMU integrated system, respectively. With external aid from all on-board vehicle sensors, horizontal positioning accuracy can be further improved on the basis of one double differenced GPS satellite by 93.1% for low cost IMU and by 67.9% for tactical grade IMU.

The well tuned Kalman filter is implied by a good agreement between actual RMS error and the average estimated standard deviation in the open-sky test processed in post-mission with simulated GPS outages. In all real-time tests, most actual position errors occur within a 3 Sigma (estimated standard deviation) boundary.

3. Ambiguity resolution

With a shorter duration of GPS outage and a higher quality IMU, the stand-alone INS or INS/On-board vehicle sensor system outperforms the GPS-only strategy given that its

estimated standard deviation of the position error state is smaller than the position standard deviation of differential C/A code solution. For a longer duration of GPS outages or a lower quality of IMU, the benefits gained from stand-alone INS or INS/On-board vehicle sensor are expected to be somewhat limited. A faster ambiguity resolution can be expected from the INS/On-board vehicle sensor system over the stand-alone INS system.

The low cost IMU reduces the average time to fix ambiguity to a much smaller degree than that of the tactical grade IMU. With a 20 s GPS outage, 42.9% and 12.0% percentage improvement over GPS-only can be gained from stand-alone tactical grade and low cost IMUs, respectively. For a 40 s GPS outage, the percentage improvement over GPS-only by integrating all on-board vehicle sensors with tactical grade IMU and low cost IMU are 15.5% and 14.6%, respectively.

8.2   Recommendations

1. Use fuzzy logic theory to detect the violation of the lateral non-holonomic constraint

In this research, a predefined threshold of side slip angle was used to detect the violation of the lateral non-holonomic constraint. The detection result is sensitive to the definition of the side slip angle threshold. To be more robust, the fuzzy logic theory can be considered as an alternative.

2. Develop the low cost GPS and on-board vehicle sensor integrated system

In the land vehicle positioning system, the two dimensional horizontal positioning information is a main concern when the vehicle operates on a flat road. In a system that requires meter level accuracy and an extremely lower cost, a two dimensional land vehicle positioning system can be developed by integrating GPS with the dead-reckoning on-board vehicle sensors in two ways, namely GPS/Wheel speed sensor/Yaw rate sensor as well as GPS/G sensors/Yaw rate sensor. Without IMU, system costs can be reduced to a large degree.

3. In-motion alignment

It is difficult for the low cost IMU to align the heading or azimuth in static mode due to the rapid drift error and the large uncertainty of the vertical gyro. Furthermore, it is not feasible to initialize the INS in static mode for a certain period of time before starting the land vehicle positioning system. To increase system flexibility, it is necessary to investigate in-motion alignment by dealing with large heading uncertainty.

4. Make use of vehicle dynamic model to aid INS or on-board vehicle sensor

The vehicle dynamic model describes the relationship between the driving force, mass, moment of inertia, velocity, acceleration and angular rate based on Newton's law. It can work as an external aid for INS or on-board vehicle sensors to extend periods of high accuracy performance when GPS is not available.

5. Use high sensitivity GPS receiver and map-mapping technique

The GPS receiver used in this research was the dual frequency NovAtel OEM4 receiver. Its high price constitutes a major limitation for an extensive commercial application in land vehicle positioning systems. The development of an integrated system with a low cost high sensitivity GPS receiver, map-mapping module, a low cost IMU and/or on-board vehicle sensors can be considered. The high sensitivity GPS receiver can reduce the cost and increase the GPS availability in the urban area. With auxiliary information from the map-mapping module, a better estimation of the navigation information can be given.

6. Simulate more realistic GPS outages

In the open-sky area with a good GPS signal, it is an ideal case to simulate 12 GPS outages with 40 s durations. To be more realistic and typical, it is necessary to simulate more GPS outages with much longer outage duration as well as with attenuated or deteriorated GPS signals.

7. Long baseline length

The maximum baseline length in this research is around 4 km. This kind of short baseline length is not enough for the real application. The increase of baseline length will not only increase the magnitude of GPS errors, but also increase the complexity of GPS ambiguity resolution. The assessment of effects of longer baseline length is required.

8. Use on-board vehicle sensor to aid GPS signal tracking

As INS can aid GPS signal tracking inside GPS receivers by ultra-tight coupling strategy, it is also reasonable to make use of on-board vehicle sensors or INS/On-board vehicle sensors to aid GPS signal tracking.

9. Unscented Kalman filter (UKF) and adaptive Kalman filter

The Kalman filter implemented in this research is a standard extended Kalman filter. An extensive investigation and comparison of various Kalman filters, such as unscented Kalman filter and adaptive Kalman filter, will be helpful for the design of a more robust navigation system in terms of specific applications.

REFERENCES

Anderson, R. and D. M. Bevly (2004) "Estimation of Slip Angles Using a Model Based Estimator and GPS" in *Proceedings of the American Control Conference*. Boston, Massachusetts, pp. 2122-2127.

Bevly, D.M.(1999) "Evaluation of a Blended Dead Reckoning and Carrier Phase Differential GPS System for Control of an Off-Road Vehicle" in *Proceedings of ION GPS 1999*, September, Nashville TN, pp. 2061-2069, U.S. Institute of Navigation, Fairfax, VA, USA

Bevly, D.M.(2001) *High Speed, Dead Reckoning and Towed Implement Control for Automatically Steered Farm Tractors Using GPS*, Ph.D Thesis, Stanford University, USA.

Bisnath, S. and D Kim (2001) "A New Approach to an Old Problem Carrier-Phase Cycle Slips" in *GPS World*, May 2001, pp 46-51.

Brandit, A. and J.F. Gardner (1998) "Constrained Navigation Algorithms for Strapdown Inertial Navigation Systems with Reduced Set of Sensors" in *Proceedings of the American Control Conference*, Philadelphia, PA, pp. 1848-1852.

Bonnifait, P.H. (2003) "Fusion of Redundant ABS Sensors", *The Journal of Navigation, The Royal Institute of Navigation,* vol. 56, pp. 429-441.

Brown, R.G. and P.Y.C. Hwang (1992). *Introduction to Random Signals and Applied Kalman Filtering, 2nd Ed*, John Wiley & Sons, New York.

Carlson, C.R., J.C. Gerdes and J.D. Powell (2002) "Practical Position and Yaw Rate Estimation with GPS and Differential Wheel Speeds" in *Proceedings of AVEC2002, the 6th International Symposium on Advanced Vehicle Control,* September, 2002, Hiroshima, Japan.

Carlson, C.R.(2003) *Estimation with Applications for Automobile Dead Reckoning and Control*, Ph.D Thesis, Stanford University, USA.

Cannon, M.E. (1990) "High-Accuracy GPS Semikinematic Positioning: Modeling and Results", *Navigation, Journal of The Institute of Navigation*, vol. 37, no.1, Alexandria, VA., pp. 53-64.

Cannon, M.E. (1991) *Airborne GPS/INS with an Application to Aerotriangulation,* PhD Thesis, UCGE Report #20040, Department of Geomatics Engineering, University of Calgary, Canada

Chen, D. (1994) *Development of a Fast Ambiguity Search Filter (FASF) Method for GPS Carrier Phase Ambiguity Resolution*, PhD Thesis, Department of Geomatics Engineering, University of Calgary, Canada

Dissanayake, G., S. Sukkarieh, E. Nebot and H. DurrantWhyte (2001) "The aiding of a Low Cost Strapdown Inertial Measurement Unit using Vehicle Model Constraints for Land vehicle Applications", *IEEE Transactions on Robotics and Automation*, vol.17, no. 5, pp. 731-747.

El-sheimy, N. (2004) *Inertial Techniques and INS/GPS Integration*, ENGO 623 Course Notes, Department of Geomatics Engineering, University of Calgary, Canada

Farrell, J.A. and M.J. Barth (1998) *The Global Positioning System and Inertial Navigation,* McGraw-Hill.

Farrell, J.A., T.D. Givargis and M.J. Barth (2000) "Real-Time Differential Carrier Phase GPS-Aided INS", *IEEE Transactions on Control Systems Technology*, vol. 8, no. 4, pp. 709-720.

Gao, Y., E.J. Krakiwski, M.A. Abousalem and J.F. McLellan (1993) "Comparison and Analysis of Centralized, Decentralized, and Federated Filters", *Navigation, Journal of The Institute of Navigation,* Alexandria, VA, U.S.A., vol. 40, no. 1, pp. 69-86.

Gelb, A. (1974). *Applied Optimal Estimation*. The Massachusetts Institute of Technology Press.

Grewal, M.S., L.R. Weil and A.P. Andrews(2001) *Global Positioning Systems, Inertial Navigation, and Integration*, A John Wiley & Sons, New York.

Godha, S.(2006) *Performance Evaluation of Low Cost MEMS-Based IMU Integrated With GPS for Land Vehicle Navigation Application,* M.Sc. thesis, Department of Geomatics Engineering, University of Calgary, Canada (Available at http://www.geomatics.ucalgary.ca/research/publications/GradTheses.html)

Han, S. and C. Rizos (1997) "Comparing GPS Ambiguity Resolution Techniques" *GPS World*, October, 1997, Advanstar Communications, pp. 54-61.

Harvey, R.S. (1998) *Development of a Precision pointing System Using an Integrated Multi-Sensor Approach,* M.Sc. thesis, Department of Geomatics Engineering, University of Calgary, Canada.

Hatch, R. (1994) "Comparison of Several AROF Kinematic Techniques" in *Proceedings of ION GPS 1994,* U.S. Institute of Navigation, Alexandria, VA, USA, pp. 363-370.

Hay, C. (2005) "Turn, Turn, Turn Wheel-Speed Dead Reckoning for Vehicle Navigation", *GPS World*, October, 2005, pp 37-42.

Hein, G. and W. Werner (1995) "Comparison of Different On-The-Fly Ambiguity Resolution Techniques" in *Proceedings of GPS 1995*, U.S. Institute of Navigation, Alexandria, VA., pp. 1137-1144.

Hofmann-Wellenhof, B, H. Lichtenegger and J. Collins (1997). GPS theory and practice, Springer-Verlag.

Jekeli, C. (2000) *Inertial Navigation Systems with Geodetic Applications*, Walter de Gruyter, New York, NY, USA.

Kaplan, E.D and C.J. Hegarty (2006). *Understanding GPS Principles and Applications* (2nd ed.), Artech House, Norwood, MA, USA.

Kubo, J., T. Kindo, A. Ito and S. Sugimoto (1999) "DGPS/INS/Wheel Sensor Integration for High Accuracy Land-Vehicle Positioning" in *Proceedings of ION GPS 1999,* September, Nashville, TN, pp. 555-564

Lachapelle, G. (2003) *Advanced GPS Theory and Applications,* ENGO 625 Course Notes, Department of Geomatics Engineering, University of Calgary, Canada.

Lachapelle, G., M.G. Petovello and H.Zhang (2003). Assessment of a Motorola Single-Axis IMU, Technical Report, Department of Geomatics Engineering, University of Calgary, 20 pages.

Liu, J. (2003).) *Implementation and analysis of GPS Ambiguity Resolution Strategies in Single and Multiple Reference Station Scenarios*, M.S.c. Thesis, Department of Geomatics Engineering, University of Calgary, Canada.

Masson, A., D. Burtin and M. Sebe (1996). "Kinematic DGPS and INS Hybridization for Precise Trajectory Determination" in *Proceedings of GPS 1996*, pp. 965-973, The Institute of Navigation, Alexandria, VA,USA

Maybeck, P. (1979) *Stochastic Models, Estimation and Control*, Volume 1, *Academic Press,* New York, NY, USA.

Misra, P. and P. Enge (2001) *Global positioning system- Signals, Measurements, and performance*, Ganga-Jamuna Press.

Numajima, T., M. Kihara, Y. Kubo and T. Seki (2002) "INS/DGPS/VMS Integration for In-motion Alignment" in *Proceedings of ION GPS 2002*, September, Portland, VR, pp. 556-564.

Omerbashich, M. (2002) "Integrated INS/GPS Navigation From Popular Perspective" *Journal of Air Transportation*, vol. 7, no.2, 103-118.

Petovello, M.G. (2003) *Real-Time Integration of Tactical Grade IMU and GPS for High-Accuracy Positioning and Navigation,* PhD Thesis, Department of Geomatics Engineering, University of Calgary, Canada (Available at http://www.geomatics.ucalgary.ca/research/publications/GradTheses.html)

Petovello, M.G., G. Lachapelle and M.E. Cannon (2005) "Using GPS and GPS/INS systems to Assess Relative Antenna Motion Onboard an Aircraft Carrier for Shipboard Relative GPS" *in Proceedings of ION NTM 2005*, January 2005, San Diego, CA, pp. 219-229.

Ray, L.R. (1995) "Nonlinear State and Tire Force Estimation for Advanced Vehicle Control", *IEEE Transactions on Control System Technology*, vol.3, no. 1, 1995, pp. 117-124.

Redmill, K.A., T. Kitajima and U. Ozguner (2001) "DGPS/INS Integrated Positioning for Control of Automated Vehicle", *IEEE Intelligent Transportation Systems Conference Proceedings, August, Oakland, CA, USA*, pp. 172-178.

Rogers R.M. (2000) *Applied Mathematics in Integrated Navigation Systems.* American Institute of Aeronautics and Astronautics, Inc., Reston, VA, USA

Savage, P.G. (2000) Strapdown Analytics, Volume 1. Strapdown Associates, Inc, Maple Plain, MA, USA.

Stephen, J. (2000) *Development of a Multi-Sensor GNSS Based Navigation system*, M.S.c. Thesis, Department of Geomatics Engineering, University of Calgary, Canada (Available at http://www.geomatics.ucalgary.ca/research/publications/GradTheses.html)

Salychev, O.S., V.V. Vornov, M.E. Cannon, R. Nayak and G. Lachapelle (2000) "Low Cost INS/GPS Integration: Concepts and Testing" *in Proceedings of the National Technical Meeting,* pp. 98-105, 2000, U.S. Institute of Navigation, Alexandria, VA.

Scherzinger, B.M. (2000) "Precise Robust Positioning with Inertial/GPS RTK" *in Proceedings of GPS 2000*,   pp. 155-162., U.S. Institute of Navigation, Alexandria, VA.

Scherzinger, B.M. (2002) "Robust Positioning with Single Frequency Inertially Aided RTK" *in Proceedings of ION NTM 2002* pp. 911-917.   Alexandria, VA, USA). pp. 911-917.

Scherzinger, B.M. (2001) "Robust Intertially-Aided RTK Positioning Measurement" in *Proceedings of KIS 2001*. Department of Geomatics Engineering, University of Calgary, Canada.

Scherzinger, B.M. (2004) *Estimation with Application to Navigation*, ENGO 699.11 Course Notes, Department of Geomatics Engineering, University of Calgary, Canada.

Schwarz, K.P. and M. Wei (1999) *INS/GPS Integration for Geodetic Applications*, ENGO 623 Course Notes, Department of Geomatics Engineering, The University of Calgary, Canada.

Schwarz, K.P., M. Wei and M. Van Gelderen (1994) "Aided Versus Imbedded A Comparison of Two Approaches to GPS/INS Integration" in *Proceedings of the IEEE PLAN, 1994*, pp. 314-322.

Skaloud, J. (1998) "Reducing The GPS Ambiguity Search Space By Including Inertial Data" in *Proceedings of ION GPS 1998*, The Institute of Navigation, Alexandria, VA., pp. 2073-2080.

Shin, E.H. (2001) *Accuracy Improvement of Low Cost INS/GPS for Land Applications*, M.Sc. thesis, Department of Geomatics Engineering, University of Calgary, Canada (Available at http://www.geomatics.ucalgary.ca/research/publications/GradTheses.html)

Shin, E.H. (2005) *Estimation Techniques for Low-Cost Inertial Navigation*, Ph.D thesis, Department of Geomatics Engineering, University of Calgary, Canada (Available at http://www.geomatics.ucalgary.ca/research/publications/GradTheses.html)

Sukkarieh, S. (2000) *Low Cost, High Integrity, Aided Inertial Navigation System for Autonomous Vehicles*, Ph.D Thesis, Australian Centre for Field Robotics, The University of Sydney, Australia

Teunissen, P.J.G., and A. Kleusberg (1996). *GPS for Geodesy*. Springer press.

Tseng, H.E., B. Ashrafi, D. Madau, T.A. Brown and D. Recker (1999) "The Development of Vehicle Stability Control at Ford", *IEEE/ASME Transactions on Mechatronics*, vol.4, no.4, pp. 223-234.

Woolven, S. and B.M. Scherzinger (1997) "POS/MV-System Performance with Inertial/RTK GPS Integration" in *Proceedings of IEEE PLAN 1997*, pp. 1104-1108.

Wang, C.C. (2003) *Development of a Low-cost GPS-based Attitude Determination System*, M.Sc. thesis, Department of Geomatics Engineering, University of Calgary, Canada. (http://www.geomatics.ucalgary.ca/research/publications/GradTheses.html)

Walker, J.S. (1999) *A Primer on Wavelet and Their Scientific Applications,* Chapman & Hall CRC.

Zhang, H.T., M.G. Petovello and M.E. Cannon (2005) "Performance Comparison of Kinematic GPS Integrated with Different Tactical Level IMUs" *in Proceedings of ION NTM 2005,* January, San Diego, CA, USA, pp. 243-254.

Appendix A

Skew-Symmetric Matrix, Gravity Vector and Tensor of Gravity Gradients

- **Symmetric Matrix**

Assuming a 3×1 vector $a = \begin{bmatrix} x & y & z \end{bmatrix}^T$

The skew-symmetric matrix of vector a is defined by

$$A = \begin{bmatrix} 0 & -z & y \\ z & 0 & -x \\ -y & x & 0 \end{bmatrix} \tag{A.1}$$

- **Normal Gravity Vector**

The normal gravity vector is defined by

$$\gamma^e \approx -\frac{kM}{\left|r^e\right|^3} r^e - \Omega_{ie}^e \Omega_{ie}^e r^e \tag{A.2}$$

where

k is the gravitational constant,

M is the mass of the Earth,

$r^e = \begin{bmatrix} r_y & r_y & r_z \end{bmatrix}$ is the position in ECEF frame,

$\left|r^e\right| = \sqrt{r_x^2 + r_y^2 + r_z^2}$,

$$\Omega^e_{ie} = \begin{bmatrix} 0 & -\omega_e & 0 \\ \omega_e & 0 & 0 \\ 0 & 0 & 0 \end{bmatrix}, \text{ and}$$

ω_e is the rotation rate of the Earth

- **Tensor of Gravity Gradients**

$$N^e = \begin{bmatrix} \dfrac{kM}{R^3}\left(\dfrac{3r_x^2}{R^2}-1\right)+\omega_e^2 & \dfrac{kM}{R^3}\dfrac{3r_x r_y}{R^2} & \dfrac{kM}{R^3}\dfrac{3r_x r_z}{R^2} \\[2em] \dfrac{kM}{R^3}\dfrac{3r_x r_y}{R^2} & \dfrac{kM}{R^3}\left(\dfrac{3r_y^2}{R^2}-1\right)+\omega_e^2 & \dfrac{kM}{R^3}\dfrac{3r_y r_z}{R^2} \\[2em] \dfrac{kM}{R^3}\dfrac{3r_x r_z}{R^2} & \dfrac{kM}{R^3}\dfrac{3r_y r_z}{R^2} & \dfrac{kM}{R^3}\left(\dfrac{3r_z^2}{R^2}-1\right) \end{bmatrix} \quad (A.2)$$

Appendix B

Reliability Test in the Kalman Filter

The reality test in the Kalman filter is based on the analysis of the innovation sequence.

The innovation sequence is defined by

$$v = z_k - H_k \cdot x_k^-$$
(B.1)

The innovation sequence follows a zero mean Gaussian distribution. The covariance

matrix of the innovation sequence is

$$Q_v = HP^- H^T + R$$
(B.2)

Two hypotheses can be made by

$$H_0 : E[v] = 0$$
$$H_1 : E[v] = \nabla$$
(B.3)

where ∇ is the model error vector.

Assuming a single blunder, the blunder vector is defined by

$$m_{ki} = \begin{bmatrix} 0 & ... & 0 & 1 & 0 & ... & 0 \end{bmatrix}^T$$
(B.4)

On the basis of the null hypothesis H_0 and the alternative hypothesis H_1, the test

statistics is given by

$$t_{ki} = \frac{m_{ki}^T Q_v^{-1} v}{\sqrt{(Q_v^{-1})_{ii}}}$$
(B.5)

The distribution of the single blunder test statistics follows Gauss normal distribution,

$$\begin{cases} t_k \big|_{H_0} \to N(0,1) \\ t_k \big|_{Ha} \to N(\delta_0,1) \end{cases}$$

<div align="right">(B.6)</div>

where δ_0 is the non-centrality parameter, $\delta_0 = \left| \nabla_{k_i} \right| \sqrt{(Q_k^{-1})_{ii}}$

Appendix C

Supplementary Results for Real-Time Test
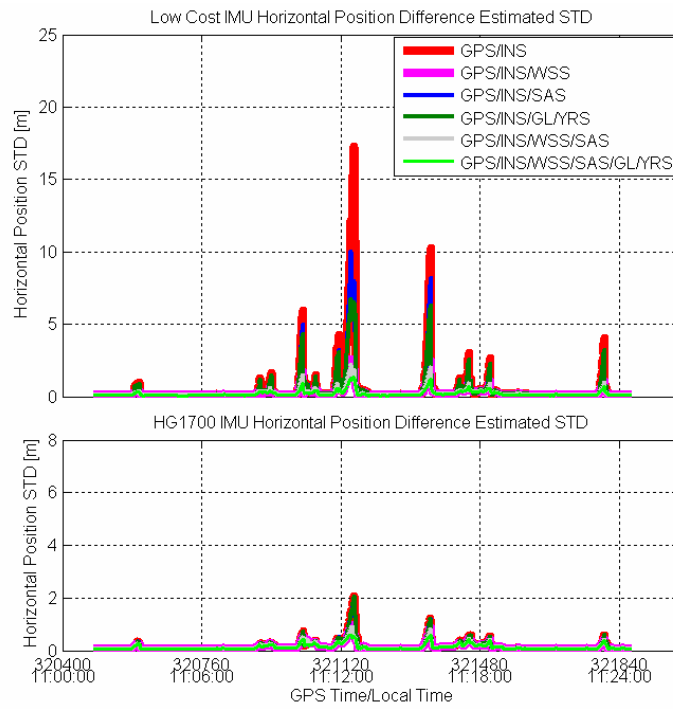
Figure A 1 Estimated position differences with respect to the reference of all integration

strategies (Suburban area test)
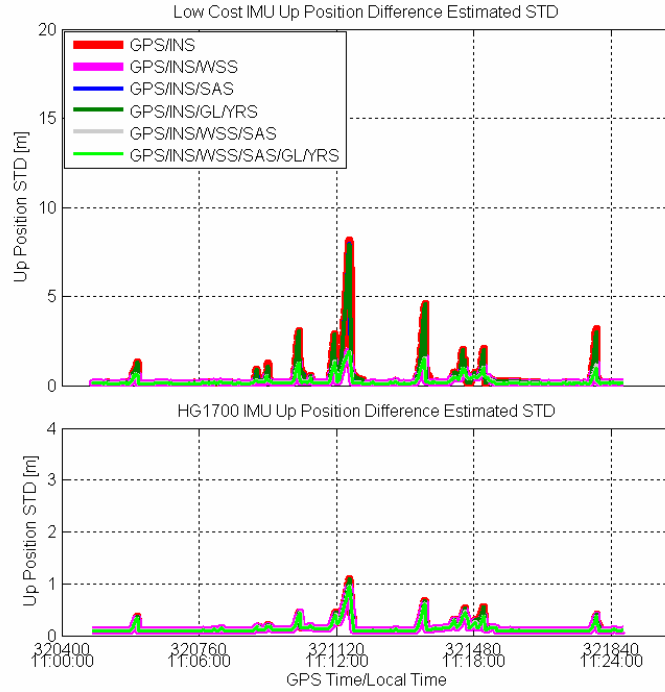
Figure A 2 Estimated standard deviations of the up position difference of all integration
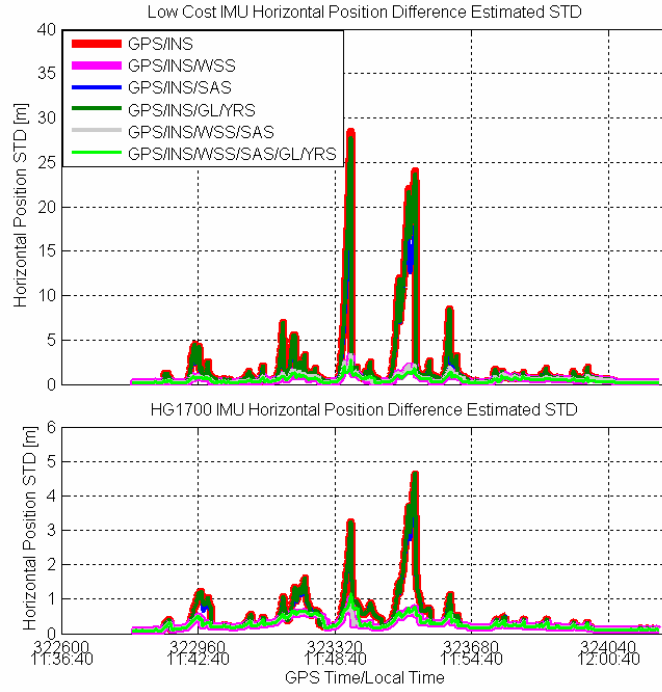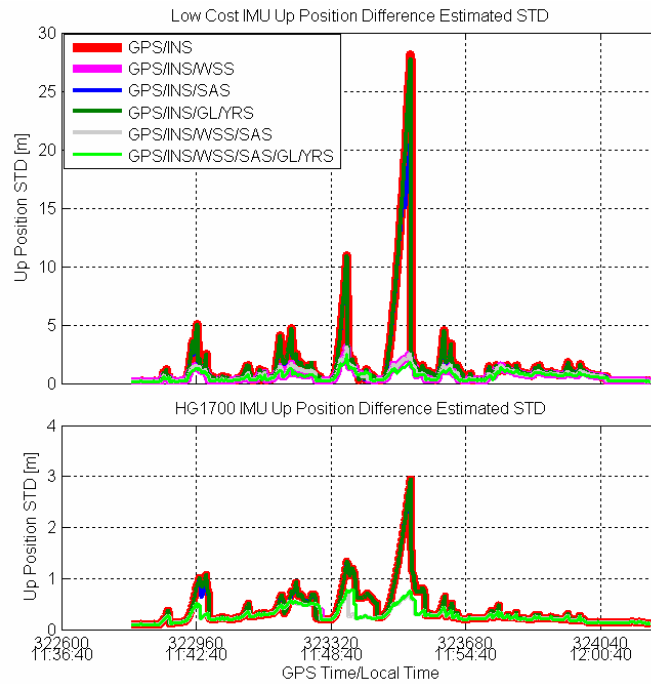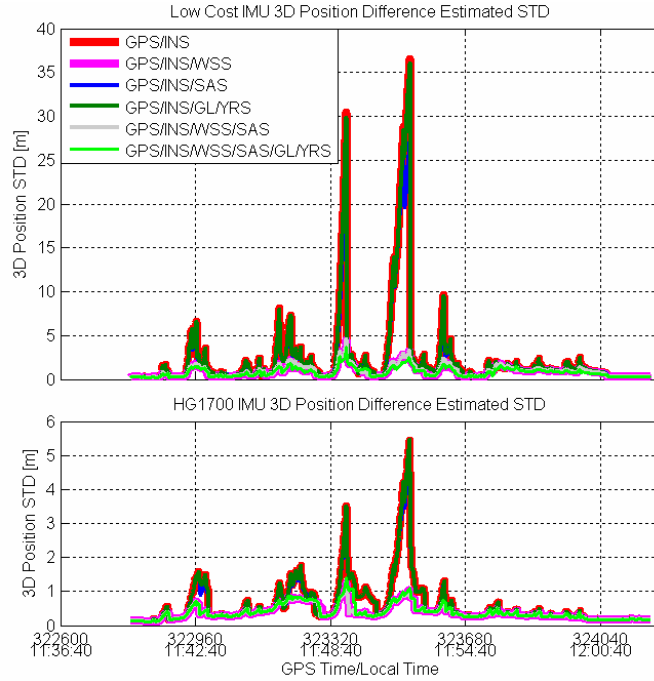
strategies (Suburban area test)
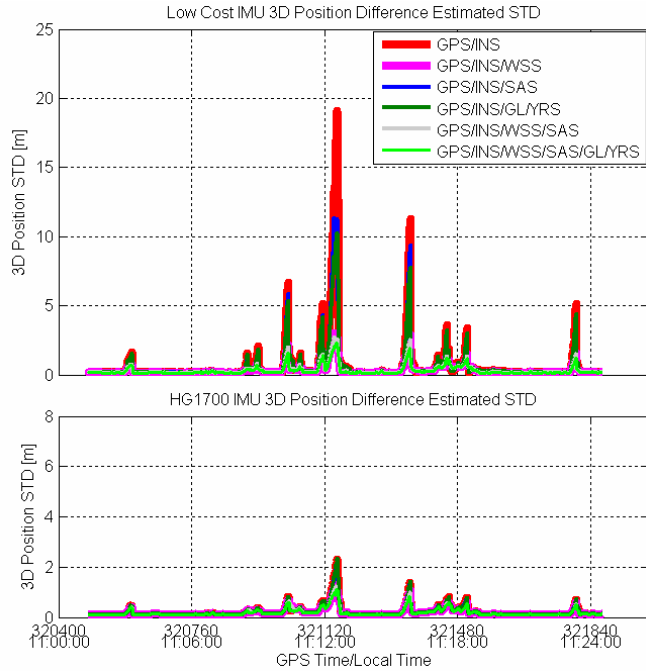
Figure A 3 Estimated standard deviations of the 3D position difference for all integration

strategies (Suburban area test)
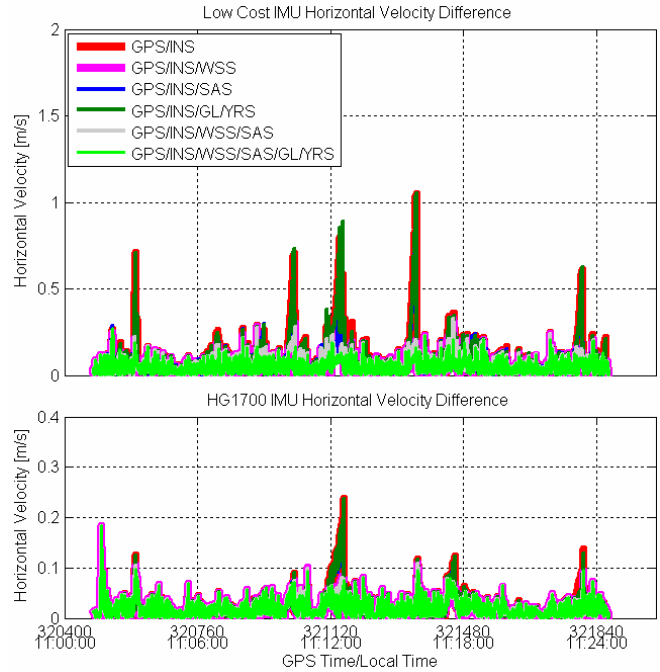
Figure A 4 Horizontal Velocity differences with respect to GPS/CIMU for all integration

strategies (Suburban area test)
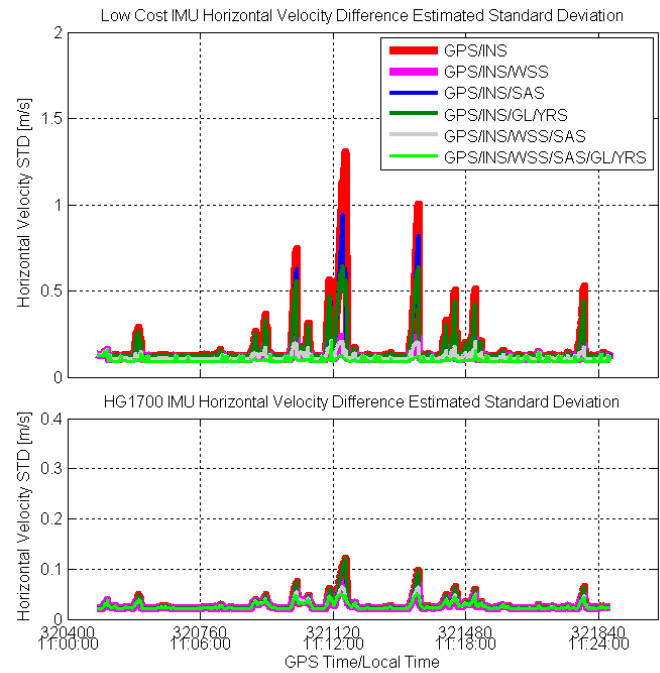
Figure A 5 Horizontal estimated standard deviations of the horizontal velocity difference
for all integration strategies (Suburban area test)
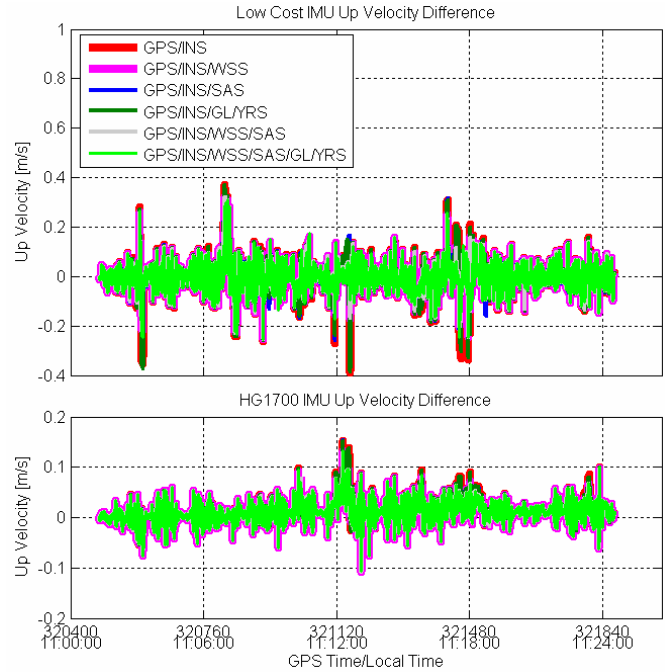
Figure A 6 Up velocity differences with respect to the reference for all integration

strategies (Suburban area test)
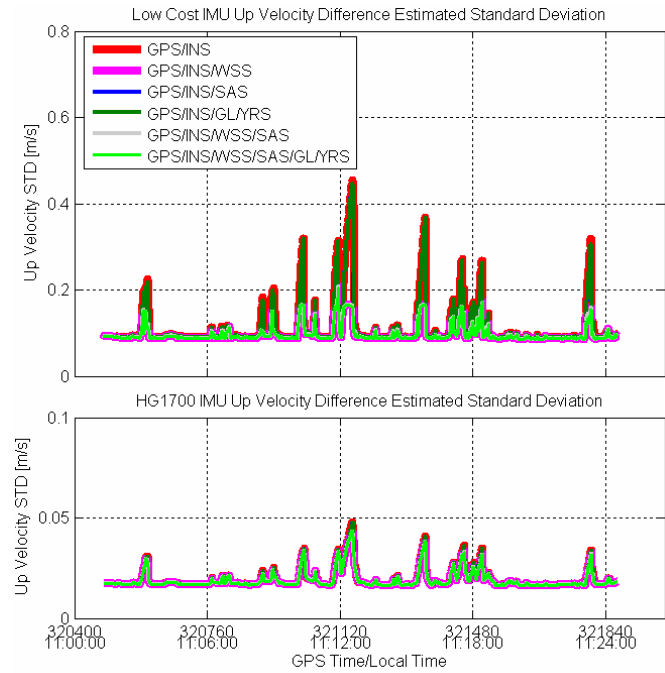
Figure A 7 Estimated standard deviations of up velocity difference for all integration

strategies for the real-time test in suburban area
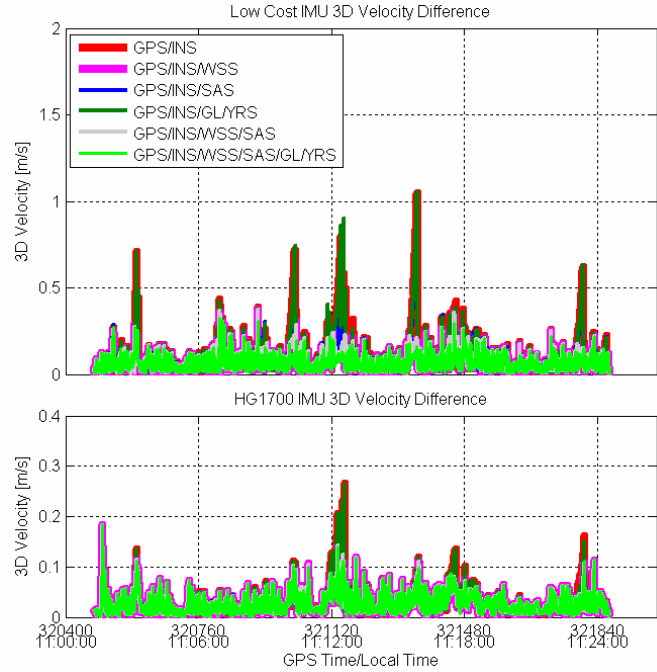
Figure A 8 3D velocity differences with respect to the reference of all integration

strategies for the real-time test in suburban area
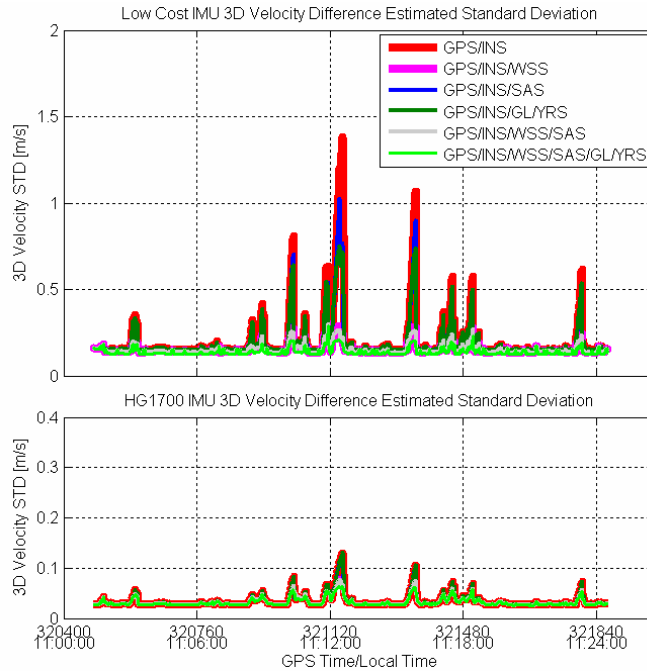
Figure A 9 Estimated standard deviations of 3D velocity difference for all integration

strategies for real-time test in suburban area

Figure A 10 Estimated standard deviations of horizontal position difference for all
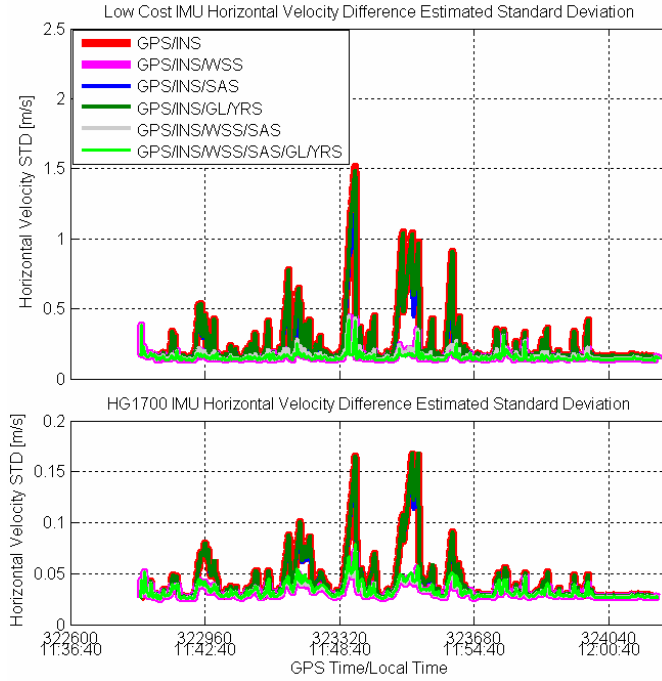
integration strategies for real-time pseudo-urban area test

Figure A 11 Estimated standard deviations of the up position difference for all integration

strategies (Pseudo-urban area test)

Figure A 12   Estimated 3D position differences of all integration strategies

(Pseudo-urban area test)
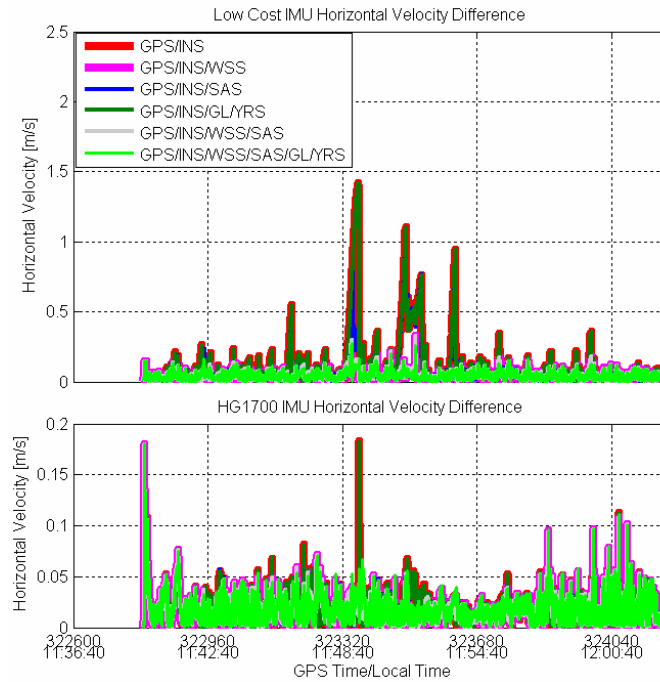
Figure A 13 Horizontal velocity differences of all integration strategies (Pseudo-urban

area test)

Figure A 14 Estimated standard deviations of the horizontal velocity difference for all

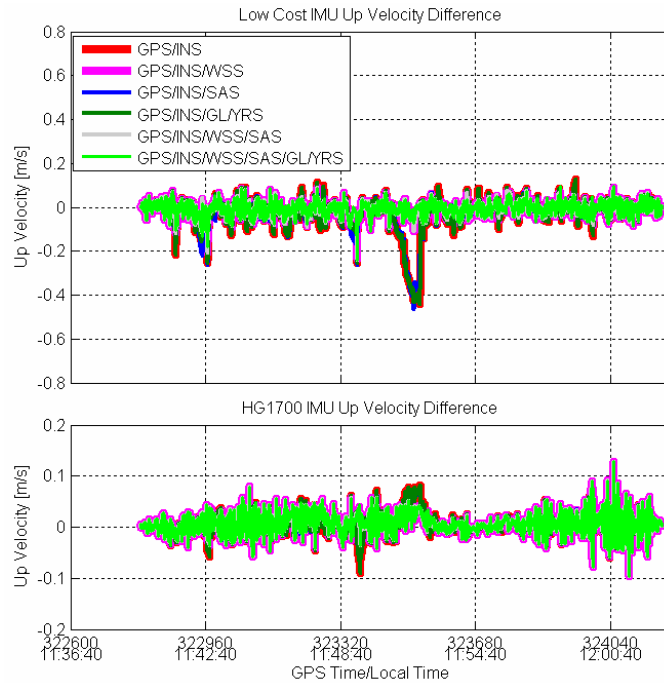integration strategies (Pseudo-urban area test)

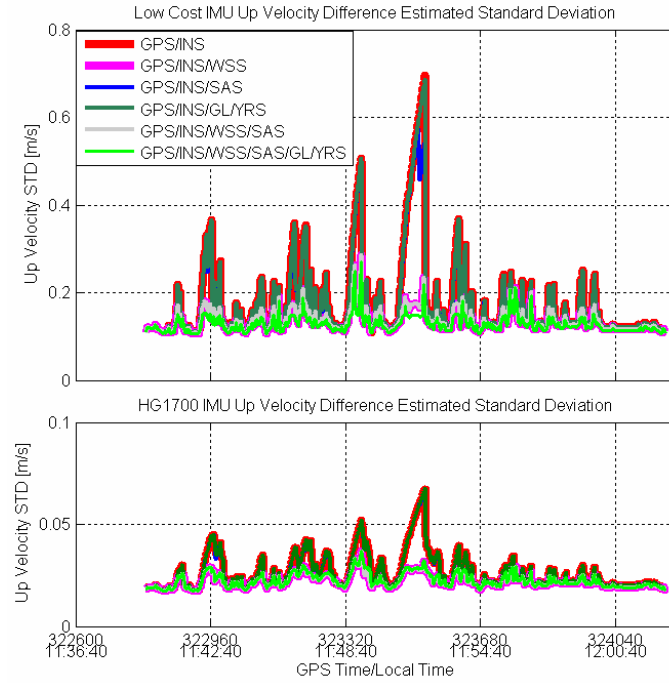Figure A 15 Up velocity differences of all integration strategies (Pseudo-urban area test)

Figure A 16 Estimated standard deviations of up velocity difference for all integration strategies (Pseudo-urban area test)
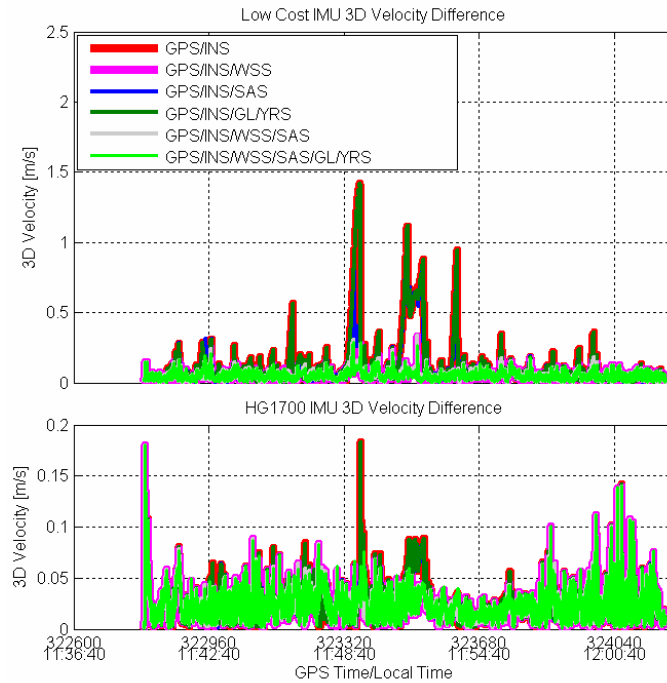

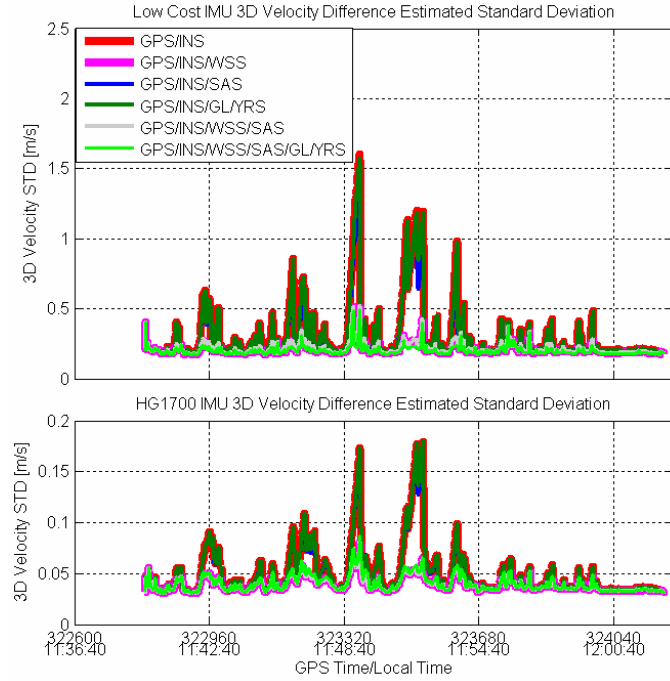Figure A 17 3D velocity differences of all integration strategies (Pseudo-urban area test)

Figure A 18 Estimated standard deviations of 3D velocity for all integration strategies
(Pseudo-urban area test)